



MetOceanWorks

Metocean Data Overview

North Sea I Offshore Wind Farm

24 October 2024

MetOceanWorks Reference:

Energinet_C00001_R02_Metocean_Data_Overview

Commercial in Confidence

Andrew Watson MSc CSci CMarSci MIMarEST

Senior Metocean Consultant & Director

andrew.watson@metoceanworks.com

Contact +44 (0)7763 896635

MetOceanWorks Ltd is Registered in England and Wales, Company Number 8078702

Revision	Description	Prepared	Reviewed	Date
R02	Final	Dave Quantrell	Andrew Watson	24 October 2024
R01	Draft	Jamie Hernon Dave Quantrell Andrew Watson	Andrew Berkeley Dave Quantrell	14 August 2024



Table of contents

1	Definitions	9
1.1	Units and Conventions.....	9
1.2	Glossary of commonly used metocean terms	9
2	Introduction.....	11
2.1	Background.....	11
2.2	Document Structure	12
2.3	Data Deliverables.....	13
2.4	Metocean Overview	14
3	Bathymetry and Coastline	17
3.1	Bathymetry	17
3.2	Coastline	20
4	Winds	21
4.1	Introduction	21
4.2	Measured Wind Data.....	21
4.3	ERA5 Modelled Data.....	22
4.4	Vertical Interpolation and Extrapolation	25
4.5	Model Calibration and Validation	26
5	Hydrodynamics	43
5.1	Measured Hydrodynamic Data	43
5.2	Modelling Software	44
5.3	Model Boundary Conditions and Spatial Extent	45
5.4	Model Sensitivity Testing.....	46
5.5	Final Model Parameter Settings	51
5.6	Hindcast Uniformity.....	51
5.7	Model Validation	52
6	Waves.....	67
6.1	Measured Wave Data	67
6.2	Modelling Software	68
6.3	Model Boundary Conditions.....	69
6.4	Model Sensitivity Testing.....	69



6.5	Final Model Parameter Settings	77
6.6	Model Validation	77
7	Additional Parameters	93
7.1	Atmospheric Data	93
7.2	Lightning Strike Data.....	93
7.3	Seawater Data.....	93
	References	94
	Appendix A. Bathymetry Merging.....	96
	Appendix B. Wind Field Calibration	102
B.1	Introduction	102
B.2	Measured Wind Data.....	102
B.3	ERA5 Modelled Data	103
B.4	Calibration at 10 m	104
B.5	Calibration at Hub Height	110
B.6	Theoretical Wind Profiles	116
	Appendix C. Wind Averaging Periods.....	117
C.1	Overview	117
C.2	Diagnostic Plots	119
C.3	Averaging Period Conversion.....	120
	Appendix D. Measured Currents	121
D.1	Introduction	121
D.2	Dataset Overview	121
D.3	Data Quality Review	122
D.4	Dataset Comparisons.....	124
D.5	Vertical Profile Shapes: Metocean Guidelines.....	137
D.6	Depth Averages.....	139
D.7	Vertical Profile Shapes	142
	Appendix E. Zero-crossing Period Validation	162
E.1	Overview	162
E.2	Example Spectrum	163
E.3	Validation.....	165



E.4	Summary	166
Appendix F. Spectral Wave Validation		167
F.1	Introduction	167
F.2	Measured Spectra	167
F.3	Mean Spectra	168
F.4	Selected Events	181
Appendix G. JONSWAP Fitting		202
G.1	Introduction	202
G.2	Partitioning	202
G.3	Fitting of Spectral Shapes	210



List of Figures

Figure 2-1: Project development area	11
Figure 2.2: Negative and positive phases of the North Atlantic Oscillation (Source: ossfoundation.us).	14
Figure 2.3: Tidal patterns in the North Sea (modified after [7]).	15
Figure 2.4: Circulation currents in the North Sea (modified after [7]).	16
Figure 3-1: Energinet multi beam bathymetry data.	17
Figure 3-2: EMODnet 2020 bathymetry dataset local to the site.	18
Figure 3-3: EMODnet 2022 bathymetry dataset local to the site.	19
Figure 3-4: Elevation difference between EMODnet 2020 and multi beam survey data.	20
Figure 4-1: Wind measurement locations.	22
Figure 4-2: Geopotential height of lowest 11 model levels, example location.	23
Figure 4-3: Wind speed at 10 m from ERA5 single level parameters (Params) and model levels (Levels), example location.	24
Figure 4-4: Wind speed at 100 m from ERA5 single level parameters (Params) and at 106.54 m from ERA5 model levels (Levels), example location.	24
Figure 4-5: Validation scatter with overlaid QQ plot of raw ERA5 10 m wind speeds at NSI-1-LB.	26
Figure 4-6: Validation plot of calibrated ERA5 wind speeds, 10 m ASL, NSI-1-LB.	27
Figure 4-7: Validation plot of calibrated ERA5 wind speeds, 10 m ASL, NSI-2-LB.	28
Figure 4-8: Validation plot of calibrated ERA5 wind speeds, 10 m ASL, NSI-3-LB.	29
Figure 4-9: Validation plot of calibrated ERA5 wind speeds, 10 m ASL, EINS-1-LB.	30
Figure 4-10: Validation plot of calibrated ERA5 wind speeds, 10 m ASL, EINS-2-LB.	31
Figure 4-11: Validation plot of calibrated ERA5 wind speeds, 10 m ASL, Thor LiDAR.	32
Figure 4-12: Validation plot of calibrated ERA5 wind speeds, 10 m ASL, FINO 1.	33
Figure 4-13: Validation plot of calibrated ERA5 wind speeds, 10 m ASL, FINO 3.	34
Figure 4-14: Validation plot of calibrated ERA5 wind speeds, 150 m ASL, NSI-1-LB.	35
Figure 4-15: Validation plot of calibrated ERA5 wind speeds, 150 m ASL, NSI-2-LB.	36
Figure 4-16: Validation plot of calibrated ERA5 wind speeds, 150 m ASL, NSI-3-LB.	37
Figure 4-17: Validation plot of calibrated ERA5 wind speeds, 150 m ASL, EINS-1-LB.	38
Figure 4-18: Validation plot of calibrated ERA5 wind speeds, 150 m ASL, EINS-2-LB.	39
Figure 4-19: Validation plot of calibrated ERA5 wind speeds, 150 m ASL, Thor LiDAR.	40
Figure 4-20: Validation plot of calibrated ERA5 wind speeds, 150 m ASL, IJmuiden LiDAR.	41
Figure 4-21: Validation plot of calibrated ERA5 wind speeds, 150 m ASL, Dogger Bank East LiDAR.	42
Figure 5-1: Measured datasets considered for hydrodynamic model validation.	44
Figure 5-2 MIKE21 flexible model mesh.	45
Figure 5-3. Hydrodynamic mesh with low resolution.	46
Figure 5-4. Hydrodynamic mesh with medium resolution.	47
Figure 5-5. Hydrodynamic mesh with high resolution.	47
Figure 5-6. Results of model runs with differing mesh resolutions, at the Centre Array. Top row = water level, middle row = current speed, bottom row = current direction. Left column Medium Resolution vs. High Resolution. Middle column High Resolution vs. Low Resolution. Right column = Low Resolution vs. Medium Resolution.	48
Figure 5-7. Results of model runs with differing mesh resolutions, at the Centre West. Top row = water level, middle row = current speed, bottom row = current direction. Left column Medium Resolution vs. High	



Resolution. Middle column High Resolution vs. Low Resolution. Right column = Low Resolution vs. Medium Resolution.....	49
Figure 5-8. Results of model runs with differing mesh resolutions, at ECC Central. Top row = water level, middle row = current speed, bottom row = current direction. Left column Medium Resolution vs. High Resolution. Middle column High Resolution vs. Low Resolution. Right column = Low Resolution vs. Medium Resolution.....	50
Figure 5-9: Comparison of measured and modelled water levels at Hvide Sande.....	53
Figure 5-10: Comparison of measured and modelled water levels at Thorsminde.....	53
Figure 5-11: Comparison of measured and modelled water levels at NSI-1-CP.....	54
Figure 5-12: Comparison of measured and modelled water levels at NSI-2-CP.....	54
Figure 5-13: Scatter and rose validation of depth-average current speed, NSI-1-CP.....	55
Figure 5-14: Time-Series validation of depth-average current speed, NSI-1-CP.....	56
Figure 5-15: Scatter and rose validation of depth-average current speed, NSI-1-LB.....	57
Figure 5-16: Time-Series validation of depth-average current speed, NSI-1-LB.....	58
Figure 5-17: Scatter and rose validation of depth-average current speed, NSI-2-CP.....	59
Figure 5-18: Time-Series validation of depth-average current speed, NSI-2-CP.....	60
Figure 5-19: Scatter and rose validation of depth-average current speed, NSI-2-LB.....	61
Figure 5-20: Time-Series validation of depth-average current speed, NSI-2-LB.....	62
Figure 5-21: Scatter and rose validation of depth-average current speed, NSI-3-CP.....	63
Figure 5-22: Time-Series validation of depth-average current speed, NSI-3-CP.....	64
Figure 5-23: Scatter and rose validation of depth-average current speed, NSI-3-LB.....	65
Figure 5-24: Time-Series validation of depth-average current speed, NSI-3-LB.....	66
Figure 6-1: Locations of the wave measurement devices.....	68
Figure 6-2: Wave model domains.....	69
Figure 6-3. Results of model runs with differing mesh resolutions, at the Centre Array. Top row = significant wave height, middle row = mean zero-crossing wave period, bottom row = mean wave direction. Left column Medium Resolution vs. High Resolution. Middle column High Resolution vs. Low Resolution. Right column = Low Resolution vs. Medium Resolution.....	70
Figure 6-4. Results of model runs with differing mesh resolutions, at the Centre West. Top row = significant wave height, middle row = mean zero-crossing wave period, bottom row = mean wave direction. Left column Medium Resolution vs. High Resolution. Middle column High Resolution vs. Low Resolution. Right column = Low Resolution vs. Medium Resolution.....	71
Figure 6-5. Results of model runs with differing mesh resolutions, at ECC Central. Top row = significant wave height, middle row = mean zero-crossing wave period, bottom row = mean wave direction. Left column Medium Resolution vs. High Resolution. Middle column High Resolution vs. Low Resolution. Right column = Low Resolution vs. Medium Resolution.....	72
Figure 6-6. Results of model runs with differing numbers of directional bins, at the Centre Array. Top row = significant wave height, middle row = mean zero-crossing wave period, bottom row = mean wave direction. Left column 36 directional bins vs. 48 directional bins. Middle column 48 directional bins vs. 24 directional bins. Right column = 24 directional bins vs. 36 directional bins.....	74
Figure 6-7. Results of model runs with differing numbers of directional bins, at the Centre West. Top row = significant wave height, middle row = mean zero-crossing wave period, bottom row = mean wave direction. Left column 36 directional bins vs. 48 directional bins. Middle column 48 directional bins vs. 24 directional bins. Right column = 24 directional bins vs. 36 directional bins.....	75



Figure 6-8. Results of model runs with differing numbers of directional bins, at ECC Central. Top row = significant wave height, middle row = mean zero-crossing wave period, bottom row = mean wave direction. Left column 36 directional bins vs. 48 directional bins. Middle column 48 directional bins vs. 24 directional bins. Right column = 24 directional bins vs. 36 directional bins. 76

Figure 6-9. NSI-1 LiDAR Buoy, Hm0 validation. 79

Figure 6-10. NSI-1 LiDAR Buoy, Tp validation. 80

Figure 6-11. NSI-1 LiDAR Buoy, Tm02 validation. 80

Figure 6-12. NSI-2 LiDAR Buoy, Hm0 validation. 81

Figure 6-13. NSI-2 LiDAR Buoy, Tp validation. 82

Figure 6-14. NSI-2 LiDAR Buoy, Tm02 validation. 82

Figure 6-15. NSI-3 LiDAR Buoy, Hm0 validation. 83

Figure 6-16. NSI-3 LiDAR Buoy, Tp validation. 84

Figure 6-17. NSI-3 LiDAR Buoy, Tm02 validation. 84

Figure 6-18. EINS-3 Wave Buoy, Hm0 validation. 85

Figure 6-19. EINS-3 Wave Buoy, Tp validation. 86

Figure 6-20. EINS-3 Wave Buoy, Tm02 validation. 86

Figure 6-21. EINS-4 Wave Buoy, Hm0 validation. 87

Figure 6-22. EINS-4 Wave Buoy, Tp validation. 88

Figure 6-23. EINS-4 Wave Buoy, Tm02 validation. 88

Figure 6-24. EINS-5 Wave Buoy, Hm0 validation. 89

Figure 6-25. EINS-5 Wave Buoy, Tp validation. 90

Figure 6-26. EINS-5 Wave Buoy, Tm02 validation. 90

Figure 6-27. FINO3, Hm0 validation. 91

Figure 6-28. Nymindegab, Hm0 validation. 92



List of Tables

Table 4-1: Measured datasets used for wind model validation.	21
Table 5-1: Measured datasets considered for hydrodynamic model validation.	43
Table 5-2: Final model parameter settings.	51
Table 6-1: Measured datasets used for wave model validation.	67



1 Definitions

1.1 Units and Conventions

The following list describes the units and conventions used in this report. Unless stated otherwise, units have been expressed using the SI convention.

- Wind direction is expressed in compass points or degrees, relative to true North [$^{\circ}$ N], and describes the direction **from** which the winds are blowing.
- Wind speeds are expressed in metres per second [m/s].
- Wave direction is expressed in compass points or degrees, relative to true North [$^{\circ}$ N], and describes the direction **from** which the waves are propagating.
- Wave heights are expressed in metres [m].
- Wave periods are expressed in seconds [s].
- Current direction is expressed in compass points or degrees, relative to true North [$^{\circ}$ N], and describes the direction **towards** which the currents are flowing.
- Current speeds are expressed in metres per second [m/s].
- Water levels are expressed in metres [m] relative to LAT.
- Temperature is expressed in degrees Celsius [$^{\circ}$ C].
- Salinity is expressed in practical salinity units [PSU].
- Density is expressed in kilograms per metre cubed [kg/m³].
- Relative humidity unit is expressed as a percentage [%].
- Precipitation rate is expressed in millimetres per hour [mm/h].
- Solar radiation is expressed in watts per metre squared (W/m²).
- Positions are quoted relative to WGS 84 except where stated.
- All times are quoted in Coordinated Universal Time [UTC].
- 'Hydrodynamics' refers to both water levels and currents.

1.2 Glossary of commonly used metocean terms

The following list describes common metocean terms used throughout this report.

Winds	Description
ASL	Above Sea Level. Refers to the height of the wind measurements above sea level.
U _{3-hr}	Mean wind speed averaged over a 3-hour period at 10 m ASL.
Wind gust	Wind speeds persisting for less than 1 minute are generally termed wind gusts.
Wind speed	Magnitude of local wind flow. Must be accompanied by an elevation ASL and averaging period for valid interpretation.
Waves	Description
C _{max}	The maximum individual wave crest elevation occurring within a defined period.
C _{mp}	The most probable maximum individual wave crest elevation occurring within a storm.
H _{max}	The maximum individual wave height occurring within a defined period.
H _{mp}	The most probable maximum individual wave height occurring within a storm.



Metocean Data Overview – North Sea I Offshore Wind Farm

Hm0	Significant wave height. Approximately the average height of the highest one third of the waves in a defined period, estimated from the wave spectrum as $4\sqrt{m_0}$.
m_0, m_1, m_2	The zeroth, first and second moments of the wave spectrum respectively.
T_p	The spectral peak period. The period at which most energy is present in the wave spectrum.
T_{m02}	The mean zero-crossing wave period. Estimated from the wave spectrum as $\sqrt{m_0/m_2}$.
Wave crest elevation	The vertical distance between the still water level and the maximum elevation of an individual wave.
Wave height	The vertical distance between the minimum and maximum elevations of an individual wave.
Levels	Description
HAT	Highest Astronomical Tide. Maximum level of sea surface due to tidal forcing alone.
LAT	Lowest Astronomical Tide. Minimum level of sea surface due to tidal forcing alone.
MHW	Mean High Water. Mean of all high water levels.
MHWN	Mean High Water Neap. Mean high water level during neap phase of tidal cycle.
MHWS	Mean High Water Spring. Mean high water level during spring phase of tidal cycle.
MLW	Mean Low Water. Mean of all low water levels.
MLWN	Mean Low Water Neap. Mean low water level during neap phase of tidal cycle.
MLWS	Mean Low Water Spring. Mean low water level during spring phase of tidal cycle.
MSL	Mean Sea Level. Mean sea surface elevation over a prolonged period of time.
Still water level	Instantaneous water level in the absence of waves, but including water level variations due to tide and meteorologically induced forcing.
Surge level	Difference between the tidal level estimated by harmonic analysis/prediction and the actual level. Includes any errors due to failure to adequately resolve the tidal signal. Includes meteorologically induced storm surge.
Tidal level	Still water level relative to a defined datum due to astronomical forcing. Tidal elevations exclude all meteorologically induced forcing.
Currents	Description
Current speed	Magnitude of local current flow.
Residual current	Current driven by processes excluding astronomical forcing and wave induced motions.
Tidal current	Current driven by astronomical forcing.
Total current	Combination of tidal and residual current.

2 Introduction

2.1 Background

The Danish Energy Agency has tasked Energinet with undertaking site metocean conditions assessments for the development of the offshore wind farm area North Sea I. Figure 2-1 shows the location of the wind farm area in the North Sea off the west coast of Jutland.

To support the development of offshore wind farms within the North Sea I area, Energinet has contracted MetOceanWorks to characterise the site metocean conditions for the area. The results of the Site Metocean Conditions Assessment will be used for the Front-End Engineering and Design (FEED) of offshore wind turbine generators (WTG) and other support structures for the offshore wind farms, particularly in early-stage integrated load analyses.

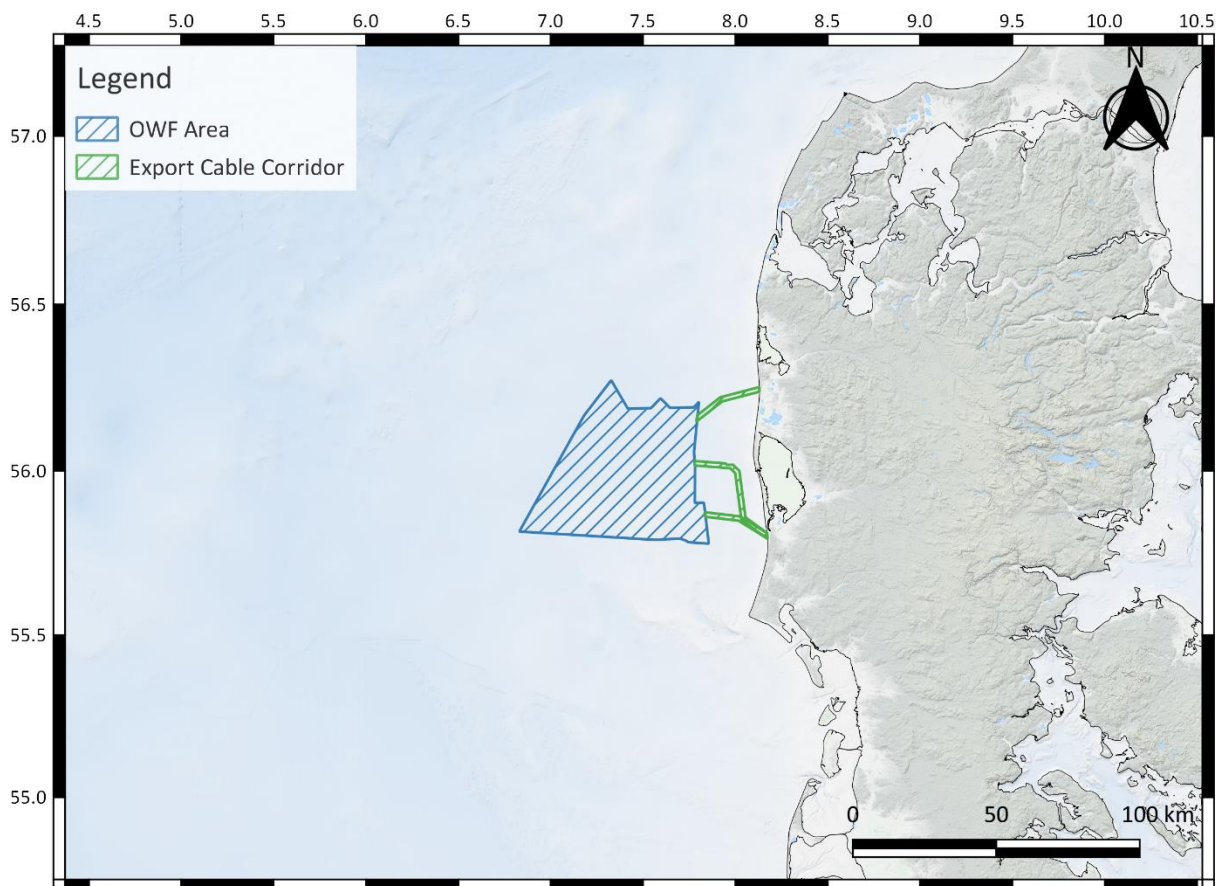


Figure 2-1: Project development area.

Energinet requires full metocean modelling, including wave and hydrodynamic modelling at a suitable resolution over a relevant time period, from which a suite of analyses will be conducted resulting in an appropriate level of information to enable FEED. The results will be issued to a certification body, who will give a feasibility statement related to the work. Hence, a full certification is not expected and in this manner the work differs from a full site metocean conditions assessment exercise.



2.2 Document Structure

For convenience, data sources, methodology details and design criteria are split across several documents as follows:

- **NSI Metocean Data Overview (Energinet_C00001_Rxx_Metocean_Data_Overview):** Describes the data sources and models used to support this study, including numerous validations of models against measurements in the region of interest to demonstrate suitability in this regard.
- **NSI Metocean Analysis Overview (Energinet_C00001_Rxx_Metocean_Analysis_Overview):** Details analysis methods used to derive the criteria presented in all other documents, as well as including all spatial analyses which consider the project development area as a whole.
- **NSI [LocationID] Criteria (Energinet_C00001_Rxx_[LocationID]_Design_Criteria):** Metocean design criteria for individual locations, wherein [LocationID] should be replaced by the identifier for the location. For example, criteria for the A3W site can be found in the document **NSI A3W Criteria (Energinet_C00001_Rxx_A3W_Design_Criteria)**.

Throughout, Rxx denotes the report revision, for example R01 is used for the first revision, R02 the second, etc.

This Metocean Data Overview describes the various data sources and models used to support this study.

Modelling details are discussed in Sections 3 to 6, initially introducing common model inputs (Section 3) before moving onto the models themselves. By way of introduction to the overall approach:

- **Wind** data used to drive wave and hydrodynamics models, as well as derive criteria, originate from the European Centre for Medium-Range Weather Forecasts (ECMWF) Reanalysis v5 (ERA5) model. See Section 4 for details.
- **Hydrodynamics** were modelled using the MIKE21FM 2D flexible mesh modelling package, a comprehensive modelling system for two-dimensional water modelling developed by DHI. Modelled currents and water levels have been validated against several site-specific and regional measurements. See Section 5 for details.
- **Waves** were modelled with a bespoke SWAN (Simulating Waves Nearshore) model with a high-resolution regional nest, to produce a long-term wave hindcast. The model has been extensively validated against measured datasets. See Section 6 for details.

Thereafter, Section 7 discusses additional data sources, for example as used to derive sea water and atmospheric statistics. The document concludes with a list of the references used throughout and various appendices providing more detail on a number of topics outlined in preceding sections.



2.3 Data Deliverables

In addition to the reports, time-series data are supplied separately in .mat file format¹ for each model grid/mesh location. Two database structures are provided corresponding to the ~84,000 and ~60,000 locations described by the hydrodynamic and wave model cases respectively. For each location represented, hindcast timeseries data is available in .mat format. An additional .mat file called *contents.mat* is provided for each database which includes a list of the geographic locations represented and a mapping to individual timeseries filenames. For ease of use, scripts are also provided which enable data to be extracted from each database on the basis of latitude and longitude using either the MATLAB or Python programming environments (*readMOWdatabase.m* and *readMOWdatabase.py*).

The data cover approximately 45 years starting in January 1979, using SI units, except for directions, which are given in °N and temperatures which are provided in degrees Celsius rather than Kelvin. The following describes the MATLAB structure and parameters provided in the files of the two databases:

Wave database parameter data (hourly resolution):

- data.Wind.t: Time in MATLAB datenum format
- data.Wind.Spd10: Wind speed at 10 m AMSL [m/s]
- data.Wind.Dir10: Wind direction at 10 m AMSL [°N]
- data.Wind.Spd150: Wind speed at 150 m AMSL [m/s]
- data.Wind.Dir150: Wind direction at 150 m AMSL [°N]
- data.Wave.t: Time in MATLAB datenum format
- data.Wave.Hm0: Spectral significant wave height, H_{m0} [m]
- data.Wave.Hmax: Maximum individual wave height, H_{m0} [m]
- data.Wave.Cmax: Maximum individual crest height, H_{m0} [m]
- data.Wave.Tp: Peak wave period, T_p [s]
- data.Wave.Tm02: Spectral equivalent of mean zero-down-crossing wave period, T_{m02} [s]
- data.Wave.Tm01: Spectral equivalent of mean wave period, T_{m01} [s]
- data.Wave.Mdir: Mean wave direction [°N]
- data.Wave.Pdir: Peak wave direction [°N]
- data.Wave.Dspr: Directional spreading [°]
- data.Seawater.t: Time in MATLAB datenum format
- data.Seawater.SST: Seawater temperature [°C]

Hydrodynamic data parameter data (20-minute resolution):

- data.WaterLevel.t: Time in MATLAB datenum format
- data.WaterLevel.z: Water surface elevation relative to mean sea level [m]
- data.Current.t: Time in MATLAB datenum format
- data.Current.Spd: Depth-averaged current speed [m/s]
- data.Current.Dir: Depth-averaged current direction [°N]

Importing the data using the MATLAB and Python scripts provided should result in identical data structures, as detailed above. In the Python case, however, note that the Python dictionary datatype is used which has a slightly different syntax to MATLAB structs (e.g. `data['Wave']['Hm0']`) and timestamps are converted from MATLAB's datenum format into Python's native Datetime format.

¹ .mat files are binary data files for storing variables that are common to the MATLAB software developed by MathWorks



2.4 Metocean Overview

2.4.1 Introduction

The eastern North Sea is strongly influenced by large-scale weather systems from the west which drive anticlockwise circulation. The open northern boundary of the North Sea allows some circulation of Atlantic water, while more limited circulation occurs through the English Channel and the strait of the Skagerrak from the Baltic Sea. The southern North Sea has shallow water depths of approximately 15 to 30 m and is generally well mixed by tides [1].

The annual near-surface temperature cycle across the North Sea shows a north-west and south-east distribution with lower temperatures at the south-eastern German and Danish coasts in the winter than Scotland, and warmer temperatures in the German Bight in summer. Coastal areas have significantly higher frequency of heavy rain than inland locations [2].

2.4.2 Winds

The North Sea is known for its large-scale weather storms, particularly in winter (November to February) which impact the site from the west. On the west coast of Jutland, measurements at the Høvsøre at the National Centre for Wind Turbines, the predominantly north-westerly winds have a 10-minute mean wind speed at 100 m of 9.3 m/s [3] with a maximum hourly mean between 2005 to 2013 of 35 m/s. Inter-annual variability was found to be in the region of 10% for adjacent years.

Winter conditions particularly are influenced by the North Atlantic Oscillation (NAO), whereby the pressure difference between the Azores and Iceland causes increased westerlies and warmer than average temperatures in winter. During the positive phase of the NAO, northern Europe is warm and wet, with more frequent and stronger storms, while the negative phase leads to dry and cold conditions (Figure 2.2). In the summer months, surface heating disrupts the large-scale circulation caused by the NAO, and winds are therefore milder.

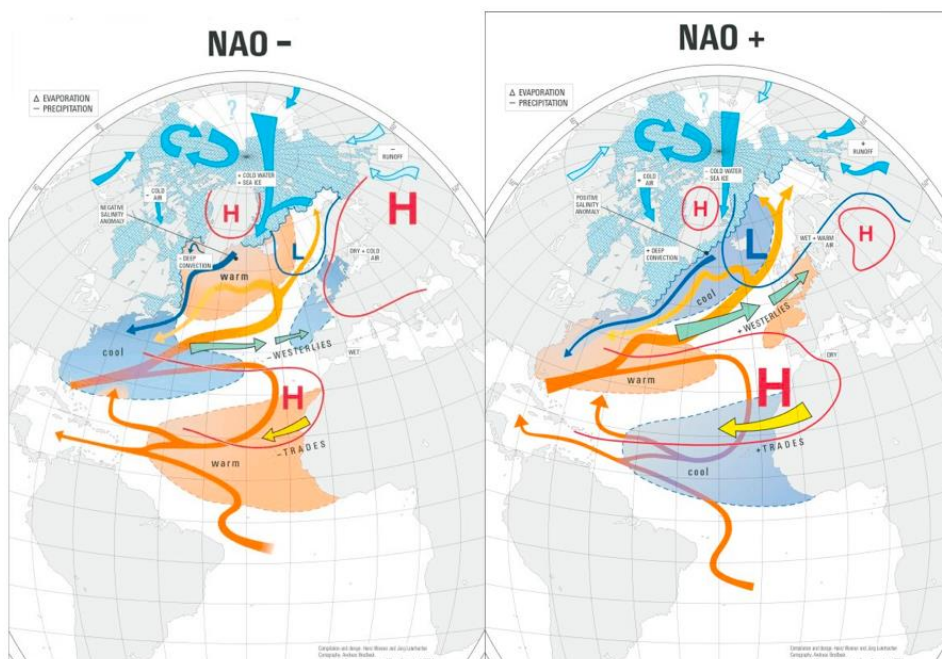


Figure 2.2: Negative and positive phases of the North Atlantic Oscillation (Source: ossfoundation.us).

2.4.3 Waves

The large-scale weather systems forming in the North Sea generate significant wave activity, particularly in the winter months. Waves arrive at the site from the south through to north-west, with large fetch lengths of more than 500 km allowing waves to fully develop such that wave heights can exceed 10 m during extreme events [4].

Examination of Norwegian 10 km Reanalysis Archive (NORA10) data [5] showed the dominant large waves occur in the central North Sea from north to south-west, with smaller waves from the south-east. Maximum individual wave heights exceeded 24 m in the 54-year period examined. Westerly extreme wave heights in the North Sea are correlated to the NAO [5]. Bell et al. [6] concluded that the largest wave events occur in the central North Sea when low pressure systems are located over southern Scandinavia, allowing the strongest winds to develop in-line with the longest northerly fetch. However, they found that winds from the south can also create large wave events despite a more limited fetch.

2.4.4 Currents and Tides

Water levels in the region of interest are strongly affected by the presence of a nearby amphidromic point, approximately 100 km east-southeast from the site (see Figure 2.3). Tidal ranges are therefore micro-tidal, at a maximum of approximately 1.2 m.

Figure 2.3 shows the position of the tidal amphidrome and tidal co-range lines, relative to the proposed development, after the work of Dalrymple [7]. The tidal wave in the German Bight travels from south to north along the coast of Jutland, circumventing in an anticlockwise direction the amphidromic points off the Netherlands and the east coast of Jutland. Because of the small tidal ranges in this region, wind and pressure can, and frequently do, have a relatively large impact on water surface elevations, increasing the overall water level range by up to approximately 1.4 m.

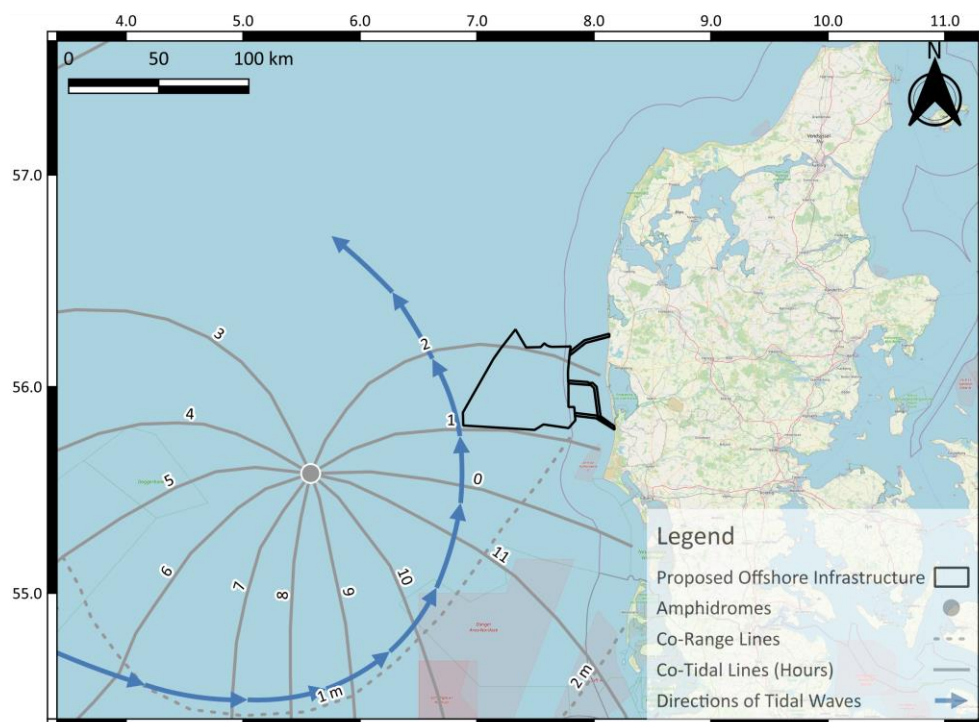


Figure 2.3: Tidal patterns in the North Sea (modified after [7]).



Circulation currents in the German Bight are driven by those present in the North Sea. Circulation in the North Sea is driven by currents such as the Gulf Stream combining with other local current systems as shown in Figure 2.4.

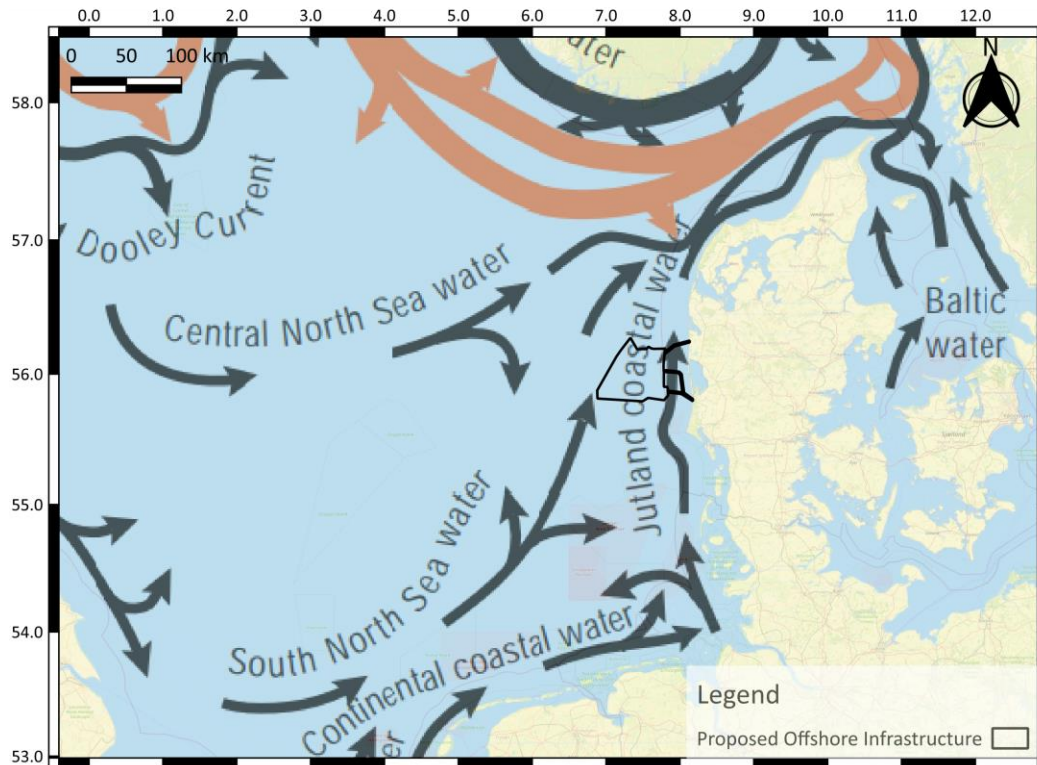


Figure 2.4: Circulation currents in the North Sea (modified after [7]).

Circulation currents at the proposed development are generally northward, with a gyre offshore of the site created by the confluence of southerly flowing Central North Sea water, and northward flowing South North Sea water. These circulation currents are relatively weak and the current regime at the project site is dominated by tides.

Denmark is susceptible to storm tides (strong storm surge during periods of high tide) associated with extratropical cyclones as they move over the shallower southern North Sea. In one storm tide in 1825, the coastline was altered such that the North Jutlandic Island was separated from the Jutland Peninsula.

2.4.5 Other Features

Internal waves are not expected to be a regular feature due to the dynamic mixing in this area [8].

West of Jutland is known for being a highly dynamic environment, with sediment transport driven by the strong tides as well as wave induced currents [9]. For example, a survey of the Thor offshore wind farm area found that sand made up 75 % of the seabed sediment, while gravel compose a further 14 % [10]. Data from subsequent surveys showed that seabed sediments could significantly change within two years [10] and coastal erosion can remove 3 to 4 m per year [11]. The impact of the changing seabed on wave heights over time off the Danish coast should be considered.



3 Bathymetry and Coastline

3.1 Bathymetry

A representative bathymetry dataset was required as input to the wave and hydrodynamic models. This was achieved by merging three different datasets which originated from:

- European Marine Observation and Data Network (EMODnet)
- Oceanwise raster charts
- Various multi-beam bathymetry survey data supplied by Energinet at a spatial resolution of 5 m, including;
 - the project site and cable routes
 - the Horns Rev 3 Offshore Wind Farm site
 - the Thor Offshore Wind Farm site
 - the Energy Island Project site
 - the Vesterhav Nord and Vesterhav Syd Offshore Wind Farms.

All of the multi-beam bathymetry survey data supplied by Energinet either use the DVR90 vertical elevation system, represented by the DKGEOID02 geoid model from the Danish Geodata Agency (which is considered a valid approximation to the Mean Sea Level (MSL)), or mean sea level.

The coverage of multi-beam data supplied by Energinet is shown in Figure 3-1.

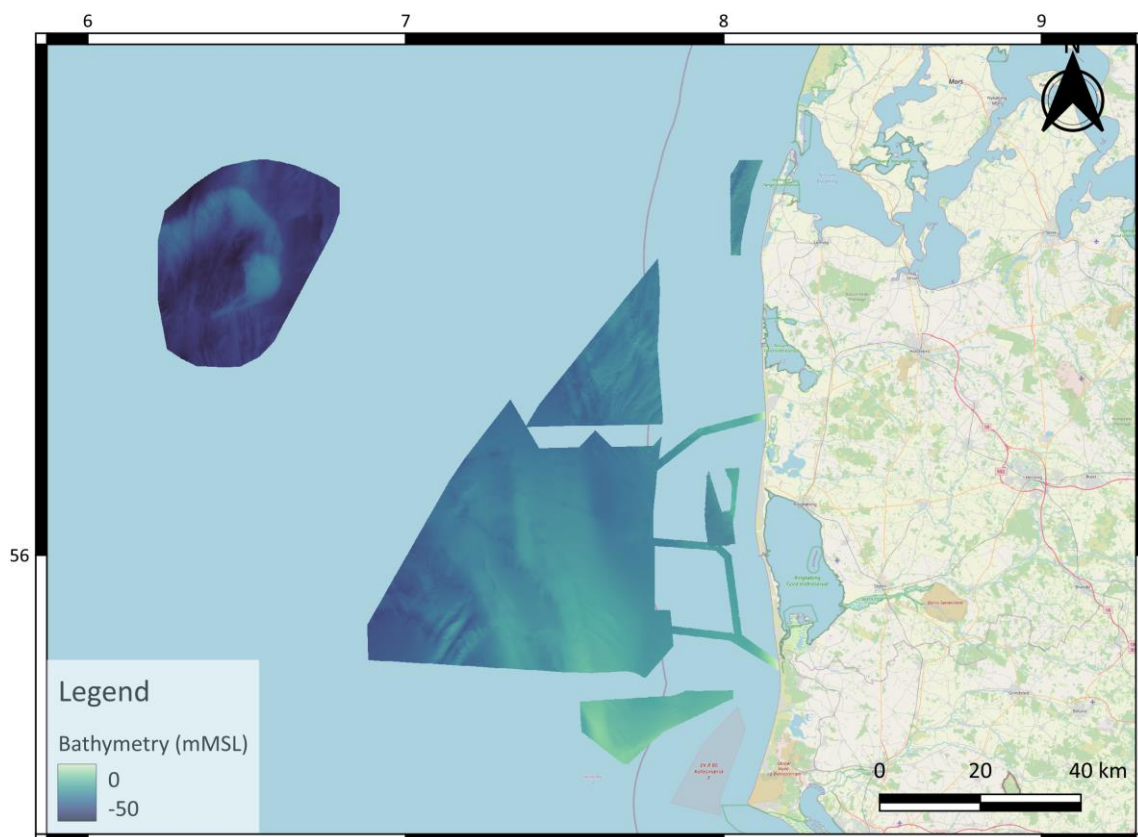


Figure 3-1: Energinet multi beam bathymetry data.



Bathymetry data further from the site were sourced from the EMODnet Bathymetry Data Portal². EMODnet provides a service for viewing and downloading a harmonised Digital Terrain Model (DTM) for the European sea regions. This is generated by an ever-increasing number of bathymetric survey datasets provided by national hydrographic institutions, research bodies and academia. These data are available at a resolution of approximately 130 m. The most recent EMODnet 2022 dataset was considered for use in the study, but investigations revealed that a greater degree of interpolated data has been used therein, compared to the 2020 dataset. This is shown in Figure 3-2 and Figure 3-3.

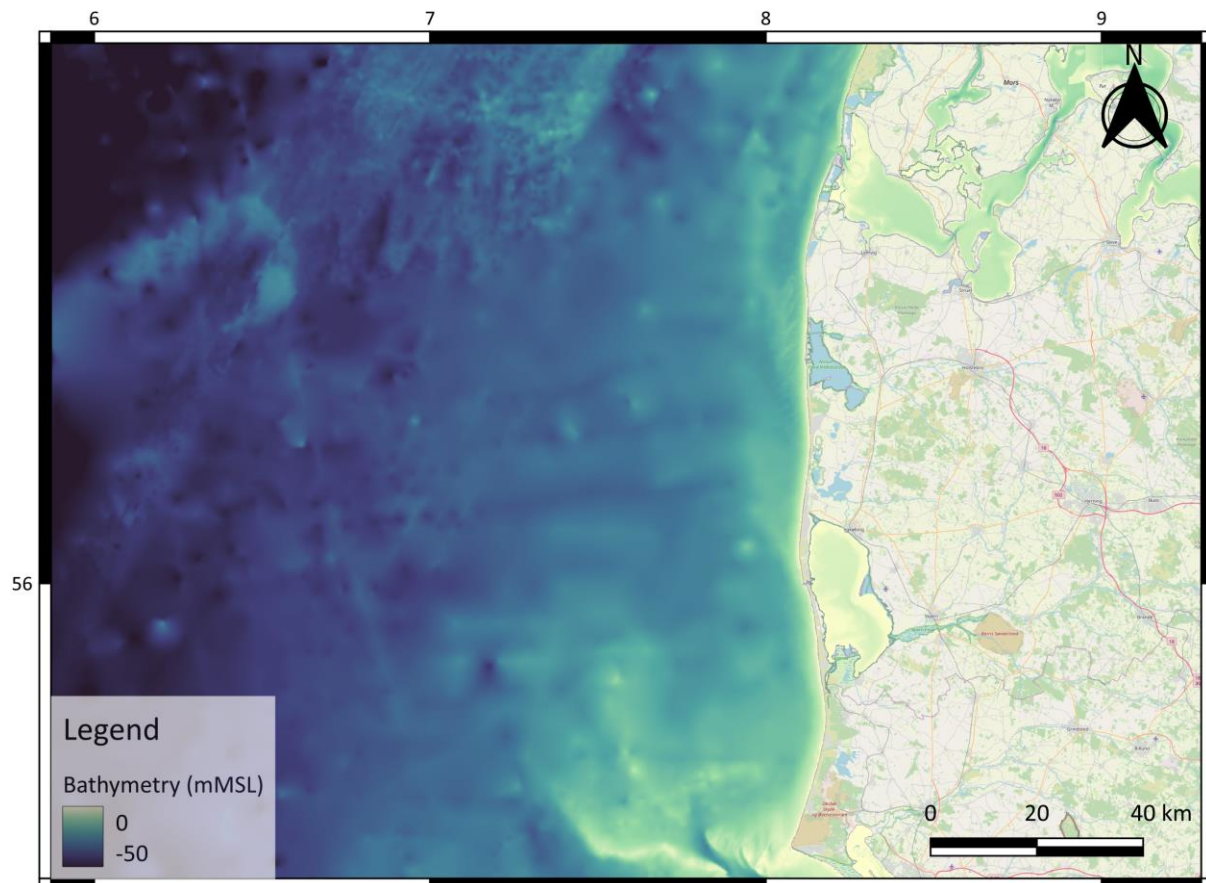


Figure 3-2: EMODnet 2020 bathymetry dataset local to the site.

² <http://www.emodnet-bathymetry.eu>

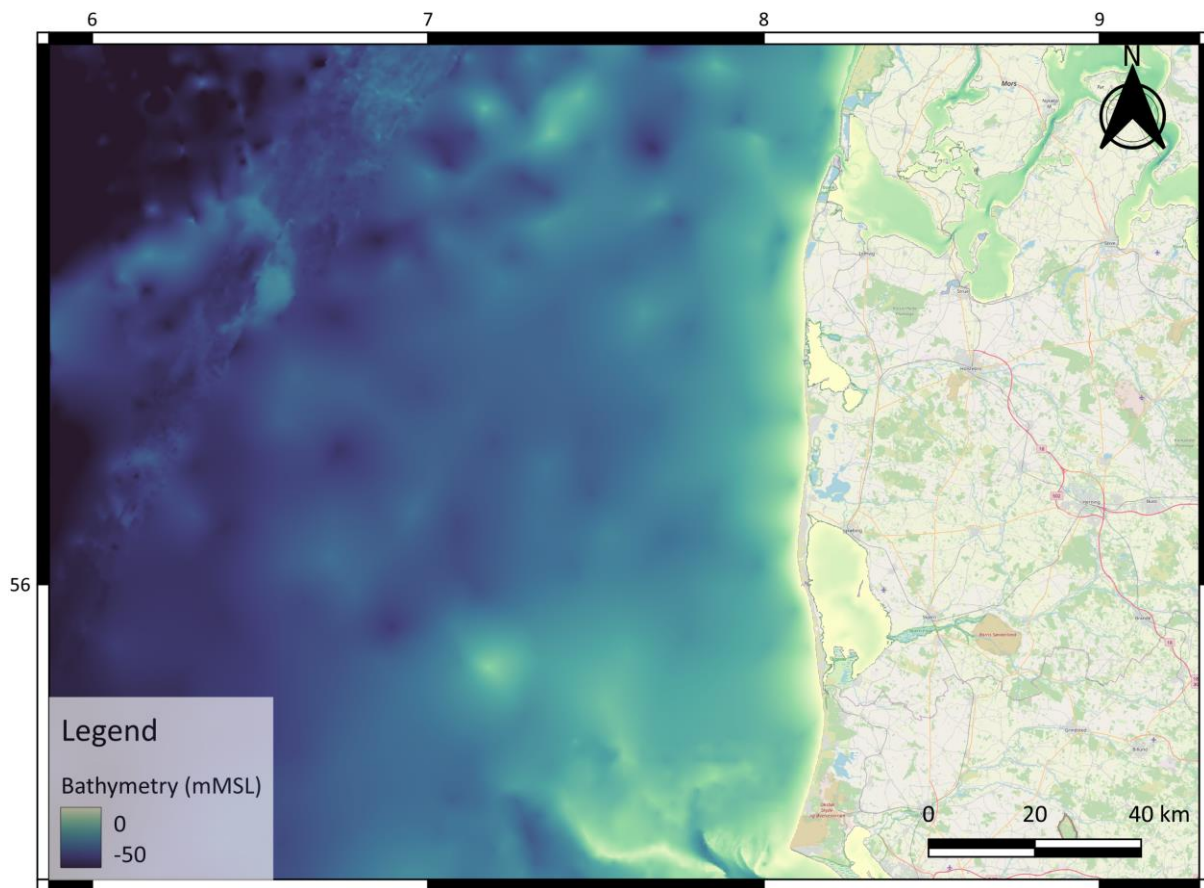


Figure 3-3: EMODnet 2022 bathymetry dataset local to the site.

On this basis, EMODnet 2020 was selected for use in the study. These data were then merged with Oceanwise raster charts which provide bathymetry around the coast of the UK. The Oceanwise data have a resolution of 1 arc-second (or approximately 25 m, depending on latitude), whereby physical features such as trenches, ridges, sand banks and sand waves are well represented.

Finally, these data have been augmented with the high-resolution survey data provided by Energinet presented in Figure 3-1. The vertical difference between the multibeam survey data and EMODnet 2020 is shown in Figure 3-4.

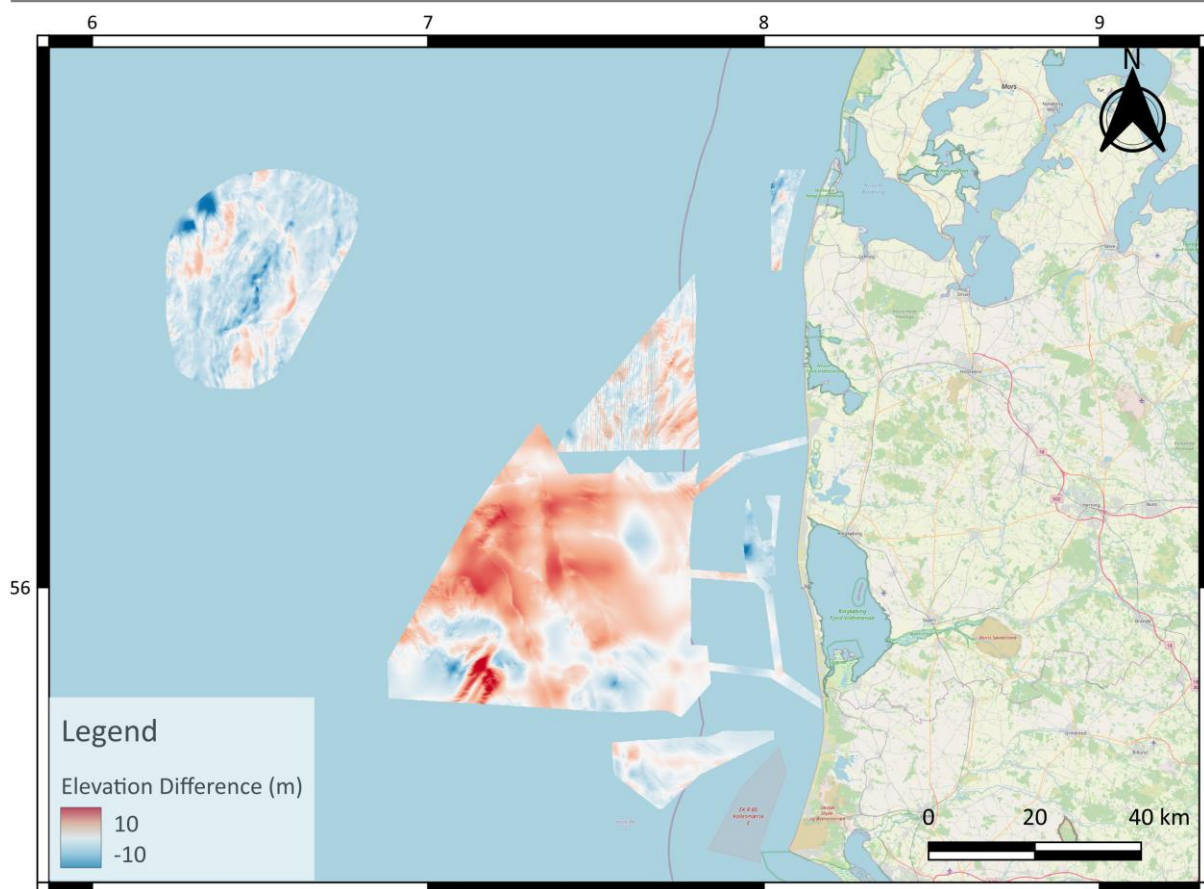


Figure 3-4: Elevation difference between EMODnet 2020 and multi beam survey data.

The survey data were exported to a 10 m resolution, and a cosine tapering method used to merge with EMODnet 2020, ensuring a smooth transition between the two. Please see Appendix A for further details.

The data from the two Vesterhav sites were not used because of their relatively small geographical coverage and because of the irregular shape of the Vesterhav Syd dataset. A spatial interpolation was carried out to fill the gaps in the Thor dataset.

3.2 Coastline

The coastline of Europe was discretised using the coastline layer from OpenStreetMap. These data were used in conjunction with satellite imagery to provide the most accurate and appropriate coastline description for the models. The local coastline is further refined using a GIS tool in conjunction with Google Earth.



4 Winds

4.1 Introduction

Regional ECMWF ERA5 modelled wind data, subjected to bespoke adjustment by MetOceanWorks, were utilised as follows:

- Wind fields at 10m above sea level (ASL) were used to drive hydrodynamic and wave models.
- Wind speeds and directions at hub height (taken to be 150 mASL) were used in the derivation of Normal Sea States (NSS) and Severe Sea States (SSS).
- Wind speeds and directions at both 10 and 150 mASL are provided as part of the time-series deliverables.

Model parameters should be considered as representative of 3-hour averages. Please see Appendix C for details.

4.2 Measured Wind Data

A number of relevant measured datasets were used for calibration and validation of the modelled wind data. Details are given in Table 4-1 and Figure 4-1 below.

In addition to the client supplied datasets, Dogger Bank East LiDAR data was acquired via the UK Crown Estate Marine Data Exchange (MDE) and Ijmuiden data originates from www.WindOpZee.net via Energy research Centre of the Netherlands (ECN). Data from the two met masts FINO1 and FINO3 were obtained from the German Federal Maritime and Hydrographic Agency (BSH).

Table 4-1: Measured datasets used for wind model validation.

Supplier	Name	WGS84	Time Period	Elevation Range	Avg Period (s)
Energinet	NSI-1-LB	55.9441°N, 7.0596°E	01-Sep-2023 to 01-May-2024	12 to 300 mASL	600
Energinet	NSI-2-LB	55.8856°N, 7.6167°E	01-Sep-2023 to 01-May-2024	12 to 300 mASL	600
Energinet	NSI-3-LB	56.0694°N, 7.6356°E	01-Sep-2023 to 01-May-2024	12 to 300 mASL	600
Energinet	EINS-1-LB	56.6280°N, 6.3007°E	15-Nov-2021 to 15-Nov-2023	30 to 270 mASL	600
Energinet	EINS-2-LB	56.3444°N, 6.4574°E	15-Nov-2021 to 15-Nov-2023	30 to 270 mASL	600
Energinet	Thor LiDAR	56.3470°N, 7.6050°E	18-May-2020 to 19-May-2021	40 to 197 mASL	600
BSH	FINO 1	6.5879°E, 54.0148°N	01-Jan-2003 to 29-Aug-2018	32.8 to 101.2 mMSL	600
BSH	FINO 3	7.1583°E, 55.1950°N	11-Sep-2009 to 31-Aug-2018	30.6 to 106.6 mMSL	600
MDE	Dogger Bank East LiDAR	2.7025°E, 55.0994°N	19-Nov-2014 to 16-Jan-2017	28 to 267 mMSL	600



ECN	Ijmuiden LiDAR	3.4357°E, 52.8482°N	01-Jan-2012 to 29-Nov-2015	89.2 to 314.2 mMSL	600
-----	----------------	------------------------	----------------------------	--------------------	-----

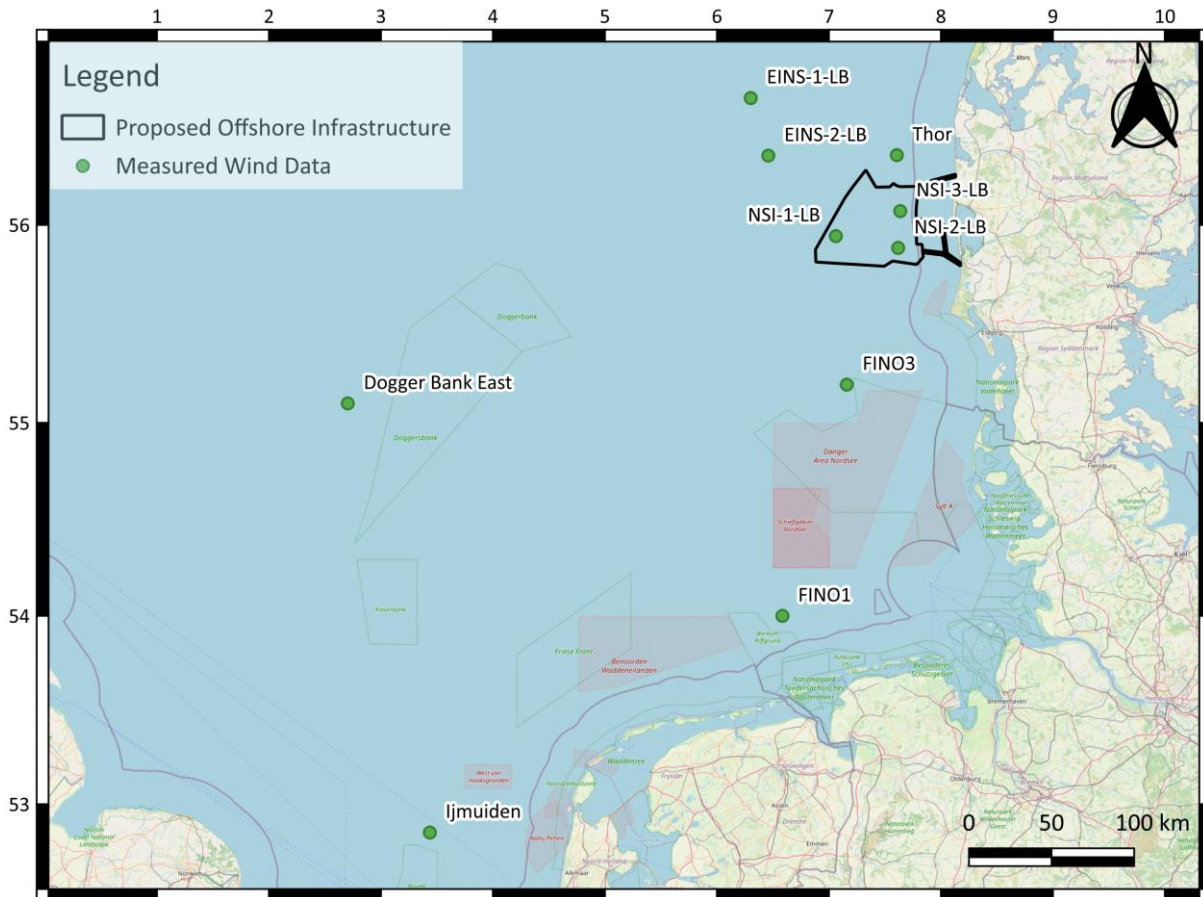


Figure 4-1: Wind measurement locations.

In addition, due to the regional scale of the wind fields needed to drive hydrodynamic and wave models, calibration at the 10 metre level is based on the analysis of more than 25 measured datasets (including over a dozen met masts) across European waters. For brevity, these are not detailed here, and validation plots are only included hereafter for the datasets shown in Table 4-1 and Figure 4-1 above.

4.3 ERA5 Modelled Data

4.3.1 Overview

European Centre for Medium-Range Weather Forecasts (ECMWF) ReAnalysis 5 (ERA5) is the fifth and latest major global reanalysis produced by ECMWF. Hourly wind speeds are available for the period 1979 to near present at various levels, including:

- **Single levels:** Hourly wind speeds at 10 m and 100 m above the surface of the earth are available on a 0.25° by 0.25° resolution grid via the Copernicus Climate Change Service (C3S) Climate Data Store (CDS).
- **Model levels:** Hourly wind speeds on 137 model levels can be accessed through the CDS application programming interface (API).



For this work, single level data at 10 m is used to drive both the wave and hydrodynamic models, as well as to provide time-series at 10 m above sea level (ASL). Winds at higher elevations are based on ERA5 model levels. Since these levels are not at the exact elevations required, some interpolation is necessary, and is described in Section 4.4.

In both cases, prior to any usage, the raw ERA5 data is calibrated according to the steps outlined in Section 4.5.

4.3.2 Horizontal Interpolation to Locations

To obtain a data set at a required location, wind speed components are bilinearly interpolated from the four grid points surrounding the location. Each timestamp and elevation level is interpolated independently, and in particular no change of elevation is included in this step.

4.3.3 Model Levels

The elevation of model levels varies with each time-step, but not sufficiently to have an impact on this project, as shown in Figure 4-2 for an example location in the North Sea. For this project, we make the simplifying approximation that all model levels are at a constant height, with the elevations of the model levels used taken to be³:

10.00 m, 30.96 m, 53.92 m, 79.04 m, 106.54 m, 136.62 m, 169.51 m, 205.44 m, 244.69 m, 287.52 m, 334.24 m

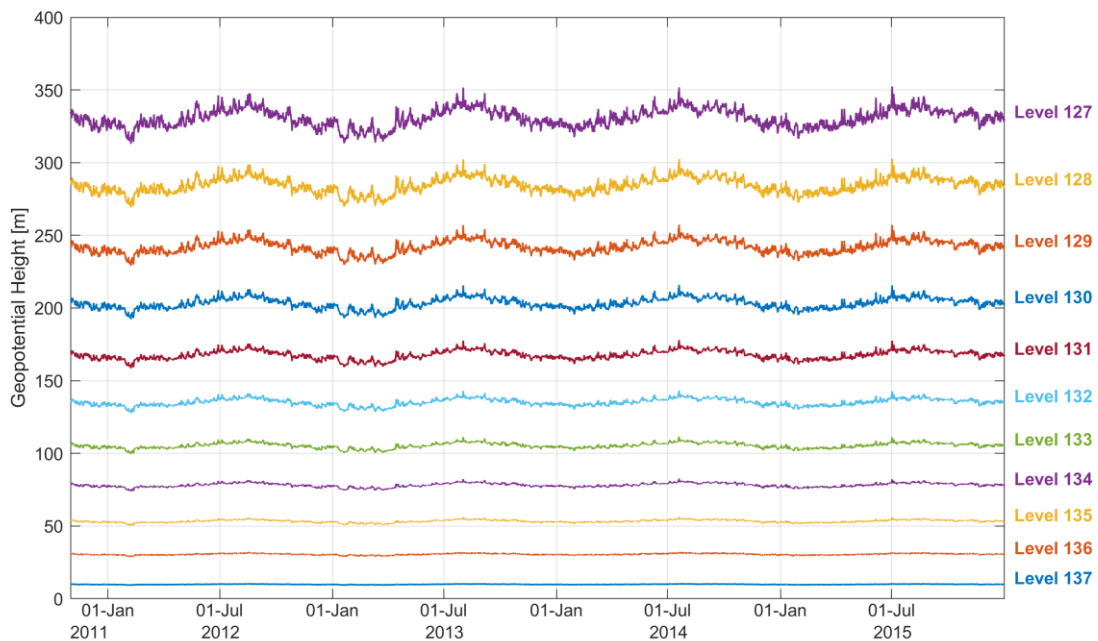


Figure 4-2: Geopotential height of lowest 11 model levels, example location.

Though this simplification will introduce some errors, they are expected to be small. For example, Figure 4-3 compares the 10 m wind speeds from the ERA5 single levels dataset with those from model level 137 (approx. 10 m) whilst Figure 4-4 compares the 100 m wind speeds from the ERA5 single levels dataset with model level 133 (approx. 106.54 m).

³ Please see <https://confluence.ecmwf.int/display/UDOC/L137+model+level+definitions> for more details.

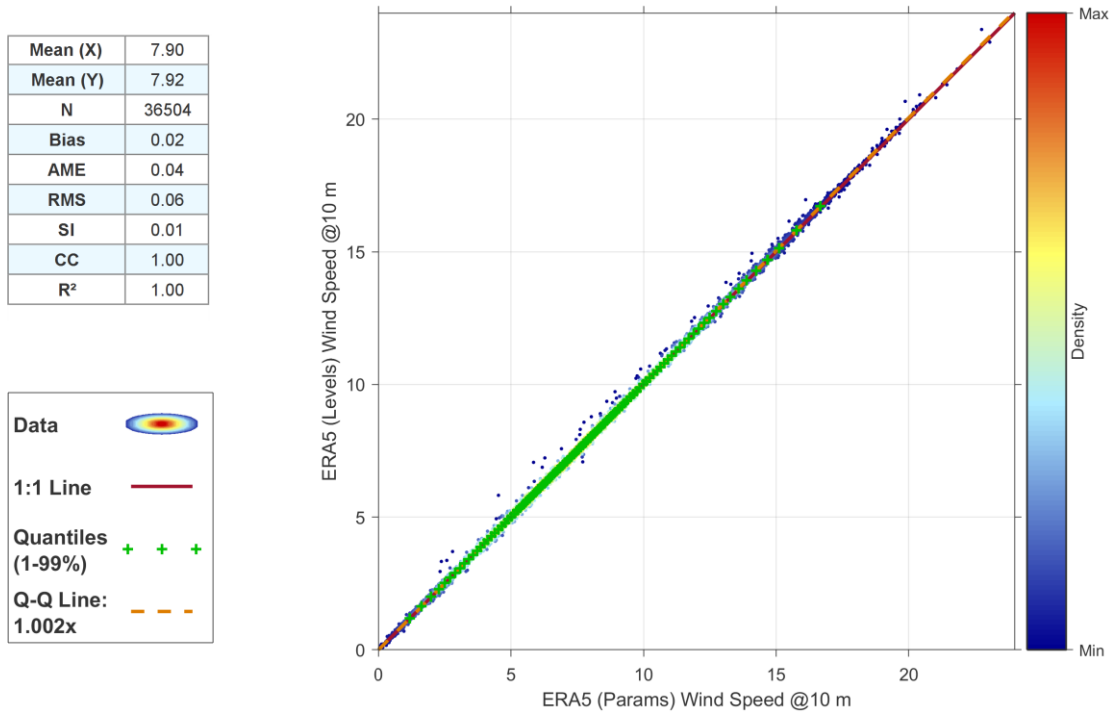


Figure 4-3: Wind speed at 10 m from ERA5 single level parameters (Params) and model levels (Levels), example location.

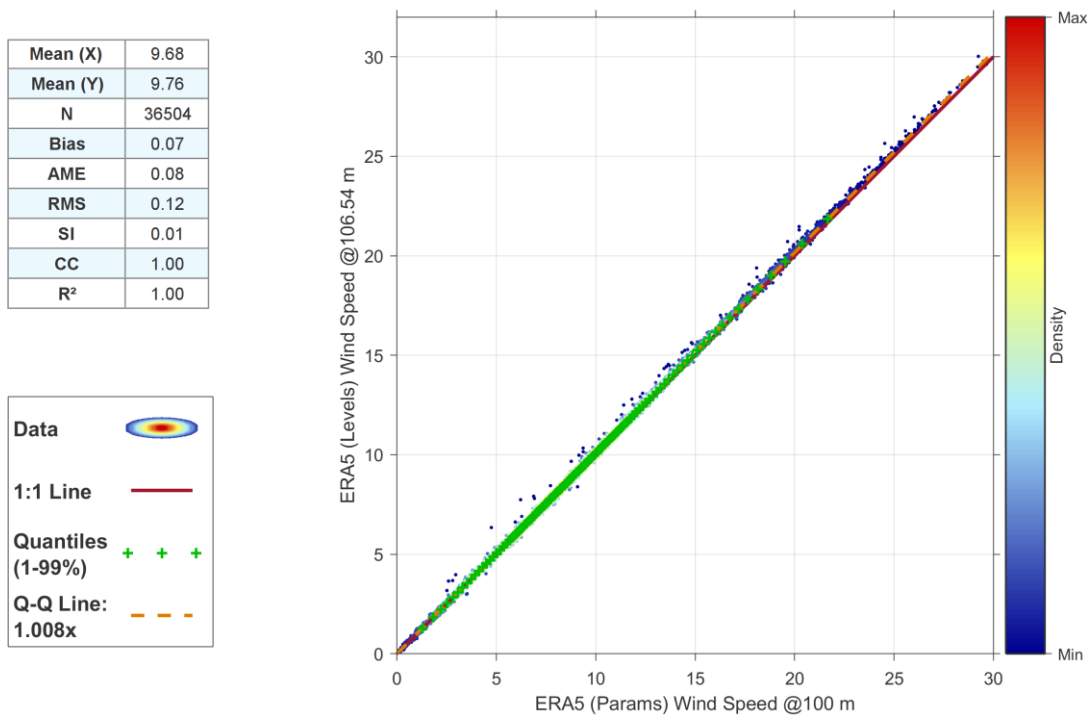


Figure 4-4: Wind speed at 100 m from ERA5 single level parameters (Params) and at 106.54 m from ERA5 model levels (Levels), example location.



4.4 Vertical Interpolation and Extrapolation

Wind fields are required at elevations of 10 and 150 m. As noted above, the 150m level does not match exactly any of the ERA5 model levels, and so the following interpolation method is used (independently for each modelled time-step):

- Take modelled wind speeds at the ERA5 levels immediately above and below the elevations required, i.e., 136.62 and 169.51 m.
- If wind speed increases with height between the two ERA5 levels used, a power law profile (see B.6 of Appendix B) is fitted to them and used to determine wind speed at the required level.
- If wind speed is the same, or decreases with height between the two levels, a linear profile is fitted to them and used to determine wind speed at the required level.

In a similar manner, to compare the resultant modelled data to measurements, adjustments are also required for the measurements to account for differences in heights. For the 150 m level, an analogous method is used to that outlined above. Only measurements from LiDARs have been used, and thus only interpolation between levels, rather than extrapolation upwards, is required.

For the 10 m level:

- Where at least two measurement levels are available, a downwards extrapolation is applied as follows (again, independently for each modelled time-step):
 - Measurements are taken from the lowest two elevations.
 - If wind speed increases with height, a power law profile is fitted to them and used to determine wind speed at 10 m.
 - If wind speed does not increase with height, 10 m wind speed is based on measurements at the lowest level only, and a fixed power law exponent of 0.12. This exponent is that given in DNV-RP-C205 [12] guidelines for “open sea with waves”.
- For buoy measurements where only one elevation is available, the Frøya profile (see B.6 of Appendix B) is used to estimate 10 metre winds.
- Data from the Dogger Bank East and IJmuiden LiDARs are not used at this level. The lowest measurements for the IJmuiden LiDAR is 89.2 m and significant downward extrapolation would be needed; the Dogger Bank East LiDAR shares a platform with a met mast which would be expected to impact the measurements at these lowest levels. Furthermore, both locations are some distance from the region of interest, and are predominantly included in this report for hub height comparisons.



4.5 Model Calibration and Validation

ERA5 wind data are biased low for higher wind speeds and so require adjustment prior to use. For example, Figure 4-5 shows validation against measurements for data at 10 m ASL from the NSI-1-LB location.

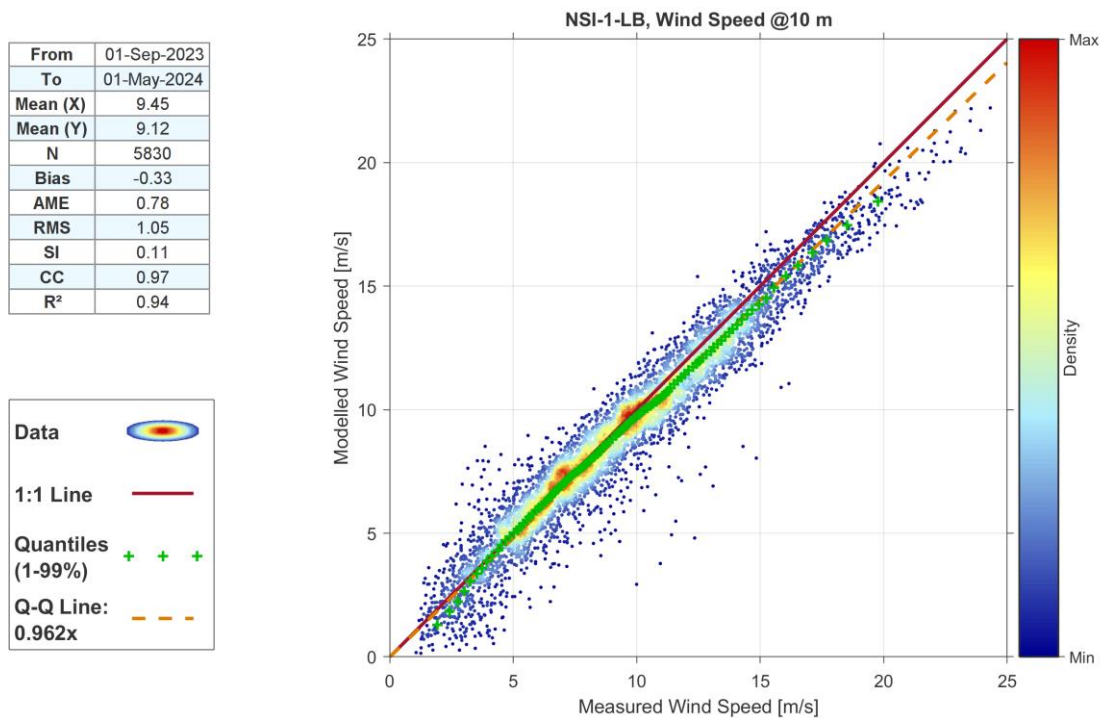


Figure 4-5: Validation scatter with overlaid QQ plot of *raw* ERA5 10 m wind speeds at NSI-1-LB.

Full details of the calibration process used can be found in Appendix B, however, by way of summary:

- **Wind Fields at 10 m ASL:** A regionwide calibration is applied to all offshore locations, with a further correction applied in coastal regions. This process is based on detailed analyses at over a dozen met masts in European waters and a similar number of coastal buoys, piers and platforms.
- **Wind Fields at 150 m ASL:** A calibration based on appropriate higher-level measurements from the datasets outlined in Table 4-1 is used. Note that similar regionwide analyses to those outlined for the 10 m wind fields indicate that at higher levels coastal effects are far less significant, and as such no additional correction is applied.

It should be noted that the calibration process is designed specifically to address the behaviour of ERA5 at higher wind speeds. It has very little effect at lower speeds, and as a result, leads to only small changes in the statistical parameters seen to the top left of each validation plot. However, as seen throughout the validation plots which follow, the resultant calibrated ERA5 data shows good performance and provides a suitable description of wind conditions for each measurement location.

Validation plots, showing 3-hour mean measured wind speeds against calibrated ERA5 wind fields are included below for a selection of locations. Those for the 10 m level are shown in Figure 4-6 through Figure 4-13, followed by those for 150 m in Figure 4-14 through Figure 4-21.

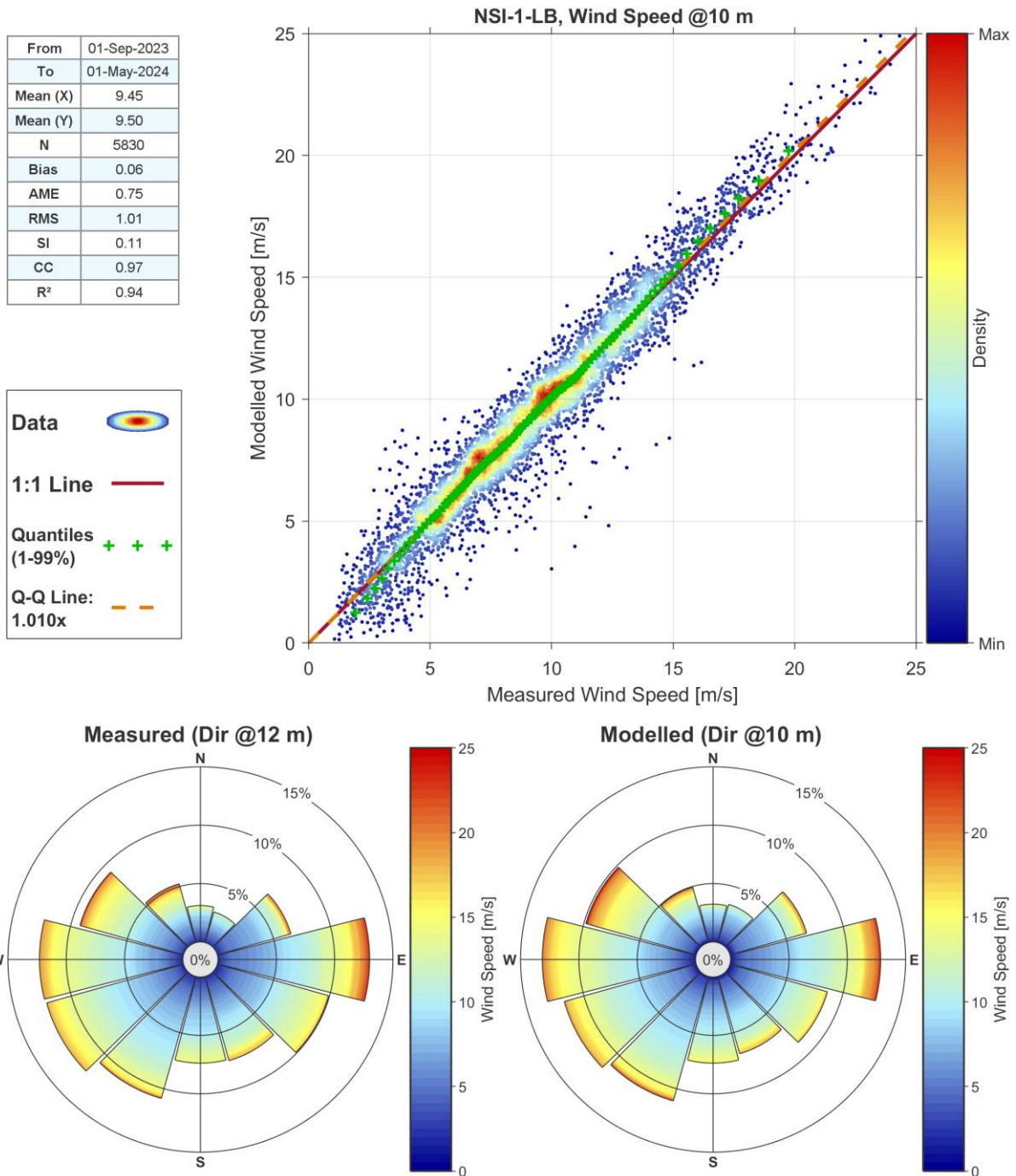


Figure 4-6: Validation plot of calibrated ERA5 wind speeds, 10 m ASL, NSI-1-LB.

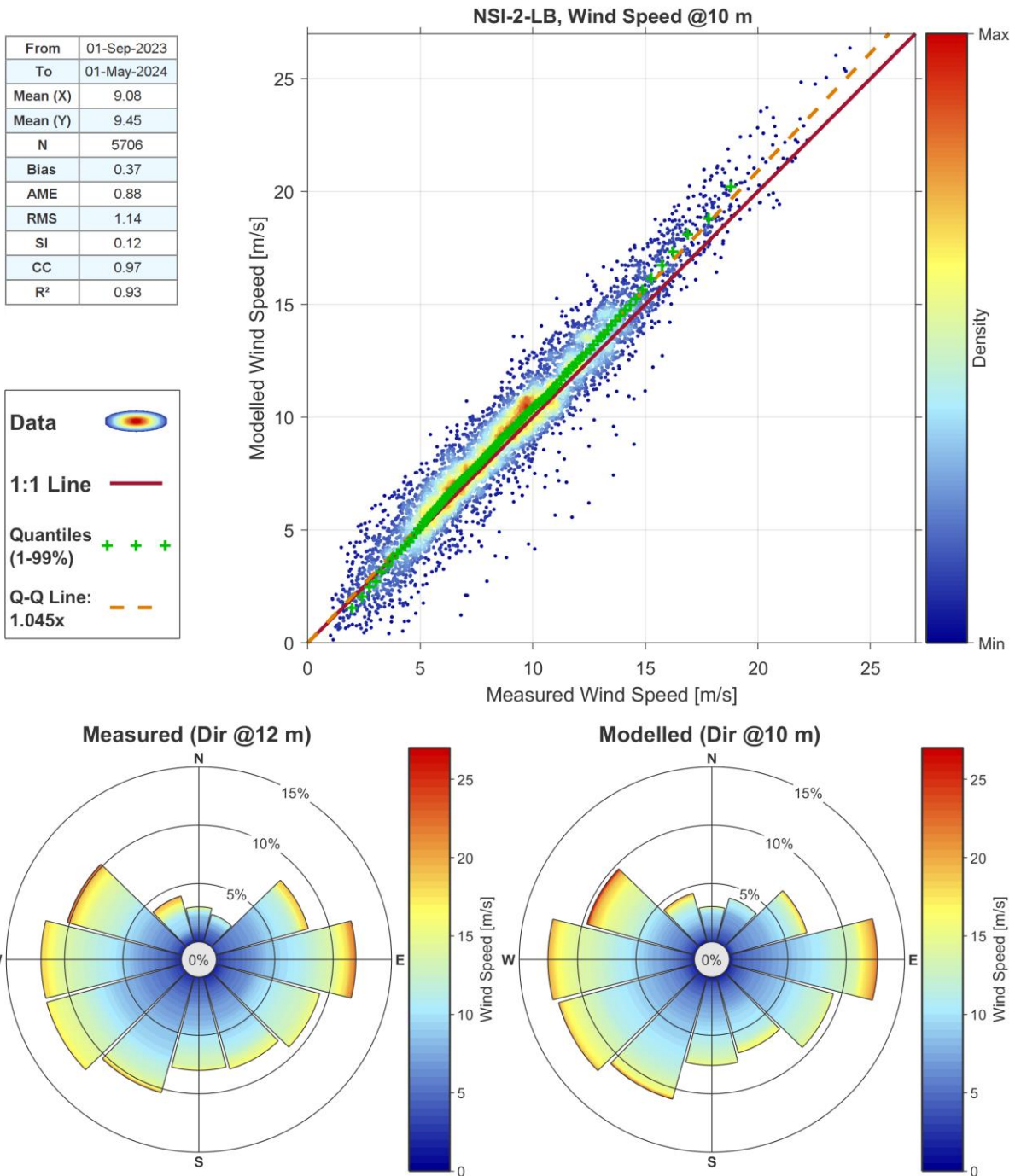


Figure 4-7: Validation plot of calibrated ERA5 wind speeds, 10 m ASL, NSI-2-LB.

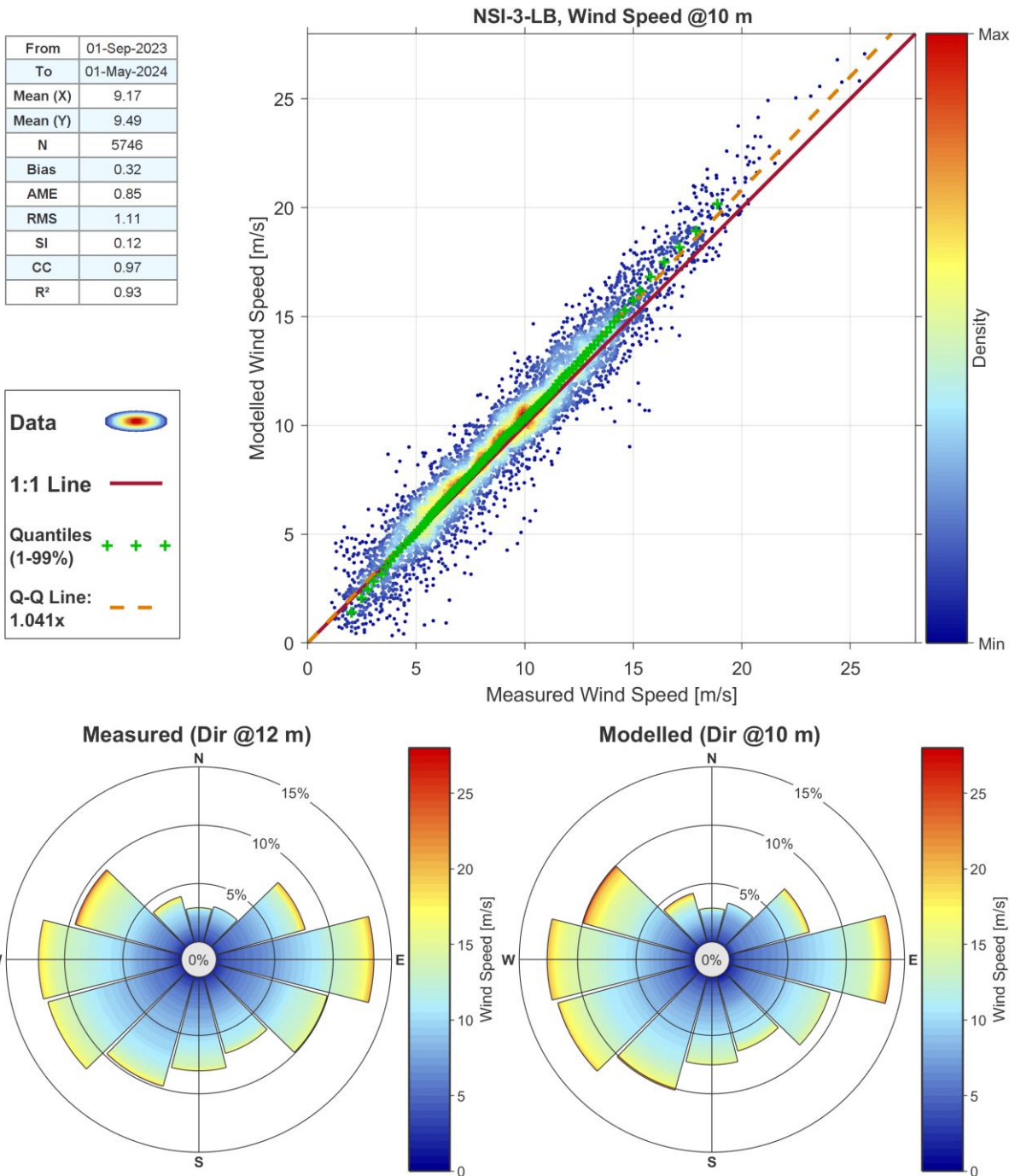


Figure 4-8: Validation plot of calibrated ERA5 wind speeds, 10 m ASL, NSI-3-LB.

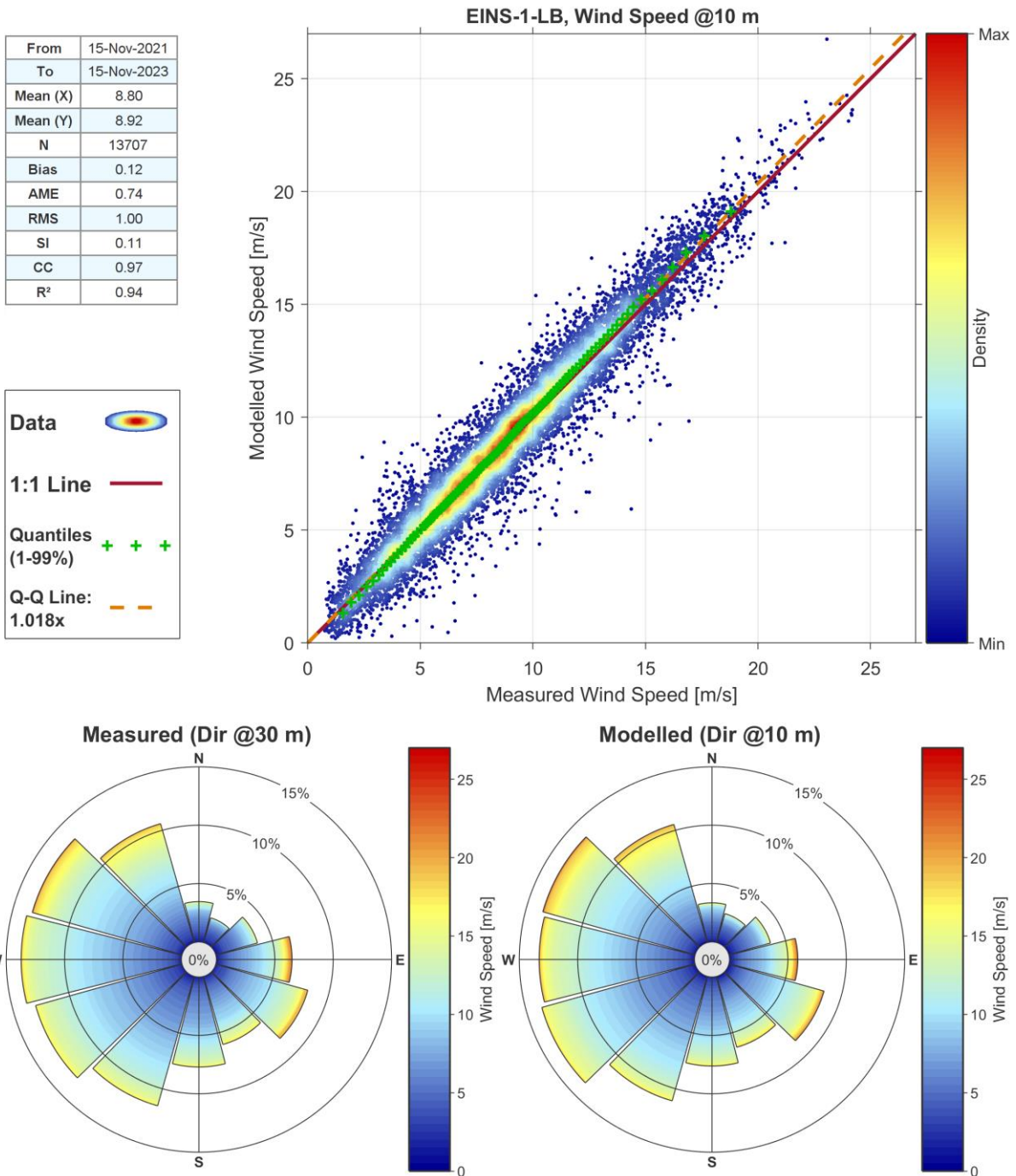


Figure 4-9: Validation plot of calibrated ERA5 wind speeds, 10 m ASL, EINS-1-LB.

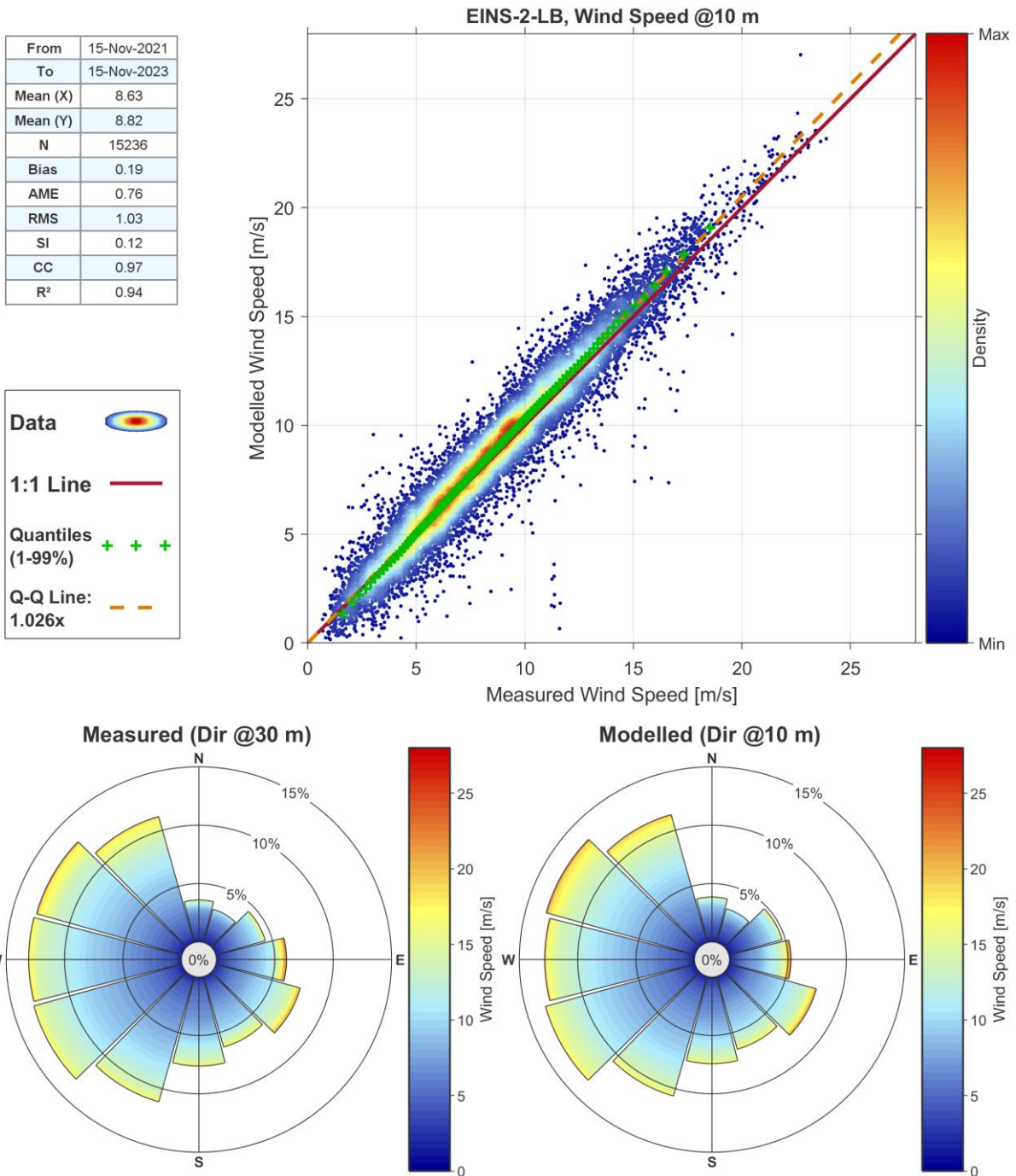


Figure 4-10: Validation plot of calibrated ERA5 wind speeds, 10 m ASL, EINS-2-LB.

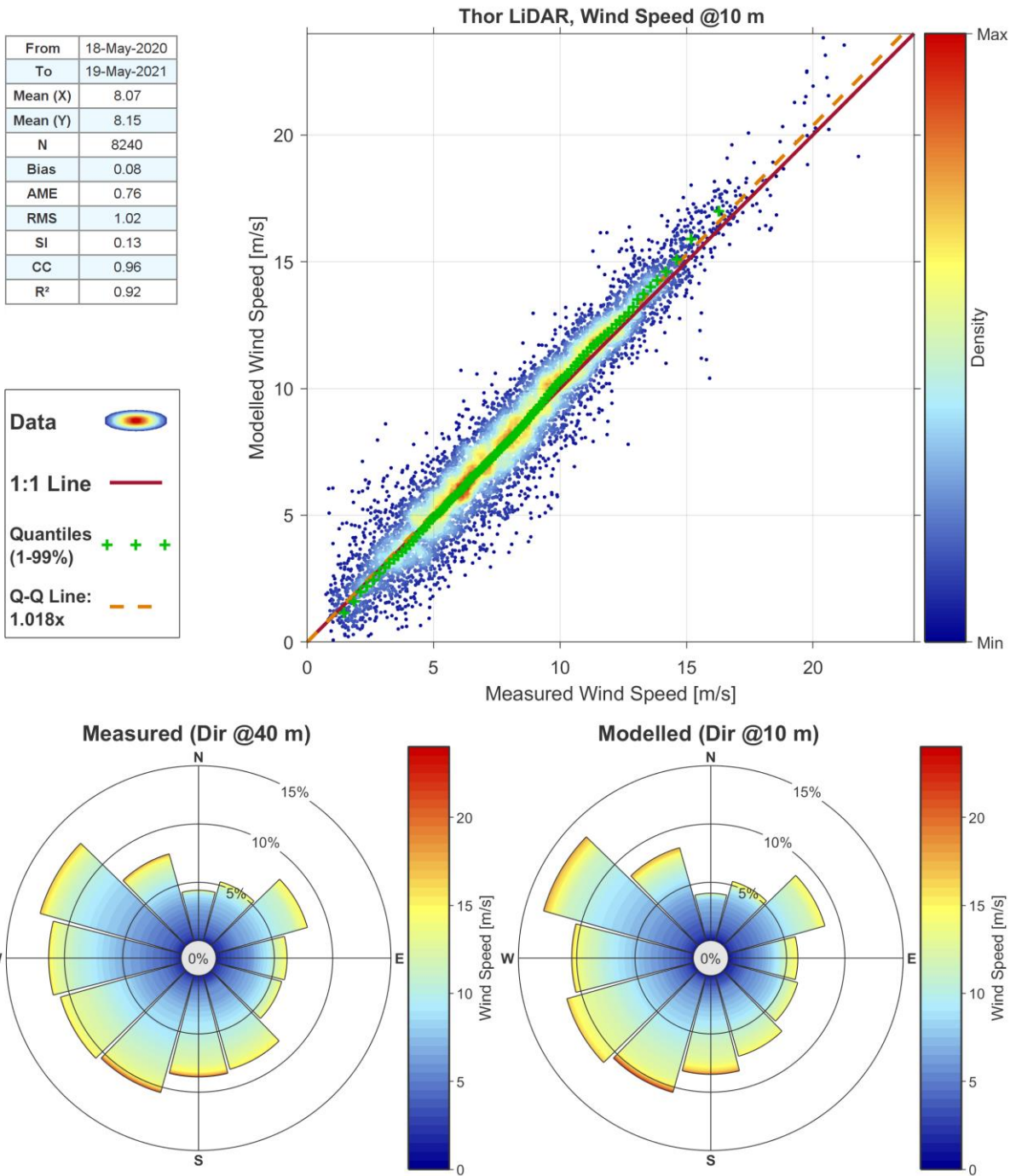


Figure 4-11: Validation plot of calibrated ERA5 wind speeds, 10 m ASL, Thor LiDAR.

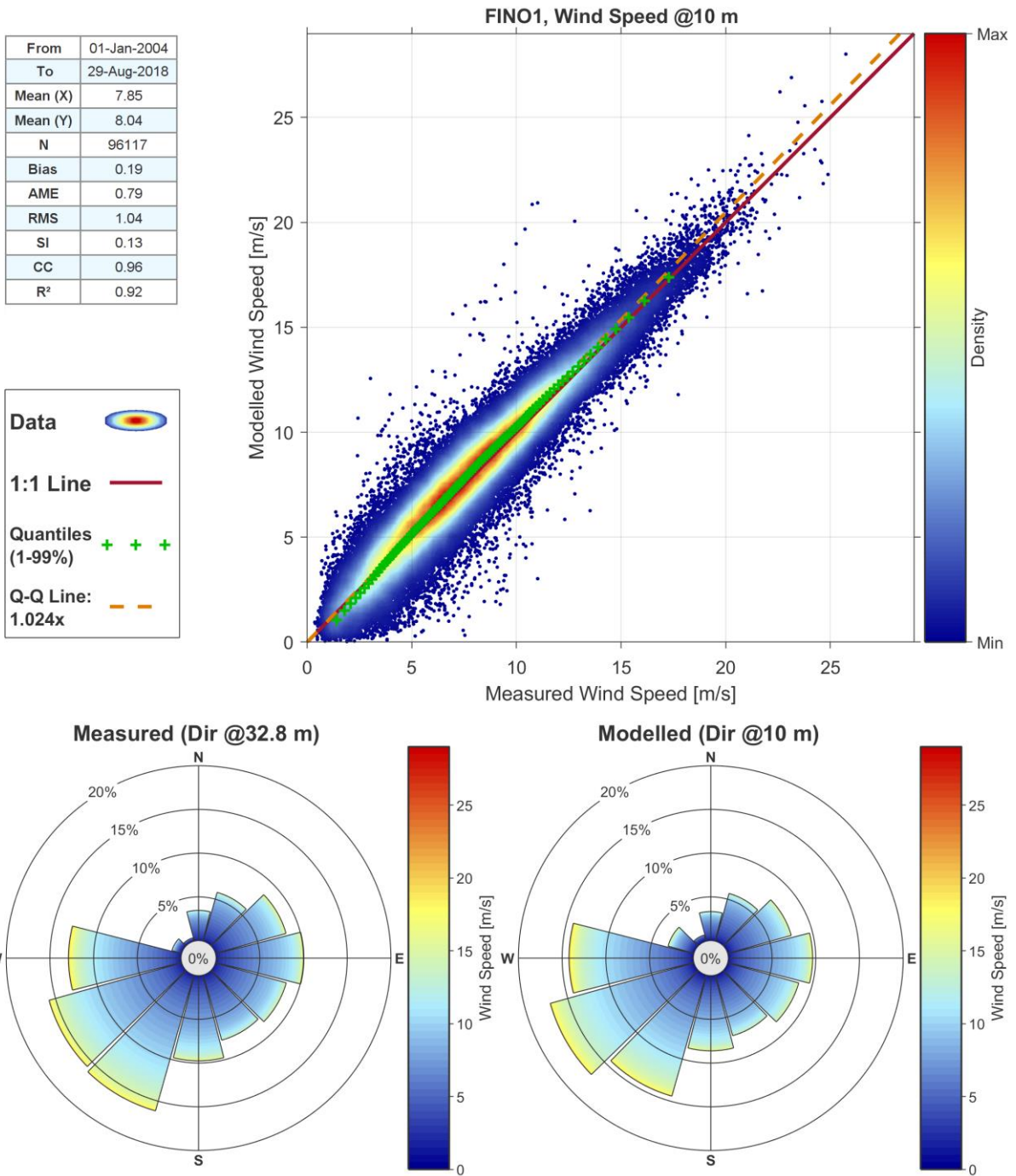


Figure 4-12: Validation plot of calibrated ERA5 wind speeds, 10 m ASL, FINO 1.

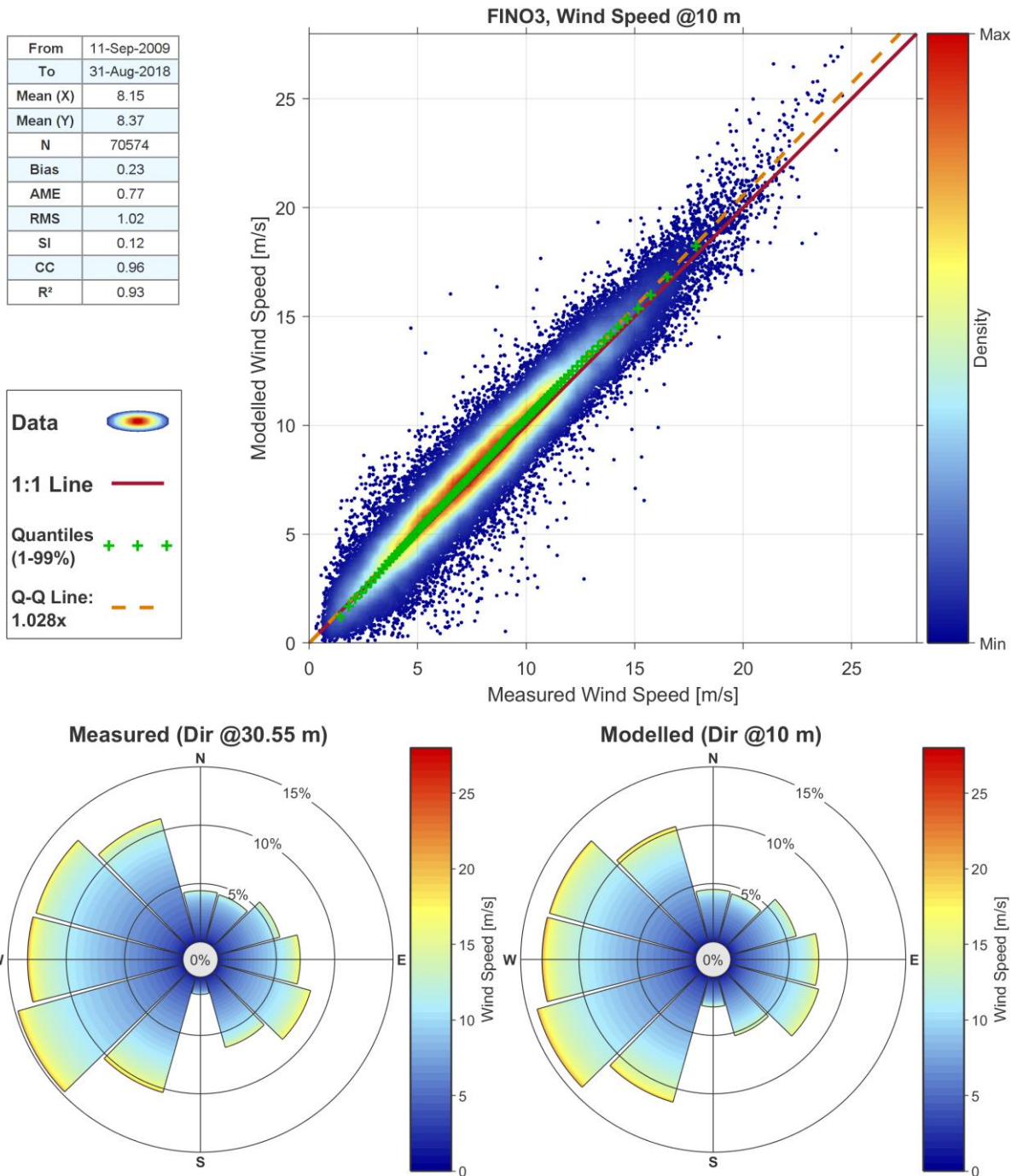


Figure 4-13: Validation plot of calibrated ERA5 wind speeds, 10 m ASL, FINO 3.

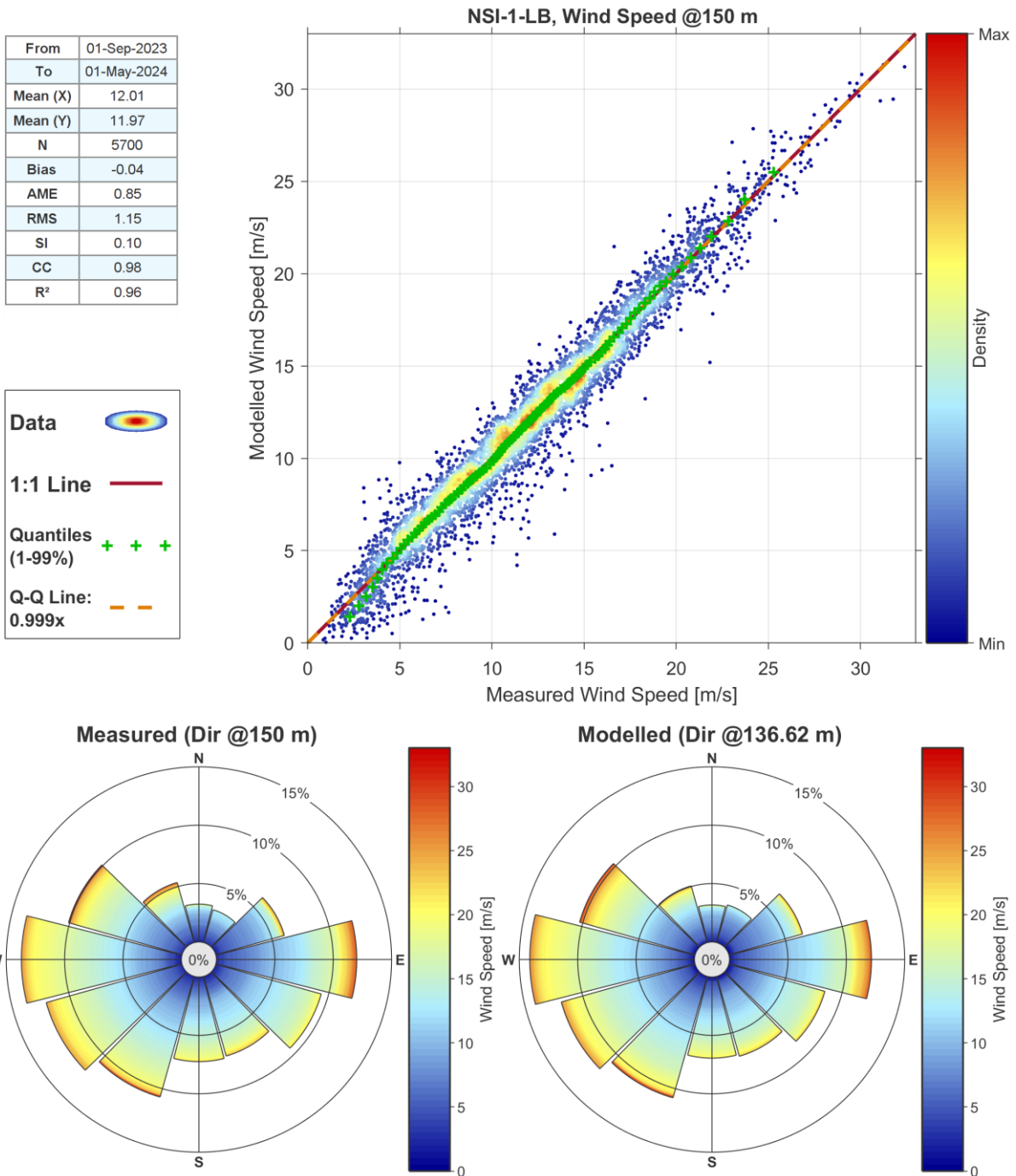


Figure 4-14: Validation plot of calibrated ERA5 wind speeds, 150 m ASL, NSI-1-LB.

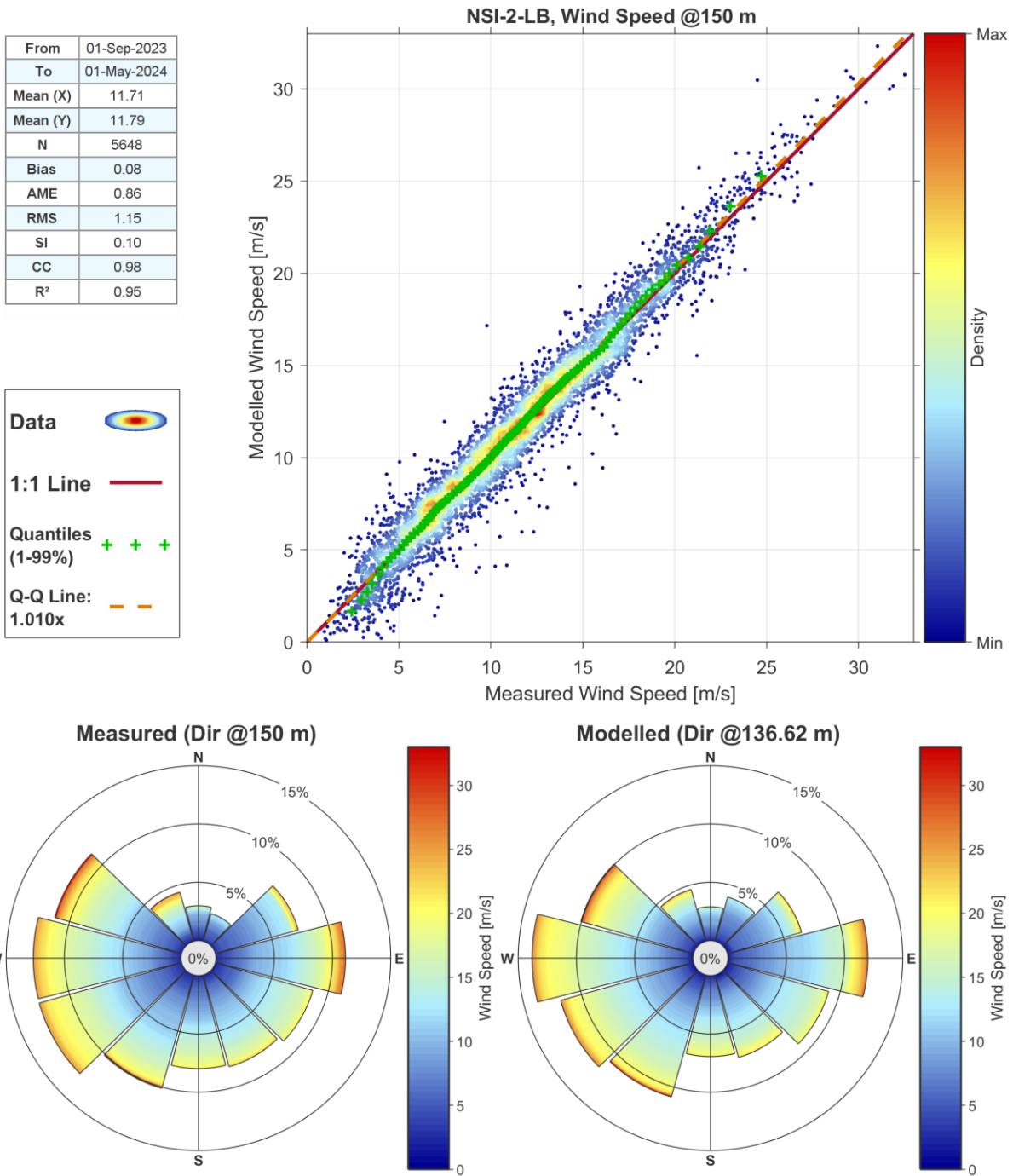


Figure 4-15: Validation plot of calibrated ERA5 wind speeds, 150 m ASL, NSI-2-LB.

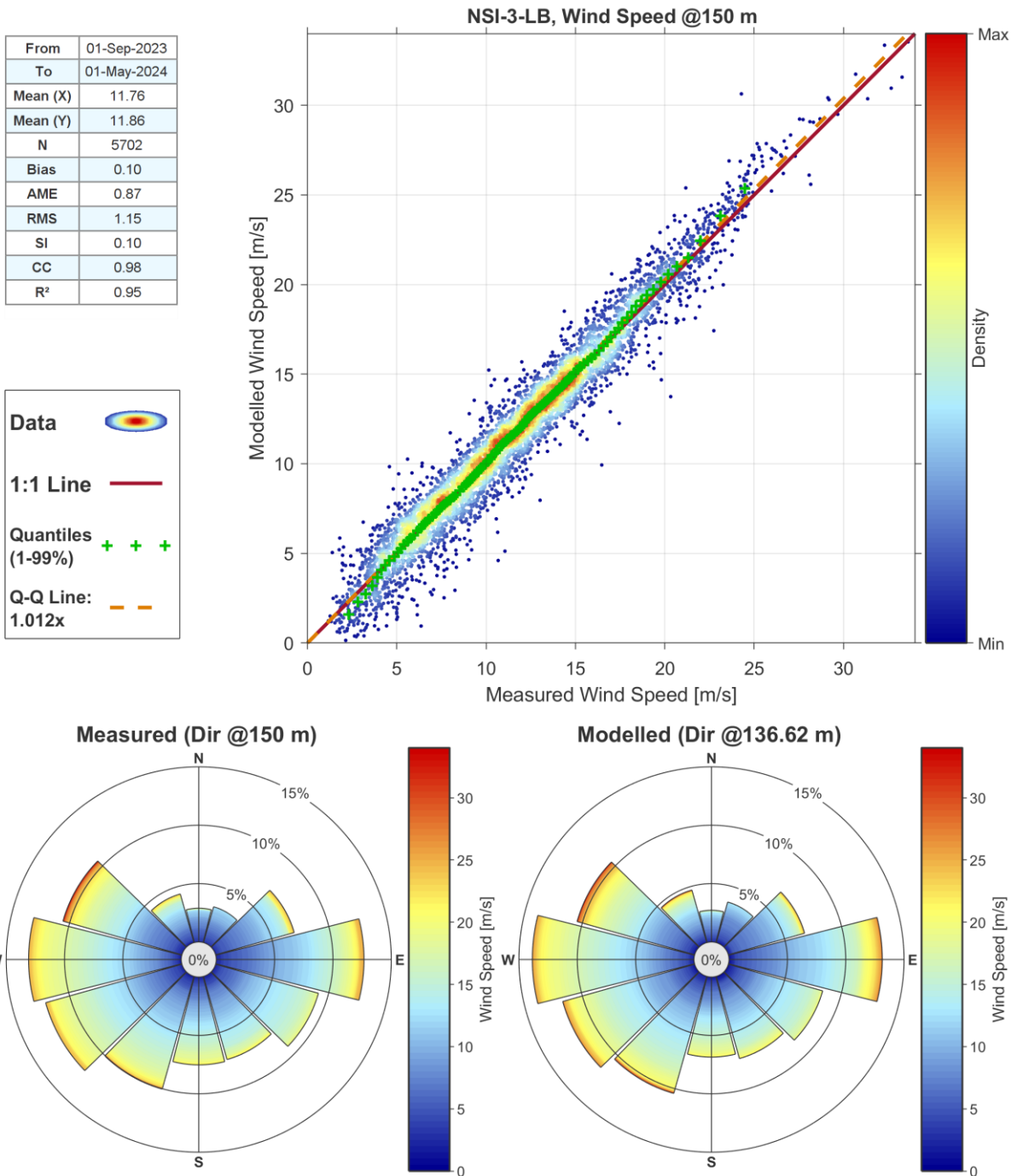


Figure 4-16: Validation plot of calibrated ERA5 wind speeds, 150 m ASL, NSI-3-LB.

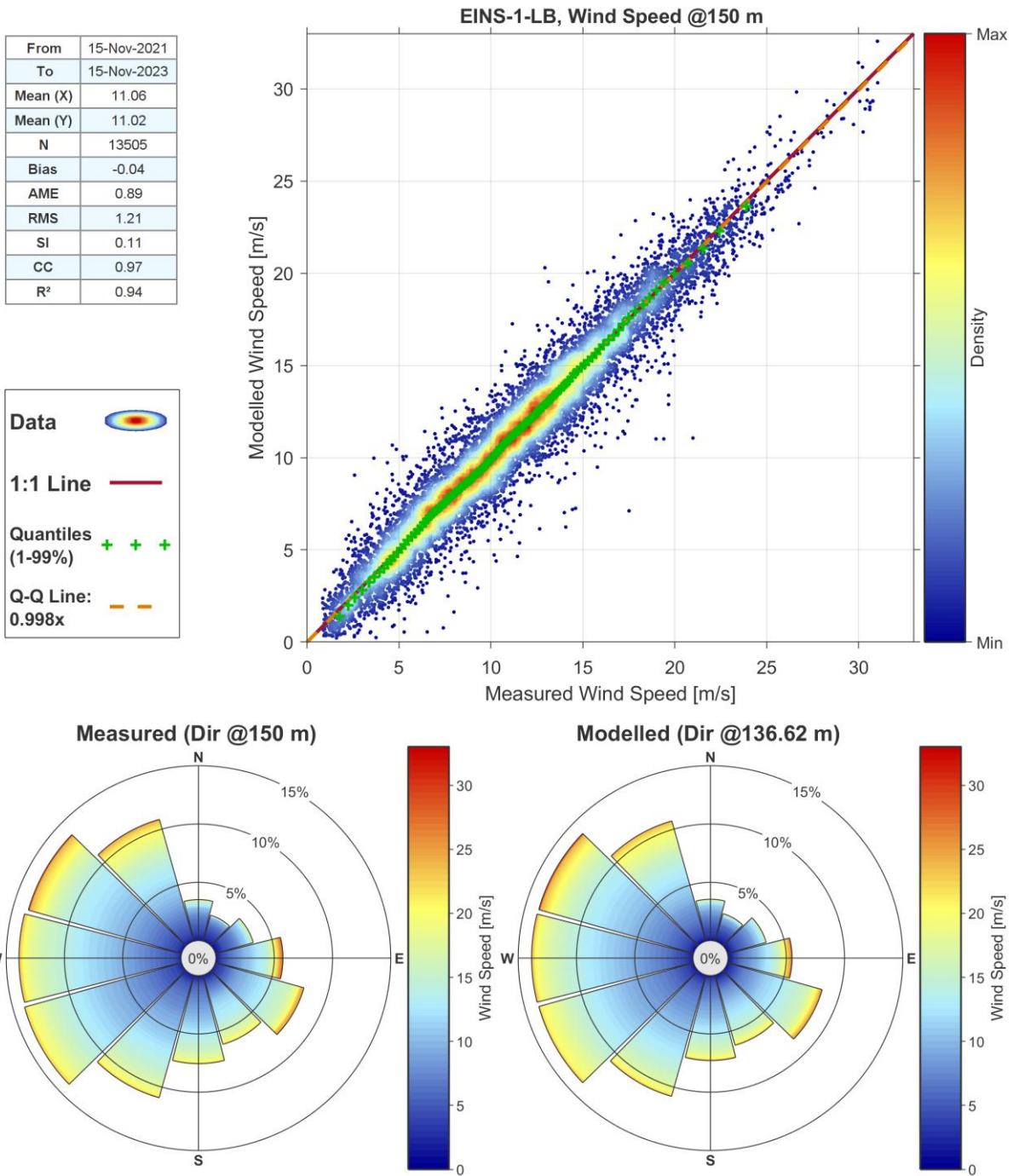


Figure 4-17: Validation plot of calibrated ERA5 wind speeds, 150 m ASL, EINS-1-LB.

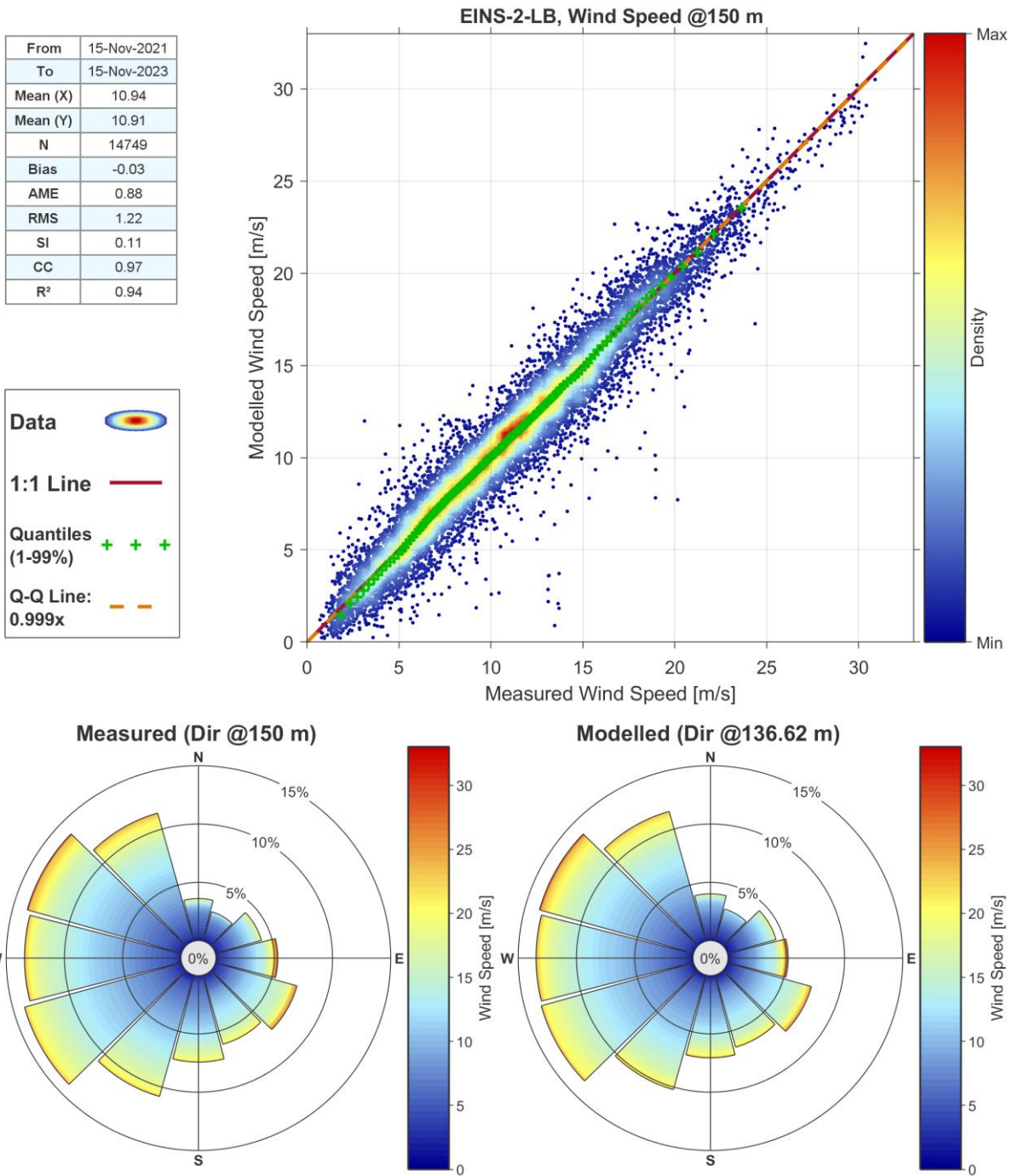


Figure 4-18: Validation plot of calibrated ERA5 wind speeds, 150 m ASL, EINS-2-LB.

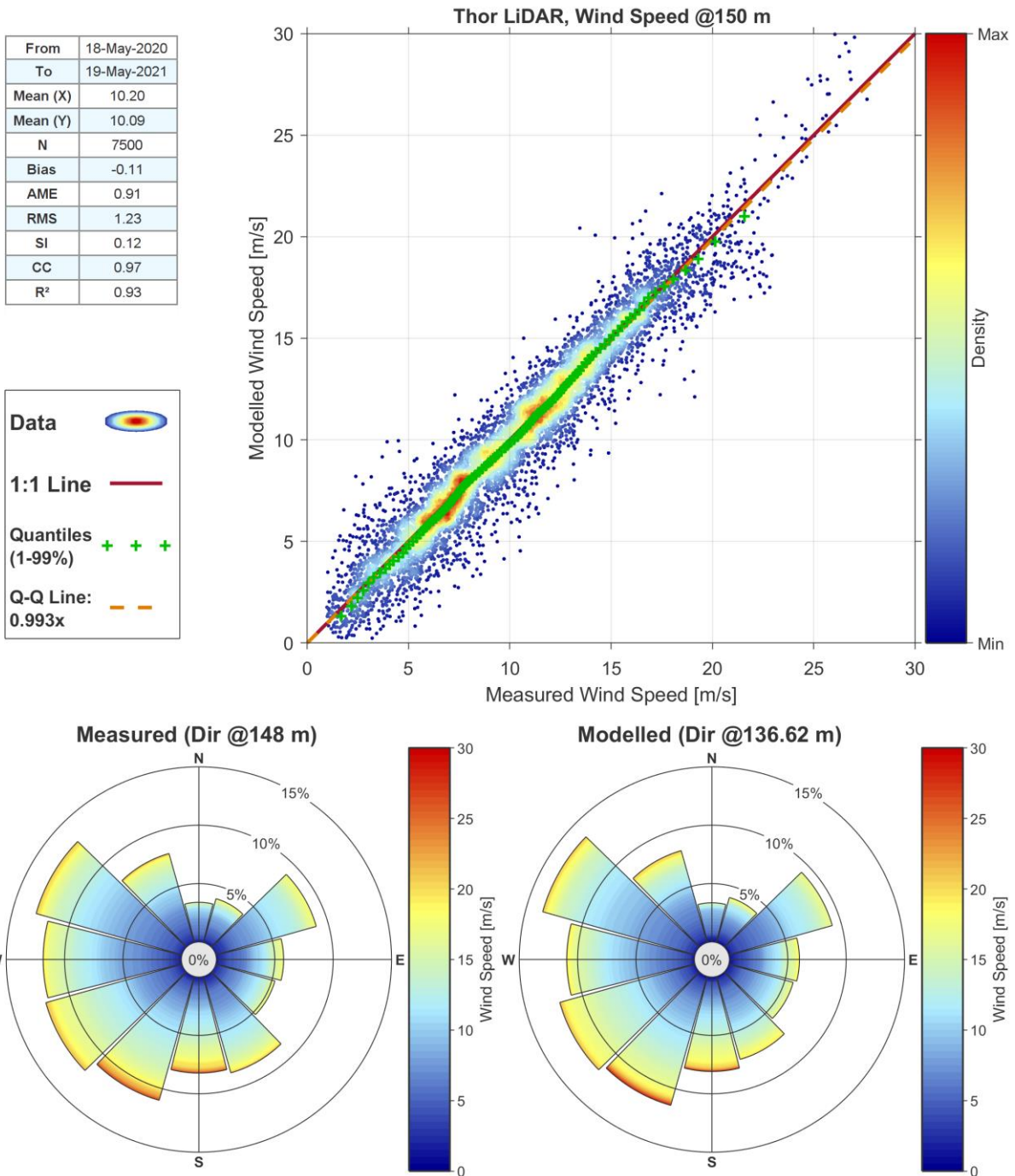


Figure 4-19: Validation plot of calibrated ERA5 wind speeds, 150 m ASL, Thor LiDAR.

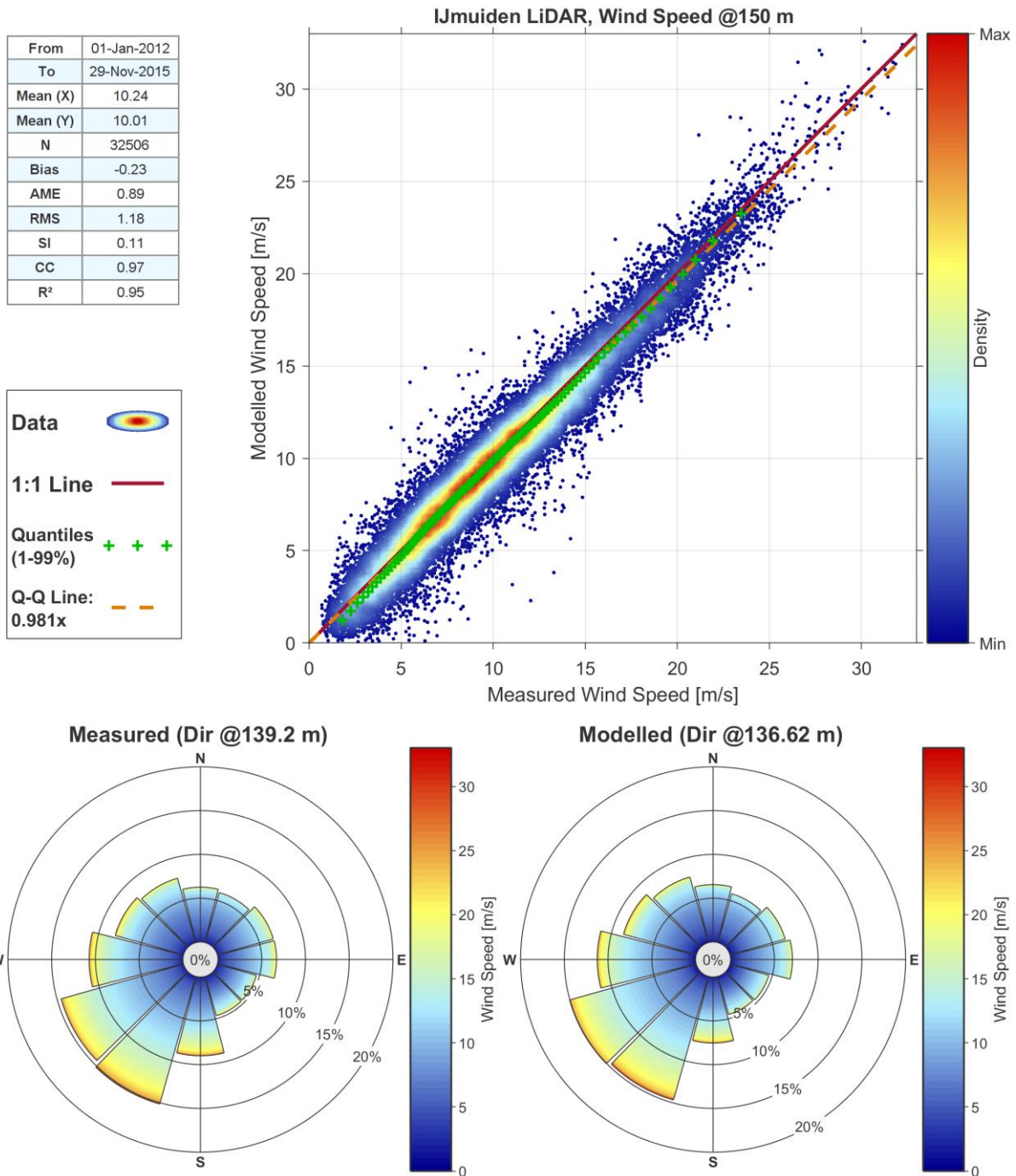


Figure 4-20: Validation plot of calibrated ERA5 wind speeds, 150 m ASL, IJmuiden LiDAR.

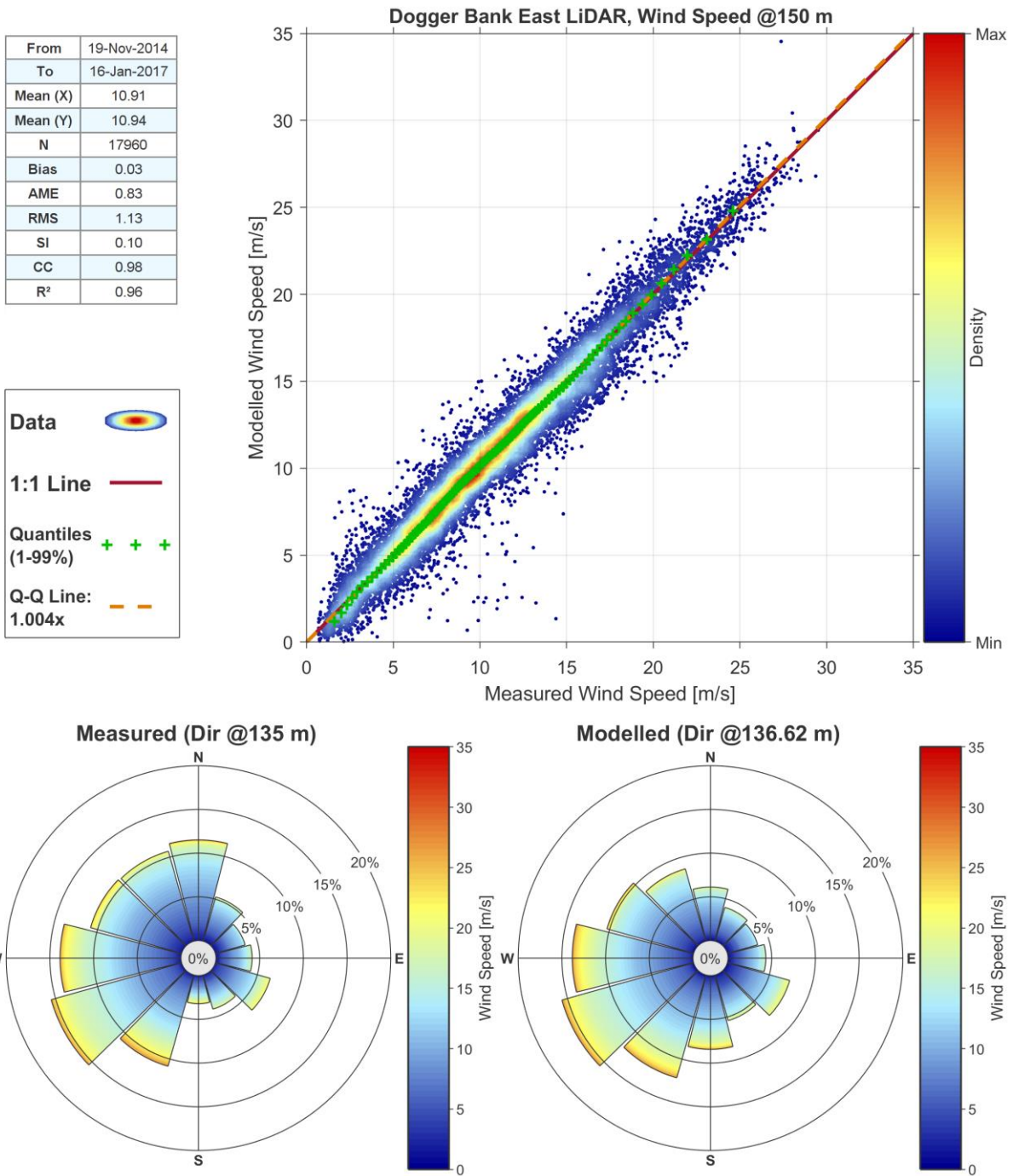


Figure 4-21: Validation plot of calibrated ERA5 wind speeds, 150 m ASL, Dogger Bank East LiDAR.



5 Hydrodynamics

Current and water level parameters were produced from a high-resolution, project-specific version of the MetOceanWorks' European Hindcast Model, which has been validated against several datasets to ensure accurate propagation of the tidal wave from open water into the North Sea. The model was subjected to sensitivity testing and validation, before depth-averaged currents and water-levels were output at 20-minute intervals for the approximate 45-year period between January 1979 and 2023.

Model parameters should be considered as representative of 10-minute averages.

5.1 Measured Hydrodynamic Data

To support calibration and validation of the hydrodynamic model, measured data were acquired from Kystdirektoratet as well as those provided by Energinet. An overview of the measured datasets can be found in Table 5-1 and Figure 5-1.

Table 5-1: Measured datasets considered for hydrodynamic model validation.

Dataset	Type	WGS84	Time Period	Water Depth [m MSL]
NSI-1 Current Profiler	Upward Looking Current Profiler	55.9441°N, 7.0596°E	1-Sep-2023 to 9-May-2024	31
NSI-1 LiDAR Buoy	Downward Looking Current Profiler	55.9441°N, 7.0596°E	1-Sep-2023 to 1-May-2024	31
NSI-2 Current Profiler	Upward Looking Current Profiler	55.8855°N, 7.6159°E	1-Sep-2023 to 9-May-2024	20
NSI-2 LiDAR Buoy	Downward Looking Current Profiler	55.8855°N, 7.6159°E	1-Sep-2023 to 1-May-2024	20
NSI-3 Current Profiler	Upward Looking Current Profilers	56.0694°N, 7.6347°E	1-Sep-2023 to 9-May-2024	30
NSI-3 LiDAR Buoy	Downward Looking Current Profiler	56.0694°N, 7.6347°E	1-Sep-2023 to 1-May-2024	30
EINS-1 Current Profiler	Upward Looking Current Profiler	56.6272°N, 6.3008°E	19-Nov-2021 to 21-Mar-2022	46
EINS-1 LiDAR Buoy	Downward Looking Current Profiler	56.6280°N, 6.3007°E	15-Nov-2021 to 15-Nov-2023	46
EINS-2 Current Profiler	Upward Looking Current Profiler	56.3442°N, 6.4552°E	19-Nov-2021 to 13-Jul-2022	40
EINS-2 LiDAR Buoy	Downward Looking Current Profiler	56.3444°N, 6.4574°E	15-Nov-2021 to 15-Nov-2023	40
EINS-3 Current Profiler	Upward Looking Current Profiler	56.4925°N, 6.5130°E	19-Nov-2021 to 30-Nov-2022	29



Hvide Sande Kyst	Tide Gauge	55.9988°N, 8.1146°E	2-Feb-1981 to 31-Dec-2018	Coastal
Thorsminde	Tide Gauge	56.3722°N, 8.1137°E	1-Nov-1979 to 31-Dec-2018	Coastal

* The term "Coastal" is used to denote water-level measurements taken by instruments mounted to a harbour wall.

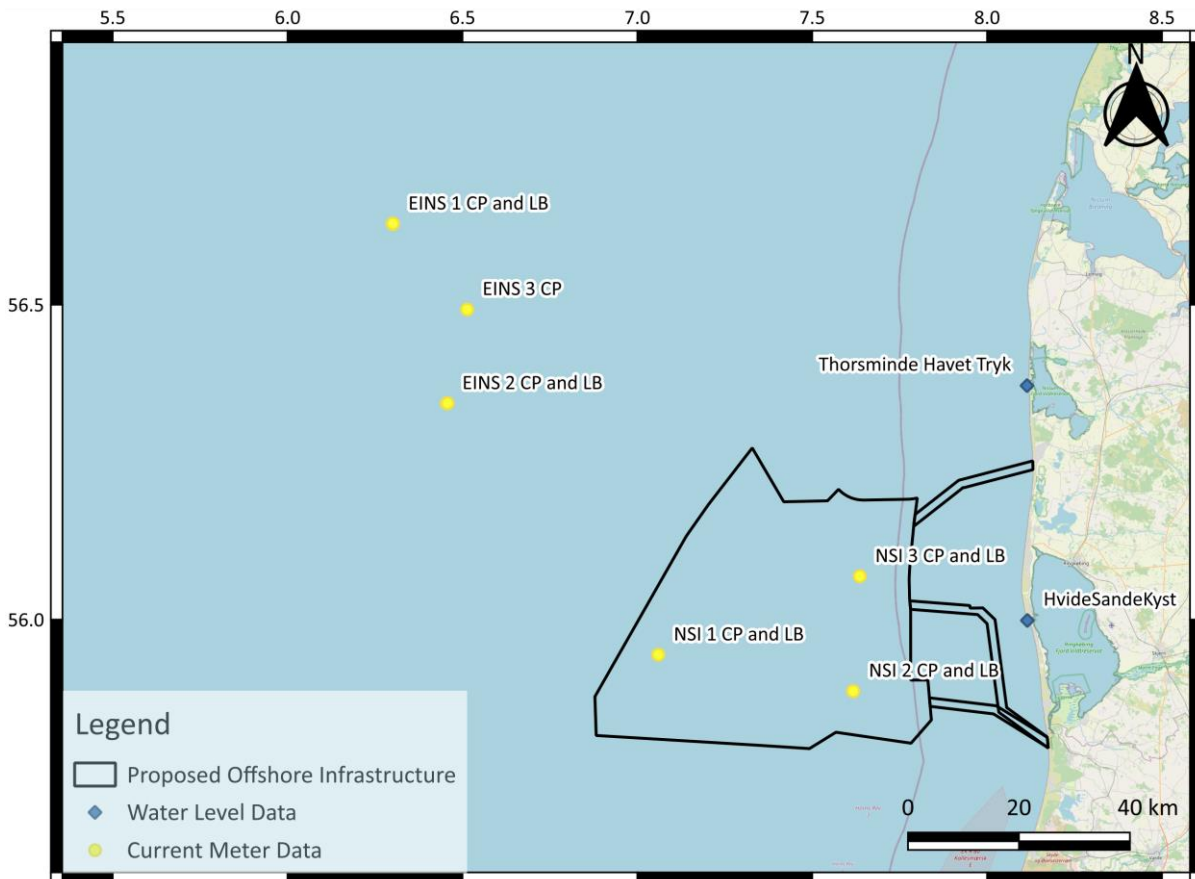


Figure 5-1: Measured datasets considered for hydrodynamic model validation.

5.1.1 Measured Current Profiles

The vertical profiles of measured currents are reviewed in Appendix D. As a result of this review, we recommend a power law profile, with exponent α of 1/8, is used to describe current speeds in the vertical for the wind farm areas.

5.2 Modelling Software

The hydrodynamic model has been developed using the MIKE21FM 2D flexible mesh modelling package [13] [14], a comprehensive modelling system for two-dimensional water modelling developed by DHI. For the production model run, Release 2023 was used.



5.3 Model Boundary Conditions and Spatial Extent

Tidal boundary conditions to the European model originate from the Finite Element Solution FES2014 dataset. This 35-constituent, global data-set has been produced using numerical modelling which assimilates satellite observations of water level and has, in our opinion, the best skill of any publicly-available global tide model. The dataset includes tide elevations (amplitude and phase) and tide currents on a 0.0625-degree (approximately 7 km) grid. The model was driven using water levels varying along three open boundaries (north, west and south), as shown in the left panel of Figure 5-2.

The model had a spatial resolution of 250 m to within 2 km of the wind farm and cable route boundaries. Beyond this, the model had a resolution of 500 m within 6 km of the wind farm and cable route boundaries, and a resolution of 1 km further offshore. The coastline was discretised to 125 m resolution within 2 km of the wind farm, and 250 m within 6 km of the wind farm. Beyond this, the coastline was discretised to 500 m resolution.

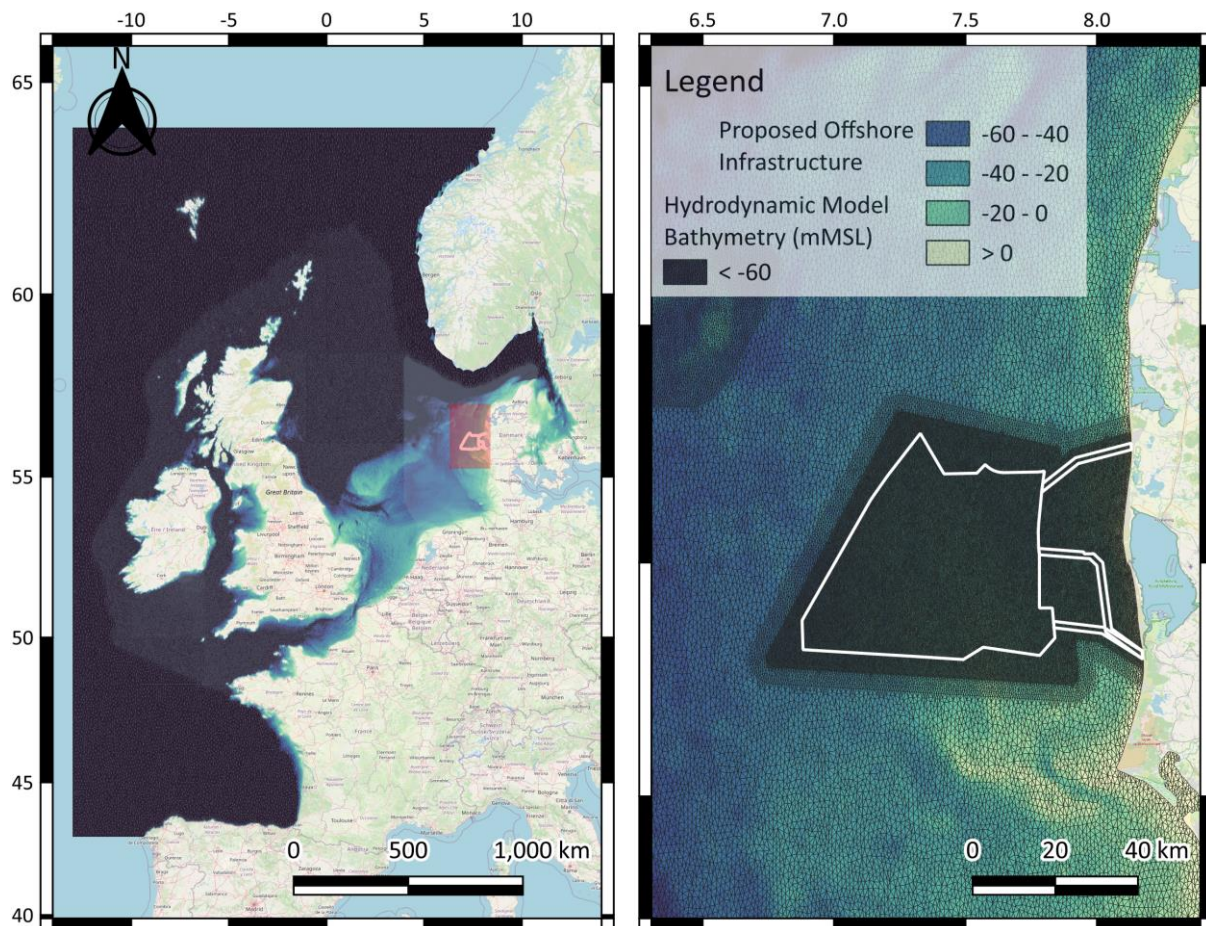


Figure 5-2 MIKE21 flexible model mesh.

Atmospheric forcing for the hydrodynamic model originated from the ECMWF ERA5 dataset and was applied to ensure that atmospheric surge effects were properly represented in the model. This comprised of MetOceanWorks adjusted wind speeds, unadjusted wind directions, and unadjusted pressure fields.



5.4 Model Sensitivity Testing

The model was subjected to a series of sensitivity tests to determine the effects of tuning various input parameters.

5.4.1 Mesh Resolution

To ensure that an appropriate mesh density was selected for the final hydrodynamic model, a series of tests were carried out to demonstrate convergence of results. Models with varying mesh resolutions within the project zone were deployed, and the effects were analysed at three locations. Low, medium and high mesh resolutions of approximately 500, 250 and 125 m within the wind farm and ECCs were used in these tests (see Figure 5-3 to Figure 5-5, which also show the analysis locations), with comparisons given in Figure 5-6 to Figure 5-8.

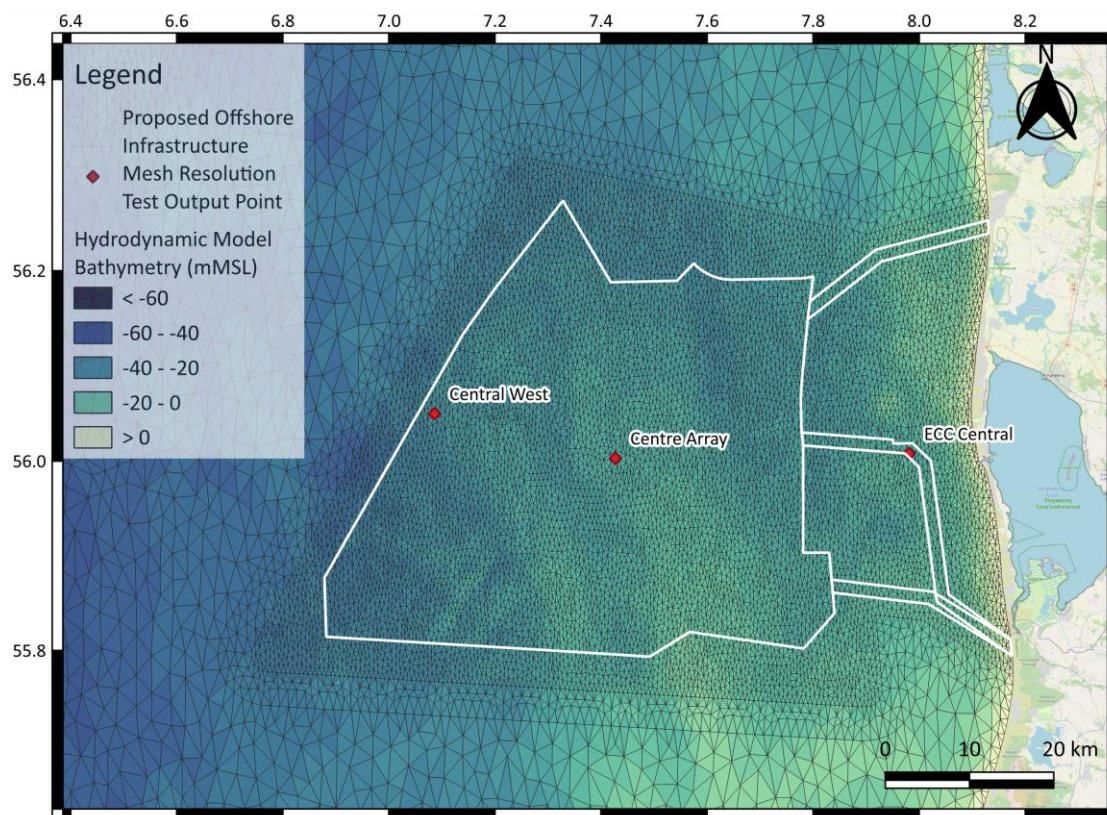


Figure 5-3. Hydrodynamic mesh with low resolution.

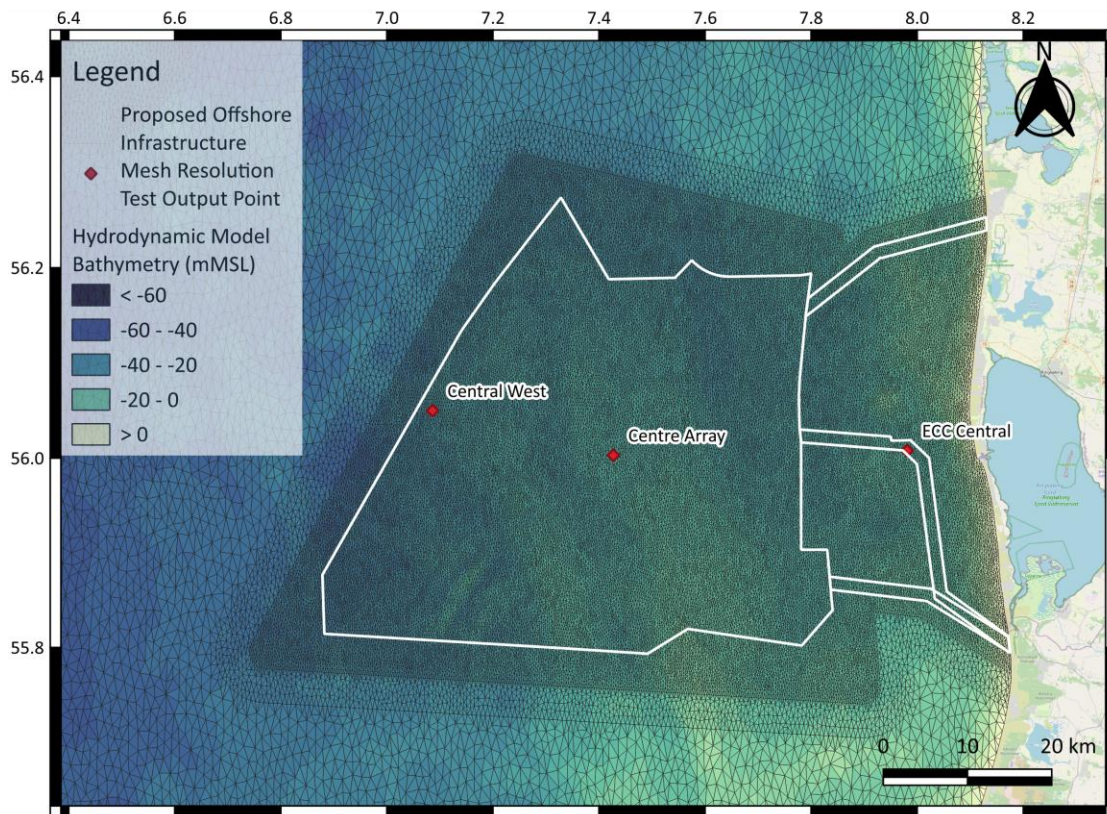


Figure 5-4. Hydrodynamic mesh with medium resolution.

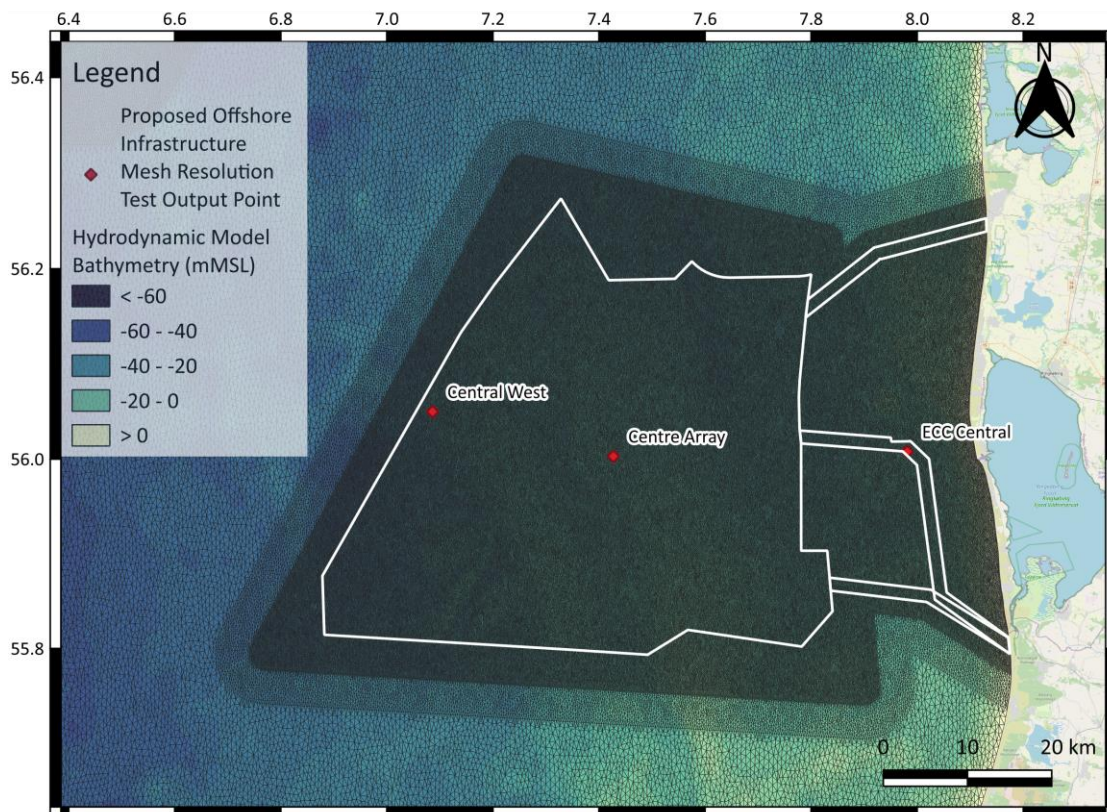


Figure 5-5. Hydrodynamic mesh with high resolution.

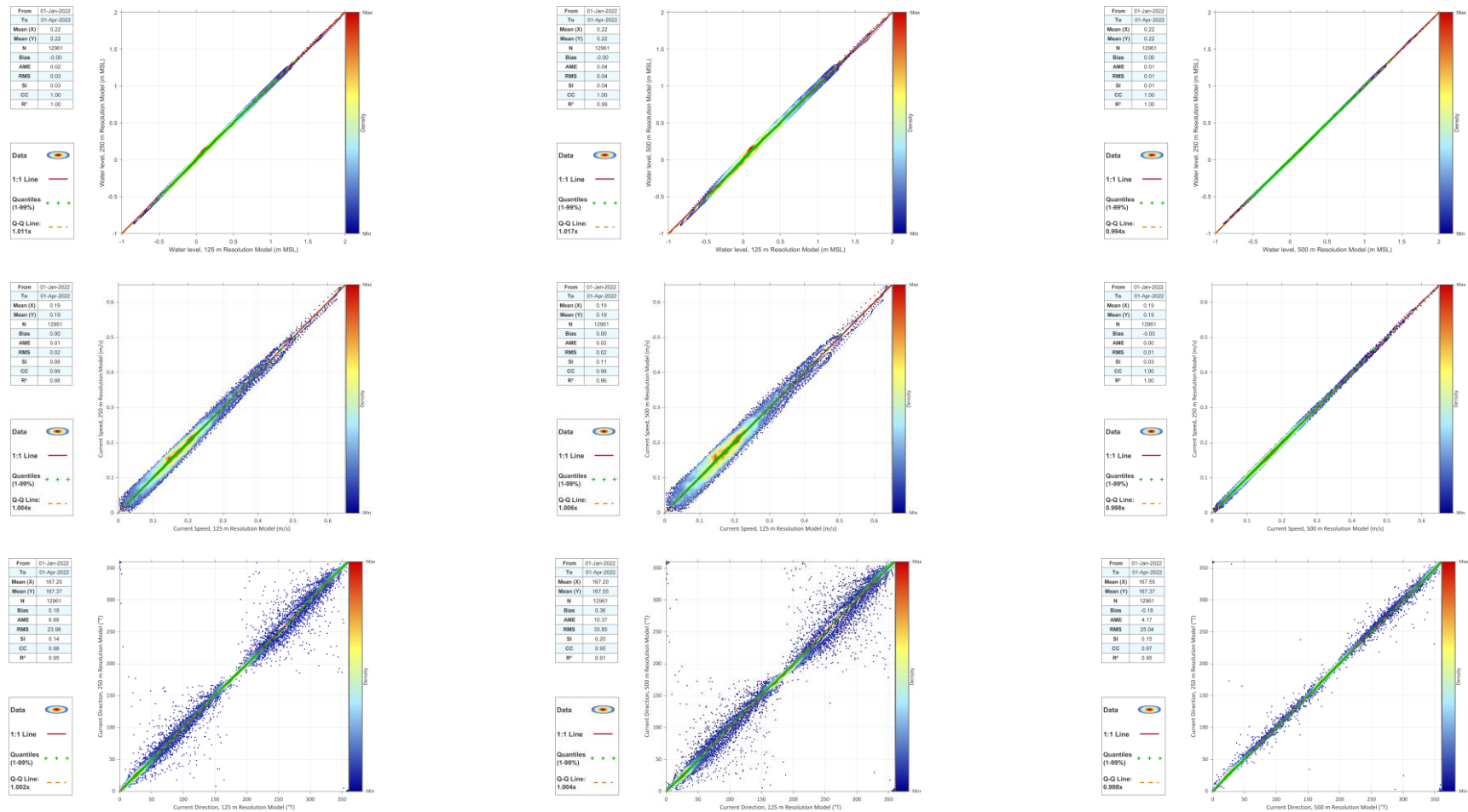


Figure 5-6. Results of model runs with differing mesh resolutions, at the Centre Array. Top row = water level, middle row = current speed, bottom row = current direction. Left column Medium Resolution vs. High Resolution. Middle column High Resolution vs. Low Resolution. Right column = Low Resolution vs. Medium Resolution.

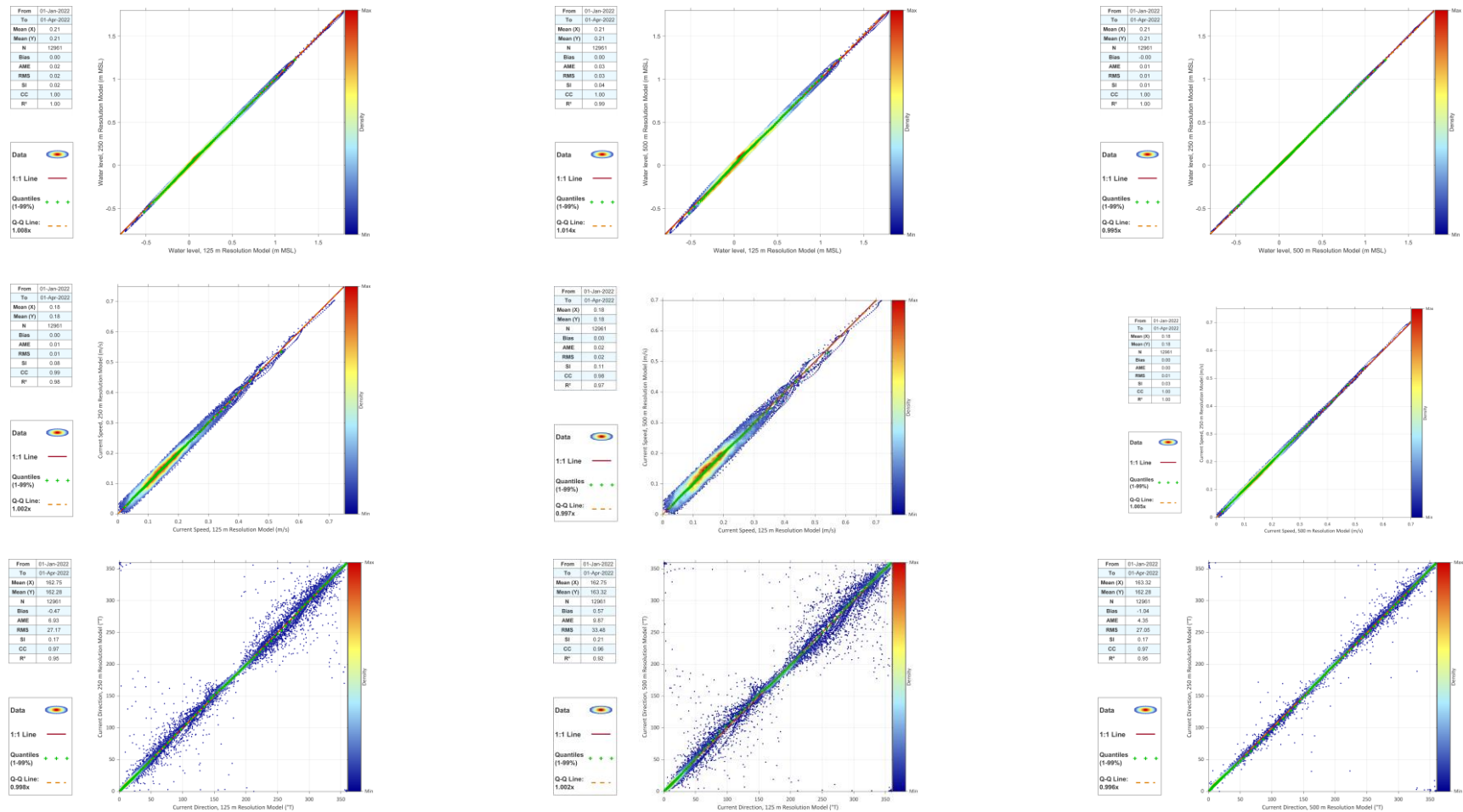


Figure 5-7. Results of model runs with differing mesh resolutions, at the Centre West. Top row = water level, middle row = current speed, bottom row = current direction. Left column Medium Resolution vs. High Resolution. Middle column High Resolution vs. Low Resolution. Right column = Low Resolution vs. Medium Resolution.

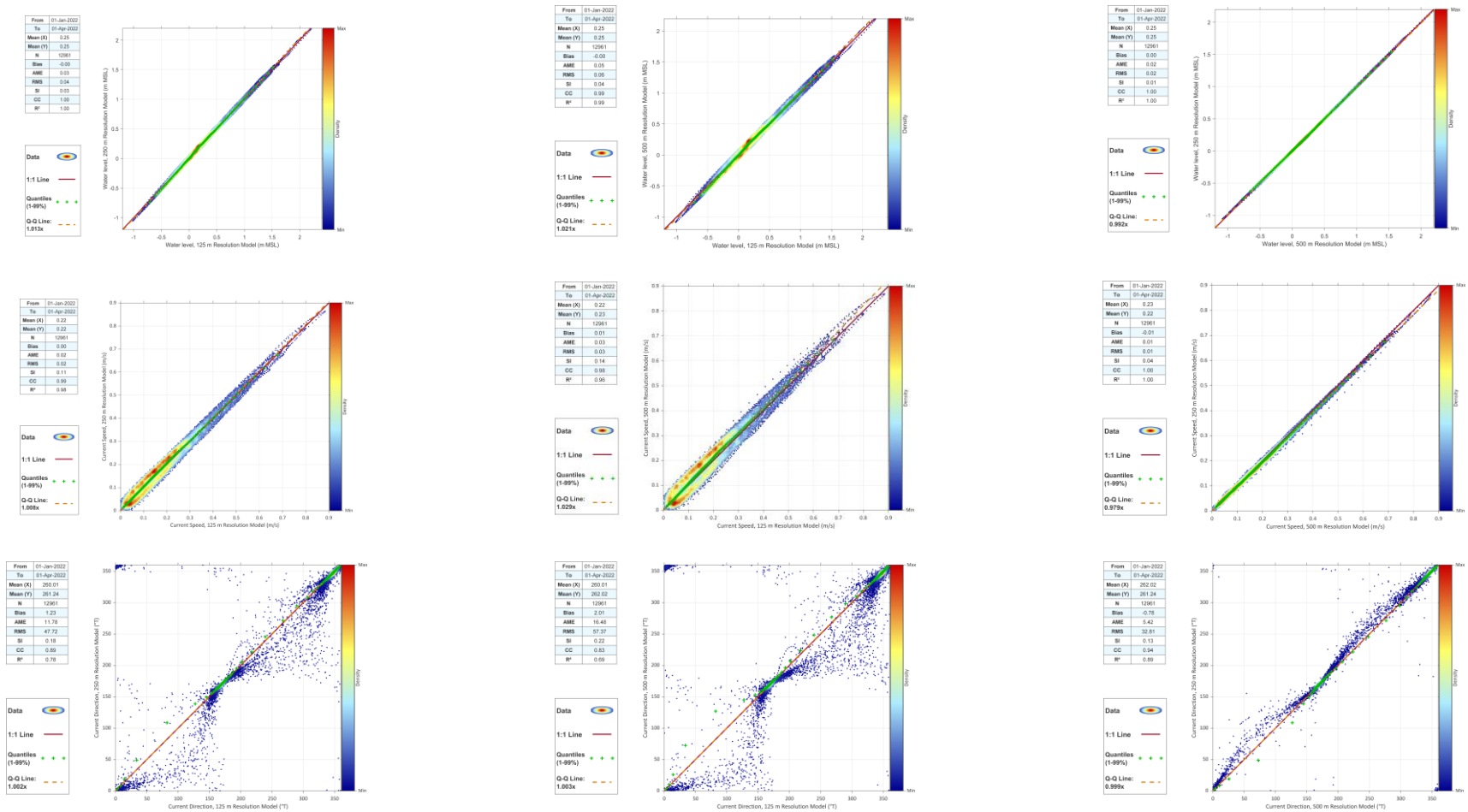


Figure 5-8. Results of model runs with differing mesh resolutions, at ECC Central. Top row = water level, middle row = current speed, bottom row = current direction. Left column Medium Resolution vs. High Resolution. Middle column High Resolution vs. Low Resolution. Right column = Low Resolution vs. Medium Resolution.



In these tests, we can consider the highest resolution model to be the ‘standard’ against which the other resolutions can be judged, on the basis that we assume that the highest resolution model should produce more accurate results.

Figure 5-6 to Figure 5-8 show that the impacts of mesh resolution on water levels, current speed, and current direction are relatively small, suggesting that only small gains in ‘accuracy’ are achieved with increased resolution. Therefore, for the production run the medium resolution model was selected, it being the highest resolution that could be achieved with an acceptable runtime.

5.4.2 Bed Resistance

Various uniform and spatially-varying bed roughness values were tested as part of model calibration. A spatially-varying bed roughness was eventually chosen for the final production hindcast run, which provided the best overall representation of water levels and currents at each validation site.

5.5 Final Model Parameter Settings

The following model settings were used for the hindcast:

Table 5-2: Final model parameter settings.

Parameter	Setting
Minimum and maximum time step	0.1 and 60 seconds
*Wind friction	0.001255 at 7m/s and 0.00303125 at 25m/s
Critical CFL number	1
Drying and wetting depth	0.01 m, 0.1 m
Horizontal eddy viscosity formulation	Smagorinsky, constant = 0.28
Minimum and maximum eddy viscosity	0.0000018, 100,000 m ² /second
Bed resistance	Variable Manning’s M (Range: 35.5-100, with mean value of 39.64 and std dev of 7.59)

*Friction is linearly interpolated between the two values based on the wind speed and if the wind speed is below the lower limit or above the upper limit the friction is given the value corresponding to that limit.

Please see the MIKE21FM User Guide [13] and Scientific Documentation [14] for more details.

The selected critical CFL number allows the use of high spatial resolutions without restrictively small-time steps, when used in conjunction with the numerical scheme selected for the hindcast.

5.6 Hindcast Uniformity

The model is expected to yield results of a uniform quality (i.e., equivalent to the level of validation detailed in the following Section 5.7) throughout the hindcast period.



5.7 Model Validation

The model was initially tuned such that modelled and measured tidal water levels agreed well. The model was then further calibrated against the measured current datasets until it demonstrated good skill.

Water levels from the model are compared against measurements at Hvide Sande and Thorsminde in Figure 5-9 and Figure 5-10 whilst on site validations at NSI-1 and NSI-2 are shown in Figure 5-11 and Figure 5-12. With low mean errors, correlation coefficients close to unity and low scatter indices, these comparisons demonstrate excellent model skill.

Site-specific current speed validations are presented in Figure 5-13 to Figure 5-24. These include time-series and scatter plots with regressions of modelled and measured current speeds which demonstrate excellent overall performance. Upward-looking instruments are expected to yield more accurate results than those obtained from downward looking instruments mounted on a moving platform such as those fitted to the floating LiDAR systems. As such, a higher level of confidence can be placed in the validations against data from the upward looking instruments.



Mean (X)	-0.00
Mean (Y)	-0.00
N	60543
Bias	-0.00
AME	0.09
RMS	0.11
SI	0.06
CC	0.97
R ²	0.95

Data	
1:1 Line	
Quantiles (1-99%)	
Q-Q Line: 1.001x	

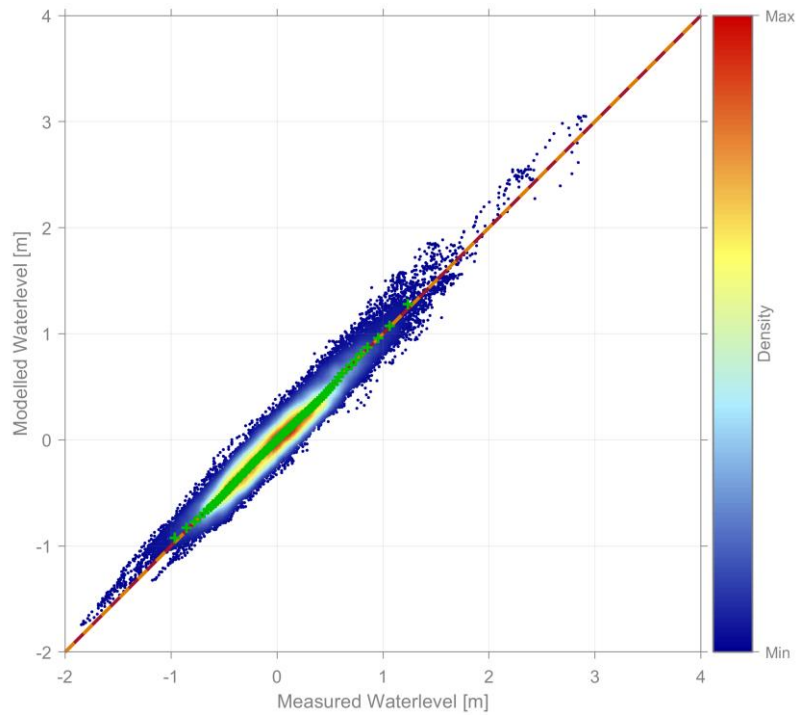


Figure 5-9: Comparison of measured and modelled water levels at Hvide Sande.

Mean (X)	0.00
Mean (Y)	-0.04
N	44083
Bias	-0.04
AME	0.09
RMS	0.11
SI	0.06
CC	0.96
R ²	0.93

Data	
1:1 Line	
Quantiles (1-99%)	
Q-Q Line: 1.046x	

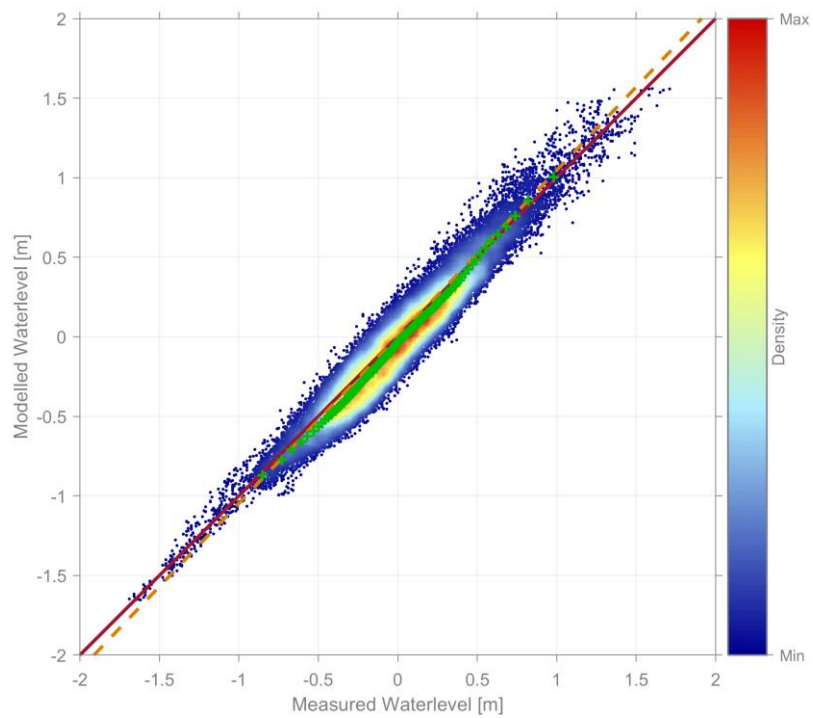


Figure 5-10: Comparison of measured and modelled water levels at Thorsminde.



From	01-Sep-2023
To	01-May-2024
Mean (X)	0.00
Mean (Y)	0.00
N	17527
Bias	0.00
AME	0.07
RMS	0.09
SI	0.06
CC	0.97
R ²	0.94

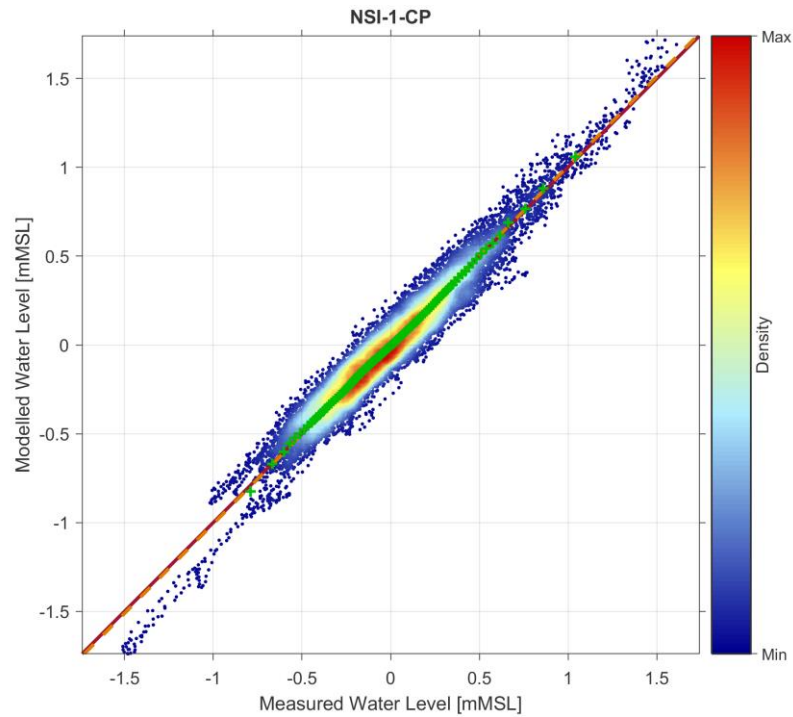
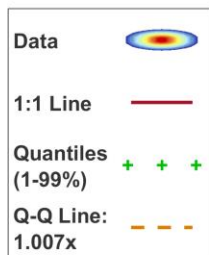


Figure 5-11: Comparison of measured and modelled water levels at NSI-1-CP.

From	01-Sep-2023
To	01-May-2024
Mean (X)	0.00
Mean (Y)	-0.00
N	17537
Bias	-0.00
AME	0.08
RMS	0.10
SI	0.05
CC	0.97
R ²	0.95

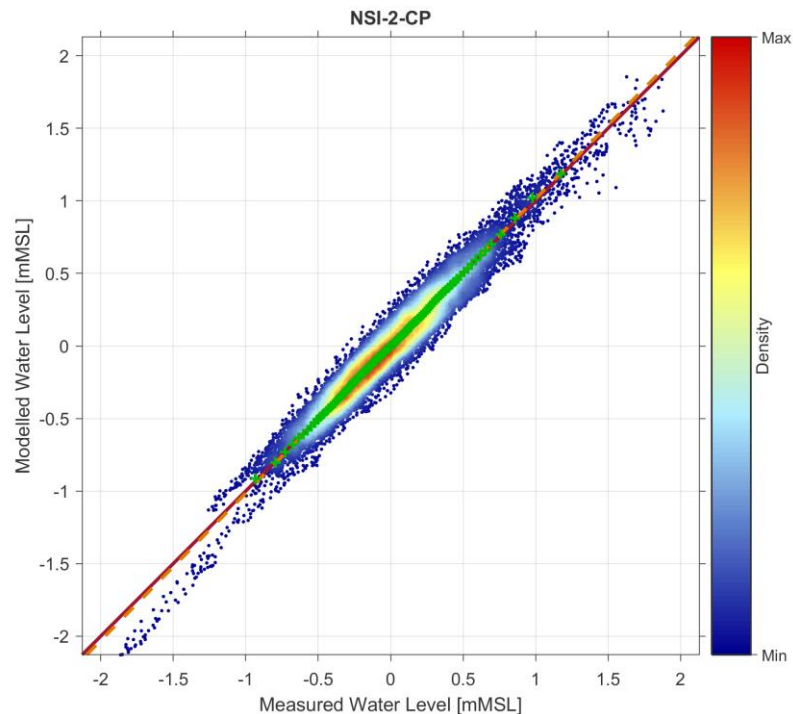
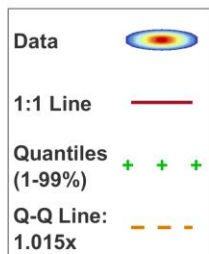


Figure 5-12: Comparison of measured and modelled water levels at NSI-2-CP.

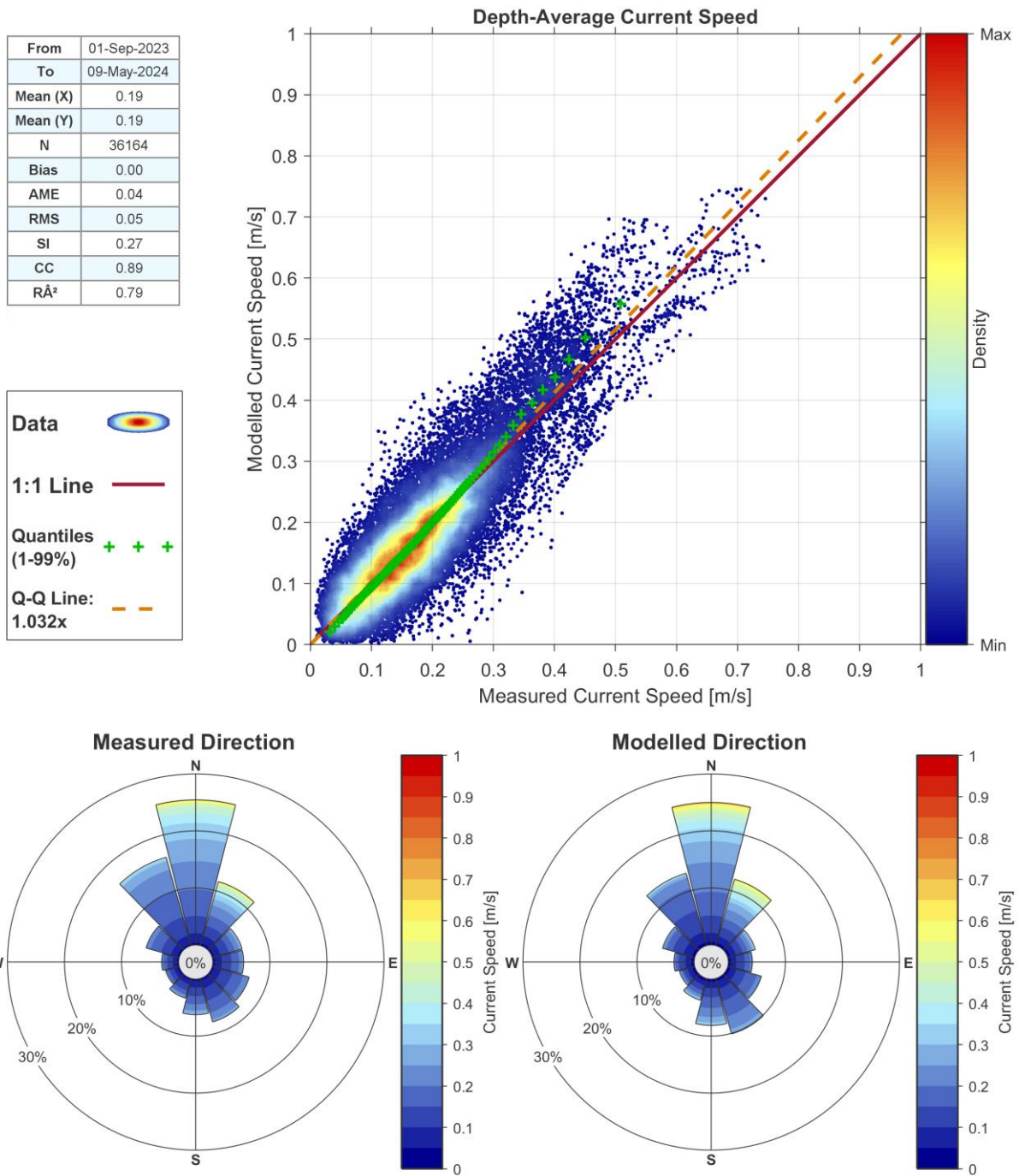


Figure 5-13: Scatter and rose validation of depth-average current speed, NSI-1-CP.

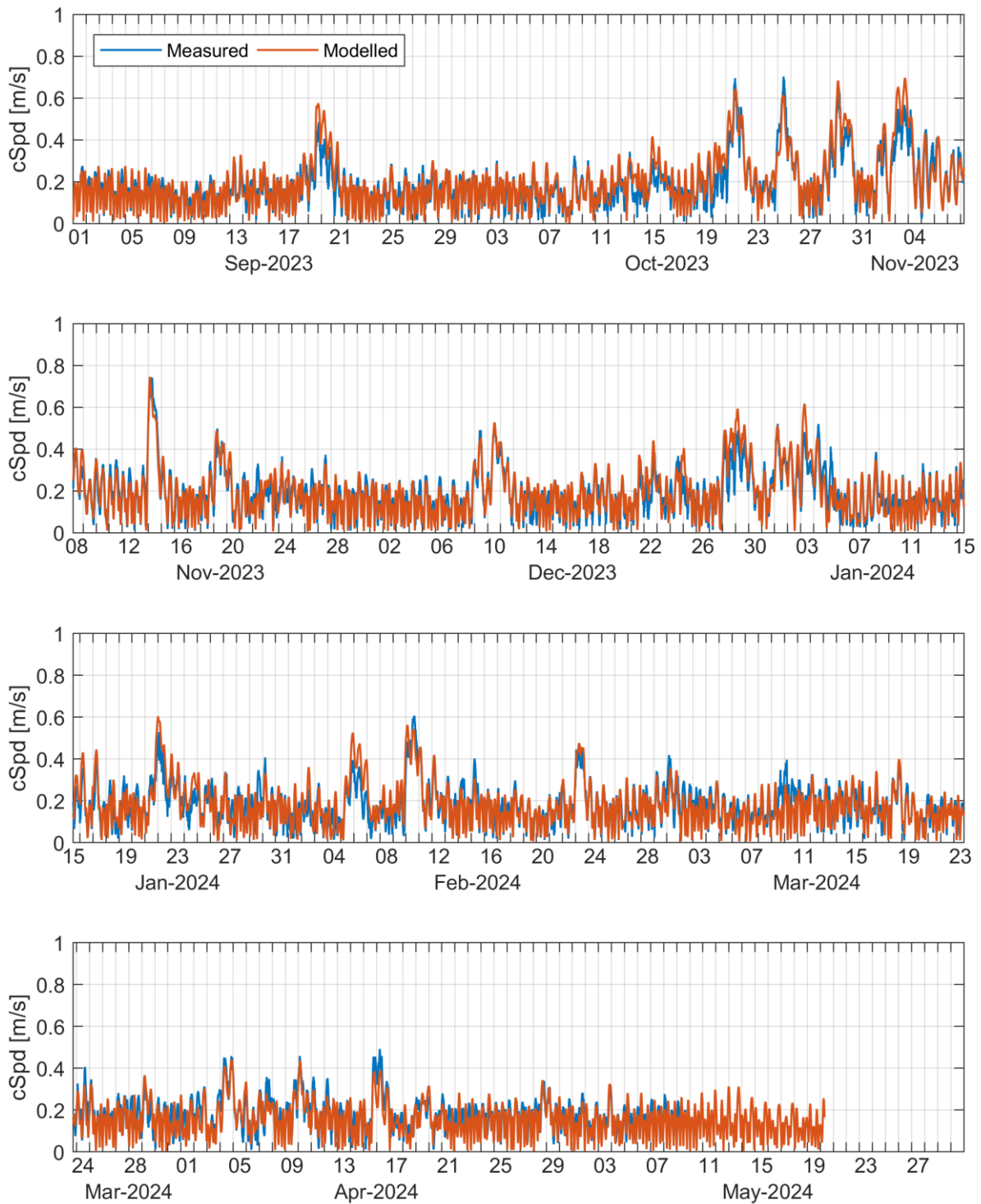


Figure 5-14: Time-Series validation of depth-average current speed, NSI-1-CP.

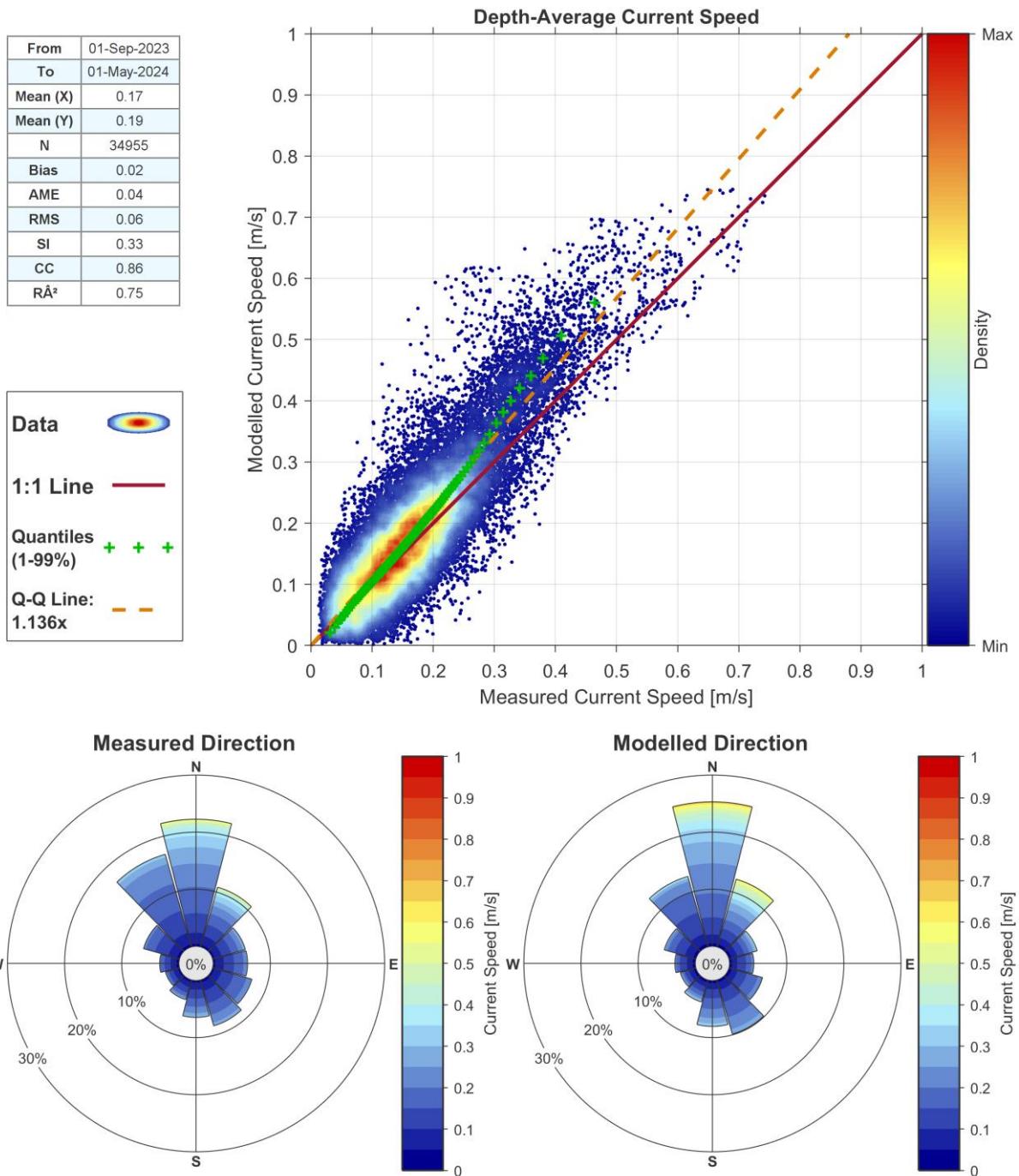


Figure 5-15: Scatter and rose validation of depth-average current speed, NSI-1-LB.

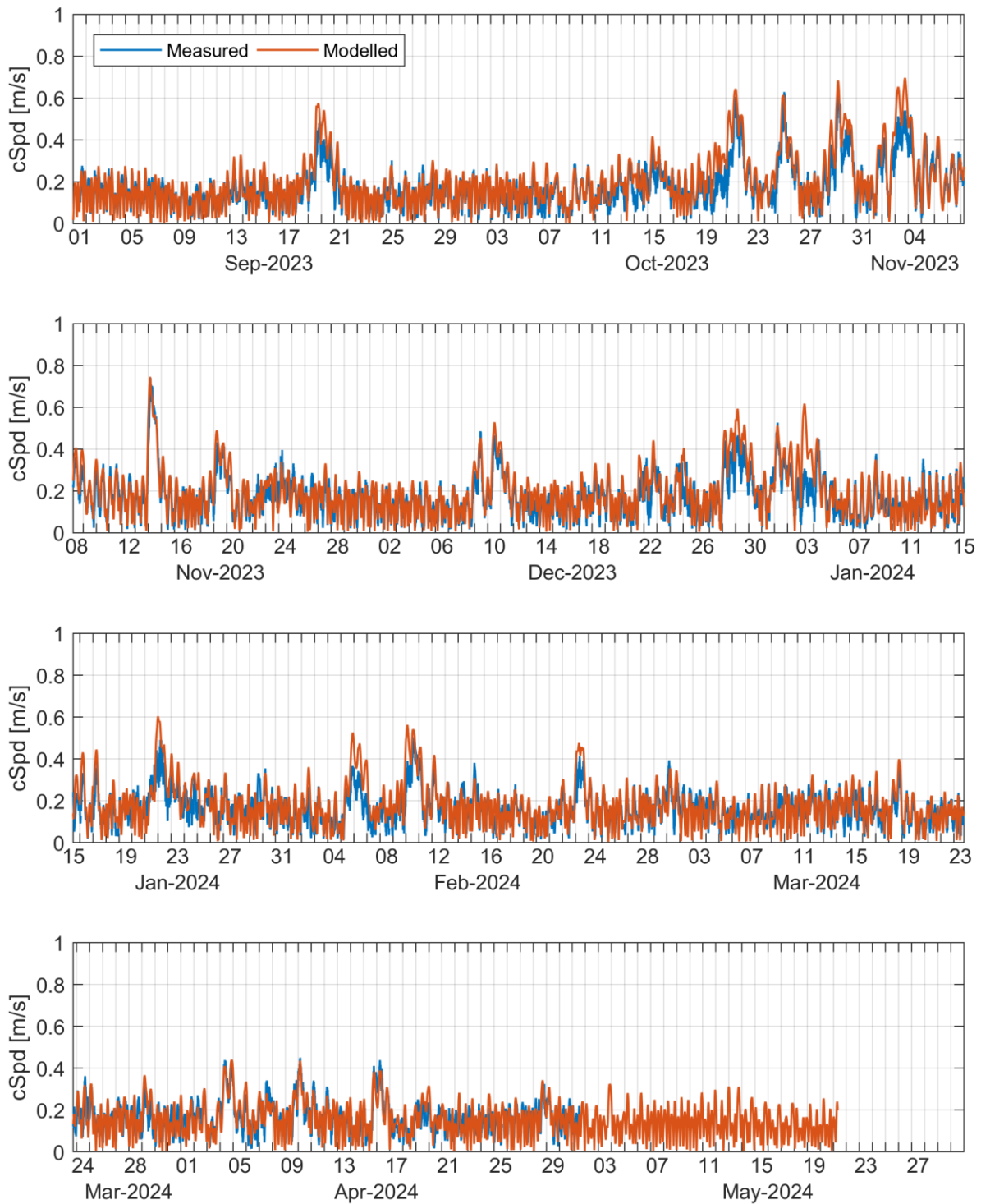


Figure 5-16: Time-Series validation of depth-average current speed, NSI-1-LB.

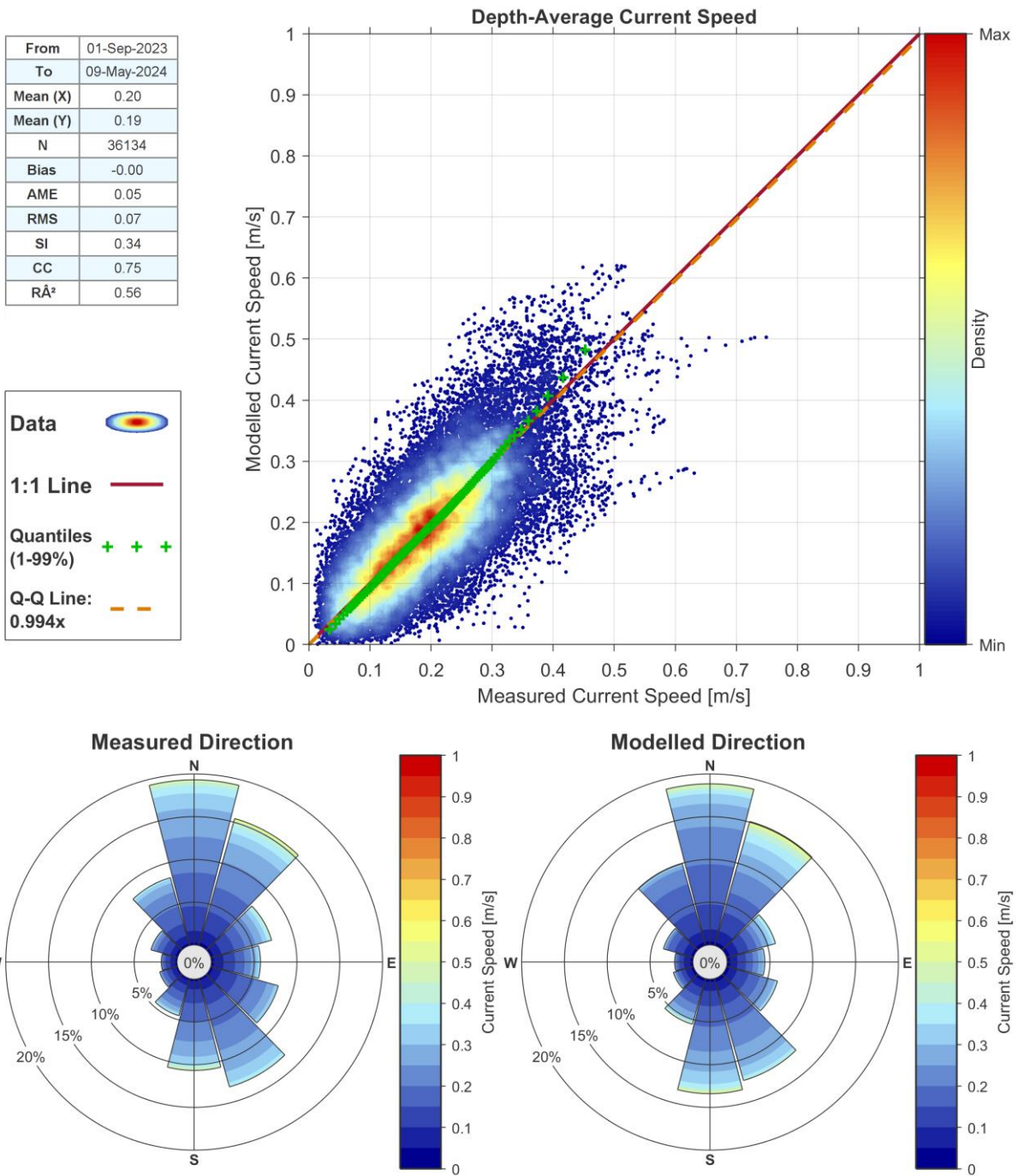


Figure 5-17: Scatter and rose validation of depth-average current speed, NSI-2-CP.

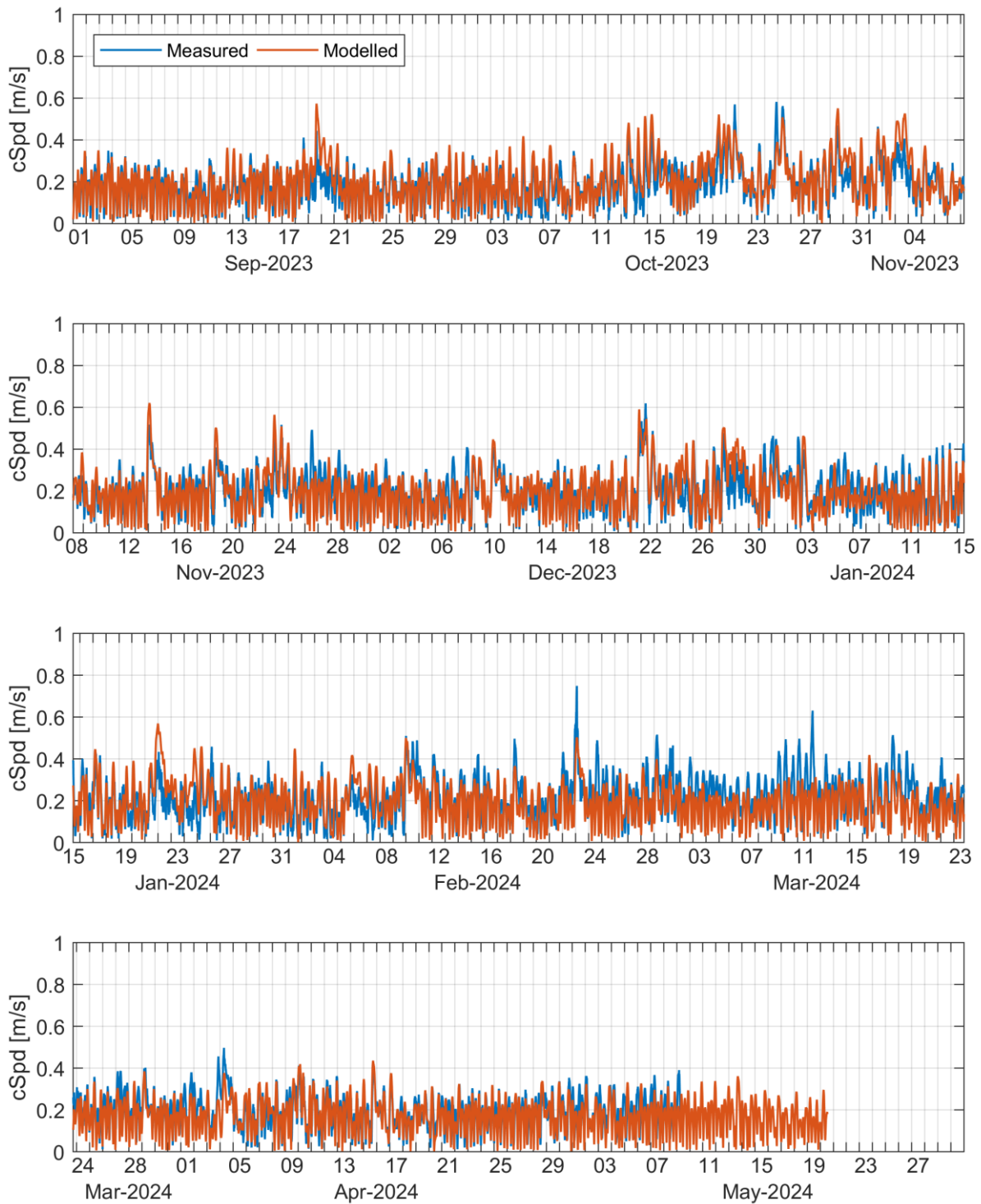


Figure 5-18: Time-Series validation of depth-average current speed, NSI-2-CP.

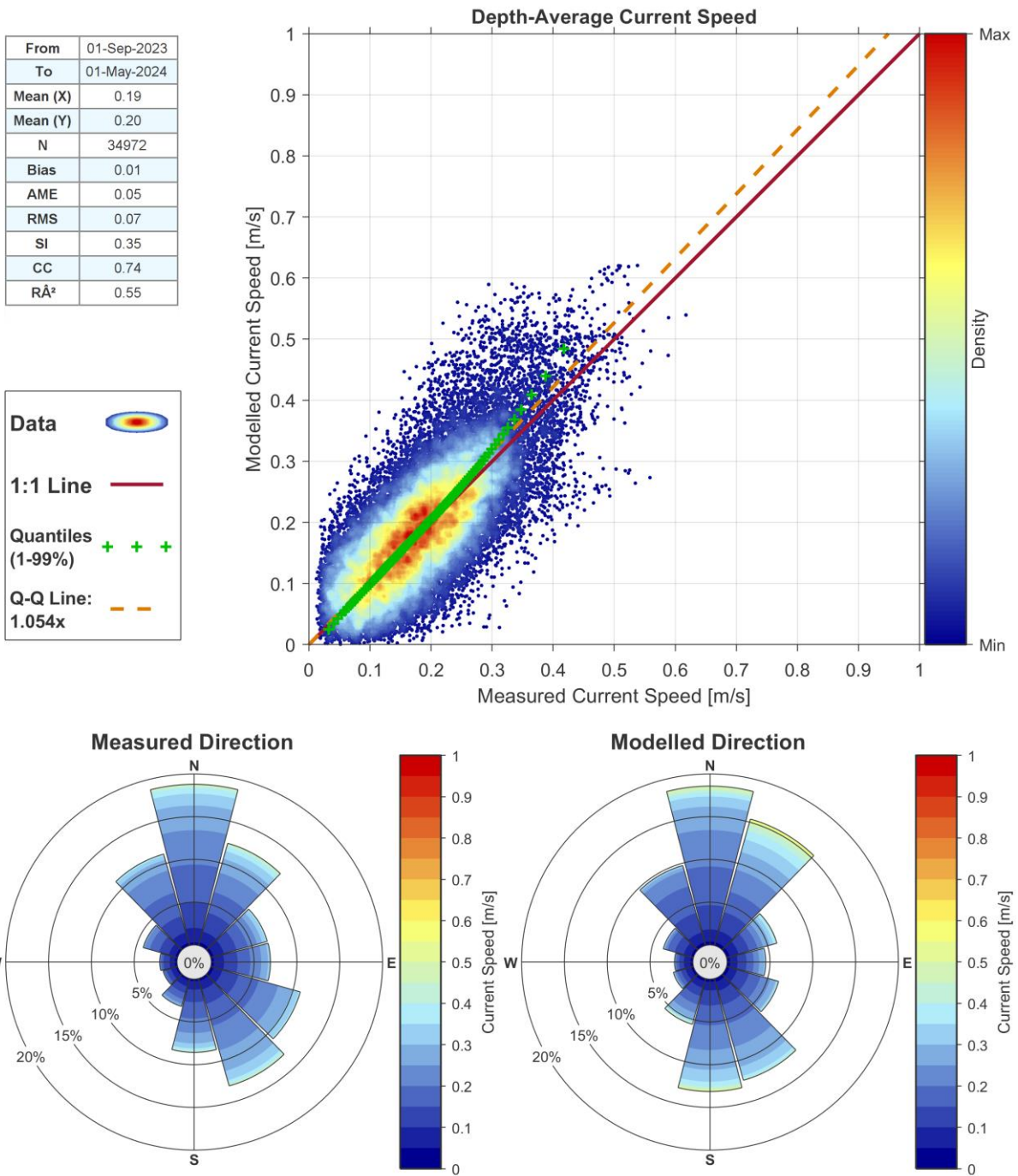


Figure 5-19: Scatter and rose validation of depth-average current speed, NSI-2-LB.

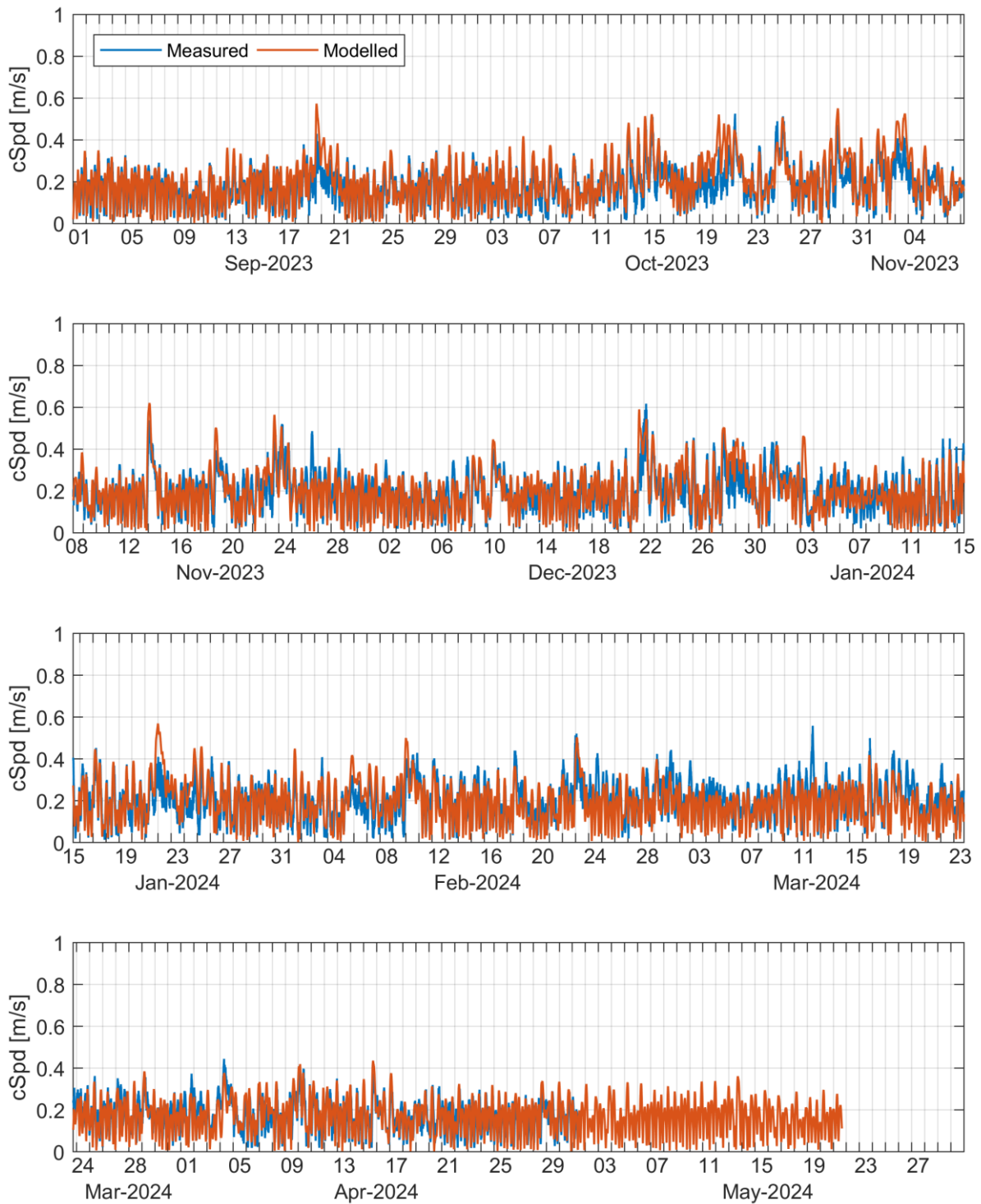


Figure 5-20: Time-Series validation of depth-average current speed, NSI-2-LB.

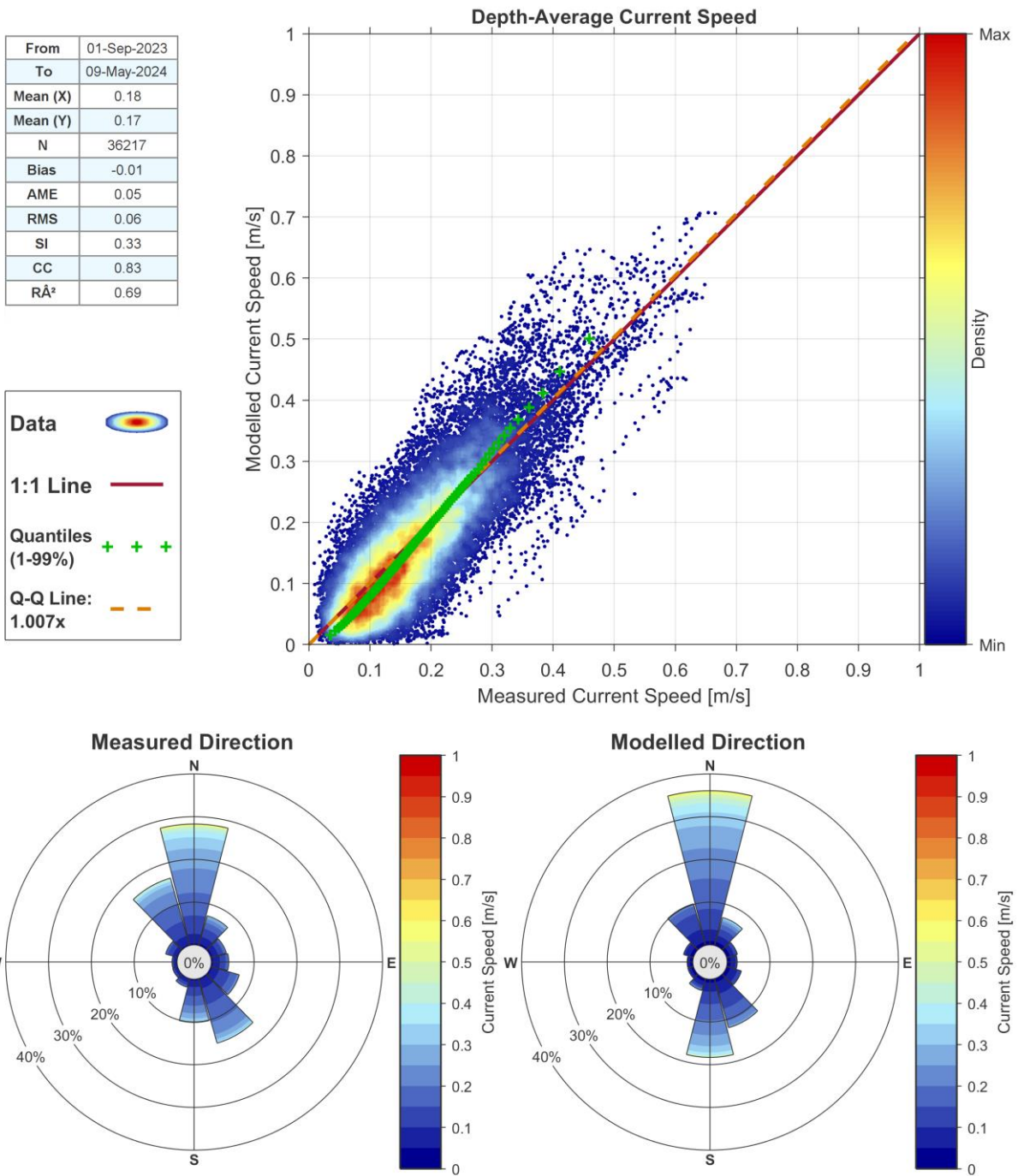


Figure 5-21: Scatter and rose validation of depth-average current speed, NSI-3-CP.

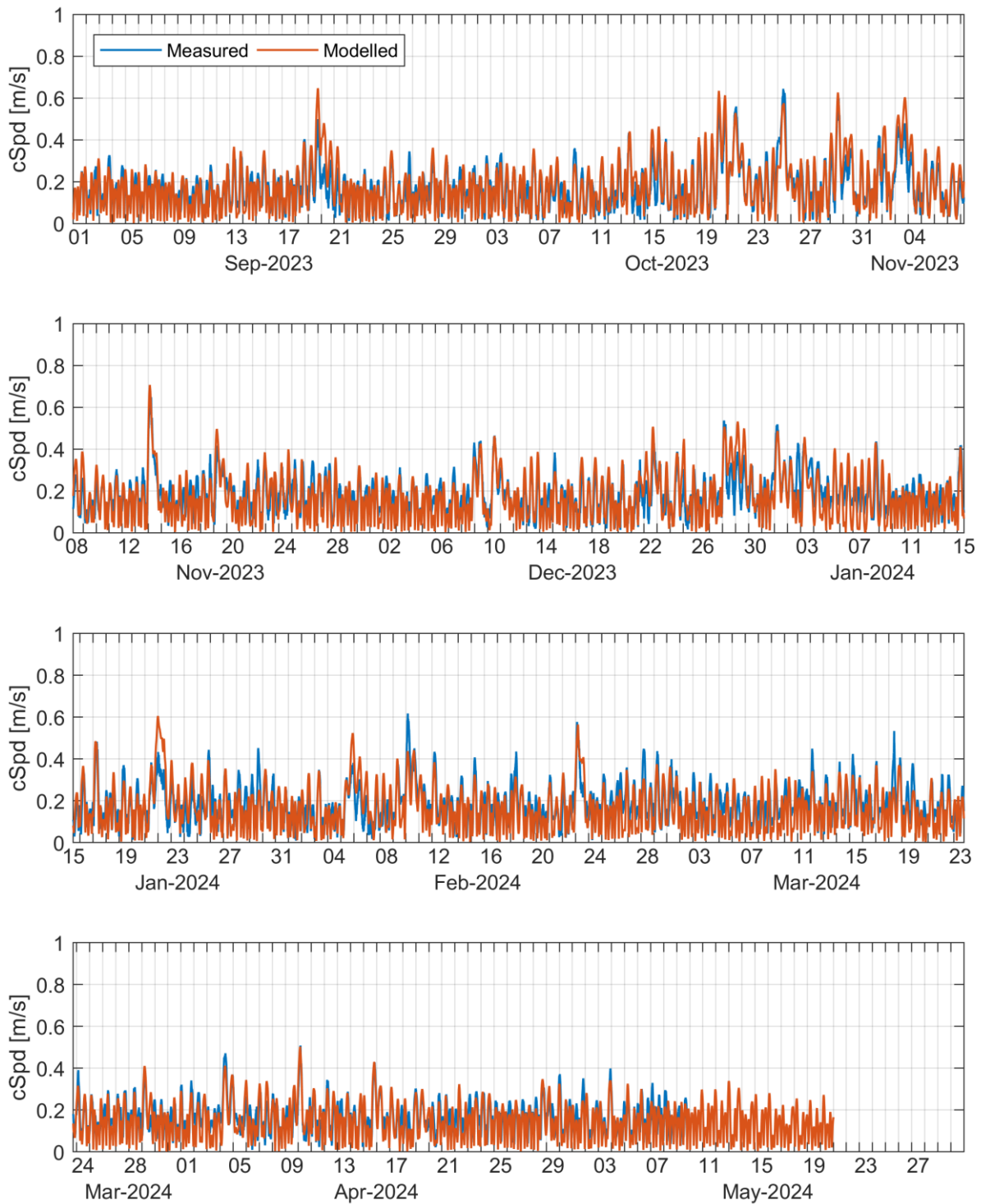


Figure 5-22: Time-Series validation of depth-average current speed, NSI-3-CP.

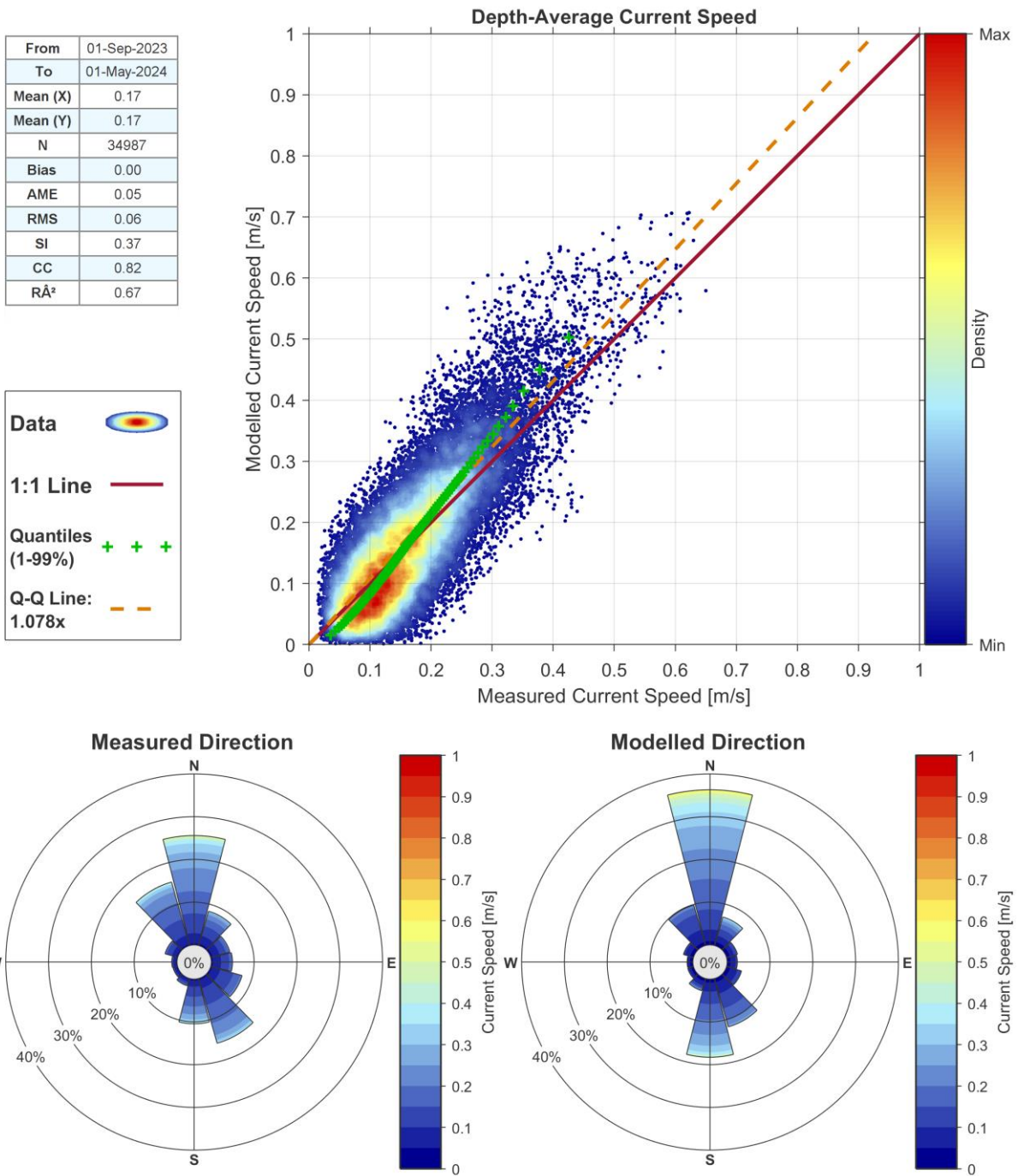


Figure 5-23: Scatter and rose validation of depth-average current speed, NSI-3-LB.

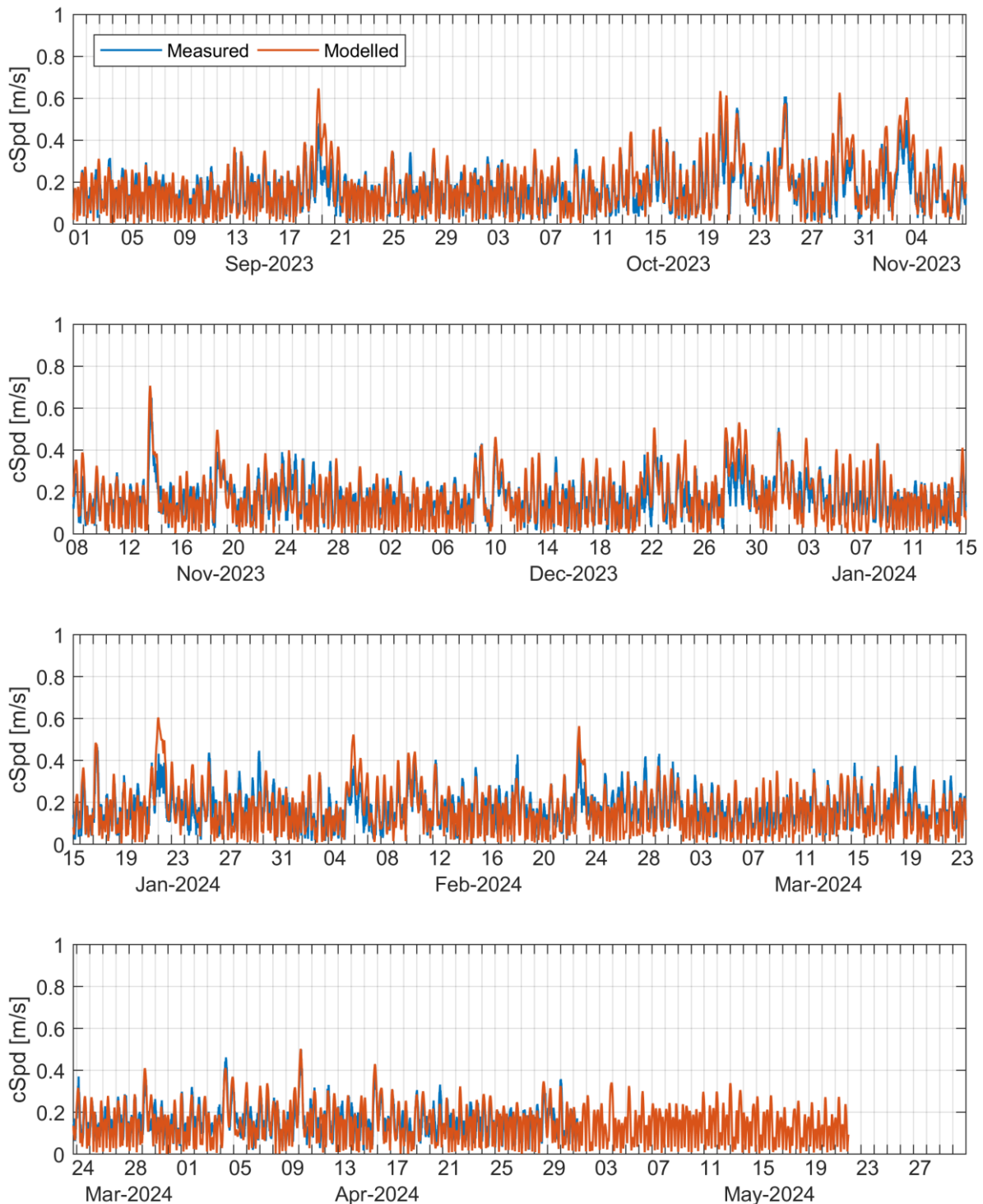


Figure 5-24: Time-Series validation of depth-average current speed, NSI-3-LB.



6 Waves

Wave data were produced using an Eastern North Sea SWAN model including higher resolution nested models local to the wind farm lease area and export cable corridor. For the production model run, SWAN cycle III version 40.91ABC [15] was used. Time-series data were output at hourly intervals for the period between January 1979 and near present.

Model parameters should be considered as representative of a 3-hour sea-state.

6.1 Measured Wave Data

To support calibration and validation of the wave models, measured data were provided by Energinet as well as acquired from Kystdirektoratet and FuE-Zentrum FH Kiel GmbH. Details of these datasets are provided in Table 6-1 below and illustrated in Figure 6-1.

Table 6-1: Measured datasets used for wave model validation.

Supplier	Name	WGS84	Time Period	Water Depth [mMSL]	Avg Period (s)
Energinet	NSI-1 LiDAR Buoy	55.9441°N, 7.0596°E	1-Sep-2023 to 1-May-2024	31	1024
Energinet	NSI-2 LiDAR Buoy	55.8856°N, 7.6167°E	1-Sep-2023 to 1-May-2024	20	1024
Energinet	NSI-3 LiDAR Buoy	56.0694°N, 7.6356°E	1-Sep-2023 to 1-May-2024	30	1024
Energinet	EINS-3 Wave Buoy	56.4929°N, 6.5108°E	15-Nov-2021 to 15-Nov-2023	29	1024
Energinet	EINS-4 Wave Buoy	56.5114°N, 6.5190°E	15-Nov-2021 to 15-Nov-2023	31	1024
Energinet	EINS-5 Wave Buoy	56.5020°N, 6.4337°E	30-Nov-2022 to 15-Nov-2023	44	1024
FuE-Zentrum FH Kiel GmbH	FINO3	55.1950°N, 7.1583°E	20-Feb-2014 to 29-Feb-2024	22	1800
Kystdirektoratet	Nymindegab	55.8100°N, 7.9410°E	4-Jun-2015 to 29-Feb-2024	19	unknown

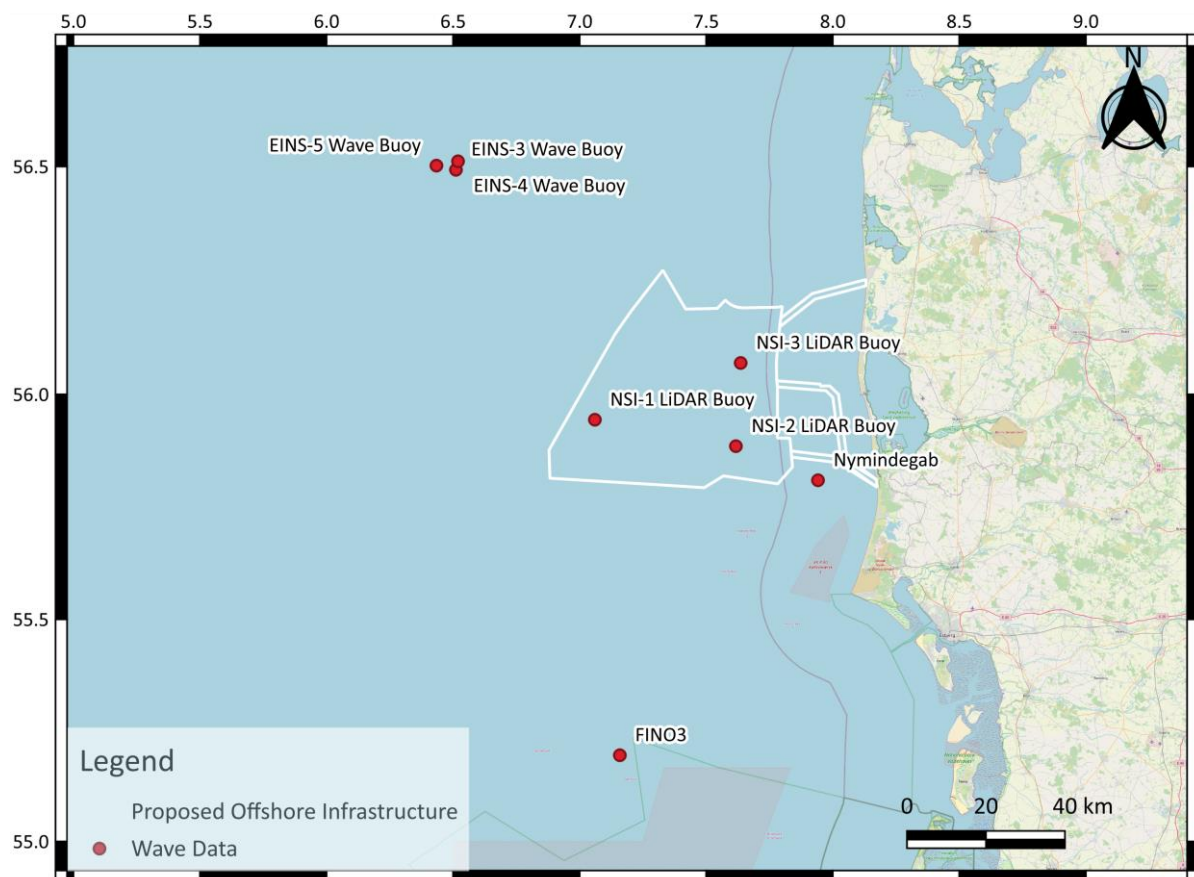


Figure 6-1: Locations of the wave measurement devices.

6.2 Modelling Software

A bespoke Eastern North Sea SWAN wave model was deployed with higher resolution nested models to produce a long-term wave hindcast between January 1979 and May 2024. The large-scale model had a spatial resolution of approximately 10 km whilst the local model had a spatial resolution of 275 m. The wave model domains are shown in Figure 6-2.

SWAN is a third-generation wave model, developed at Delft University of Technology, which computes random, short-crested wind-generated waves. SWAN accounts for the following physics:

- Wave propagation in time and space, shoaling, refraction due to current and depth, frequency shifting due to currents and non-stationary depth.
- Wave generation by wind.
- Three- and four-wave interactions.
- Whitecapping, bottom friction and depth-induced breaking.
- Wave-induced set-up.
- Transmission through and reflection (specular and diffuse) against obstacles.
- Diffraction.

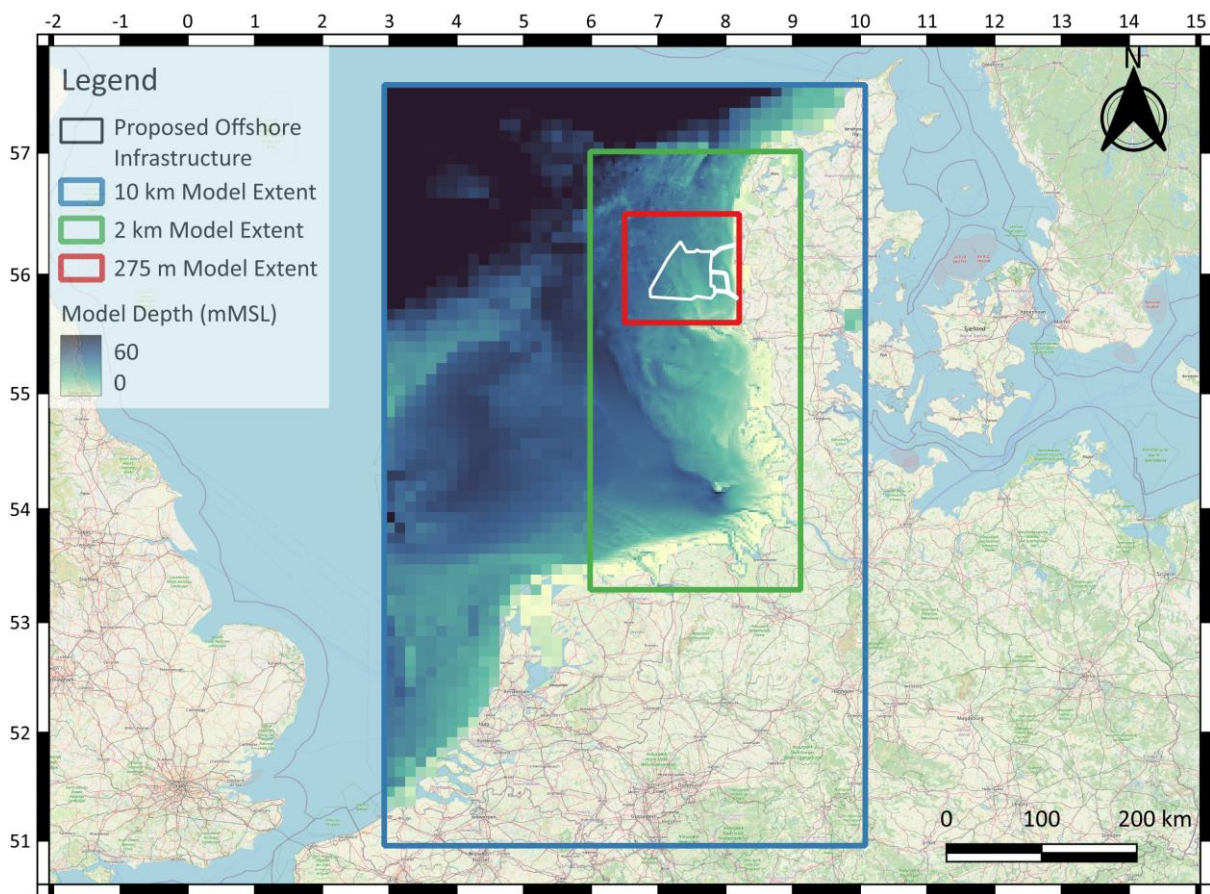


Figure 6-2: Wave model domains.

6.3 Model Boundary Conditions

Spectral wave boundary conditions to the large-scale model originated from ECMWF ReAnalysis 5 (ERA5). ERA5 incorporates a model with three fully coupled components for the atmosphere, land surface, and ocean waves. The wave model is based on the Wave Analysis Model (WAM) approach (Komen et al, 1994 [16]). The horizontal resolution of the output wave data is 0.5 degree (approximately 56 km in latitude and 30 km in longitude in the region of interest) and wave spectra are discretised using 24 directions and 30 frequencies from 0.0345 to 0.5473 Hz. Data are available every hour between 1979 and present. MetOceanWorks adjusted ERA5 wind fields (see Section 4) were applied to the sea surface at hourly intervals.

6.4 Model Sensitivity Testing

6.4.1 Grid Resolution

To ensure that an appropriate model grid resolution was selected for the final wave model, a series of tests were carried out to demonstrate convergence of results. Models with varying spatial resolutions were deployed, and the effects of varying grid resolution were analysed at three locations (shown in Figure 5-3). 550 m, 275 m and 140 m spatial resolutions were used in these tests. The comparisons are shown in Figure 6-3 to Figure 6-5.

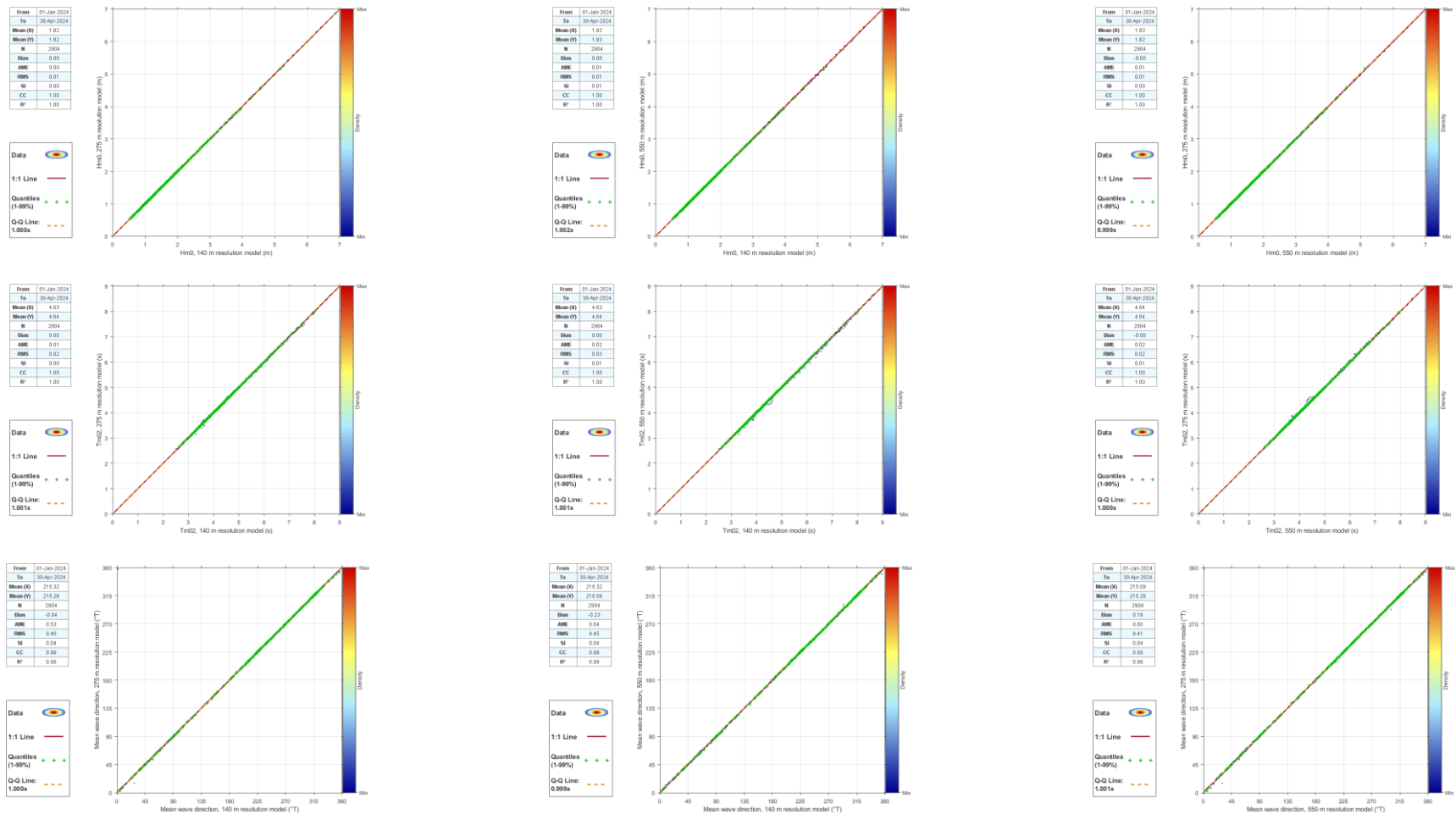


Figure 6-3. Results of model runs with differing mesh resolutions, at the Centre Array. Top row = significant wave height, middle row = mean zero-crossing wave period, bottom row = mean wave direction. Left column Medium Resolution vs. High Resolution. Middle column High Resolution vs. Low Resolution. Right column = Low Resolution vs. Medium Resolution.

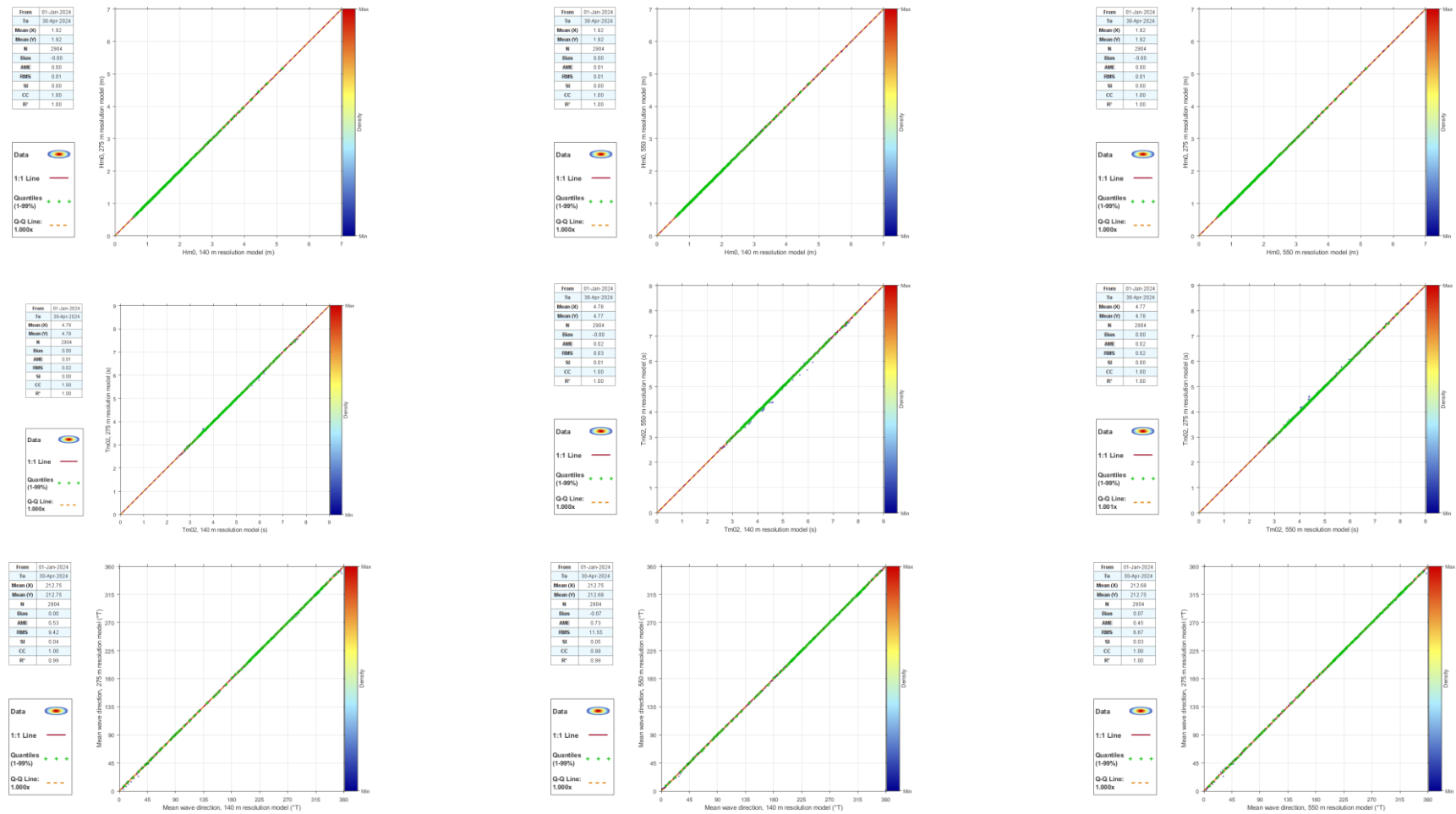


Figure 6-4. Results of model runs with differing mesh resolutions, at the Centre West. Top row = significant wave height, middle row = mean zero-crossing wave period, bottom row = mean wave direction. Left column Medium Resolution vs. High Resolution. Middle column High Resolution vs. Low Resolution. Right column = Low Resolution vs. Medium Resolution.

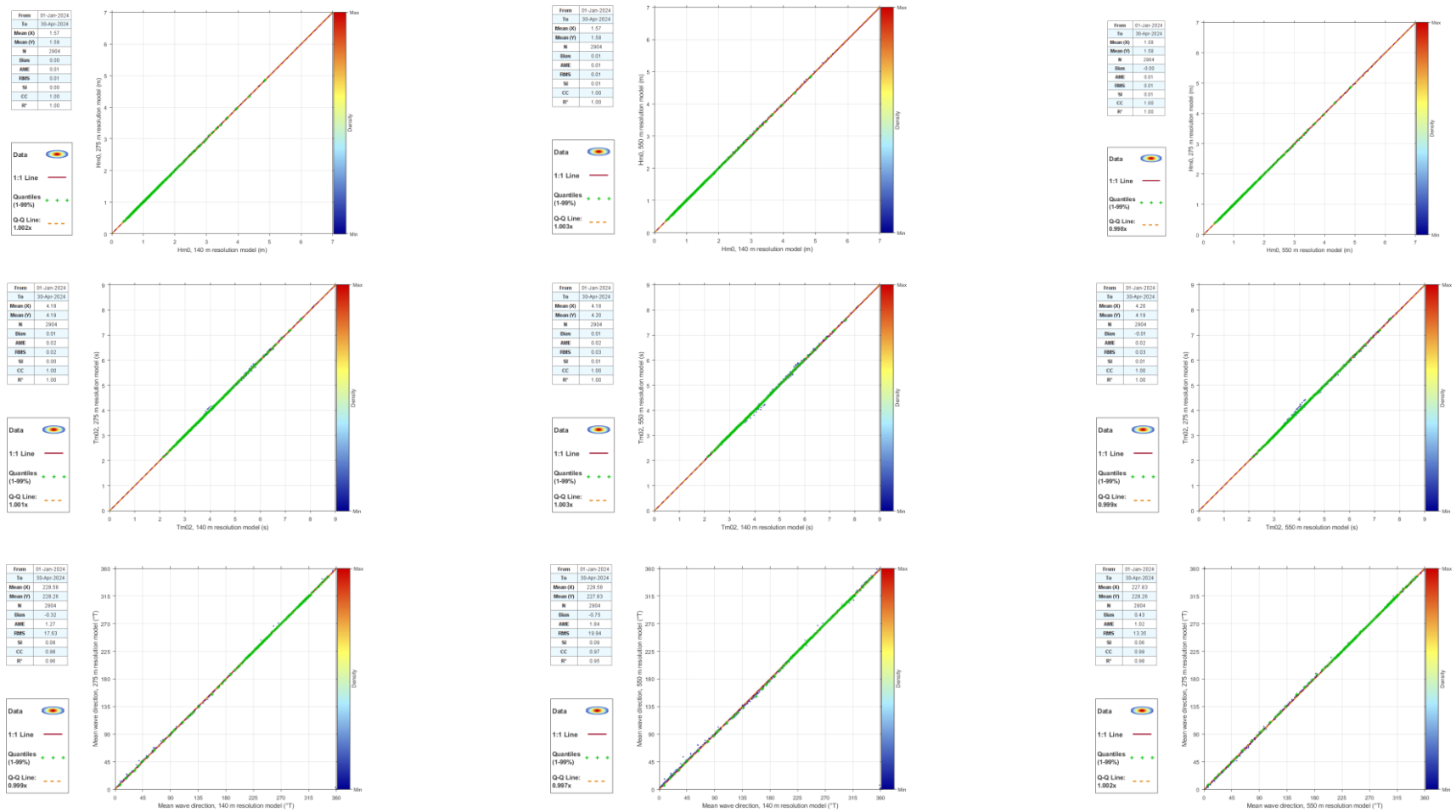


Figure 6-5. Results of model runs with differing mesh resolutions, at ECC Central. Top row = significant wave height, middle row = mean zero-crossing wave period, bottom row = mean wave direction. Left column Medium Resolution vs. High Resolution. Middle column High Resolution vs. Low Resolution. Right column = Low Resolution vs. Medium Resolution.



In these tests, we can consider the highest spatial resolution model to be the ‘standard’ against which the other resolutions can be judged, on the basis that we assume that the highest spatial resolution model should produce the more accurate results.

Figure 6-3 to Figure 6-5 show virtually no impact of spatial resolution on wave period and direction at all locations. Wave heights (top row of each figure) are also unaffected by changes in spatial resolution.

The right-hand columns of each figure show that there is no perceptible difference between a model with 275 m or 140 m spatial resolution, suggesting that there is no additional ‘accuracy’ to be achieved in increasing resolution above 275 m. Therefore, a final spatial resolution of 275 m was selected, it being the highest resolution that could be achieved with a practicable runtime.

6.4.2 Directional Discretisation

To ensure that an appropriate directional discretisation was selected for the final wave model, a series of tests were carried out to demonstrate convergence of results. Models with varying numbers of directional bins were deployed, and the effects of varying directional discretisation were analysed at the same three locations as those used in Section 6.4.1. 24, 36 and 48 directional bins were used in these tests. The comparisons are shown in Figure 5-6 to Figure 5-8.

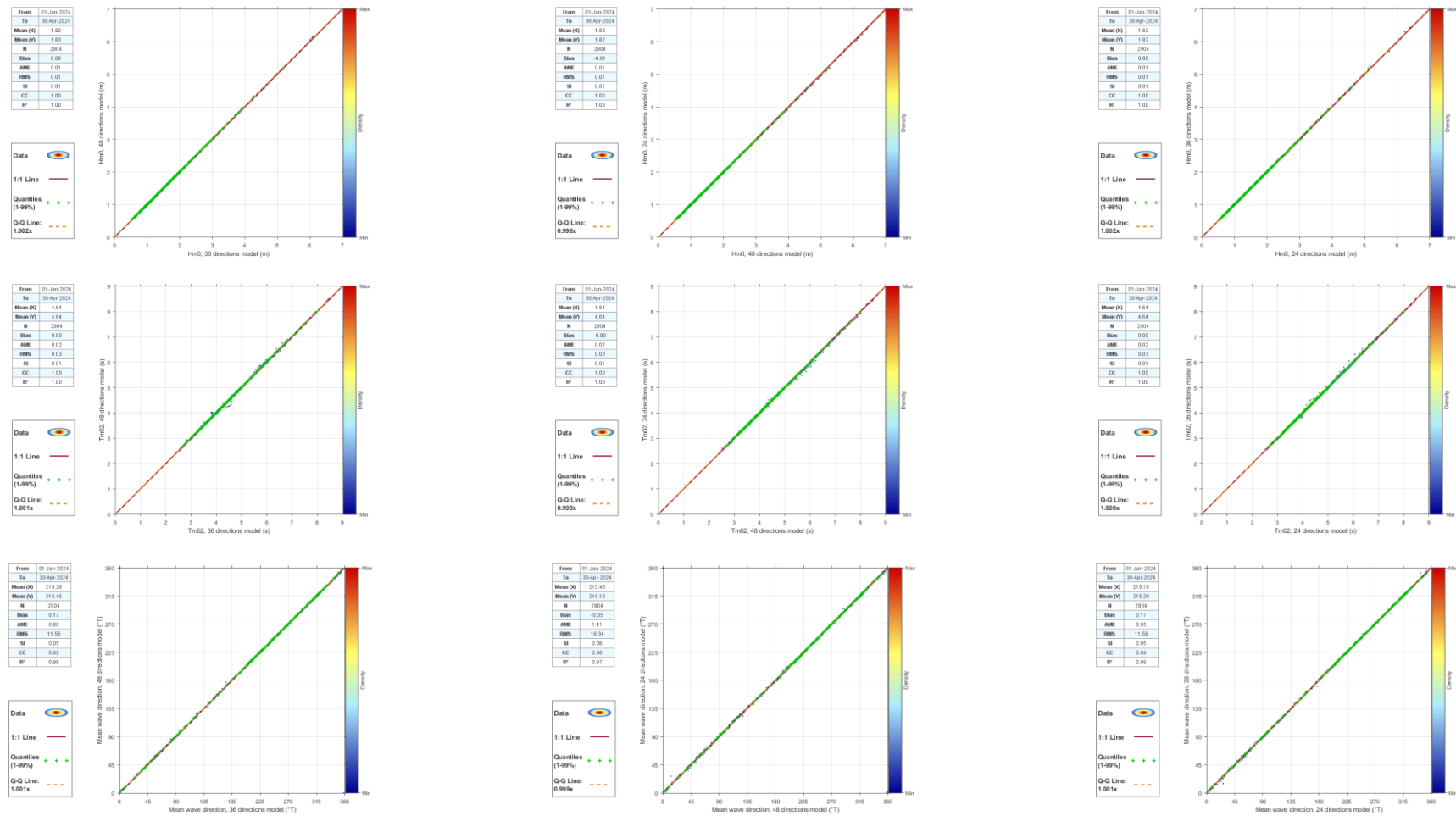


Figure 6-6. Results of model runs with differing numbers of directional bins, at the Centre Array. Top row = significant wave height, middle row = mean zero-crossing wave period, bottom row = mean wave direction. Left column 36 directional bins vs. 48 directional bins. Middle column 48 directional bins vs. 24 directional bins. Right column = 24 directional bins vs. 36 directional bins.

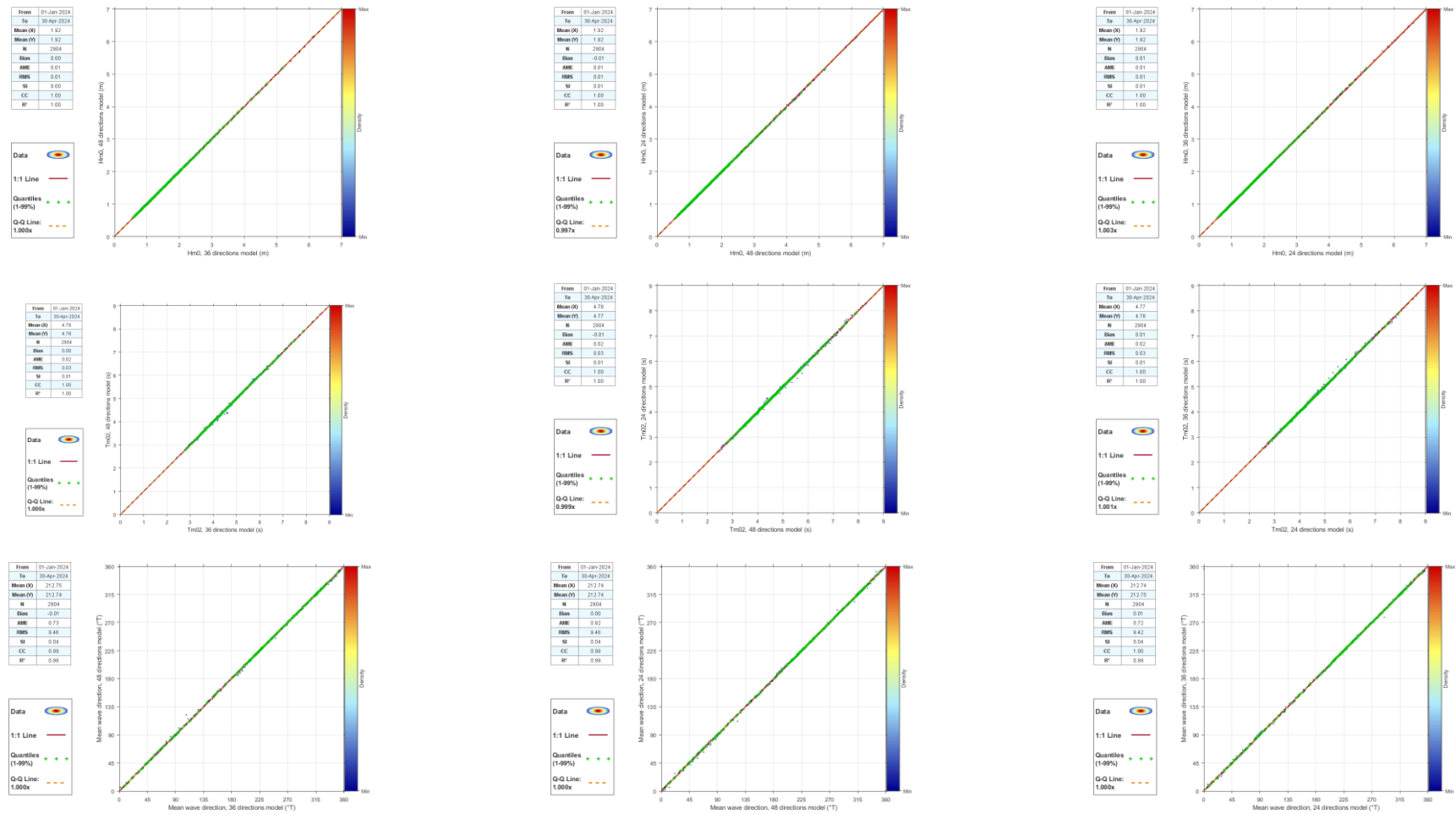


Figure 6-7. Results of model runs with differing numbers of directional bins, at the Centre West. Top row = significant wave height, middle row = mean zero-crossing wave period, bottom row = mean wave direction. Left column 36 directional bins vs. 48 directional bins. Middle column 48 directional bins vs. 24 directional bins. Right column = 24 directional bins vs. 36 directional bins.

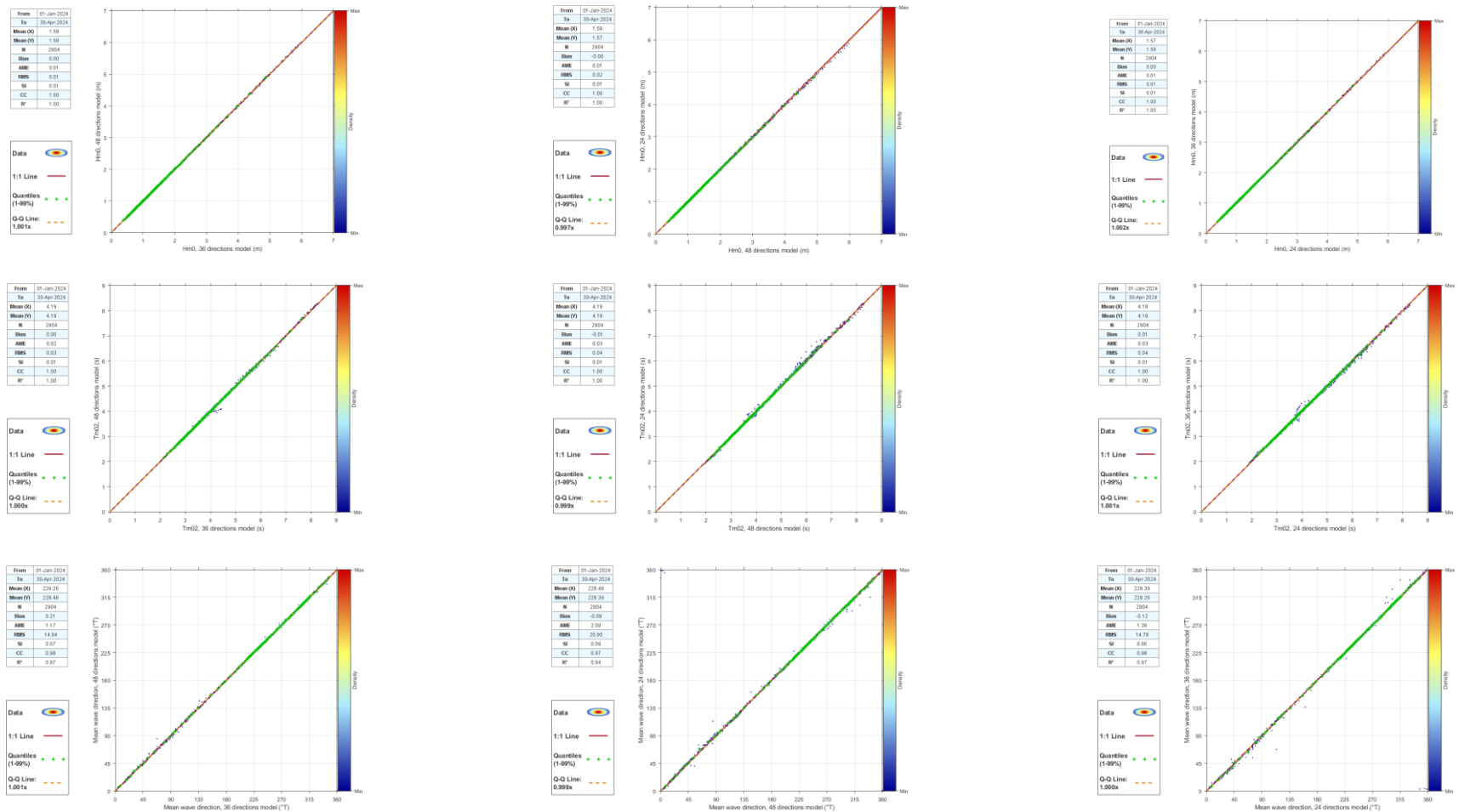


Figure 6-8. Results of model runs with differing numbers of directional bins, at ECC Central. Top row = significant wave height, middle row = mean zero-crossing wave period, bottom row = mean wave direction. Left column 36 directional bins vs. 48 directional bins. Middle column 48 directional bins vs. 24 directional bins. Right column = 24 directional bins vs. 36 directional bins.



In these tests, we can consider the highest resolution directional discretisation model to be the ‘standard’ against which the other directional resolutions can be judged, on the basis that we assume that the highest resolution model should produce the more accurate results.

Figure 5-6 to Figure 5-8 show that there is little impact of directional discretisation on wave period and direction at certain locations. In general, wave heights (top row of each figure) are unaffected by changes in directional discretisation. Therefore, a final directional discretisation of 36 bins was selected, it being the highest directional resolution that could be achieved with a practicable runtime.

6.5 Final Model Parameter Settings

The models were run in non-stationary mode to allow proper wave growth within the model domain and data were output from the model every 1 hour. Within the model, wave spectra were discretised using 36 directions and 36 frequencies from 0.0345 to 0.9695Hz. The physics schemes and parameterisations used in this model have been refined by MetOceanWorks over many years, running thousands of scenarios. For the production run, we used SWAN cycle III version 40.91ABC and employed the expression by Komen [16] for white capping and for wind induced wave growth. Triads were included and quadruplet interactions were estimated using the Discrete Interaction Approximation (DIA) by Hasselmann [17]. Refraction was turned on in the wave models. The JONSWAP (Joint North Sea Wave Project) bottom friction formulation was used and depth-limited wave breaking was modelled according to the bore-model of Battjes and Janssen [18]. Please see “Swan cycle III version 40.91 ABC - Scientific and Technical Documentation” [15] for further details.

6.6 Model Validation

The wave model has been validated against the measured wave data detailed in Table 6-1 with results presented in the following pages. As noted previously, model parameters should be considered as representative of a 3-hour sea-state. As a result, prior to validation the measured significant wave heights have been averaged and are taken as the 3-hour second power mean of measurements. That is, H_{m0} is squared; a 3-hour mean of the squared values calculated; the square-root of the 3-hour mean used in the validation plot. This simple calculation gives the equivalent result to that which would be obtained from 3-hour mean spectra and has been used across all locations. For all other parameters, such a calculation is not available without use of the spectra, and as such, values measured on the instruments are instead used directly with no averaging.

The validations demonstrate excellent model skill under both ambient and storm conditions and suggest some conservatism again on the eastern side of the wind farm. The plots include scatter plots with overlaid Quantile-Quantiles of H_{m0} for the data described in Table 6-1. These validations yield high correlation coefficients, relatively low scatter indices and slopes a little over unity. Similar validation plots of wave periods are also presented which again demonstrate very good model skill.

With regard to wave period validation, it is worth noting that:

- The nature of the peak period parameter, T_p , can lead to small populations of scatter some way from the 1:1 line of a validation plot, even when the model performs very well. In sea-states with a single dominant system, both modelled and measured T_p are expected to be similar. However, in sea-states where two or more systems of almost equal energy are present, very small differences between modelled and measured spectra can lead to very large differences in T_p . For example, consider a wave spectrum with two-peaks, one corresponding to wind-sea with a peak at 6 seconds, one corresponding to swell with a peak at 12 seconds. Modelled and measured spectra could be near-identical, but with



the wind-sea peak *slightly* bigger in the model, and the swell peak *slightly* bigger in measurements. In such a case, T_p itself will differ by 6 seconds. Though relatively rare, over the course of the measurement campaigns it is likely that this will occur for a small number of periods, and thus lead to small populations of scatter away from the 1:1 line.

- Care has been taken when comparing mean zero-crossing periods (T_{m02}) to ensure both modelled and measured values are derived using the same method. Parameters derived from higher order spectral moments, such as T_{m02} , can be somewhat sensitive to how high frequency wave energy is treated in their derivation. In particular, for the datasets considered here, T_{m02} as output directly by the SWAN model *does* make use of a theoretical high frequency extrapolation, whilst that reported by the measurement devices *does not*. Direct comparison of these parameters can be misleading, the inclusion of such a tail generally being expected to reduce the T_{m02} values. In order to more fairly compare, modelled T_{m02} have been recalculated from modelled *spectra*, without including a high frequency extrapolation and using the same high frequency cut-off as the measurements. It is these values which are compared to the measured T_{m02} . More information on this topic can be found in Appendix E.

Comparisons between measured and modelled wave spectra can be found in Appendix F.



From	01-Sep-2023
To	01-May-2024
Mean (X)	1.99
Mean (Y)	1.96
N	5832
Bias	-0.03
AME	0.20
RMS	0.27
SI	0.13
CC	0.97
R ²	0.95

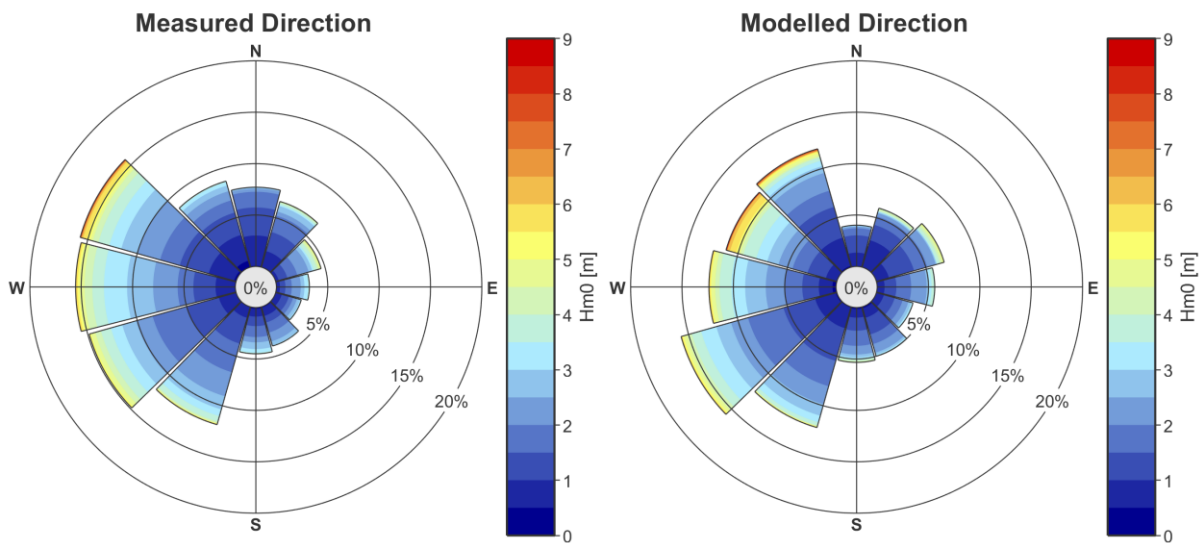
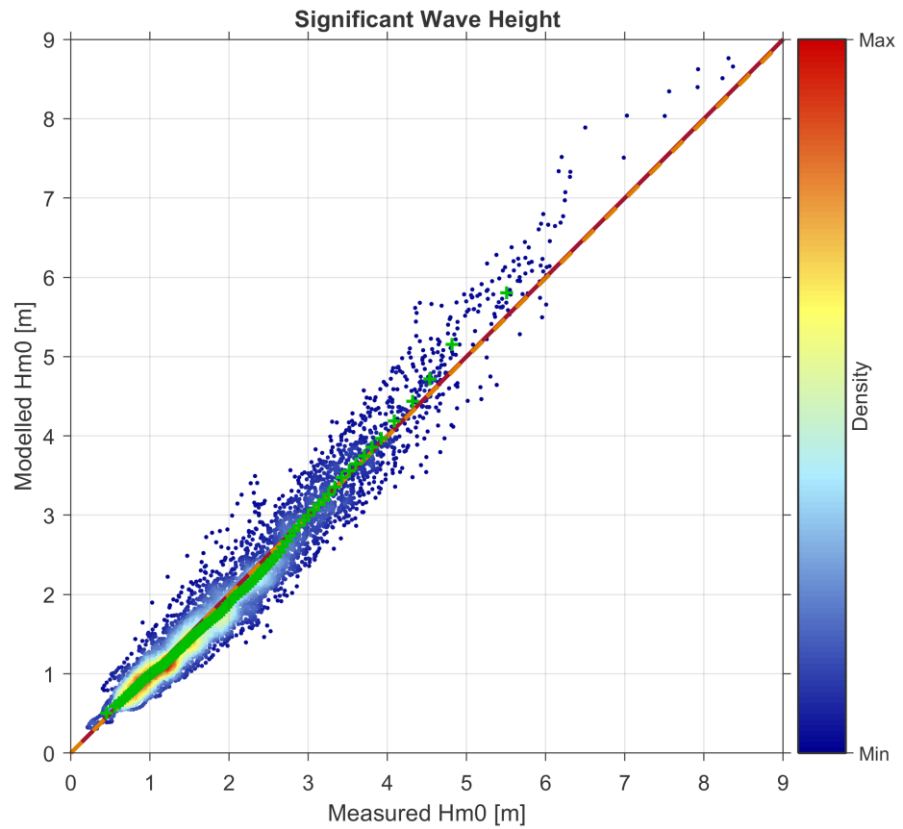
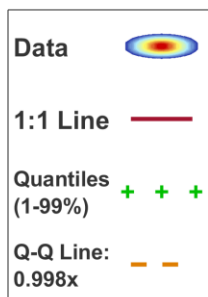


Figure 6-9. NSI-1 LiDAR Buoy, Hm0 validation.



Mean (X)	7.26
Mean (Y)	6.99
N	5745
Bias	-0.27
AME	1.00
RMS	1.76
SI	0.24
CC	0.60
R ²	0.36

Data	
1:1 Line	
Quantiles (1-99%)	
Q-Q Line: 0.956x	

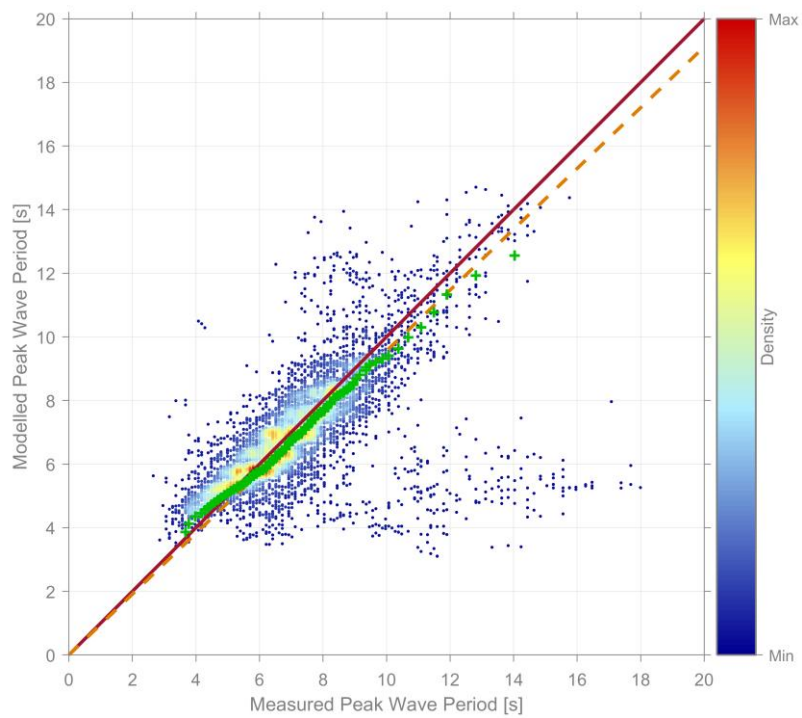


Figure 6-10. NSI-1 LiDAR Buoy, Tp validation.

Mean (X)	5.17
Mean (Y)	5.04
N	5745
Bias	-0.13
AME	0.36
RMS	0.52
SI	0.10
CC	0.89
R ²	0.79

Data	
1:1 Line	
Quantiles (1-99%)	
Q-Q Line: 0.979x	

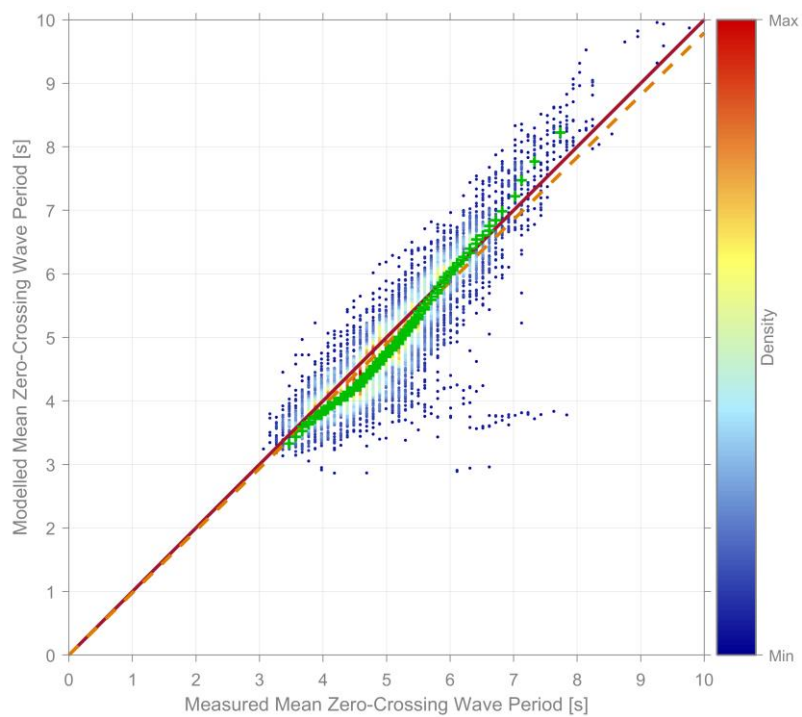


Figure 6-11. NSI-1 LiDAR Buoy, Tm02 validation.

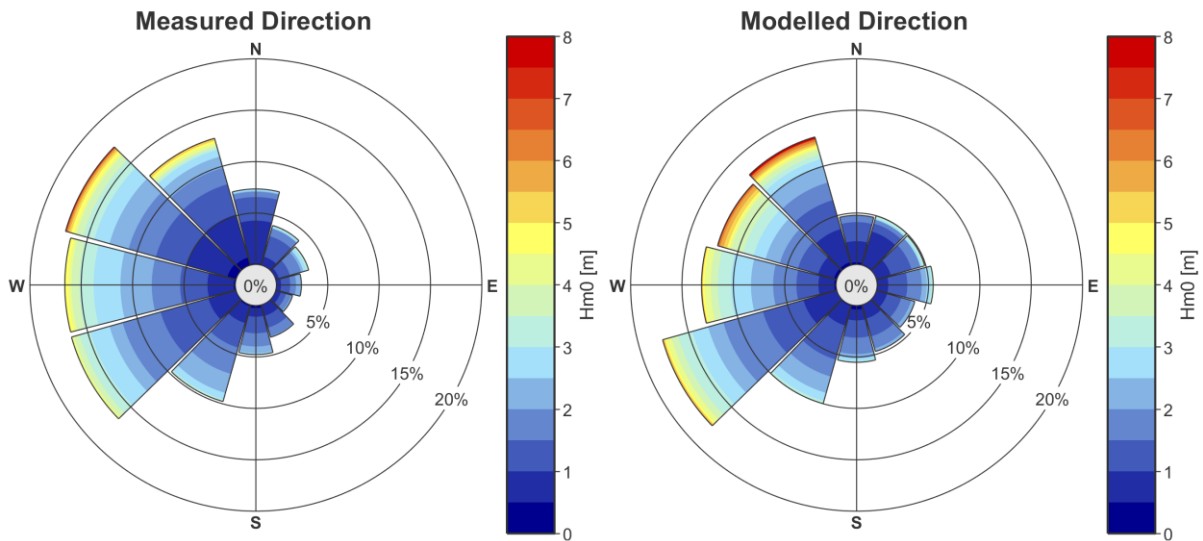
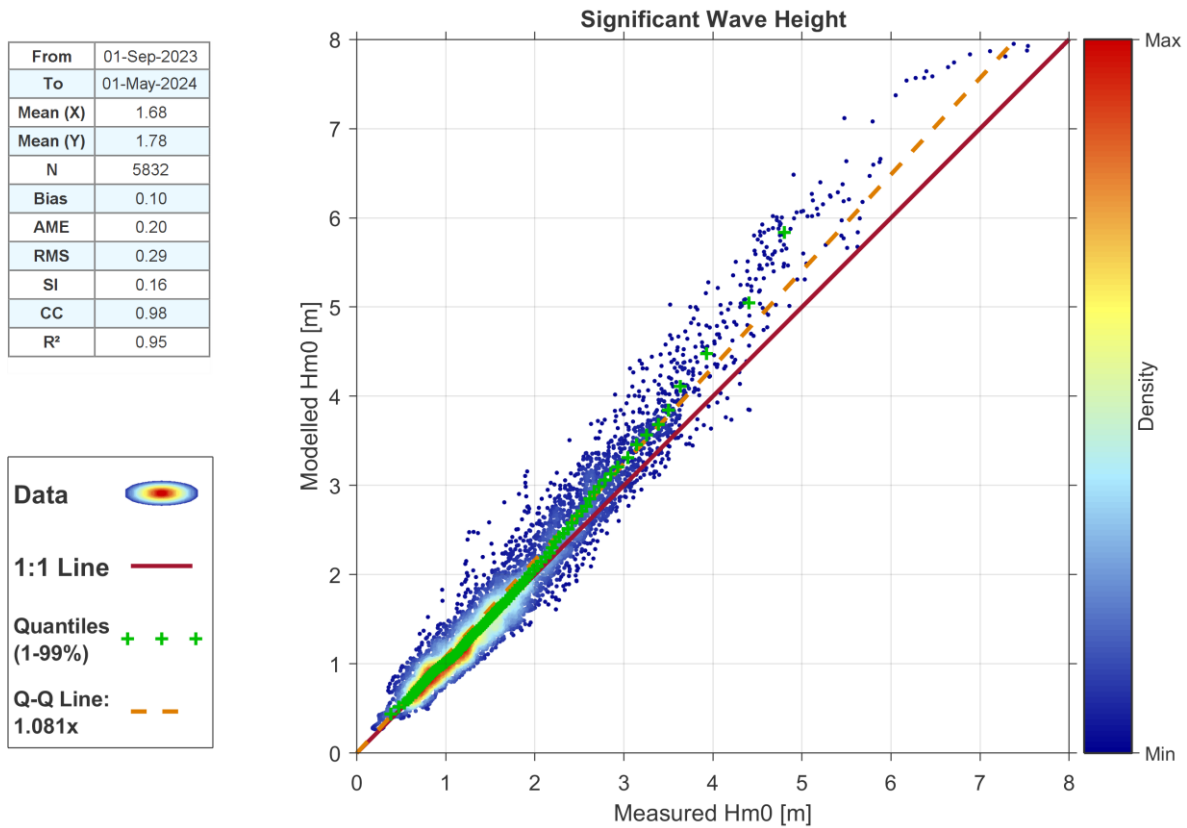
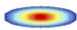






Figure 6-12. NSI-2 LiDAR Buoy, Hm0 validation.




Mean (X)	7.26
Mean (Y)	6.99
N	5745
Bias	-0.27
AME	1.00
RMS	1.76
SI	0.24
CC	0.60
R ²	0.36

Data 

1:1 Line 

Quantiles (1-99%)   

Q-Q Line: 0.956x 

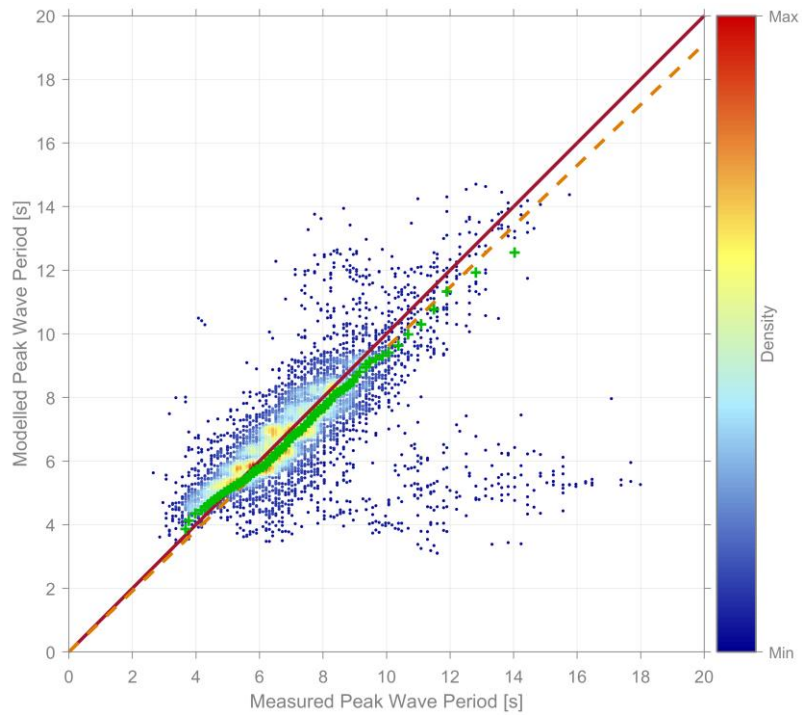
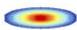







Figure 6-13. NSI-2 LiDAR Buoy, Tp validation.

Mean (X)	4.93
Mean (Y)	4.83
N	5684
Bias	-0.10
AME	0.40
RMS	0.55
SI	0.11
CC	0.88
R ²	0.78

Data 

1:1 Line 

Quantiles (1-99%)   

Q-Q Line: 0.987x 

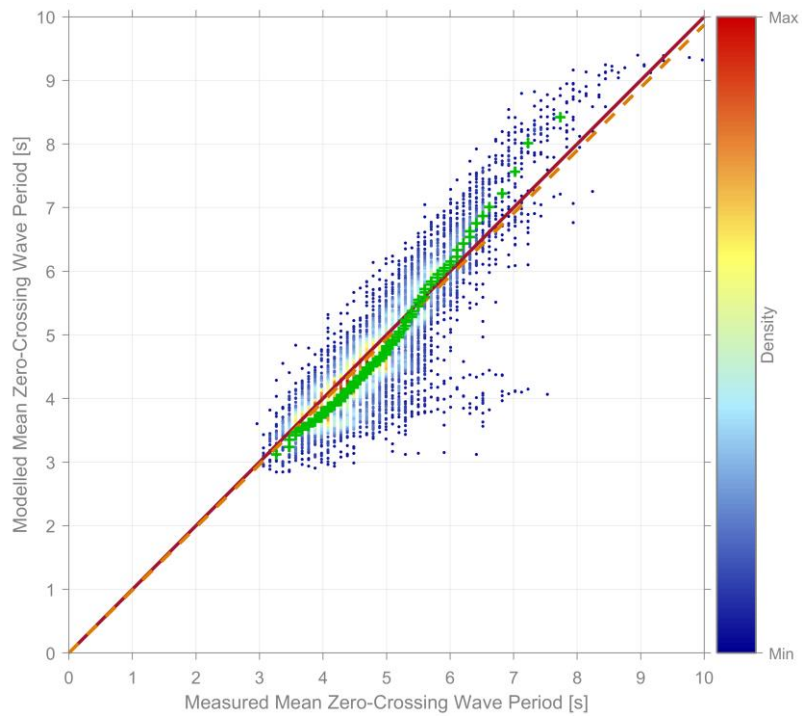


Figure 6-14. NSI-2 LiDAR Buoy, Tm02 validation.



From	01-Sep-2023
To	01-May-2024
Mean (X)	1.76
Mean (Y)	1.81
N	5832
Bias	0.06
AME	0.19
RMS	0.26
SI	0.15
CC	0.98
R ²	0.95

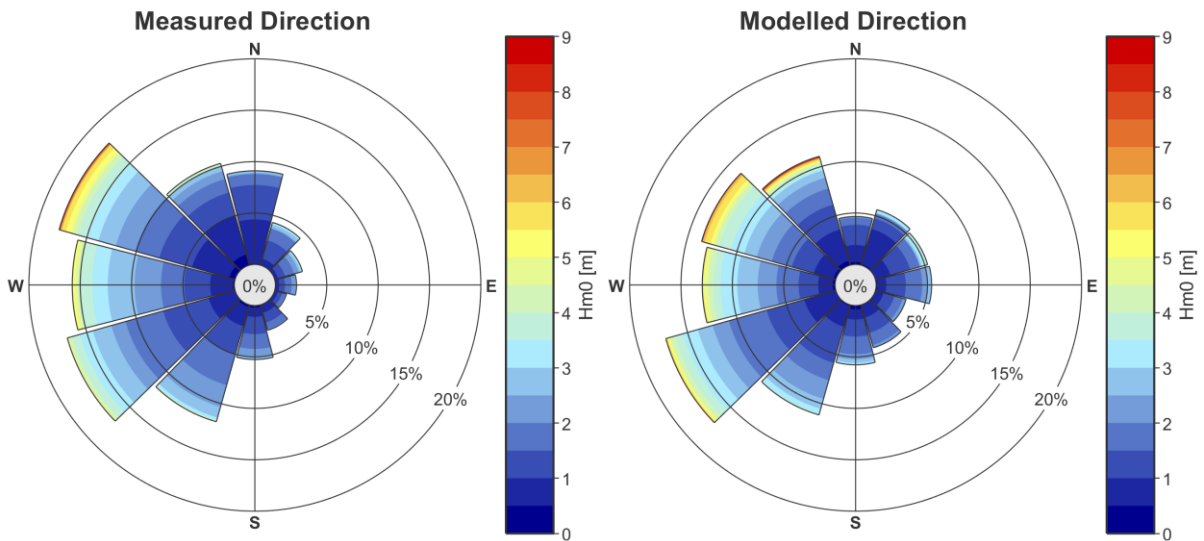
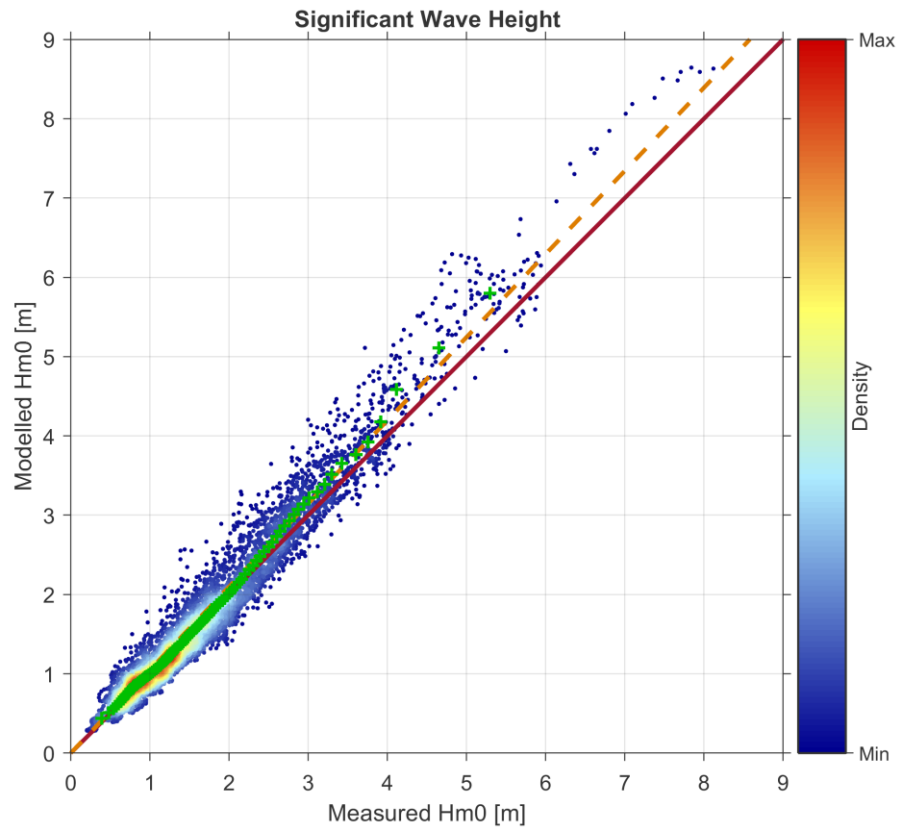
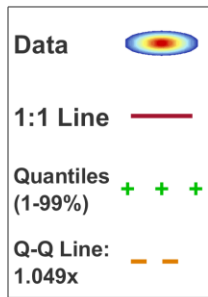


Figure 6-15. NSI-3 LiDAR Buoy, Hm0 validation.



Mean (X)	7.13
Mean (Y)	6.83
N	5687
Bias	-0.30
AME	1.06
RMS	1.76
SI	0.24
CC	0.65
R ²	0.42

Data

1:1 Line

Quantiles (1-99%)

Q-Q Line: 0.953x

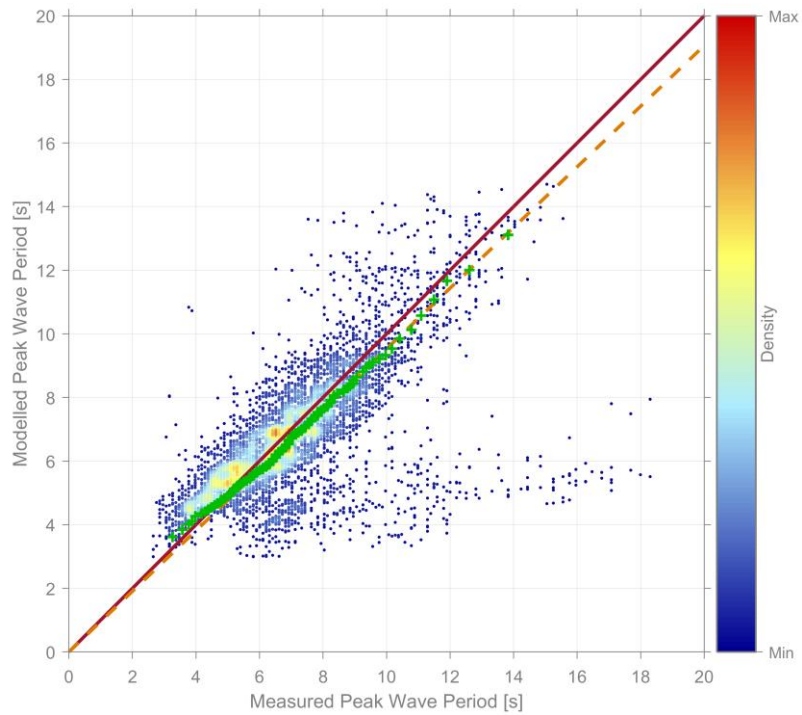


Figure 6-16. NSI-3 LiDAR Buoy, Tp validation.

Mean (X)	4.93
Mean (Y)	4.83
N	5684
Bias	-0.10
AME	0.40
RMS	0.55
SI	0.11
CC	0.88
R ²	0.78

Data

1:1 Line

Quantiles (1-99%)

Q-Q Line: 0.987x

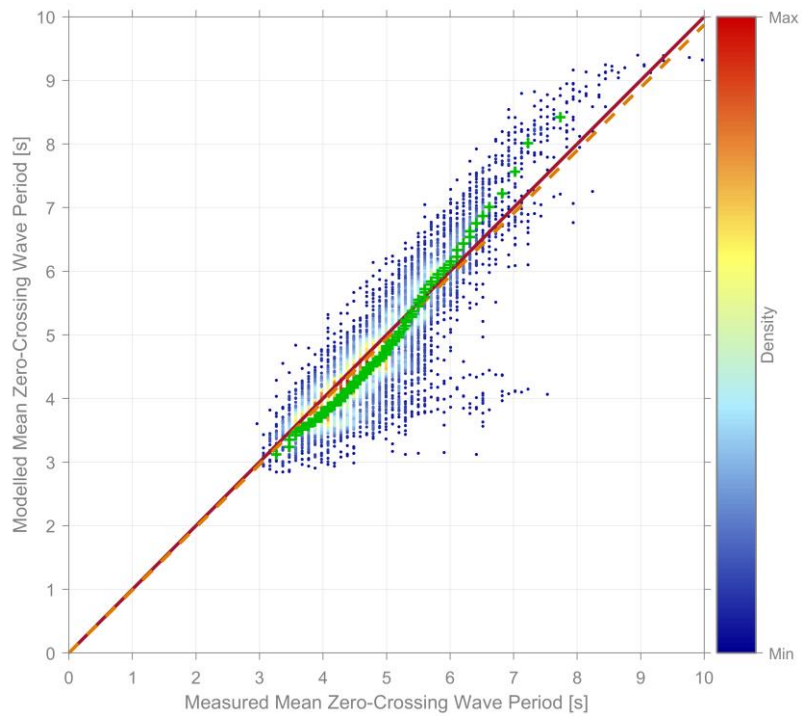


Figure 6-17. NSI-3 LiDAR Buoy, Tm02 validation.



From	15-Nov-2021
To	15-Nov-2023
Mean (X)	1.70
Mean (Y)	1.71
N	16068
Bias	0.01
AME	0.18
RMS	0.24
SI	0.14
CC	0.97
R ²	0.95

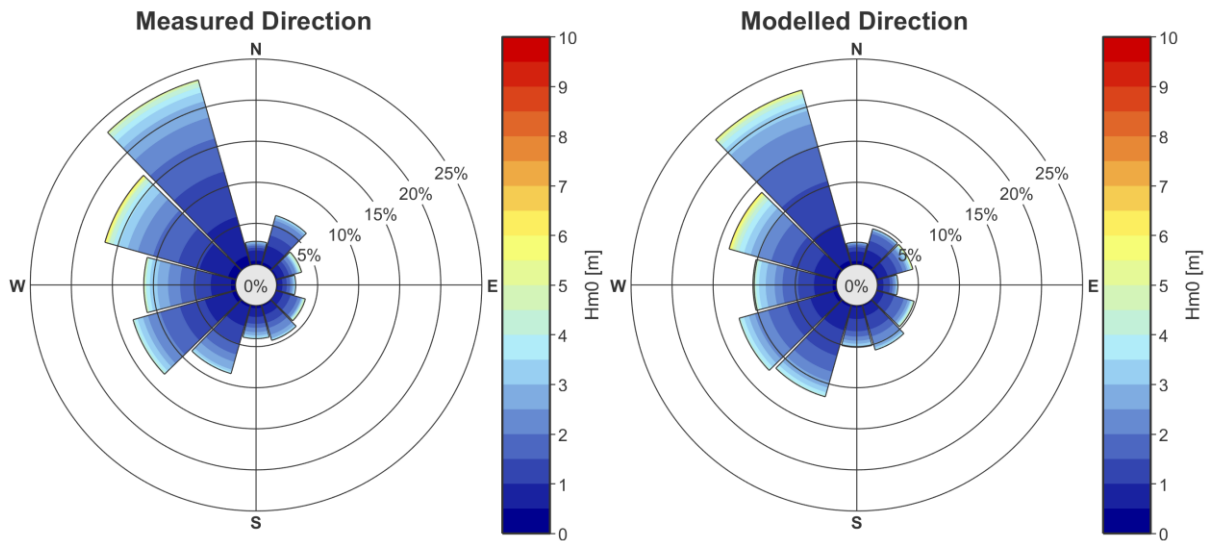
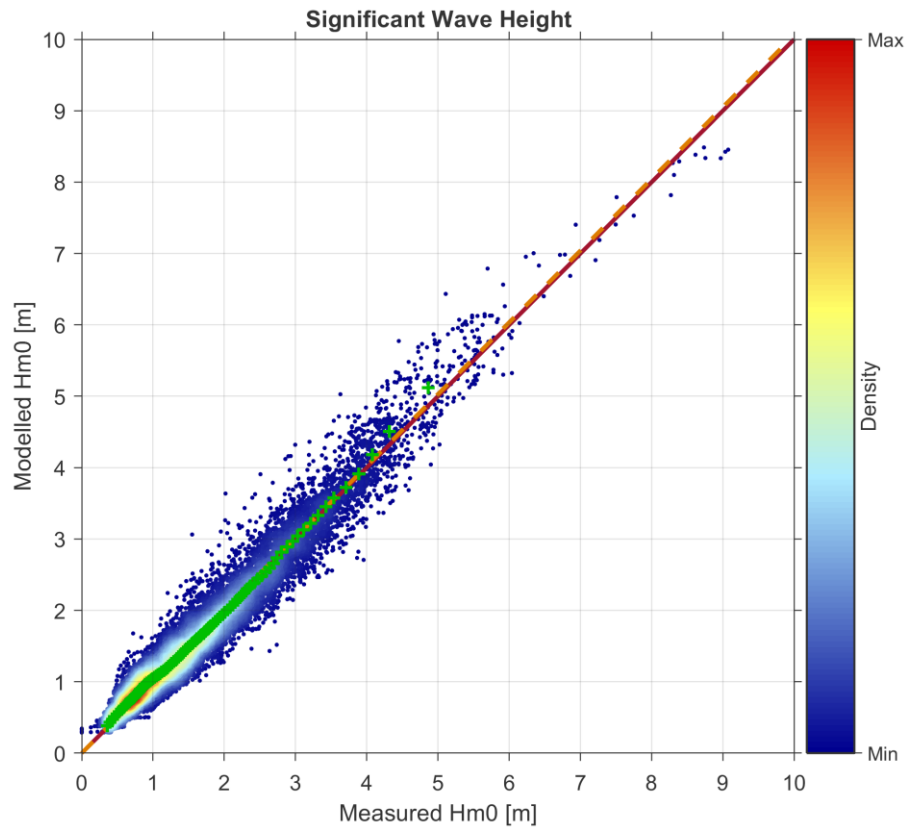
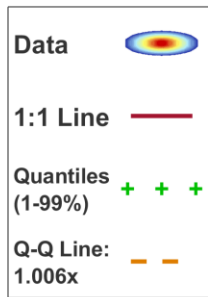


Figure 6-18. EINS-3 Wave Buoy, Hm0 validation.



Mean (X)	7.27
Mean (Y)	6.90
N	14798
Bias	-0.36
AME	0.96
RMS	1.81
SI	0.24
CC	0.65
R ²	0.42

Data	
1:1 Line	
Quantiles (1-99%)	
Q-Q Line:	
0.941x	

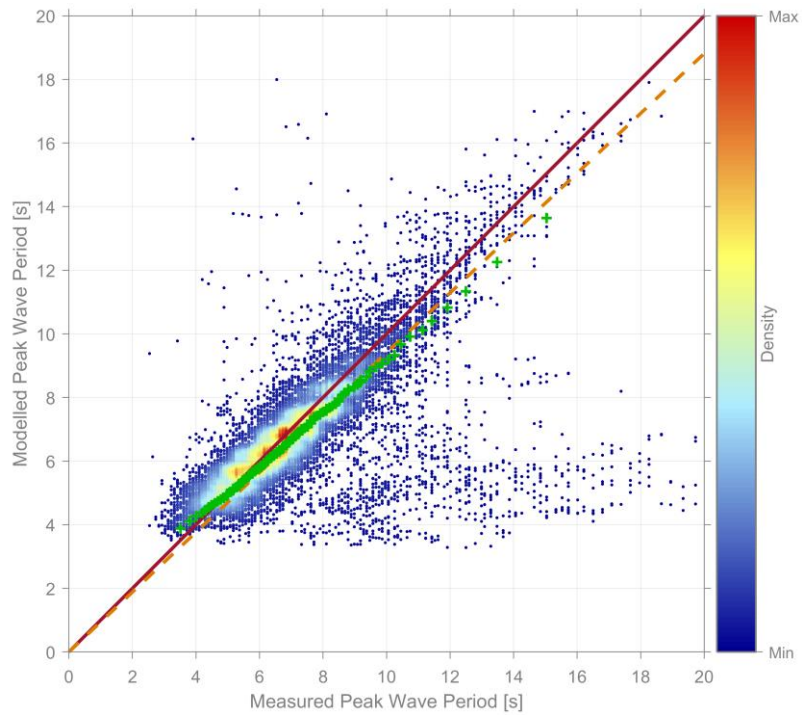


Figure 6-19. EINS-3 Wave Buoy, Tp validation.

Mean (X)	5.07
Mean (Y)	4.85
N	15236
Bias	-0.22
AME	0.35
RMS	0.53
SI	0.09
CC	0.88
R ²	0.77

Data	
1:1 Line	
Quantiles (1-99%)	
Q-Q Line:	
0.958x	

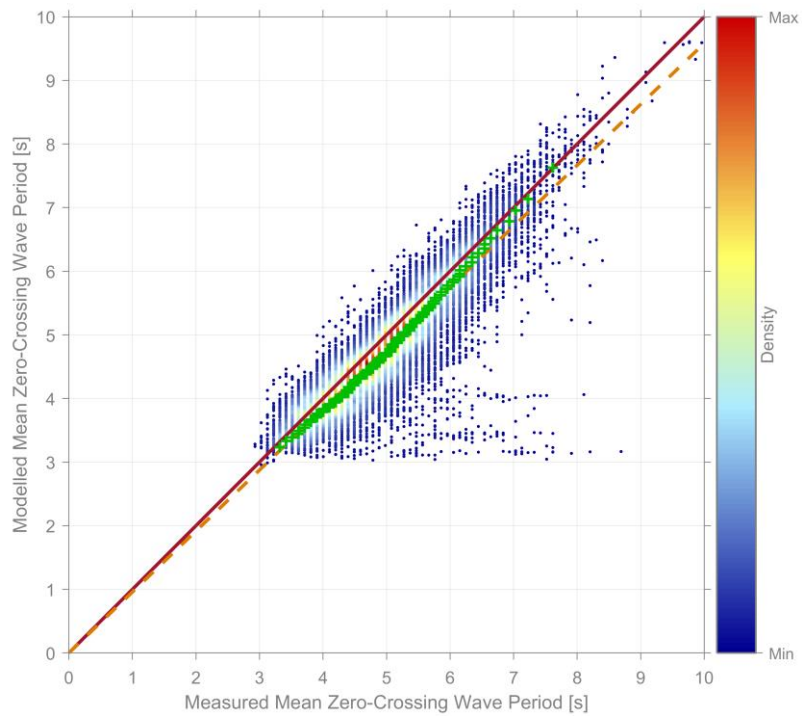


Figure 6-20. EINS-3 Wave Buoy, Tm02 validation.

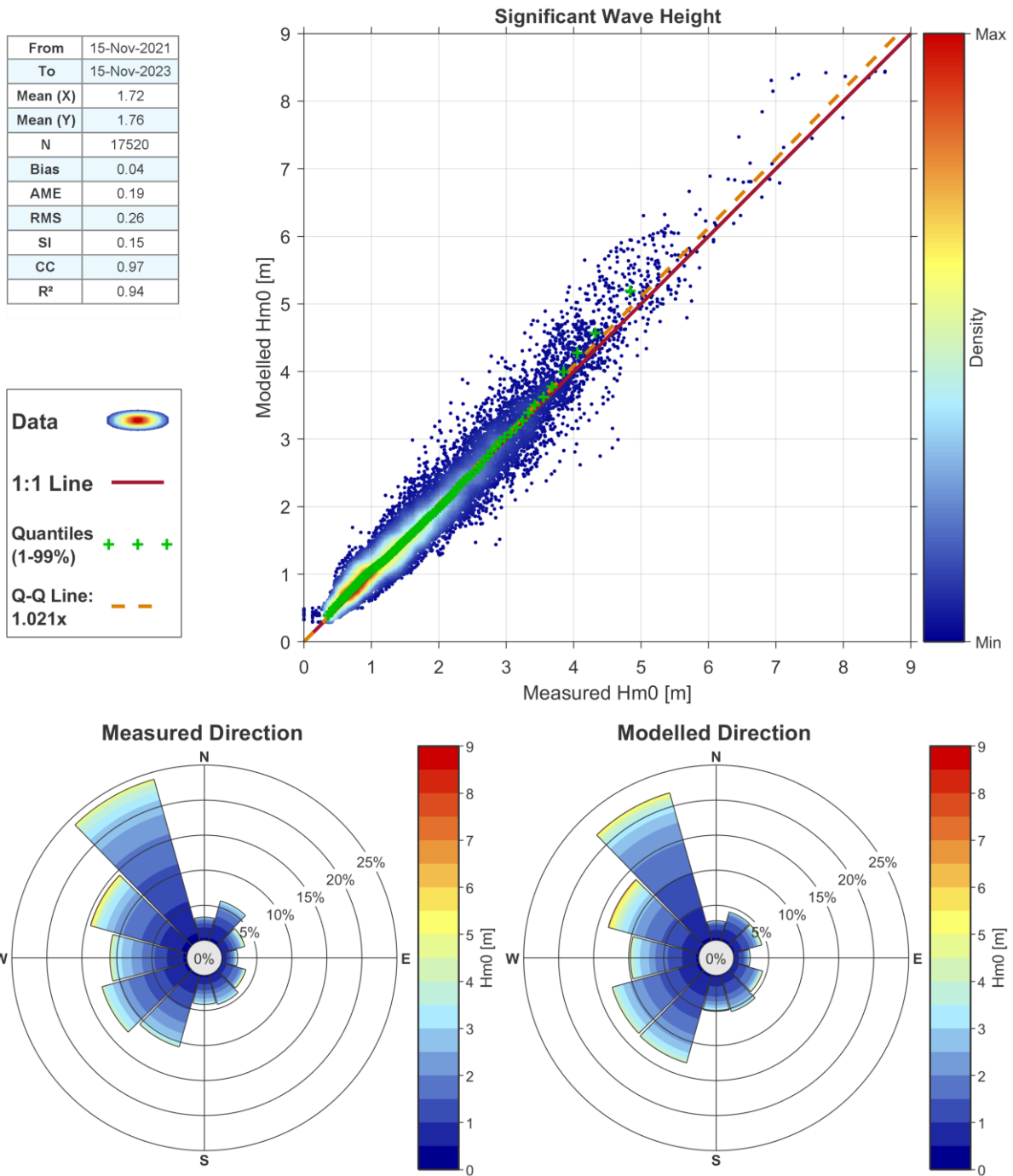


Figure 6-21. EINS-4 Wave Buoy, Hm0 validation.



Mean (X)	7.19
Mean (Y)	7.01
N	16105
Bias	-0.18
AME	0.93
RMS	1.70
SI	0.23
CC	0.65
R ²	0.42

Data

1:1 Line

Quantiles (1-99%)

Q-Q Line: 0.971x

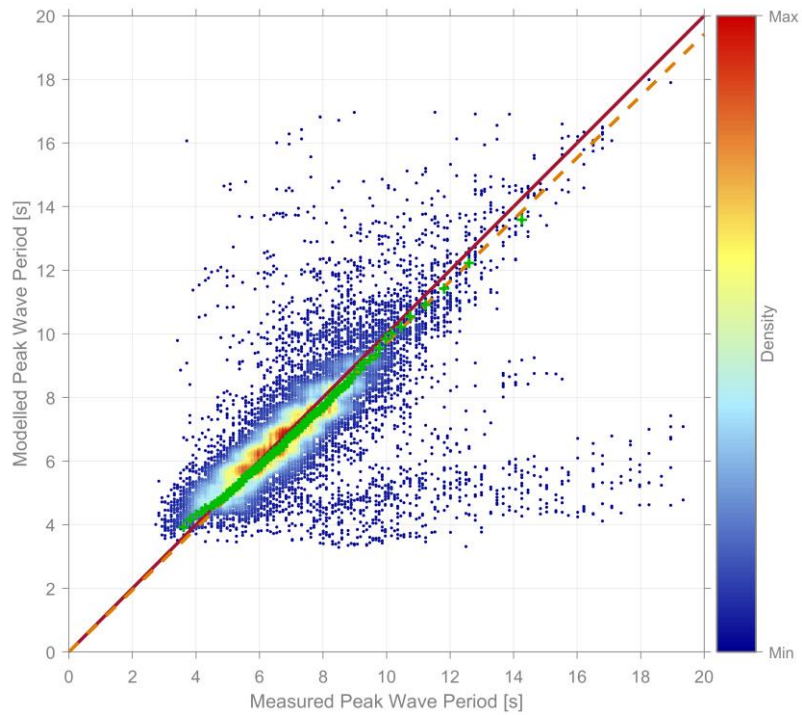


Figure 6-22. EINS-4 Wave Buoy, Tp validation.

Mean (X)	5.11
Mean (Y)	4.98
N	16652
Bias	-0.13
AME	0.35
RMS	0.51
SI	0.10
CC	0.88
R ²	0.77

Data

1:1 Line

Quantiles (1-99%)

Q-Q Line: 0.979x

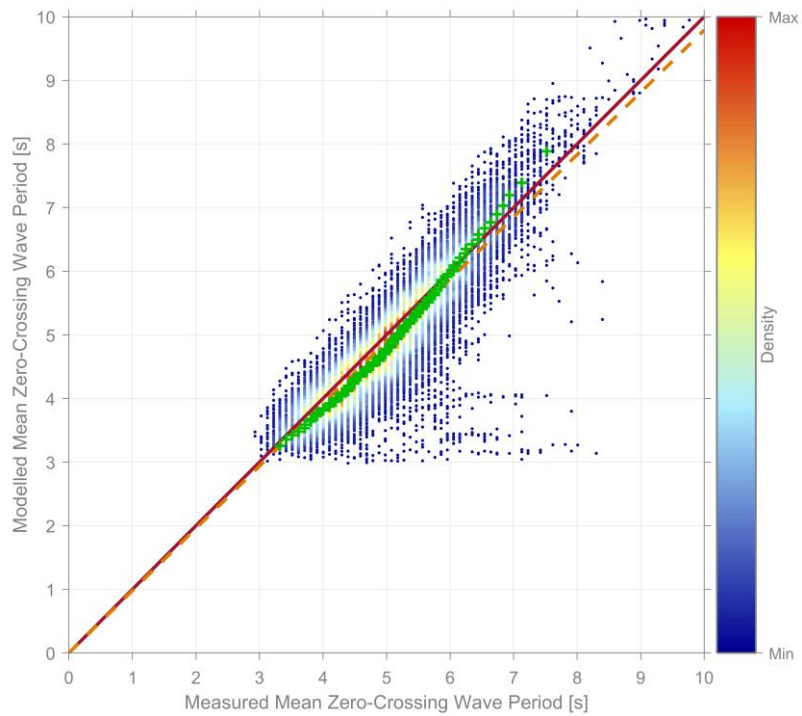


Figure 6-23. EINS-4 Wave Buoy, Tm02 validation.

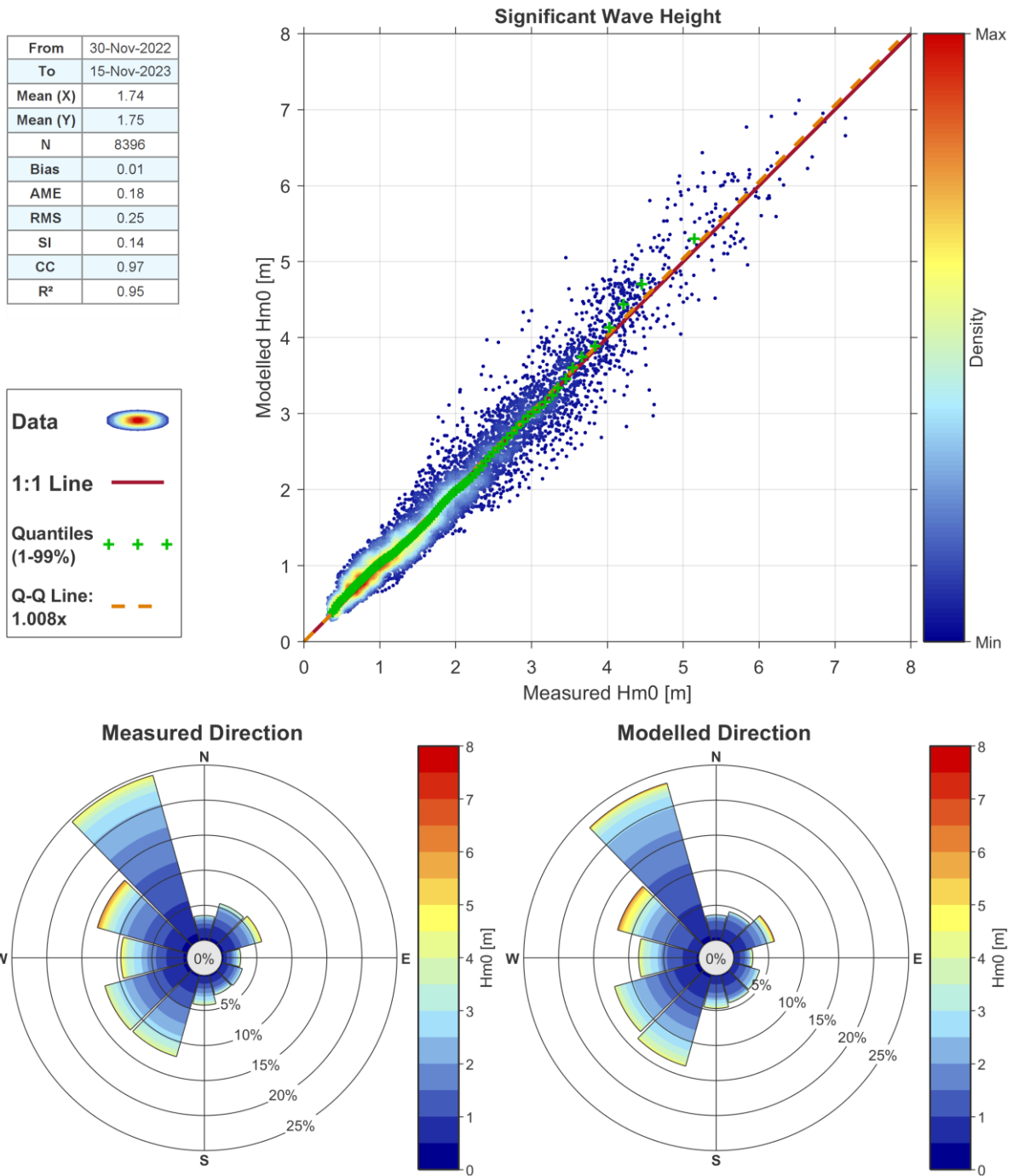


Figure 6-24. EINS-5 Wave Buoy, Hm0 validation.



Mean (X)	7.19
Mean (Y)	7.01
N	16105
Bias	-0.18
AME	0.93
RMS	1.70
SI	0.23
CC	0.65
R ²	0.42

Data

1:1 Line

Quantiles (1-99%)

Q-Q Line: 0.971x

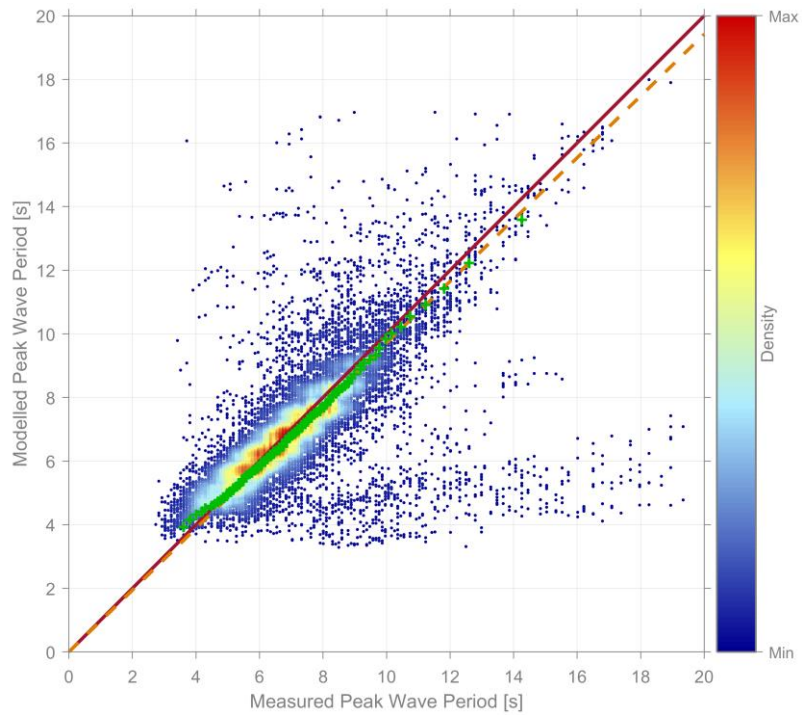


Figure 6-25. EINS-5 Wave Buoy, Tp validation.

Mean (X)	5.15
Mean (Y)	5.00
N	7934
Bias	-0.15
AME	0.34
RMS	0.49
SI	0.09
CC	0.90
R ²	0.81

Data

1:1 Line

Quantiles (1-99%)

Q-Q Line: 0.975x

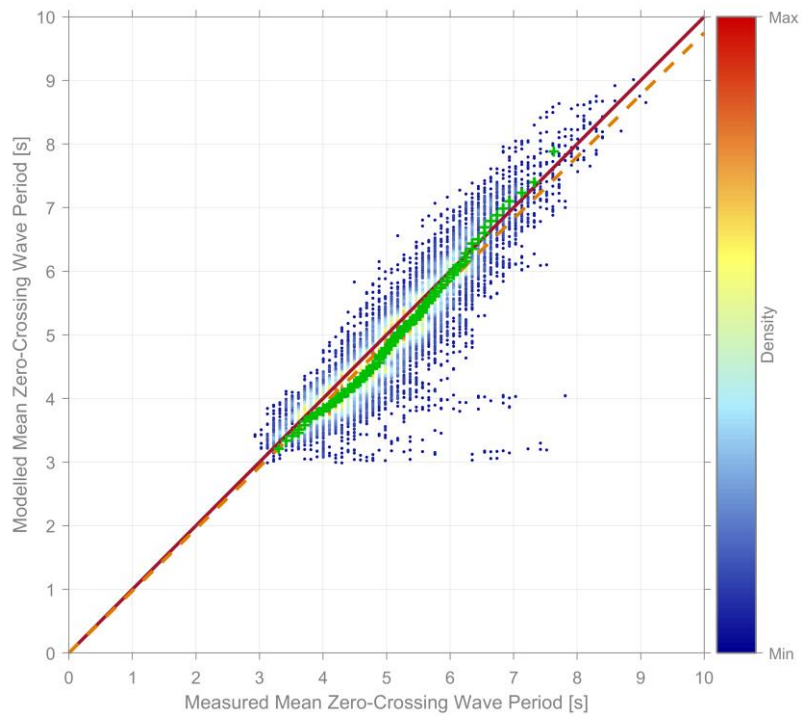


Figure 6-26. EINS-5 Wave Buoy, Tm02 validation.



From	20-Feb-2014
To	29-Feb-2024
Mean (X)	1.63
Mean (Y)	1.58
N	117380
Bias	-0.05
AME	0.18
RMS	0.25
SI	0.15
CC	0.97
R ²	0.94

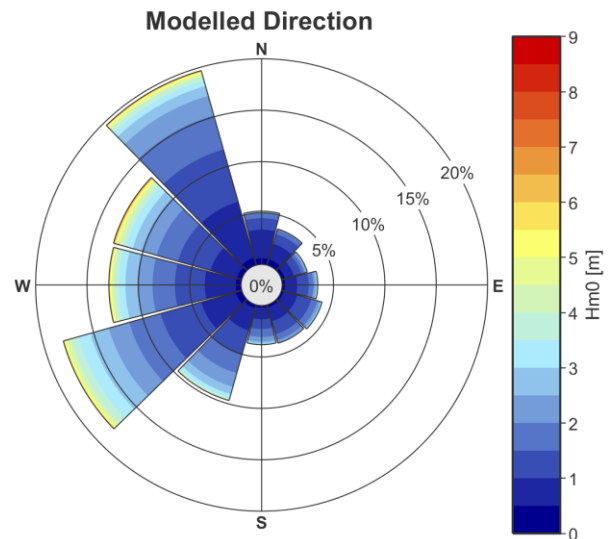
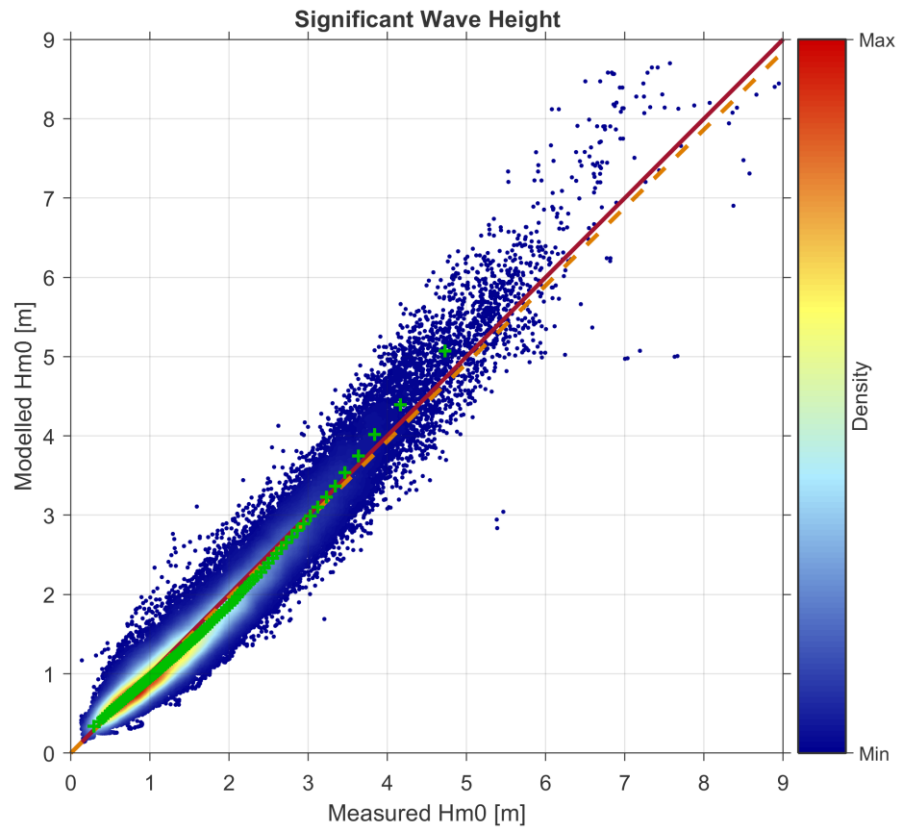
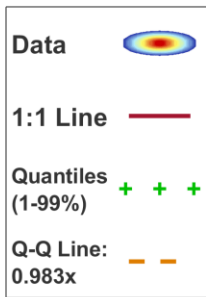


Figure 6-27. FINO3, Hm0 validation.



From	19-Jun-2017
To	29-Feb-2024
Mean (X)	1.25
Mean (Y)	1.32
N	24469
Bias	0.07
AME	0.16
RMS	0.23
SI	0.17
CC	0.97
R ²	0.94

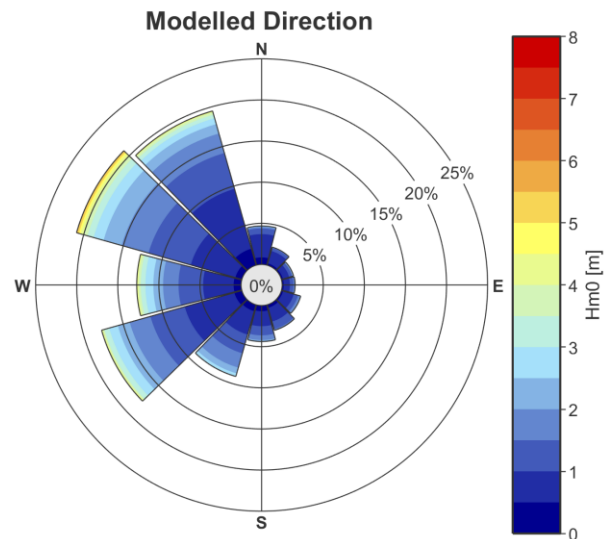
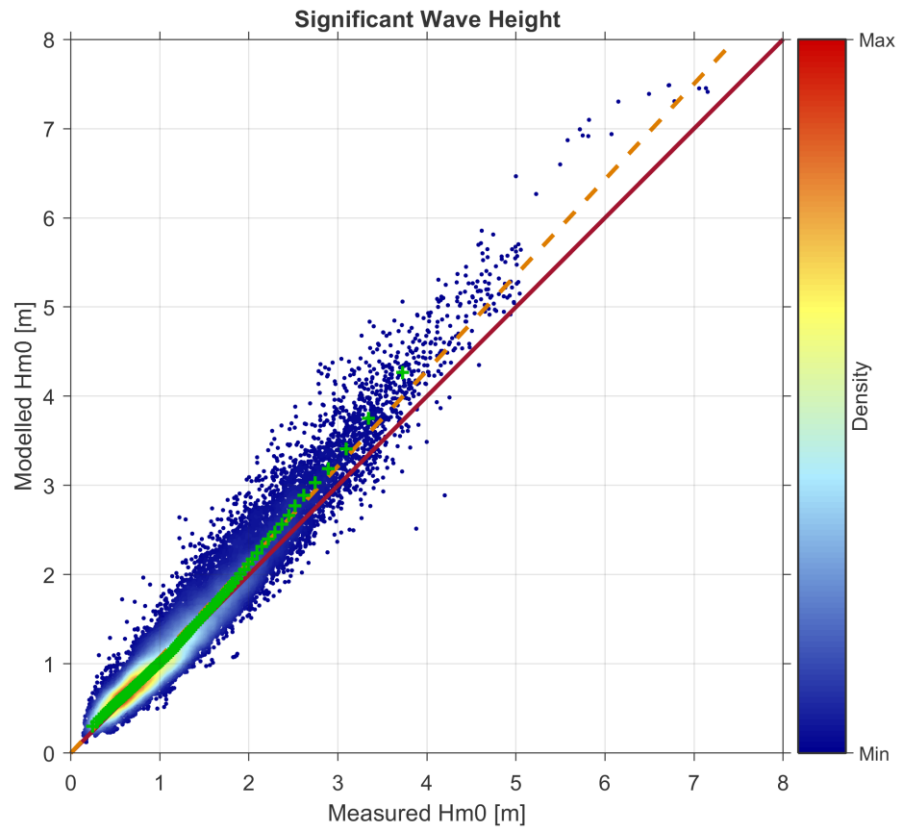
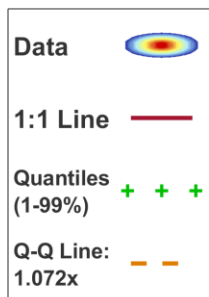


Figure 6-28. Nymindgab, Hm0 validation.



7 Additional Parameters

7.1 Atmospheric Data

Bespoke site-specific down-scaled atmospheric time-series data were sourced from Vortex Factoria de Càlculs SL (Vortex). These were derived as a 3 km resolution down-scaled implementation of ECMWF ERA5 and originates from their SERIES product. Vortex SERIES data were acquired at multiple elevations between 10 m and 250 m at hourly intervals for a representative location within the wind farm lease area between 2002 and 2023. Relative humidity was derived from these data.

Additional atmospheric parameters such as air temperature were sourced from ECMWF ERA5.

7.2 Lightning Strike Data

Lightning strike statistics were obtained from BLIDS (Blitz-Informationsdienst von Siemens - Siemens lightning information service)⁴.

7.3 Seawater Data

Seawater data were sourced from the GOFS 3.1 implementation of the HYCOM global reanalysis dataset⁵. The global model has a 1/12-degree horizontal grid resolution which equates to an approximate spacing of 9 km in latitude and 5 km in longitude in the region of interest. Up to 41 depth levels are employed in the vertical to accurately describe conditions through the entire water column. In addition, HYCOM assimilates sea-surface height and temperature derived from satellite products allowing it to properly resolve meso-scale oceanic features such as meanders and eddies. These data are available at 3-hourly intervals, from 1994-2015.

⁴ <https://new.siemens.com/de/de/produkte/services/blids.html>

⁵ <https://www.hycom.org/dataserver/gofs-3pt1/analysis>



References

- [1] J. Sündermann and T. Pohlmann, "A brief analysis of North Sea physics," *Oceanologia*, vol. 53, no. 3, pp. 663-689, 2011.
- [2] C. Hasager, F. Vejen, J. Bech, W. Skrzypiński, A.-M. Tilg and M. Nielsen, "Assessment of the rain and wind climate with focus on wind turbine blade leading edge erosion rate and expected lifetime in Danish Seas," *Renewable Energy*, vol. 149, pp. 91-102, 2020.
- [3] A. Peña, R. Floors, A. Sathe, S.-E. Gryning, R. Wagner, M. S. Courtney, X. G. Larsén, A. N. Hahmann and C. B. Hasager, "Ten Years of Boundary-Layer and Wind-Power Meteorology at Høvsøre, Denmark," *Boundary-Layer Meteorology*, vol. 158, pp. 1-26, 2015.
- [4] I. Temiz, T. Potapenko and A. V. Kumar, "Wave energy resource assessment at Hvide Sande on the west coast of Denmark," in *EWTEC 2021*, Plymouth, 2021.
- [5] H. Santo, P. H. T. and R. Gibson, "Decadal variability of extreme wave height representing storm severity in the northeast Atlantic and North Sea since the foundation of the Royal Society," *Proc. R. Soc. A*, vol. 472, no. 20160376, 2016.
- [6] R. J. Bell, S. L. Gray and O. P. Jones, "North Atlantic storm driving of extreme wave heights in the North Sea," *Journal of Geophysical Research: Oceans*, vol. 122, no. 4, pp. 3253-3268, 2017.
- [7] R. Dalrymple, "Tidal Depositional Systems," in *Facies Models: Response to Sea Level Changes*, Geological Association of Canada, 1992, p. 196.
- [8] Global Ocean Associates, "An Atlas of Oceanic Internal Solitary Waves - 2nd edition," Virginia, 2004.
- [9] J. O. Leth, B. Larsen and D. Anthony, "Sediment distribution and transport in the shallow coastal waters along the west coast of Denmark," *Geological Survey of Denmark and Greenland Bulletin*, vol. 4, pp. 41-44, 2004.
- [10] Ramboll, "Thor OWF - Technical Report Benthic Fauna and Flora," Copenhagen, 2021.
- [11] DVH Group, "Erosion Case Study - Western Coast of Jutland (Denmark)," The Netherlands, unknown year.
- [12] DNV, "DNV-RP-C205. Recommended Practice – Environmental conditions and environmental loads.," DNV, Edition 2019-09 - Amended 2021-09.
- [13] DHI, "Mike 21 Flow Model FM: Hydrodynamic Module: User Guide," DHI A/S, Denmark, 2021.
- [14] DHI, "MIKE 21 Flow Model FM: Hydrodynamic and Transport Module; Scientific Documentation," DHI A/S, Denmark, 2021.
- [15] SWAN team, Delft University of Technology, "Swan cycle III version 40.91 ABC - Scientific and Technical Documentation," 2013.



- [16] G. J. Komen, L. Cavaleri, M. Donelan, K. Hasselmann, S. Hasselmann and P. A. E. M. Janssen, *Dynamics and Modelling of Ocean Waves*, Cambridge, UK: Cambridge University Press, 1994.
- [17] K. Hasselmann, T. Barnett, E. Bouws, H. Carlson, D. Cartwright, K. Enke, J. Ewing, H. Gienapp, D. Hasselmann, P. Kruseman, A. Meerburg, P. Müller, D. Olbers, K. Richter, W. Sell and H. Walden, “Measurements of wind-wave growth and swell decay during the Joint North Sea Wave Project (JONSWAP),” *Ergaenzungsheft zur Deutschen Hydrographischen Zeitschrift, Reihe A.*, 1973.
- [18] J. Battjes and H. Janssen, “Energy loss and set-up due to breaking random waves,” *Proceedings of the 16th International Conference on Coastal Engineering*, 2978.
- [19] ISO, “ISO 19901-1:2015 Petroleum and natural gas industries – Specific requirements for offshore structures – Part 1: Metocean design and operating considerations. Second Edition.,” ISO, 2015.
- [20] IEC (International Electrotechnical Commission), “IEC 61400-3-1: Wind energy generation systems – Part 3-1: Design requirements for fixed offshore wind turbines,” IEC, 2019.
- [21] Fugro, “SWLB measurements - Danish Offshore Wind 2030, Project Measurement Plan, All Lots; C75516/C75517/C75518_Project_Measurement_Plan_All_Lots 09,” 25 November 2023.
- [22] DNV, “DNV-ST-0437. Standard - Loads and conditions for wind turbines.,” DNVGL, Edition 2016-11 - Amended 2021-11.
- [23] D. Codiga, “UTide Unified Tidal Analysis and Prediction Functions (<https://www.mathworks.com/matlabcentral/fileexchange/46523-utide-unified-tidal-analysis-and-prediction-functions>),” *MATLAB Central File Exchange*, Retrieved July 9, 2020.
- [24] J. L. Hanson and O. M. Phillips, “Automated Analysis of Ocean Surface Directional Wave Spectra,” *J. Atmos. Oceanic. Technol.*, vol. 18, pp. 277-293, 2001.
- [25] International Electrotechnical Commission, “IEC-61400-3: Wind Turbines – Part 3: Design Requirements for Offshore Wind Turbines. Edition 1.0.,” 2009-02.



Appendix A. Bathymetry Merging

In order to create model bathymetry, EMODnet bathymetry for the wider region and site-specific survey bathymetry (see Section 3.1) were merged. The two datasets are shown in Figure A.1.

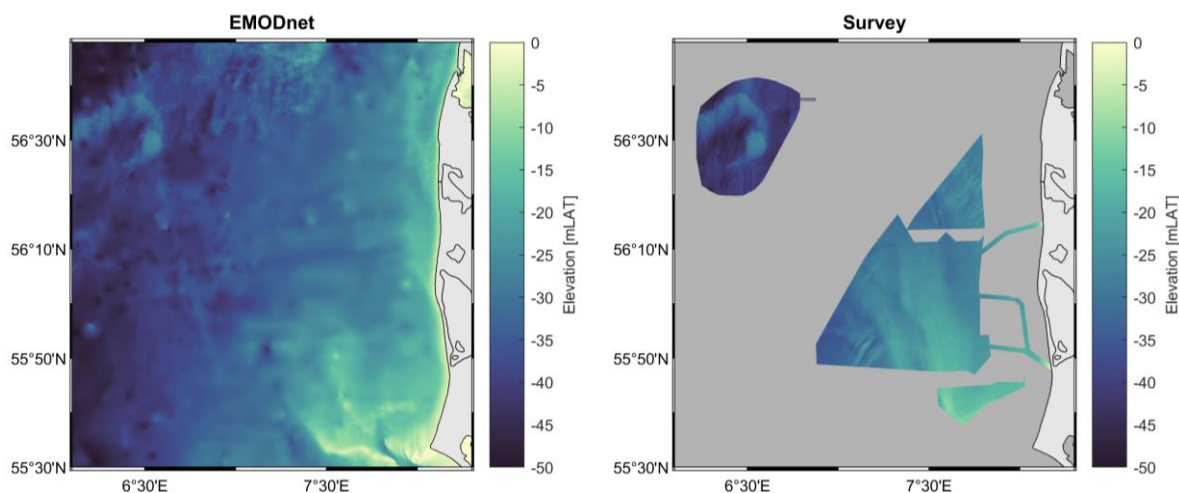


Figure A.1. EMODnet and site-specific survey bathymetry data.

To ensure the merging step did not artificially introduce any sudden jumps at the boundary between the two datasets, a tapering method was employed as follows:

STEP 1: Calculate elevations on a common grid

Calculations are performed on a regular horizontal grid with a resolution of 1/16 arc minutes: approximately 115 m in latitude and 98 m in longitude in the region of interest and higher than the resolution of the finest model grid cell. The EMODnet bathymetry and site-specific survey bathymetry were transformed to this grid by taking mean values across each grid cell.

STEP 2: Define the merging region

The region over which the bathymetry will be merged is defined in two parts:

- a) An *inner* region, in which the re-gridded site-specific survey data (from STEP 1) is used unchanged.
- b) A distance outside this region across which tapering takes place.

For this merge, the inner region is taken to be the full set of re-gridded site-specific survey data, and the taper is applied within 1000 m of this region, as shown in Figure A.2.

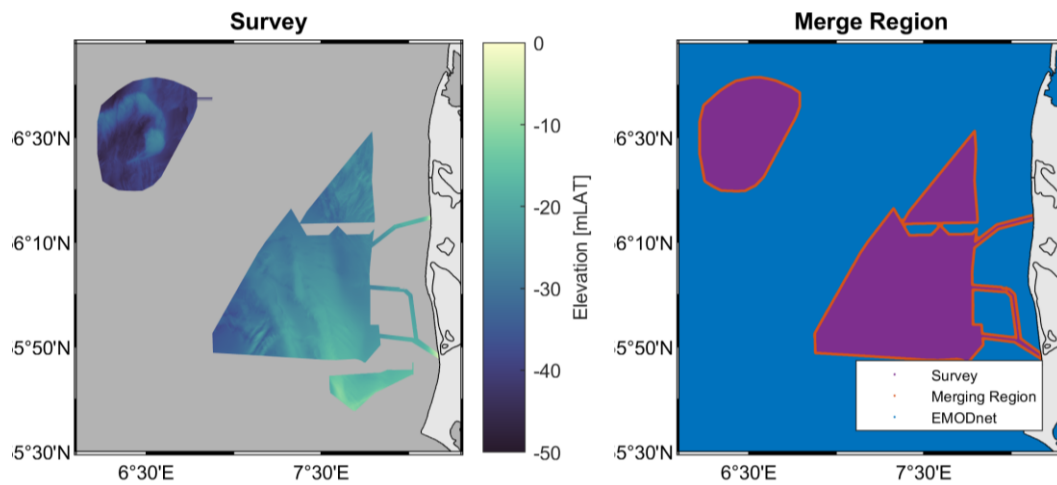


Figure A.2. Merging region.

STEP 3: Apply the taper

For each point within the merging region:

1. Find the closest point within the *inner* region, and its distance from the point being considered. This distance is denoted hereafter d_{in} .
2. Normalise this value so that it is zero on the boundary of the inner region, increasing linearly to one 1000 m away. If we denote this normalised value n_{in} then:

$$n_{in} = \frac{d_{in}}{1000}$$

Note that since we are only considering locations within 1000 m of the inner zone, this does not increase above 1.

3. Apply a cosine taper to this value such that it *smoothly* changes from *one* at the boundary of the inner region to *zero* 1000 m away. If we denote this as c_{in} then:

$$c_{in} = 0.5 \cdot \cos(n_{in}\pi) + 0.5$$

4. At the closest point found within the *inner* region found above, calculate the difference between the site-specific bathymetry and the EMODnet bathymetry, i.e.:

$$\delta_{in} = z_{survey} - z_{EMODnet}$$

This is the value we would *add* to EMODnet bathymetry that is exactly *on* the inner boundary.

5. Combine this “inner boundary offset” with the smooth distance from the inner boundary and the EMODnet to give a final adjusted elevation of:

$$z_{adjusted} = z_{EMODnet} + \delta_{in} \cdot c_{in}$$



For illustrative purposes, the values of a number of these parameters are shown across the entire merge region in Figure A.3 below.

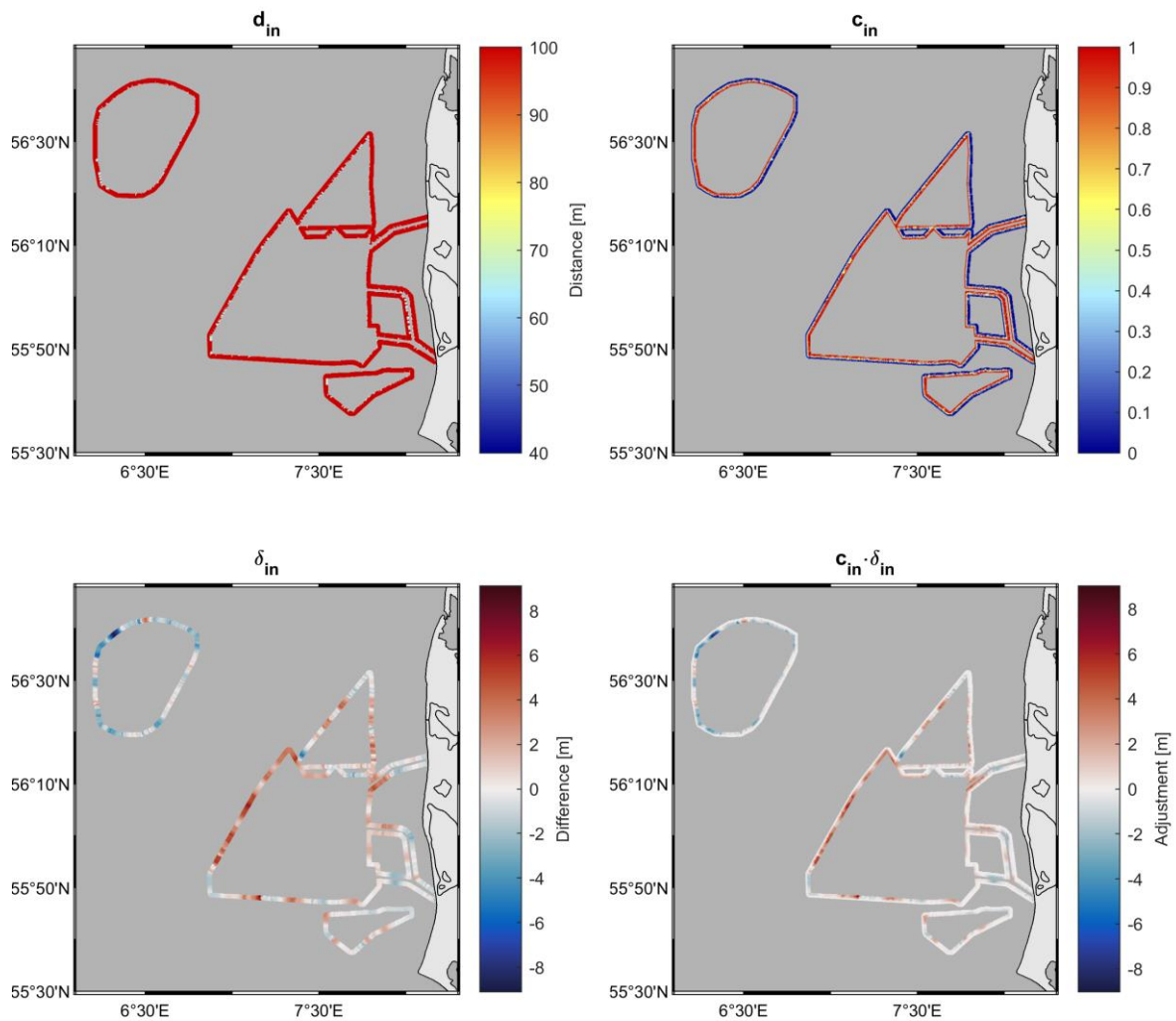


Figure A.3. Taper parameters over the entire merge region.



STEP 4: Review diagnostic plots

A number of diagnostic plots are subsequently reviewed to ensure no unwanted artifacts are introduced into the resulting bathymetry. A selection of these are shown in Figure A.4 through Figure A.8.

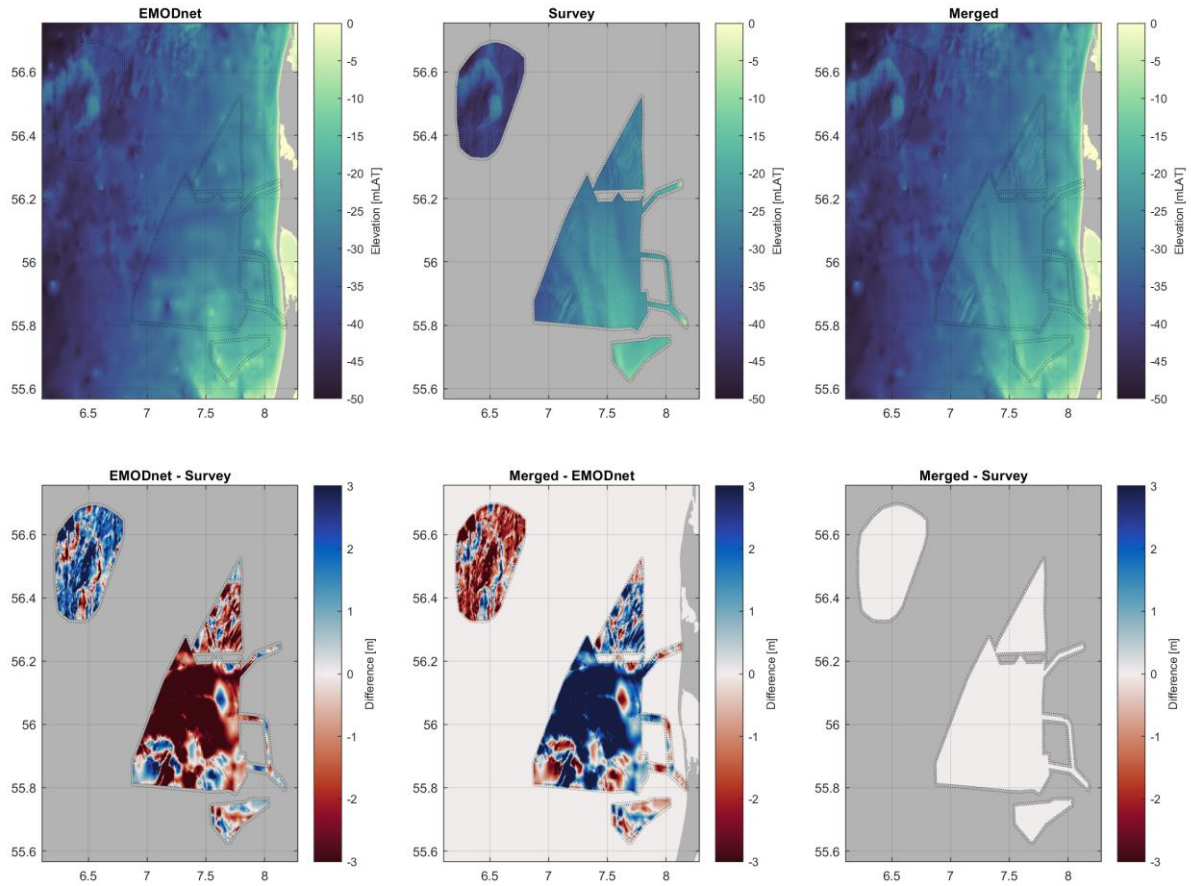


Figure A.4. EMODnet and survey bathymetry merge – diagnostic plot – overview.

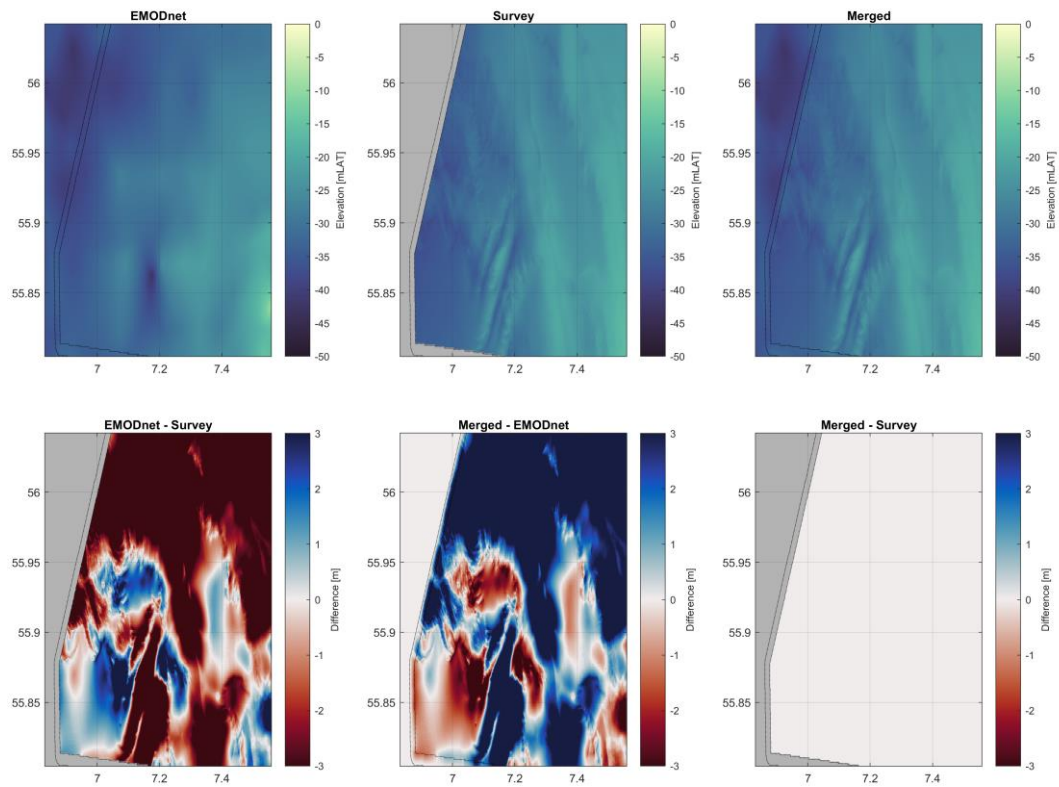


Figure A.5. EMODnet and survey bathymetry merge – diagnostic plot – southwest.

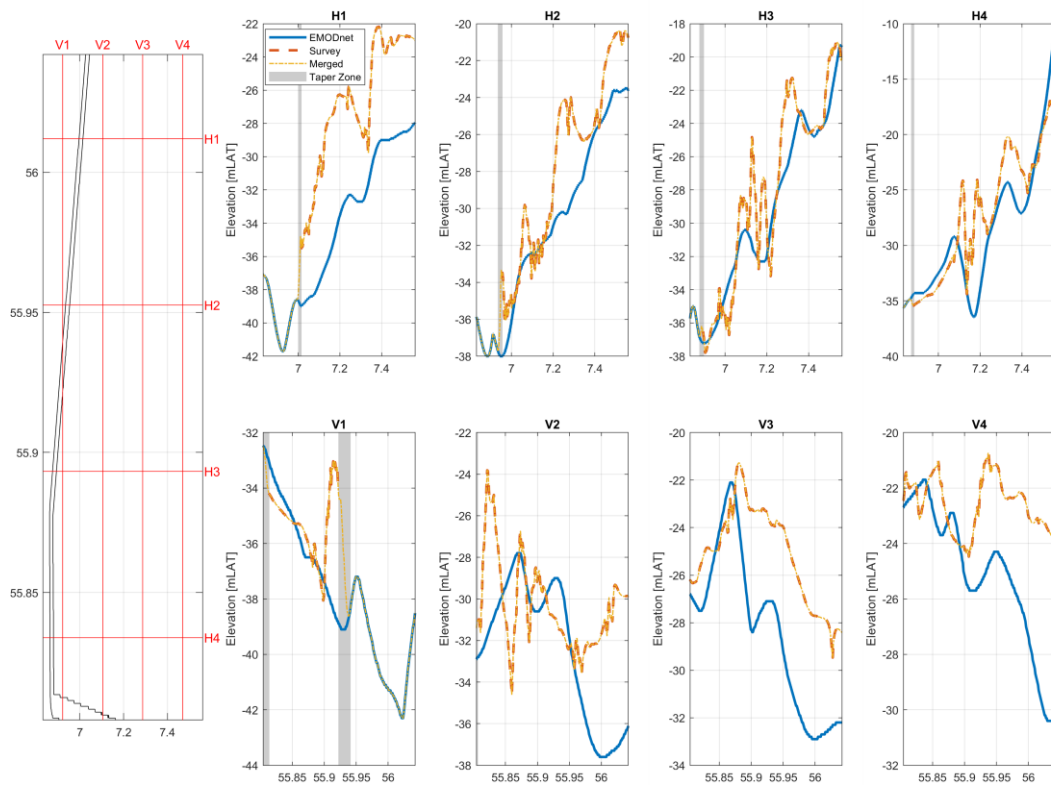


Figure A.6. EMODnet and survey bathymetry merge – transect diagnostic plot – southwest.

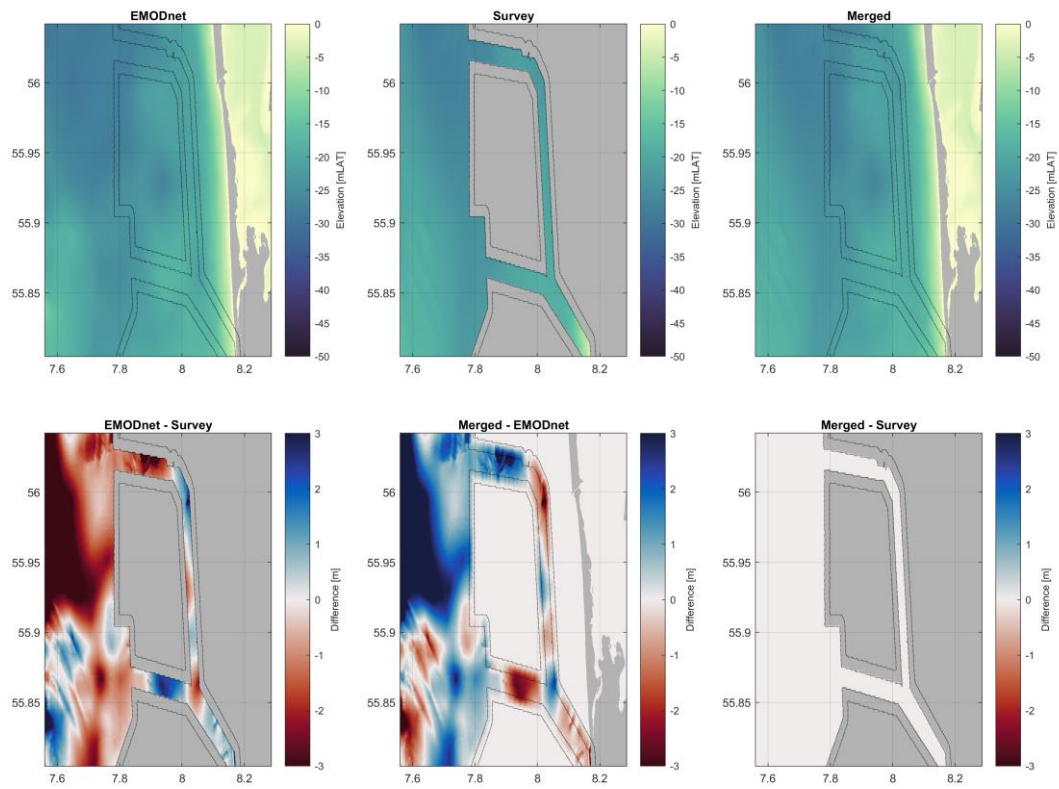


Figure A.7. EMODnet and survey bathymetry merge – diagnostic plot – east.

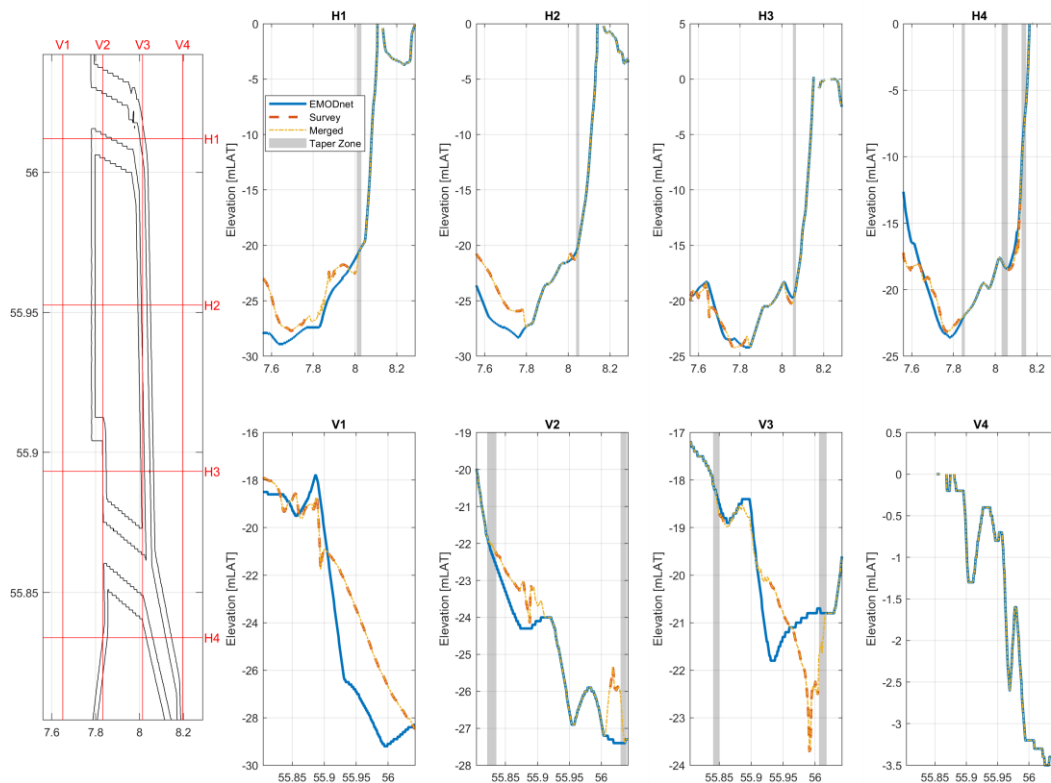


Figure A.8. EMODnet and survey bathymetry merge – transect diagnostic plot – east.



Appendix B. Wind Field Calibration

B.1 Introduction

In Section 4, modelled and measured wind datasets used in this project were introduced, and a number of validation details included, showing the suitability of the modelled data for use in both driving wave and hydrodynamic models and to represent hub height winds. As noted in Section 4.5, some calibration of modelled data is required prior to use, and such calibrations are described in more detail in this Appendix, which proceeds as follows:

- A brief summary of measured and modelled wind data is provided in Sections B.2 and B.3.
- The calibration process for 10 m wind fields is described in Section B.4.
- Details of the calibration process for wind fields at higher levels can be found in Section B.5.

B.2 Measured Wind Data

Measured wind data used during the validation and calibration process is shown in Table B.1 and Figure B.1.

Table B.1: Measured datasets used for wind model validation.

Supplier	Name	WGS84	Time Period	Elevation Range
Energinet	NSI-1-LB	55.9441°N, 7.0596°E	01-Sep-2023 to 01-May-2024	12 to 300 mASL
Energinet	NSI-2-LB	55.8856°N, 7.6167°E	01-Sep-2023 to 01-May-2024	12 to 300 mASL
Energinet	NSI-3-LB	56.0694°N, 7.6356°E	01-Sep-2023 to 01-May-2024	12 to 300 mASL
Energinet	EINS-1-LB	56.6280°N, 6.3007°E	15-Nov-2021 to 15-Nov-2023	30 to 270 mASL
Energinet	EINS-2-LB	56.3444°N, 6.4574°E	15-Nov-2021 to 15-Nov-2023	30 to 270 mASL
Energinet	Thor LiDAR	56.3470°N, 7.6050°E	18-May-2020 to 19-May-2021	40 to 197 mASL
BSH	FINO 1	6.5879°E, 54.0148°N	01-Jan-2003 to 29-Aug-2018	32.8 to 101.2 mMSL
BSH	FINO 3	7.1583°E, 55.1950°N	11-Sep-2009 to 31-Aug-2018	30.6 to 106.6 mMSL
MDE	Dogger Bank East LiDAR	2.7025°E, 55.0994°N	19-Nov-2014 to 16-Jan-2017	28 to 267 mMSL
ECN	IJmuiden LiDAR	3.4357°E, 52.8482°N	01-Jan-2012 to 29-Nov-2015	89.2 to 314.2 mMSL

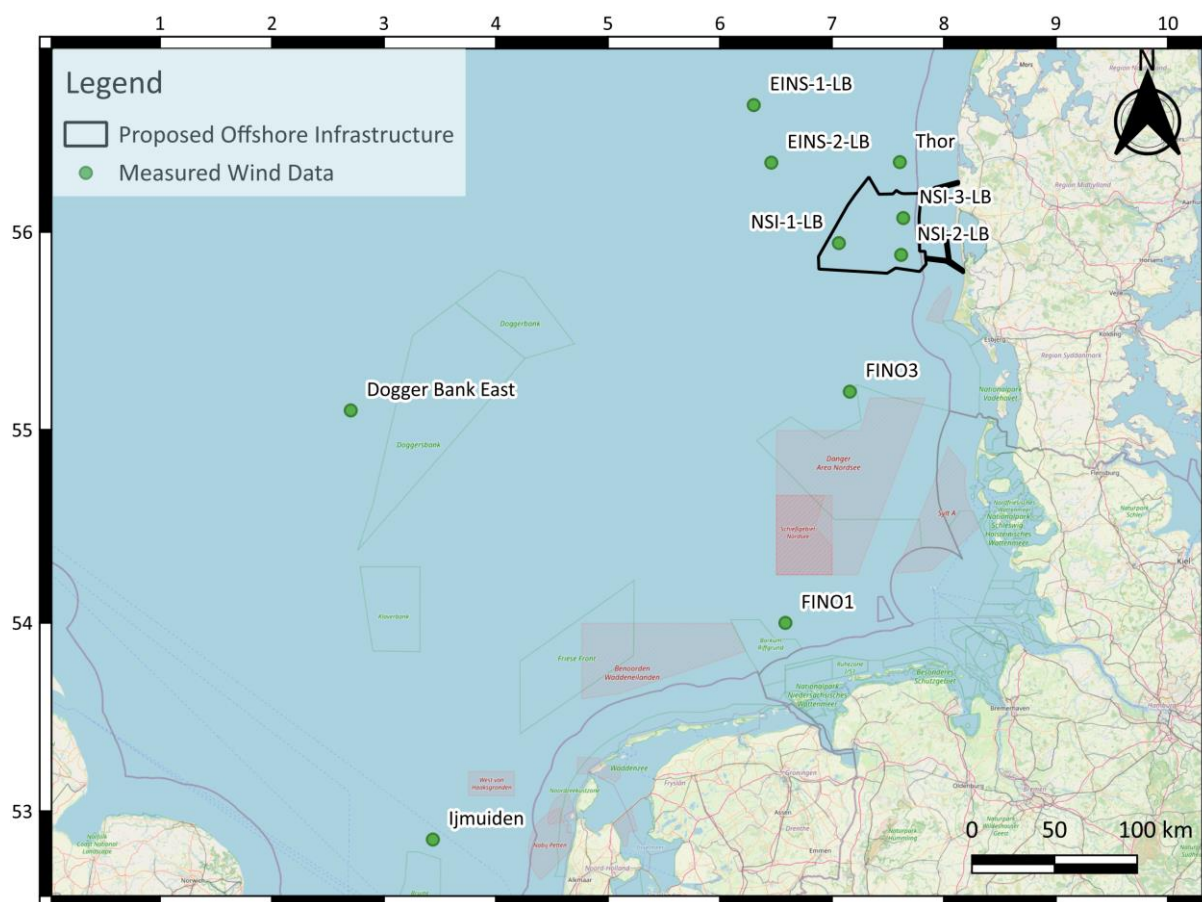


Figure B.1: Wind measurement locations.

B.3 ERA5 Modelled Data

European Centre for Medium-Range Weather Forecasts (ECMWF) ReAnalysis 5 (ERA5) is the fifth and latest major global reanalysis produced by ECMWF. Hourly wind speeds are available for the period 1979 to near present at various levels, including:

- **Single levels:** Hourly wind speeds at 10 and 100 m above the surface of the earth are available on a 0.25° by 0.25° resolution grid via the Copernicus Climate Change Service (C3S) Climate Data Store (CDS).
- **Model levels:** Hourly wind speeds on 137 model levels can be accessed through the CDS application programming interface (API).

For this work, single level data at 10 m is used to drive both the wave and hydrodynamic models, as well as to provide time-series at 10 m above sea level (ASL). Winds at hub height (taken to be 150 m ASL) are based on ERA5 model levels. Since these levels are not at the exact elevations required, some interpolation is necessary, and is described in Section 4.4.



B.4 Calibration at 10 m

ERA5 data at 10 m are used to drive the hydrodynamic and wave models used in this project. Given the larger area covered by the models, it is necessary to consider a much wider range of measurements to determine a suitable calibration. Detailed analyses of over a dozen met masts in European waters (and a similar number of coastal buoys, piers and platforms) suggest that ERA5 wind data are biased low for higher wind speeds near the surface, and in particular at the 10 m level. Our investigations suggest that two factors influence this:

1. A region wide underprediction, seen across all offshore locations.
2. Coastal effects, whereby grid cells consisting of even a small fraction of land can have a significant effect in lowering wind speeds at 10 m.

This bias low is demonstrated in Figure B.2 which presents a scatter plot with overlaid Quantile-Quantiles of raw ERA5 10 m wind speeds and measurements at FINO1.

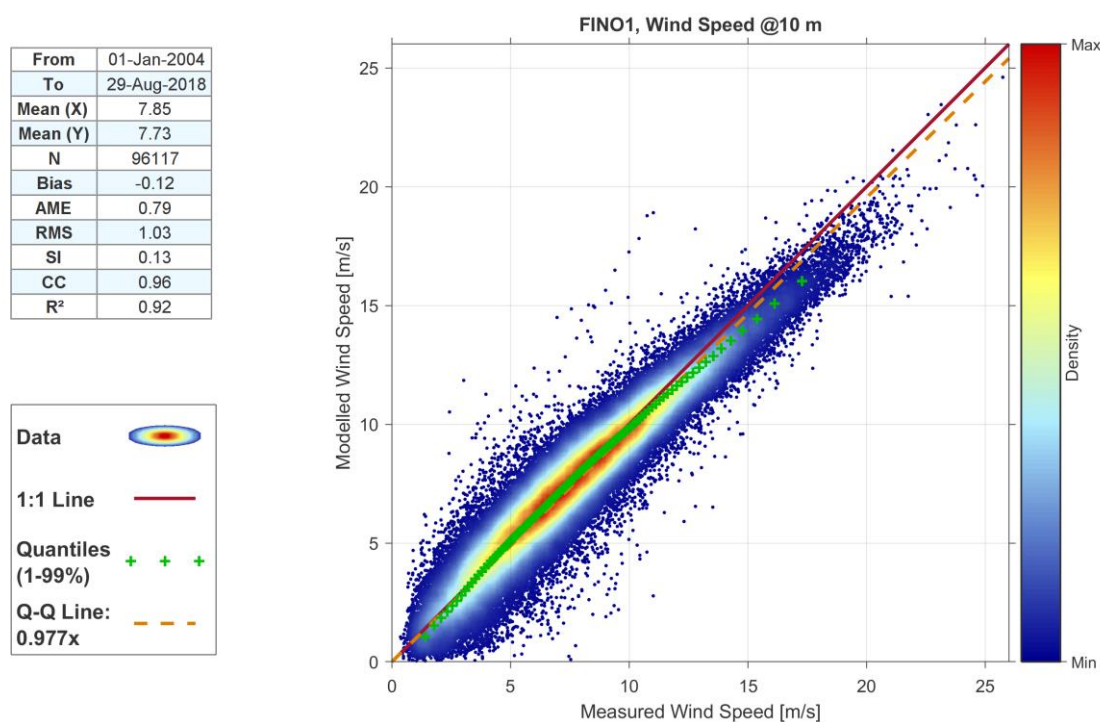


Figure B.2: Validation scatter with overlaid QQ plot of raw ERA5 10 m wind speeds at FINO1.

Our analyses have led us to a suitable set of adjustments to compensate for this bias which proceed as follows. Firstly, a region wide adjustment, based on behaviour seen consistently across all offshore locations is applied to data from all offshore ERA5 grid points. In general, ERA5 performs well offshore for “normal” wind conditions but underestimates higher wind speeds. Thus, the calibration balances three key priorities:

- Any effect on data during normal conditions is minimal.
- A smooth transition is included between normal wind speeds and higher wind speeds.
- Adjusted values better reflect measurements for higher wind speeds



Metocean Data Overview – North Sea I Offshore Wind Farm

For coastal locations, the regional adjustment alone generally provides good results at the 100 m level and above. However, at the 10 m level there is still significant bias. Thus, an additional second step is included which:

- Uses the ERA5 land-sea mask to determine whether land is expected to have an influence on each grid cell.
- Determines appropriate adjustments based on modelled values at 100 m and wind profile relationships from nearby offshore grid points. Different directional behaviours are also taken into account.

The results of including the calibration process are shown for FINO1 in Figure B.3. Significant improvements are indeed seen, though it should be noted that the met mast itself (or indeed any of the wind measurement locations used in this report) is not close enough to the coast to necessitate the second step of the process.

For reference, analogous comparisons for the NSI-1-LB, NSI-2-LB, NSI-3-LB and Thor LiDARs are shown in Figure B.4 through Figure B.11. We are happy to provide such figures for all locations upon request, though they are omitted here for brevity. Validation plots using calibrated ERA5 data at 10m can be found for all locations, except the IJmuiden and Dogger Bank East LiDARs, in Section 4.5. Both these locations are some distance from the site of interest, and are primarily included in this report to corroborate hub height wind calibrations against LiDAR measurements from *fixed* platforms. We are, however, happy to provide such validations for these locations upon request.

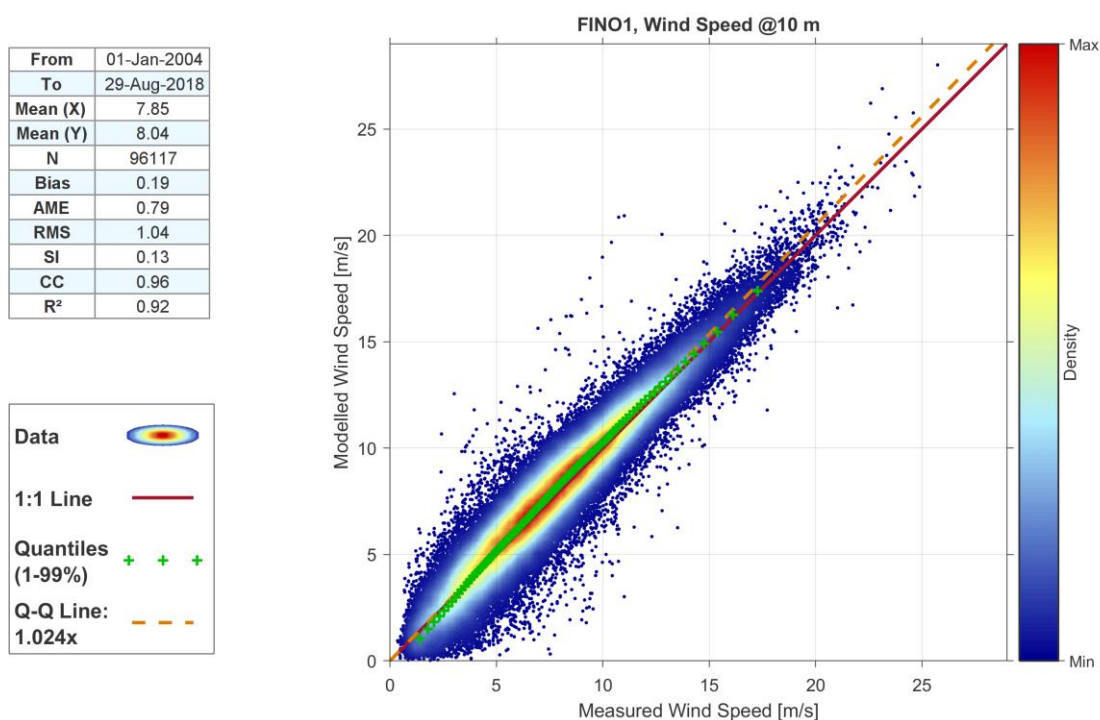


Figure B.3: Validation scatter with overlaid QQ plot of MetOceanWorks' adjusted ERA5 10 m wind speeds at FINO1.



From	01-Sep-2023
To	01-May-2024
Mean (X)	9.45
Mean (Y)	9.12
N	5830
Bias	-0.33
AME	0.78
RMS	1.05
SI	0.11
CC	0.97
R ²	0.94

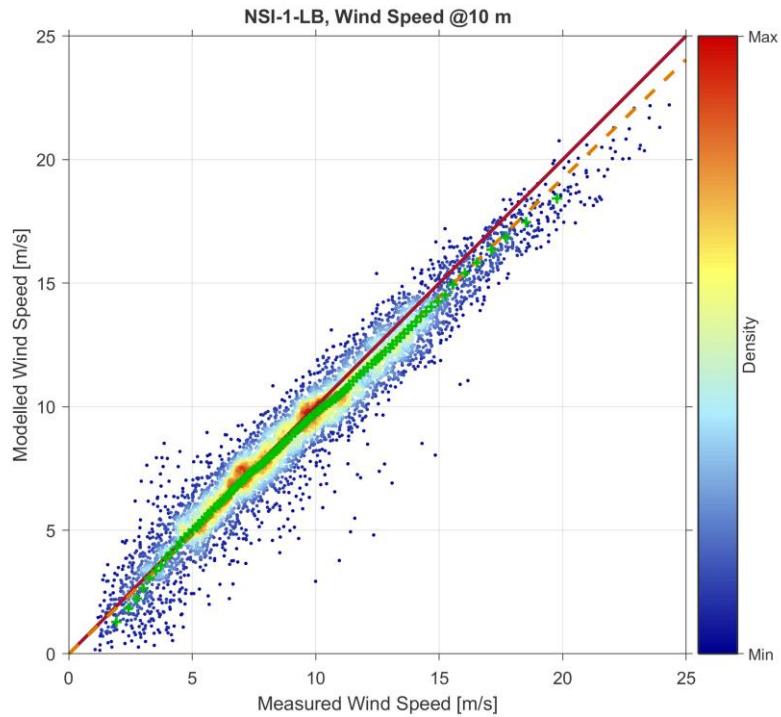
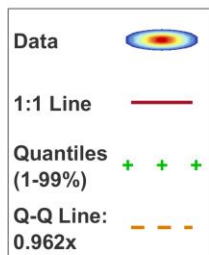


Figure B.4: Validation plot of raw ERA5 10 m wind speeds, NSI-1-LB.

From	01-Sep-2023
To	01-May-2024
Mean (X)	9.45
Mean (Y)	9.50
N	5830
Bias	0.06
AME	0.75
RMS	1.01
SI	0.11
CC	0.97
R ²	0.94

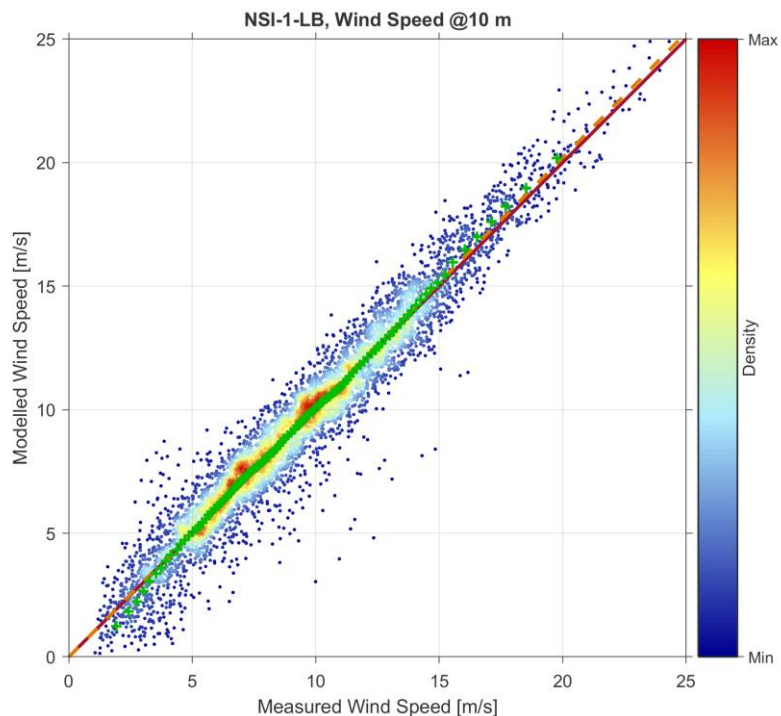
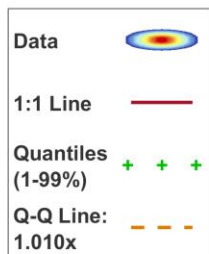


Figure B.5: Validation plot of MetOceanWorks' adjusted ERA5 10 m wind speeds, NSI-1-LB.

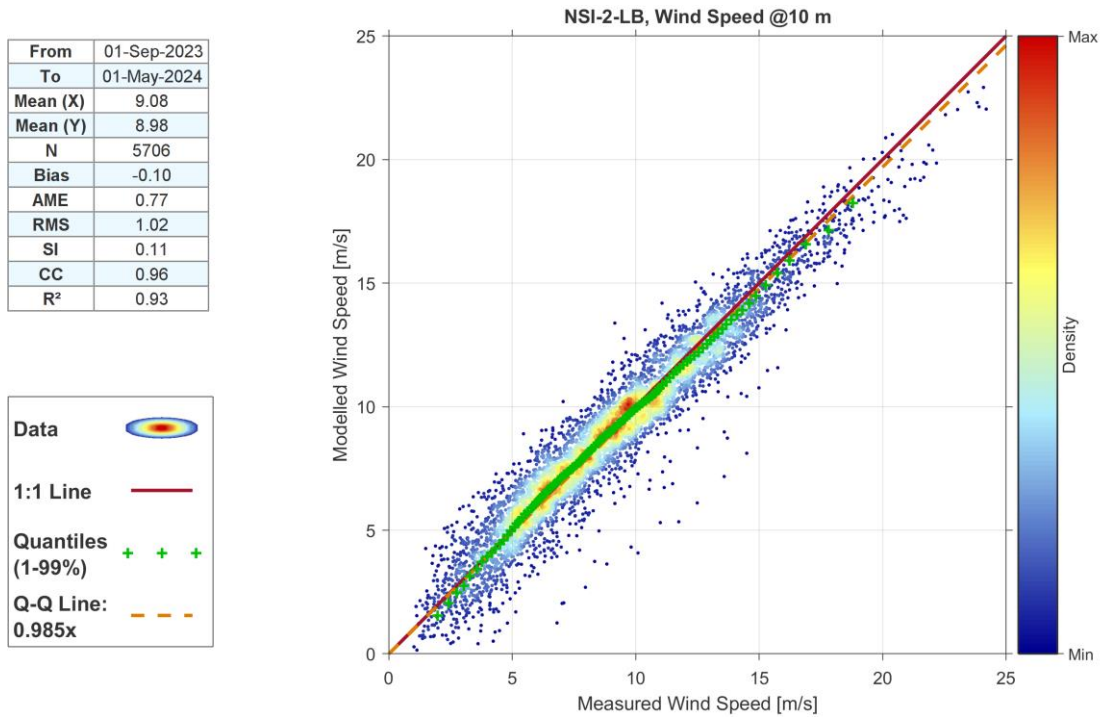


Figure B.6: Validation plot of raw ERA5 10 m wind speeds, NSI-2-LB.

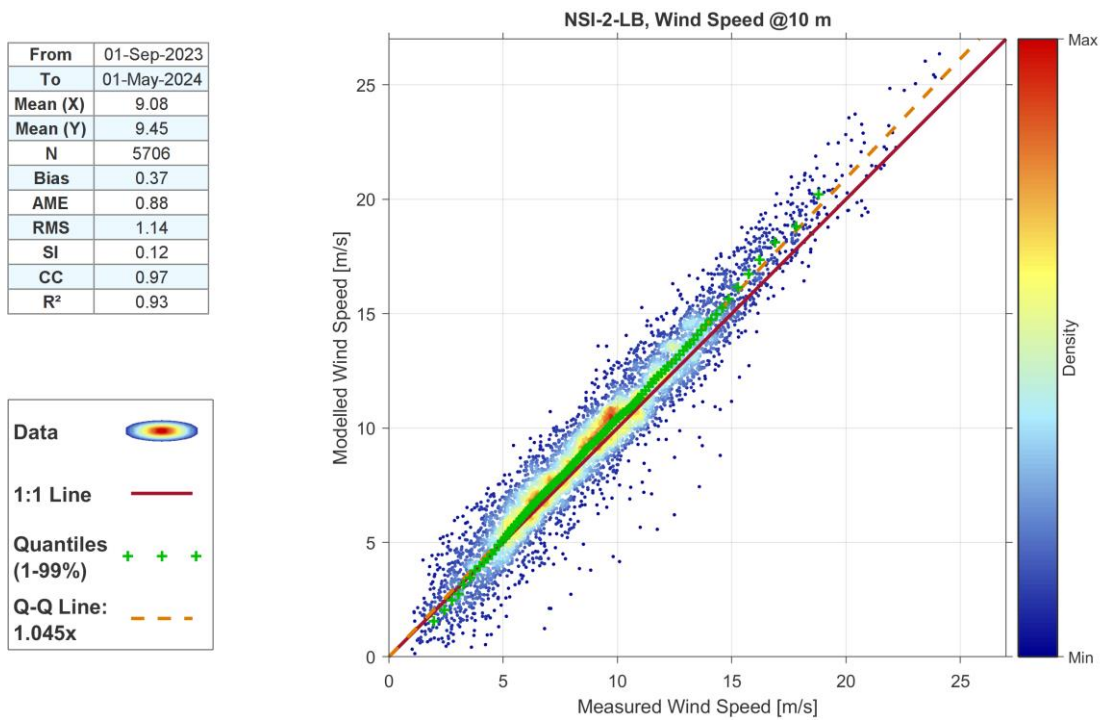


Figure B.7: Validation plot of MetOceanWorks' adjusted ERA5 10 m wind speeds, NSI-2-LB.

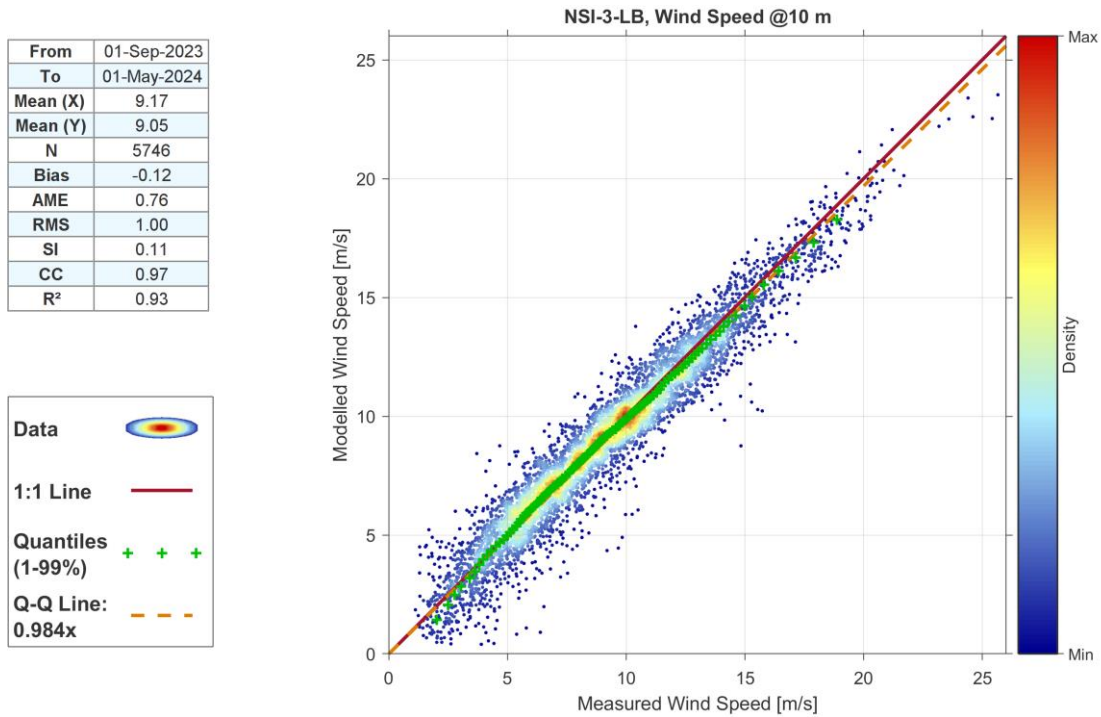


Figure B.8: Validation plot of raw ERA5 10 m wind speeds, NSI-3-LB.

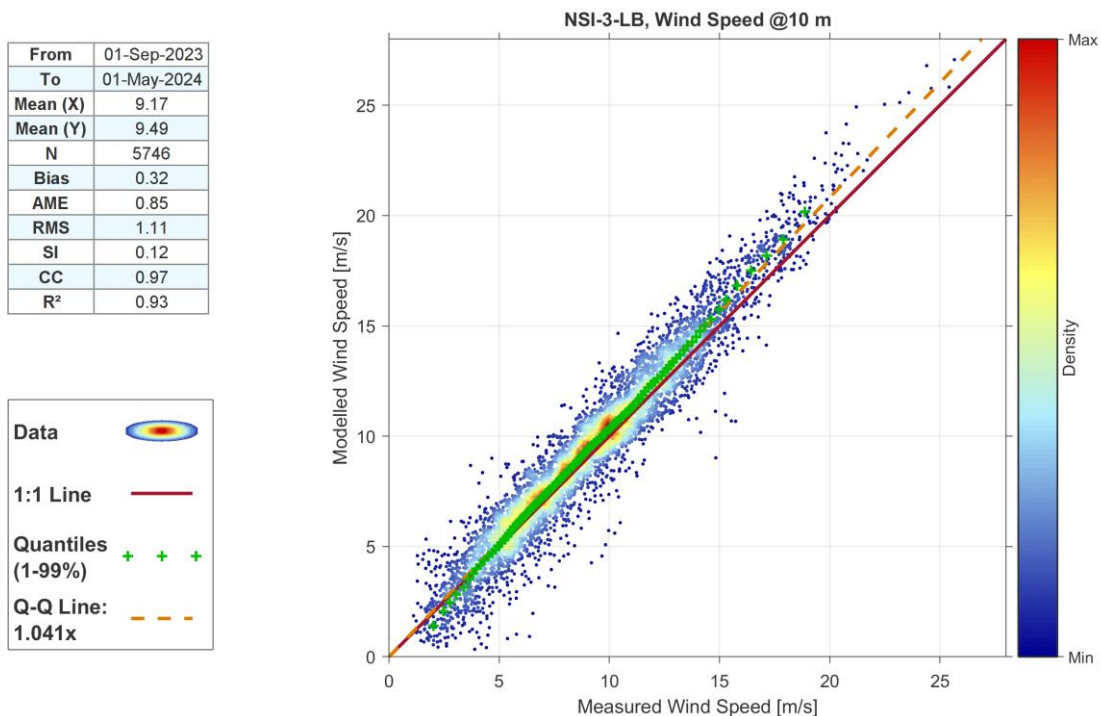


Figure B.9: Validation plot of MetOceanWorks' adjusted ERA5 10 m wind speeds, NSI-3-LB.



From	18-May-2020
To	19-May-2021
Mean (X)	8.07
Mean (Y)	7.82
N	8240
Bias	-0.25
AME	0.74
RMS	1.00
SI	0.12
CC	0.96
R ²	0.92

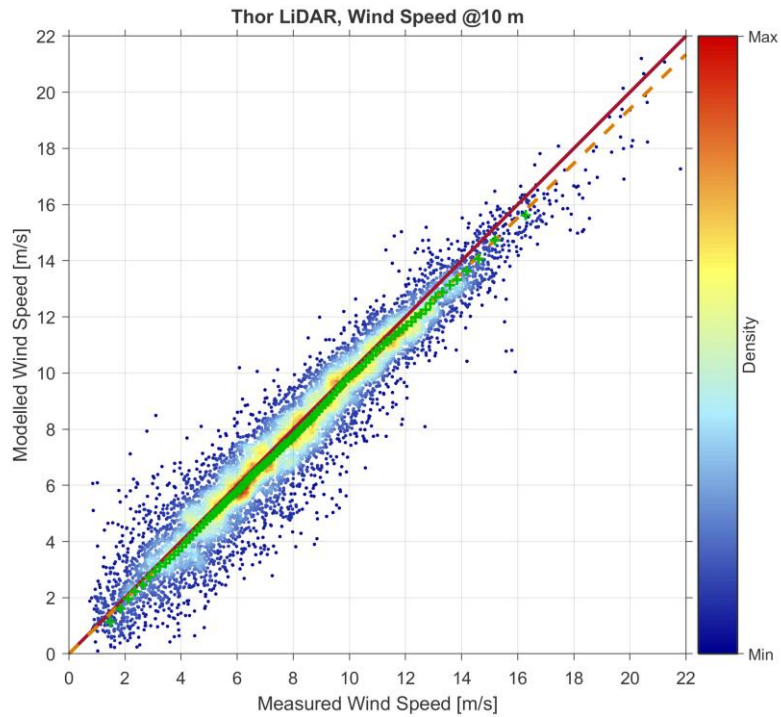
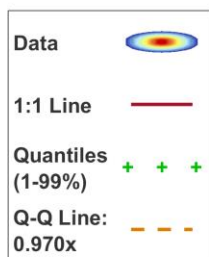


Figure B.10: Validation plot of raw ERA5 10 m wind speeds, Thor LiDAR.

From	18-May-2020
To	19-May-2021
Mean (X)	8.07
Mean (Y)	8.15
N	8240
Bias	0.08
AME	0.76
RMS	1.02
SI	0.13
CC	0.96
R ²	0.92

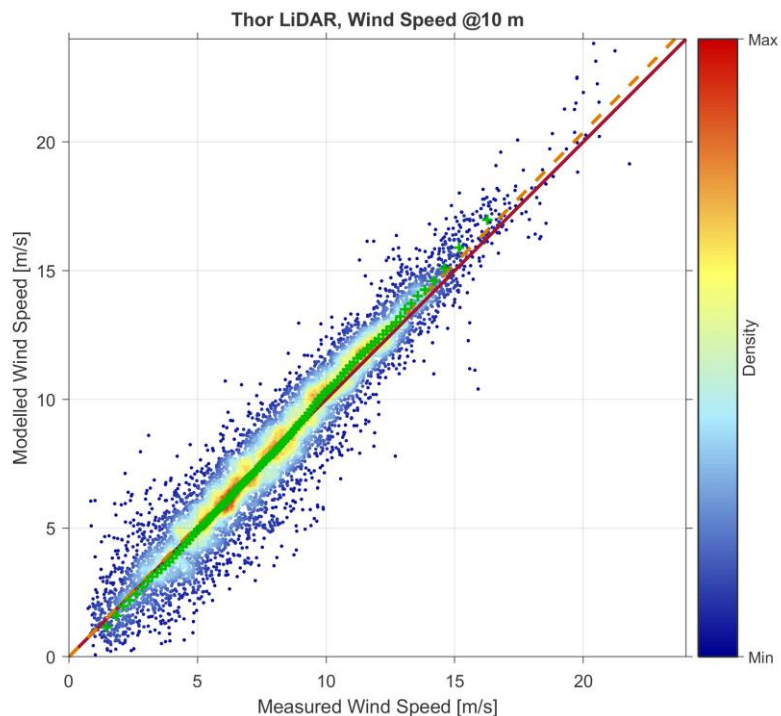
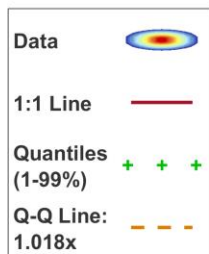


Figure B.11: Validation plot of MetOceanWorks' adjusted ERA5 10 m wind speeds, Thor LiDAR.



B.5 Calibration at Hub Height

Unlike the 10 m level, where winds are needed across the domains of wave and hydrodynamic models, at hub height (taken to be 150 m ASL for this work) winds are only required in the project area. As such, a local calibration, based only on site-specific measurements can be used.

The overall process is very similar to that used at 10 m, and to illustrate it, we begin by considering the 150 m level at NSI-1-LB, shown in Figure B.12. This exhibits similar behaviour to that seen in the previous section for 10 m winds, performing well at lower speeds, but becoming biased low as wind speeds increase.

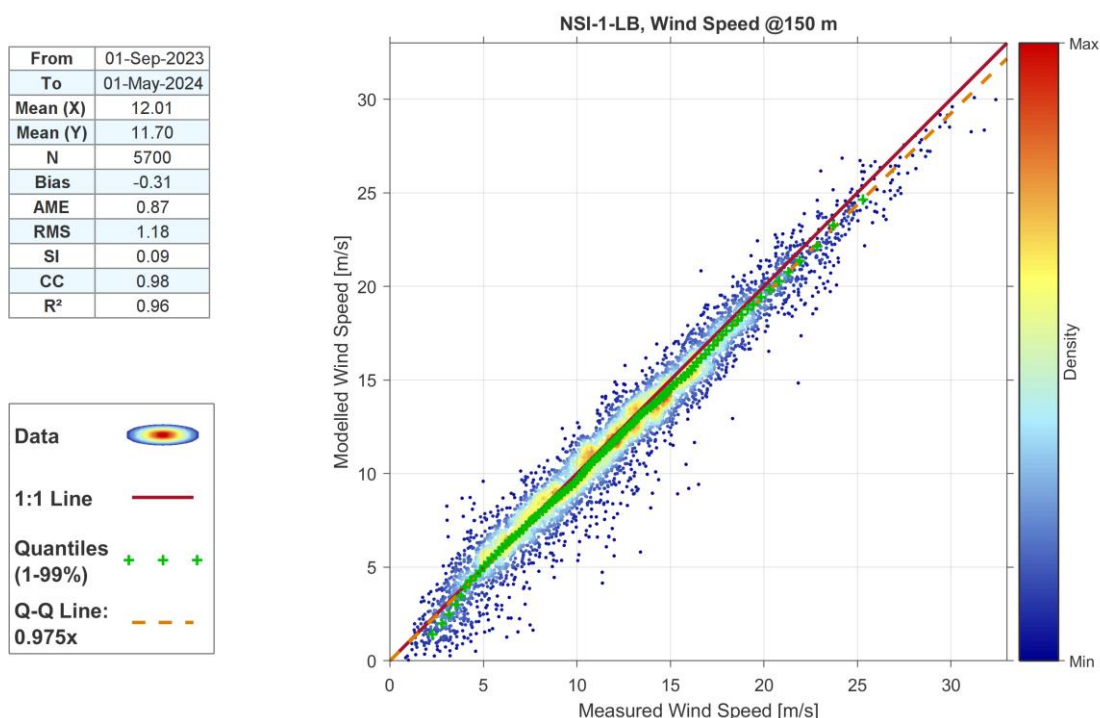


Figure B.12: Validation plot of raw ERA5 150 m wind speeds, NSI-1-LB.

Firstly, a suitable curve is fitted to the data to reflect this behaviour, for example as shown in Figure B.13.

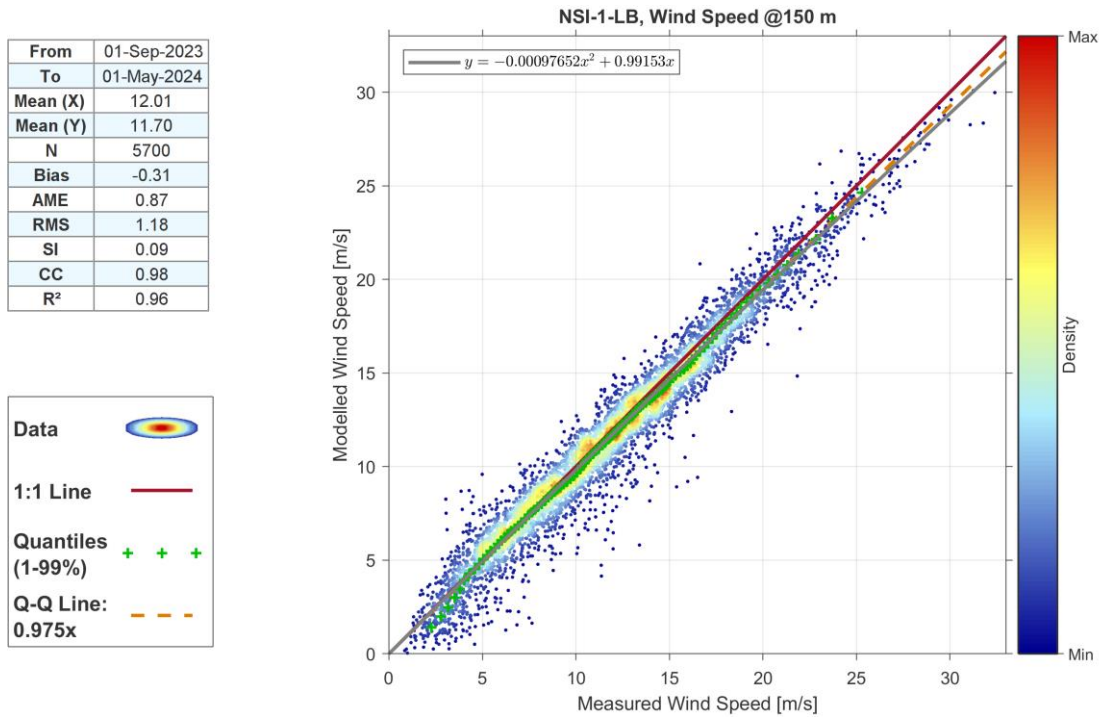


Figure B.13: Calibration curve, 150 m, NSI-1-LB.

Repeating for all three NSI floating LiDARs gives two curves, shown against data quantiles only in Figure B.14.

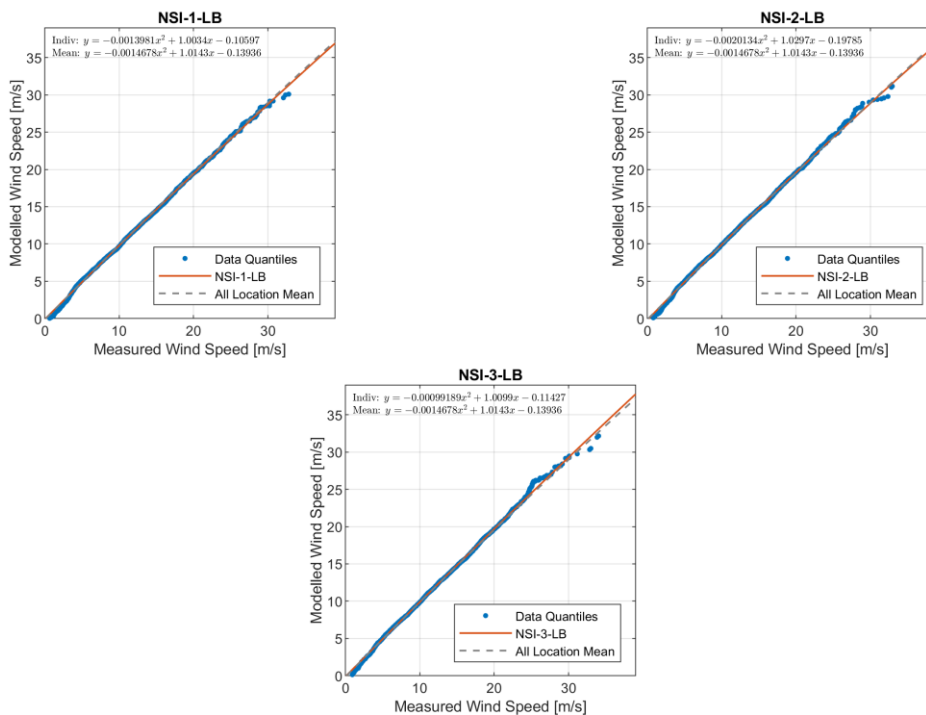


Figure B.14: Calibration curve, 150 m, all locations.



The final calibration curve is taken to be the *mean* of the two calibrations, as shown in Figure B.15.

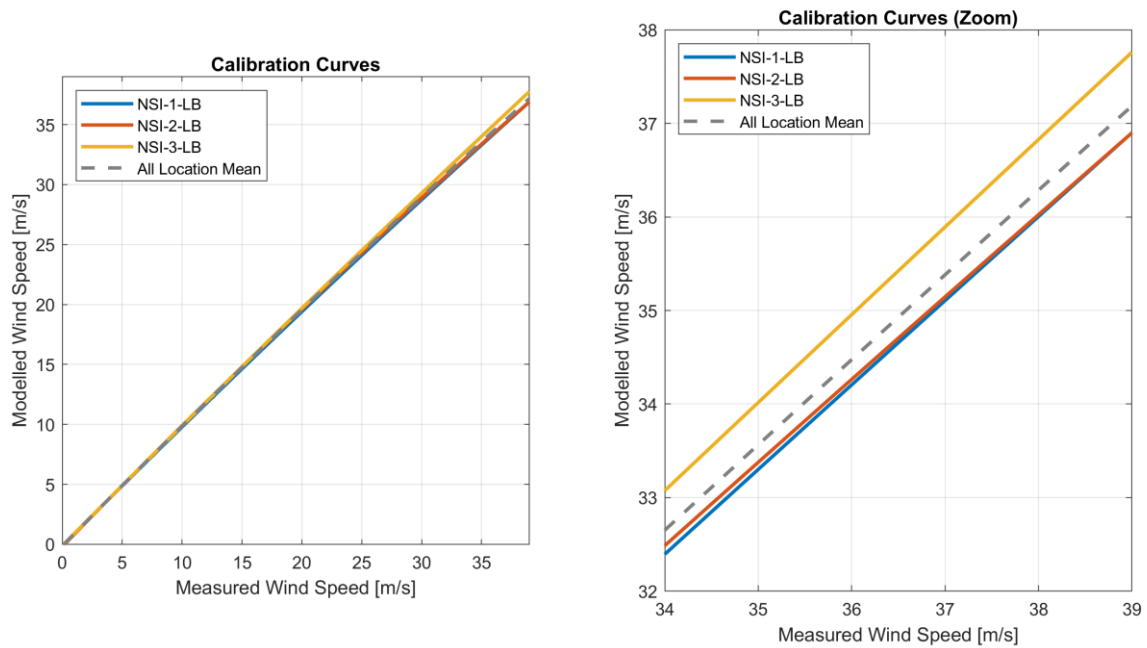


Figure B.15: Final Calibration curve, 150 m.

The impact of applying this mean curve to the three datasets is shown in Figure B.16 through Figure B.21, where throughout, a validation of raw ERA5 is followed by a validation of calibrated data for each location.

Validation plots using ERA5 data at 150m with this calibration applied can be found for all locations, except FINO1 and FINO3, in Section 4.5. Results are omitted for the two FINO masts as such a comparison would require significant upwards extrapolation from their highest measurement levels (101.2 and 106.6 mMSL).



From	01-Sep-2023
To	01-May-2024
Mean (X)	12.01
Mean (Y)	11.70
N	5700
Bias	-0.31
AME	0.87
RMS	1.18
SI	0.09
CC	0.98
R ²	0.96

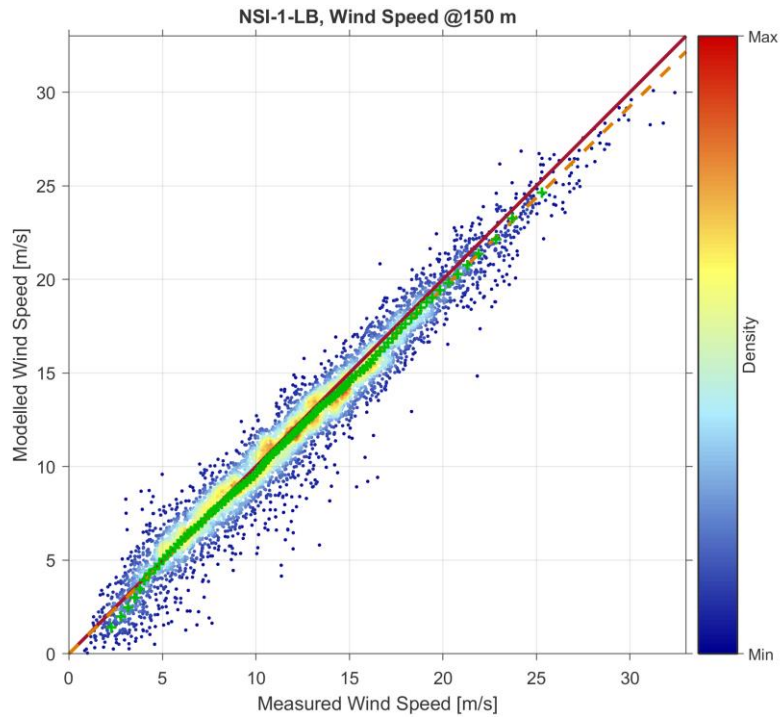
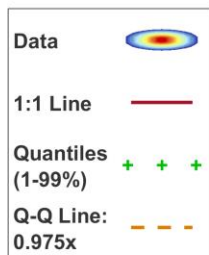


Figure B.16: Validation plot, raw ERA5, 150 m, NSI-1-LB.

From	01-Sep-2023
To	01-May-2024
Mean (X)	12.01
Mean (Y)	11.97
N	5700
Bias	-0.04
AME	0.85
RMS	1.15
SI	0.10
CC	0.98
R ²	0.96

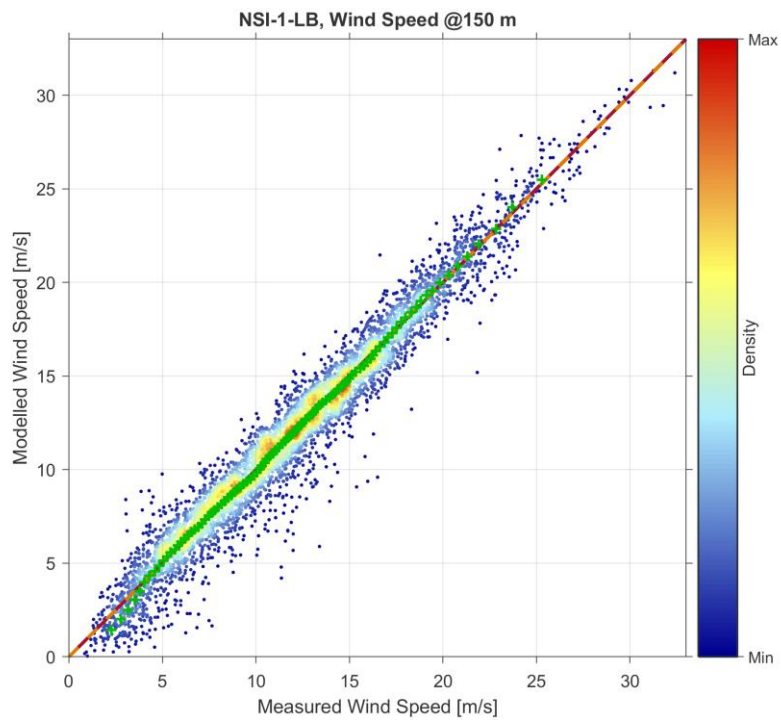
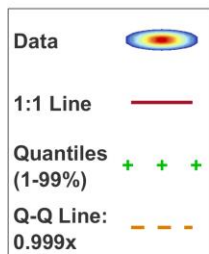


Figure B.17: Validation plot, calibrated ERA5, 150 m, NSI-1-LB.



From	01-Sep-2023
To	01-May-2024
Mean (X)	11.71
Mean (Y)	11.53
N	5648
Bias	-0.18
AME	0.85
RMS	1.14
SI	0.10
CC	0.98
R ²	0.95

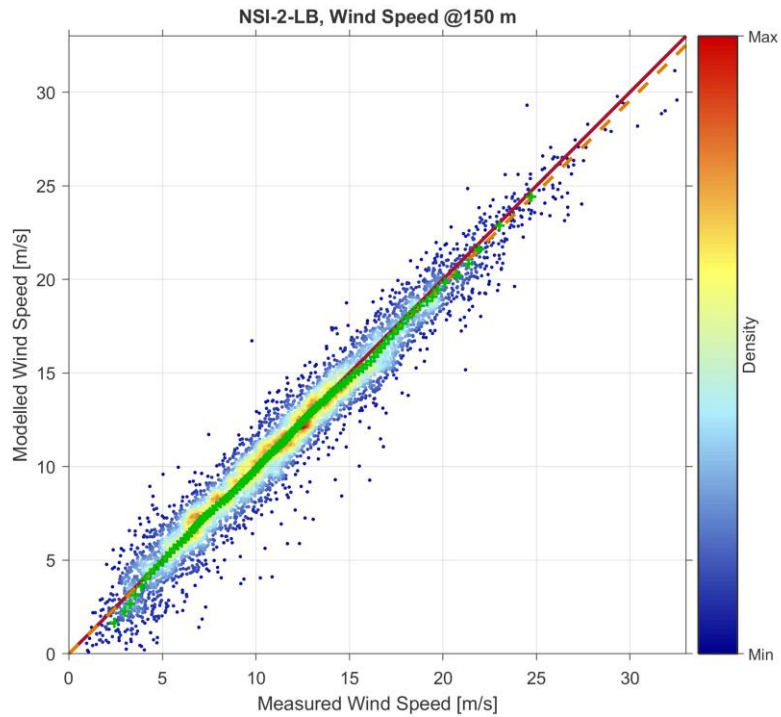
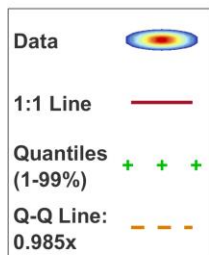


Figure B.18: Validation plot, raw ERA5, 150 m, NSI-2-LB.

From	01-Sep-2023
To	01-May-2024
Mean (X)	11.71
Mean (Y)	11.79
N	5648
Bias	0.08
AME	0.86
RMS	1.15
SI	0.10
CC	0.98
R ²	0.95

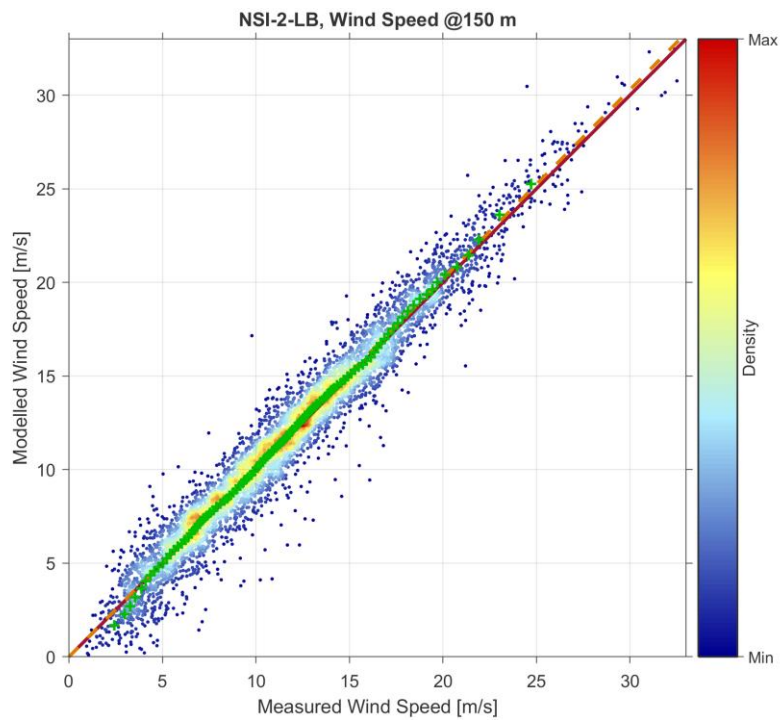
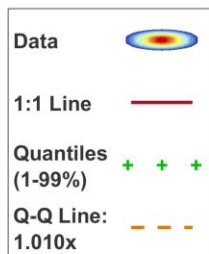


Figure B.19: Validation plot, calibrated ERA5, 150 m, NSI-2-LB.



From	01-Sep-2023
To	01-May-2024
Mean (X)	11.76
Mean (Y)	11.60
N	5702
Bias	-0.17
AME	0.85
RMS	1.13
SI	0.10
CC	0.98
R ²	0.95

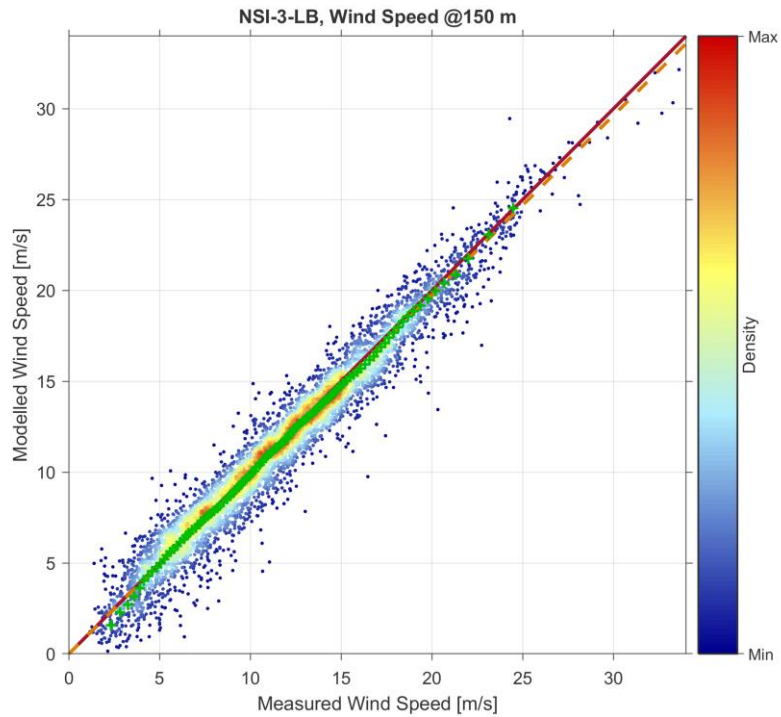
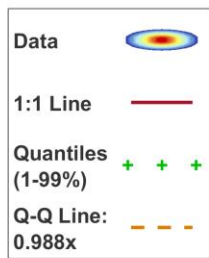


Figure B.20: Validation plot, raw ERA5, 150 m, NSI-3-LB.

From	01-Sep-2023
To	01-May-2024
Mean (X)	11.76
Mean (Y)	11.86
N	5702
Bias	0.10
AME	0.87
RMS	1.15
SI	0.10
CC	0.98
R ²	0.95

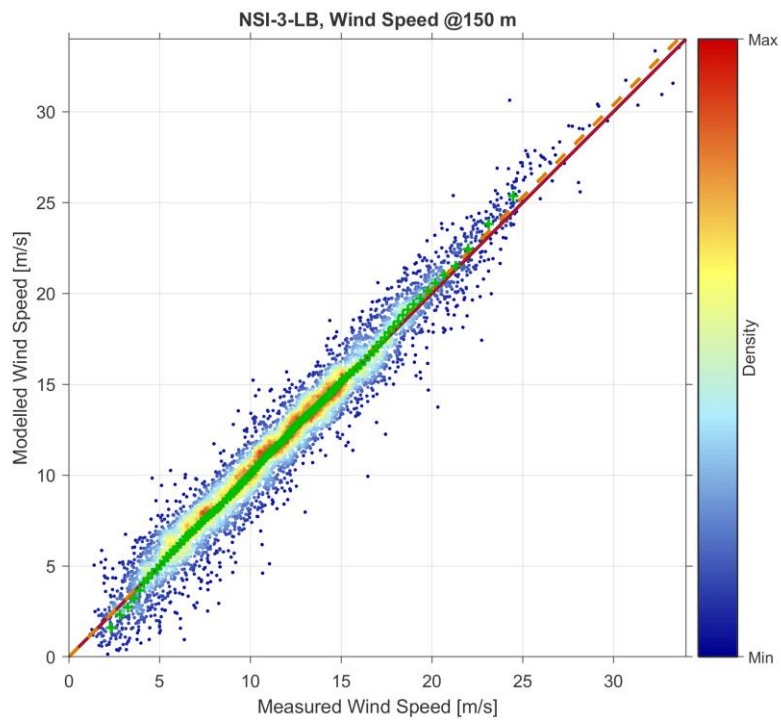
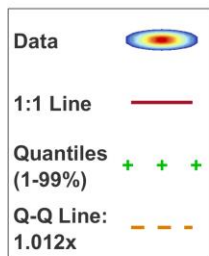


Figure B.21: Validation plot, calibrated ERA5, 150 m, NSI-3-LB.



B.6 Theoretical Wind Profiles

For reference, more details on the theoretical profiles used in this project to describe variations in wind speed in the vertical are briefly described.

B.6.1 Power Law Profile

Wind profile shapes applicable for use in normal conditions are often expressed in the form of a power law exponent, α , whereby:

$$U(z) = U(z_r) \left(\frac{z}{z_r} \right)^\alpha$$

With:

$U(z)$ being wind speed at height z .

z_r being a reference height, generally taken to be 10 metres.

The exponent, α , being dependent on terrain roughness.

B.6.2 Frøya Profile

One of the most commonly recommended (e.g., ISO [19] and DNVGL [12]) profiles for use in extreme wind conditions is the Frøya profile. In full, this is given as:

$$U(t, z) = U_0 \left(1 + C \cdot \ln \left(\frac{z}{z_r} \right) \right) \left(1 - 0.41 \cdot I_u(z) \cdot \ln \left(\frac{t}{t_r} \right) \right)$$

Where:

$$C = 5.73 \cdot 10^{-2} \sqrt{1 + 0.148 U_0}$$

$$I_u(z) = 0.06 \cdot (1 + 0.043 U_0) \left(\frac{z}{z_r} \right)^{-0.22}$$

t_r = the reference averaging period of *one hour*

z_r = the reference elevation of 10 m ASL

$U(t, z)$ = the most likely maximum mean wind speed with averaging period t (t less than one hour) at height z

U_0 = the *one hour* mean wind speed at reference height z_r , i.e. $U(t_r, z_r)$



Appendix C. Wind Averaging Periods

C.1 Overview

In this Appendix, the “effective averaging interval” of the modelled wind data is considered through comparison to available measurements. By way of overview of the overall procedure used, we begin with a simple example of modelled and measured wind speeds for an arbitrary period, as shown in Figure C.1. Here the measurements (ten-minute averages every ten-minutes) show a great deal more variation than the model values (instantaneous hourly values representative of a grid location) which are considerably smoother.

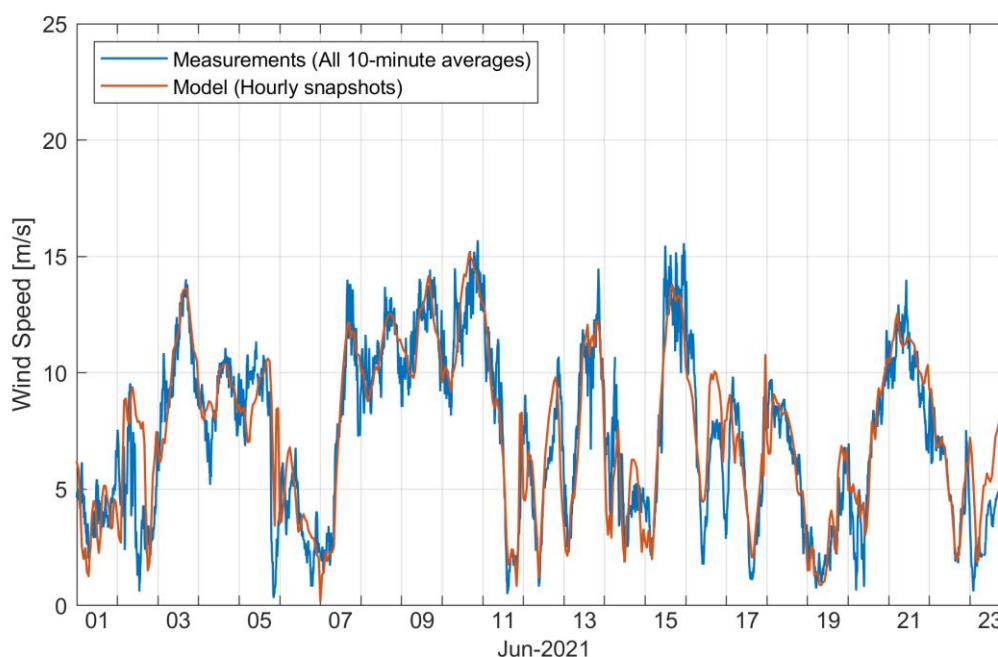


Figure C.1. Example time series, modelled and measured

To a large extent, plotting *all* measured data (i.e., a value every 10 minutes as opposed to hourly for the model) exaggerates this effect. However, if we use only *hourly* measured values, i.e., every sixth ten-minute average, we still see very similar behaviour, as shown in Figure C.2.

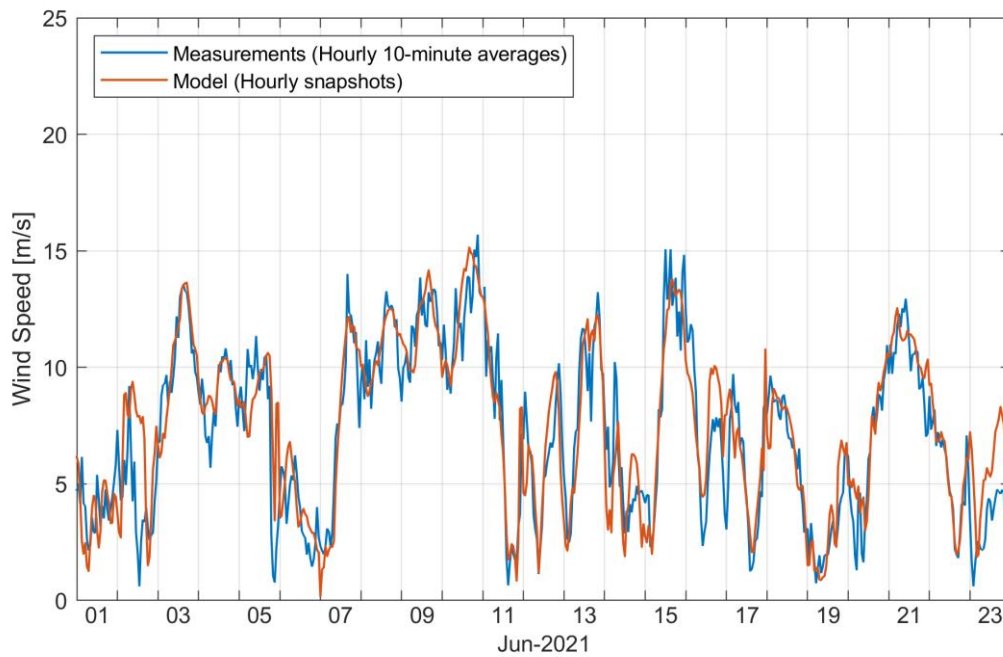


Figure C.2. Example time series, modelled and hourly measured

If, rather than taking hourly ten-minute averages, we take hourly *one-hour averages*, or *three-hour averages*, or even *six-hour averages* from the measured data, we get smoother lines, for example as shown in Figure C.3.

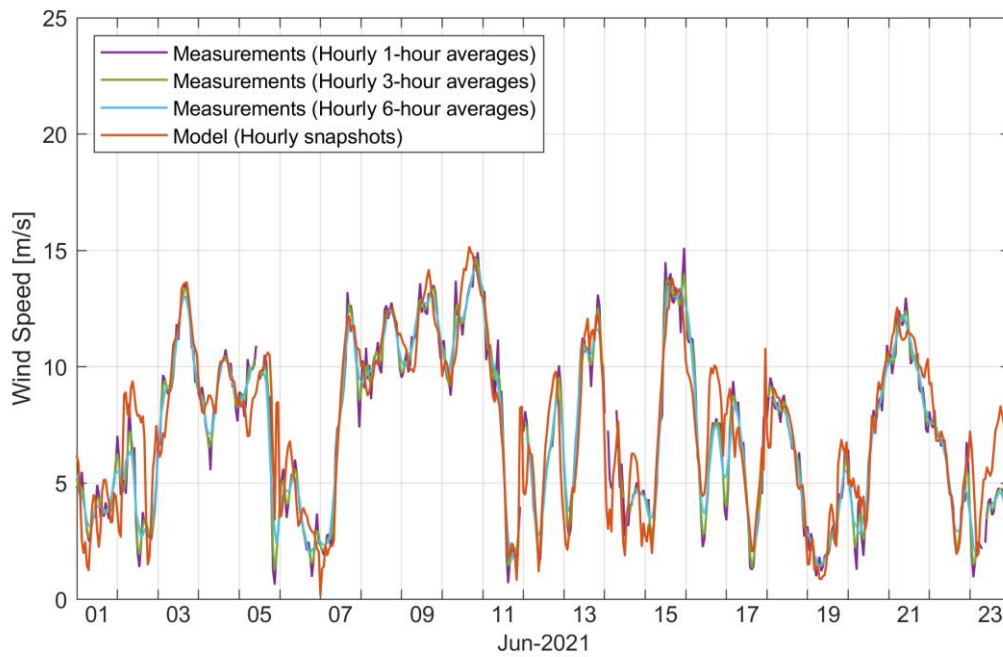


Figure C.3. Example time series, modelled and measured



Whilst it is impossible to draw firm conclusions from the above, it does appear that the one-hour average is still less smooth than the model data line, the six-hour average is smoother, and the three-hour average is quite similar.

Though the modelled data represent instantaneous wind speeds, some form of spatial averaging and/or smoothing has been included in their creation – if not in the model itself, then at least in the inputs driving the model. This has a very similar effect to *temporal averaging* of the measurements. Since our aim is to treat the model as representative of measurements at a single location, we must determine what level of such temporal averaging corresponds to the spatial averaging seen in the model, determining an effective averaging period for the model.

C.2 Diagnostic Plots

In order to assess this effective averaging period, we review a series of diagnostic plots comparing the model to measured data. An example, for wind speeds at the 150 m level of the NSI-1-LB instrument, is shown in Figure C.4.

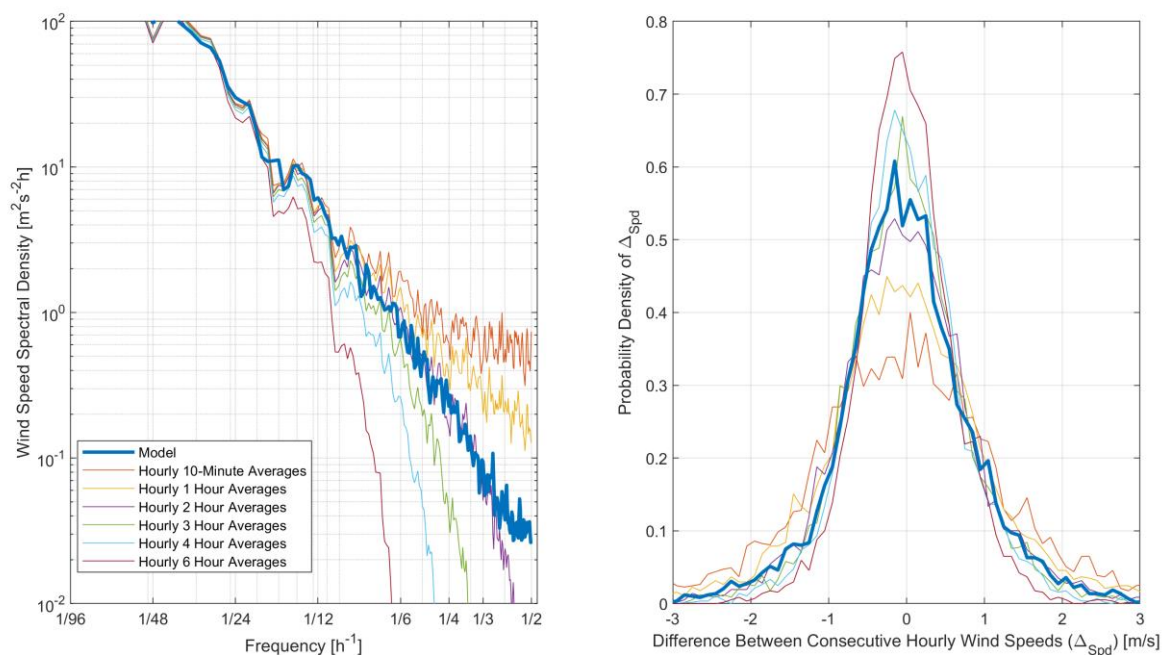


Figure C.4. Effective averaging period diagnostic, NSI-1-LB, wind speeds at 150 mASL.

To the left-hand side, a **spectral** plot of measured and modelled data is shown. For the model data, and a selection of hourly datasets of different averaging periods derived from the original measurements, the spectral density is found and all results overlaid. Those shown are calculated from overlapping 16-day windows, starting at 00:00 each day, though a variety of alternative windows were also reviewed, leading to very similar behaviour.



To the right hand-side, the **distribution of differences** between consecutive hourly values of each time-series is shown. For an hourly time-series of wind speed, U , the difference between consecutive values, Δ_{spd} , is given by:

$$\Delta_{spd}(t) = U(t) - U(t - 1\text{hour})$$

The probability (P) of all differences for each time-series is overlaid. In general, it would be expected in all cases, that the distributions would be centred around a difference of zero, but that smoother time-series would have a narrower distribution, i.e., smaller changes would be more common.

Based on review of analogous figures to Figure C.4 for all measured datasets used in this work, we have attributed a 3-hour effective averaging period to the modelled data.

C.3 Averaging Period Conversion

IEC guidelines (see section 6.4.3.1 of 61400-3-1 (2019) [20]), note that the:

long term probability distribution of mean wind speed [...] may be assumed to be independent of averaging periods in the range between 10 min and 3 h

A caveat is included, stating that the assumption may not be valid for mean wind speeds exceeding the upper limit of hub height operating wind speed range. At these high wind speeds, for example wind extremes, we would instead recommend use of the Frøya profile detailed in Section B.6.2 for such conversion.



Appendix D. Measured Currents

D.1 Introduction

This Appendix includes further details on the quality review and analysis of *measured* current datasets used in this project. It proceeds as follows:

- In Section D.2, the datasets are briefly listed for reference (see also Section 5.1)
- Section D.3 describes the quality control and review steps carried out on each dataset in turn, whilst highlighting any pertinent features which may warrant consideration through the analyses which follow.
- In Section D.4, upward and downward looking instruments at each NSI location are compared to each other.
- Thereafter, in Sections D.5 through D.7, depth-averaging and vertical profile shapes are reviewed, initially in theoretical form before proceeding through the analysis of the measurements themselves.

D.2 Dataset Overview

The measured current datasets used in this project are listed in Table D.1, and their locations shown in Figure D.1.

Table D.1: Measured datasets used for review of current profiles.

Dataset	Type	WGS84	Time Period	Water Depth [m MSL]
NSI-1	Upward and Downward-Looking Current Profilers	7.0596°E, 55.9441°N	1-Sep-2023 to 9-May-2024	31
NSI-2	Upward and Downward-Looking Current Profilers	7.6159°E, 55.8855°N	1-Sep-2023 to 9-May-2024	20
NSI-3	Upward and Downward-Looking Current Profilers	7.6347°E, 56.0694°N	1-Sep-2023 to 9-May-2024	30
EINS-1	Upward Looking Current Profiler	6.3008°E, 56.6272°N	19-Nov-2021 to 21-Mar-2022	46
EINS-2	Upward Looking Current Profiler	6.4552°E, 56.3442°N	19-Nov-2021 to 13-Jul-2022	46
EINS-3	Upward Looking Current Profiler	6.5130°E, 56.3449°N	19-Nov-2021 to 30-Nov-2022	31

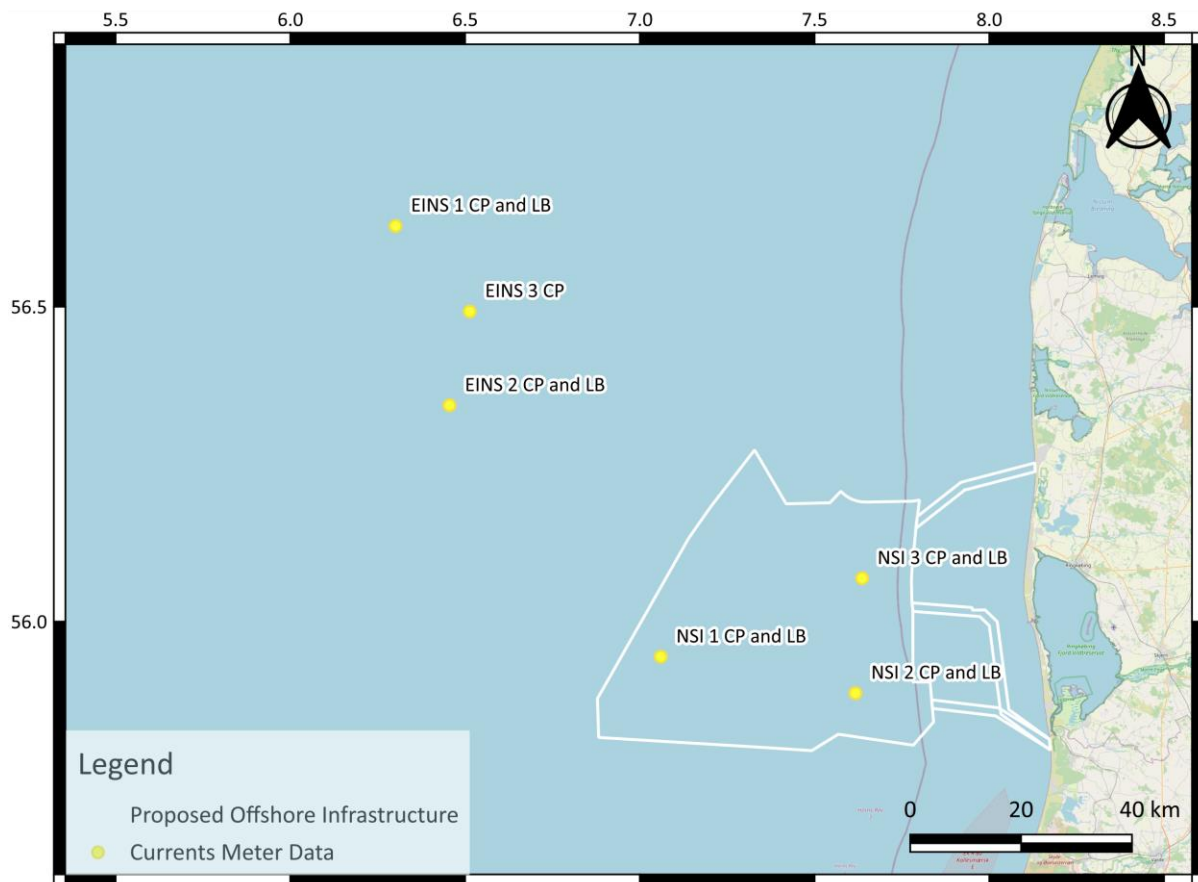


Figure D.1: Measured datasets considered for hydrodynamic model validation.

D.3 Data Quality Review

Prior to their provision to MetOceanWorks, all measured datasets were subject to quality control procedures applied by Fugro. We have subsequently manually reviewed the data as both time-series and scatter plots. No algorithmic filtering was applied; however, a number of criteria were considered during manual review. To some extent, a complete list of these criteria is impossible – there are a huge number of behaviours which, if sighted in the data, would be considered suspicious (negative speeds, very large speeds, constant derivatives, repeated patterns, etc.) – however amongst the most relevant are:

- Repeated values (including repeated zeros)
- Spikes
- Step changes
- Unexpected long-term trends
- Unexpectedly large differences between measurements at neighbouring levels



D.3.1 NSI-1-CP, NSI-2-CP and NSI-3-CP

Three upward looking Nortek Signature 500 current profilers were deployed close to the seabed at the NSI-1, NSI-2 and NSI-3 locations. In the data files provided to MetOceanWorks, their accompanying documentation, and subsequently this report, these datasets are denoted NSI-1-CP, NSI-2-CP and NSI-3-CP respectively. As outlined in “readme.txt” files provided with the data, each instrument was:

Mounted in a floating buoy resulting in a nominal depth of the transducer head at ca. 3 m above the seafloor.

All three instruments are configured to average 240 1Hz records (i.e., 4 minutes) every 10 minutes, every 1 m from a height of 4 metres to sea surface.

Quality control has been applied by Fugro. In all three cases, they note that:

Data in the remaining near-surface bins [depths vary by dataset] may periodically still be affected by sidelobe energy during rougher conditions. This can appear as spikes in the current speed data. Signal strength per beam is part of the data file and can be used to do further analysis and exclusions, if deemed necessary.

It appears, that the data in the bins near the seafloor is influenced by reflections from the seafloor when the floater is tilted. The data in the 04 and 05 m bins should be used with caution.

The motion data (heading, pitch, roll) indicates that the instrument experienced a fair bit of motion and tilt during the deployment. Averaging over the sampling interval serves as partial motion compensation. Bin mapping aligns the cells in the vertical but does not remove any motion-induced errors.

Review by MetOceanWorks is in line with these comments, and for the purposes of this project, some data has been removed from the highest and lowest bins where appropriate, but the rest of the data appears to be of good quality.

D.3.2 NSI-1-LB, NSI-2-LB and NSI-3-LB

Downward looking Nortek Signature 500 current profilers were also deployed beneath LiDAR buoys at the three NSI locations. These are denoted NSI-1-LB, NSI-2-LB and NSI-3-LB in the data files, accompanying documentation, and this report. The accompanying documentation (e.g., [21]) states that 180 seconds of 1 Hz data is averaged every 600 seconds.

As with the near bed instruments, quality control has been applied by Fugro and reviewed by MetOceanWorks; only the removal of some additional data in the highest and lowest bins considered appropriate.

D.3.3 EINS

Datasets from the further away Energy Island North Sea (EINS) site were also used for model validation. As with NSI datasets, quality control was first applied by Fugro, and then reviewed by MetOceanWorks. It should be noted that due to their more distant nature, these datasets have been treated as being of secondary importance only. In particular, they are only used for model validation, and not reviewed in detail through the remainder of this Appendix.



D.4 Dataset Comparisons

D.4.1 Current Speed and Direction

Current speed and directions for various elevations are shown for the six NSI datasets in Figure D.2 through Figure D.7.

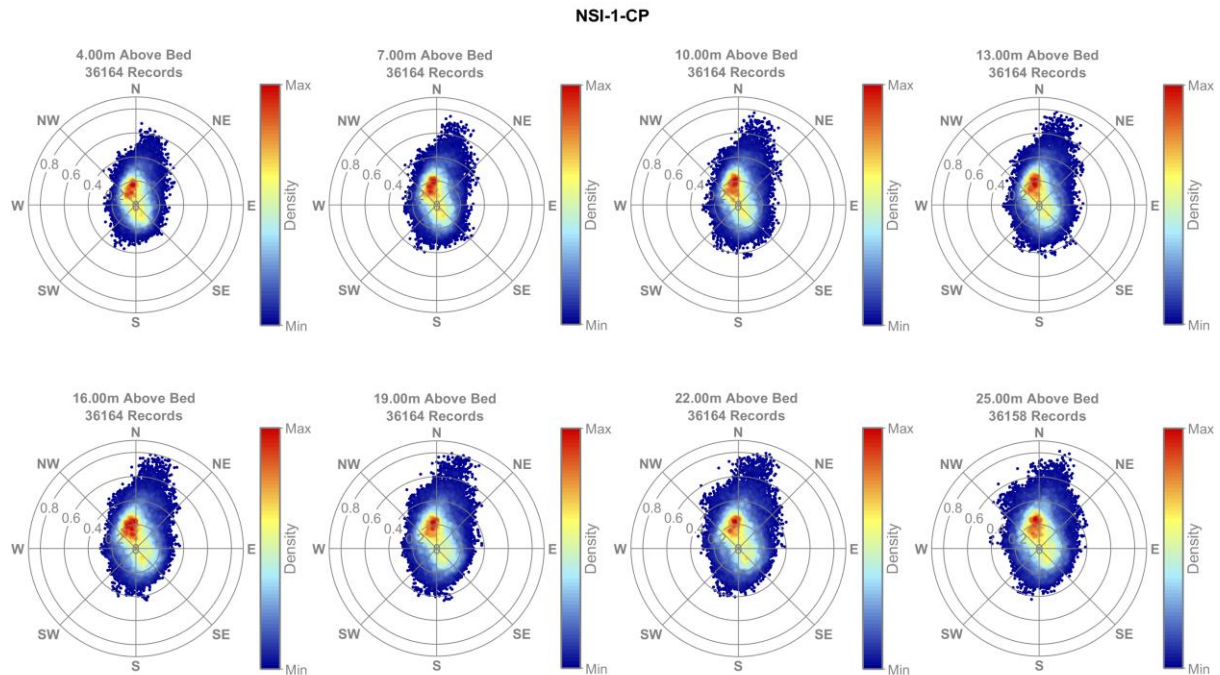


Figure D.2. Current speed and direction, NSI-1-CP.

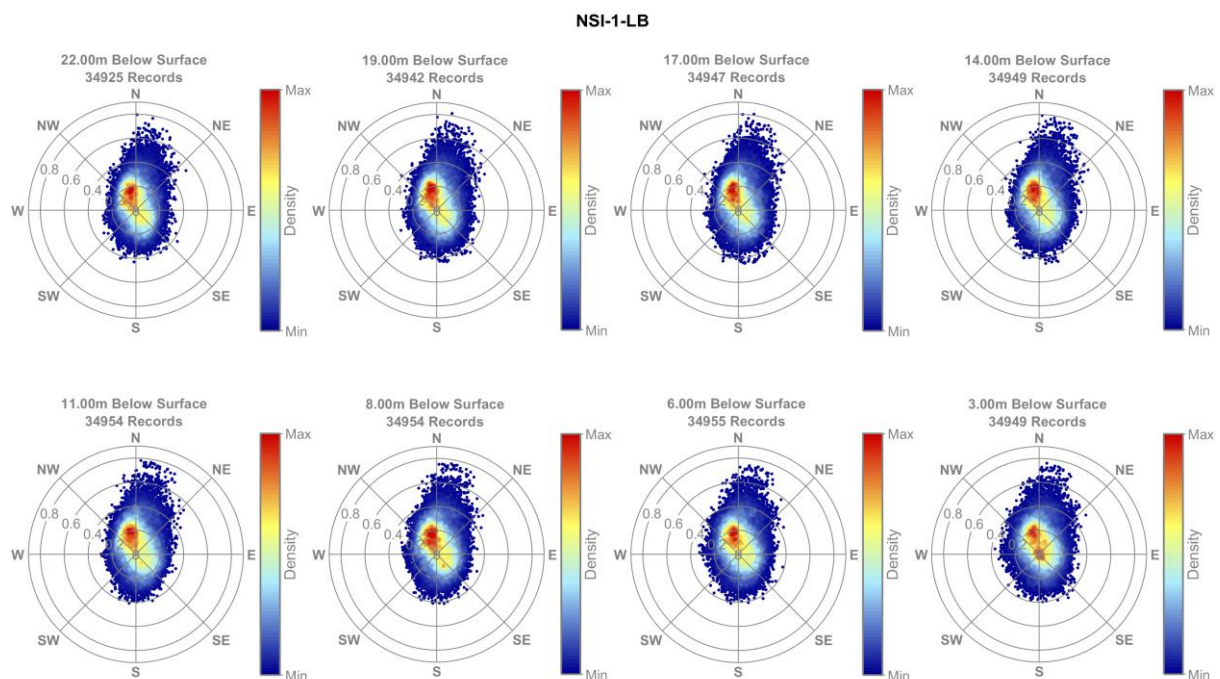


Figure D.3. Current speed and direction, NSI-1-LB.

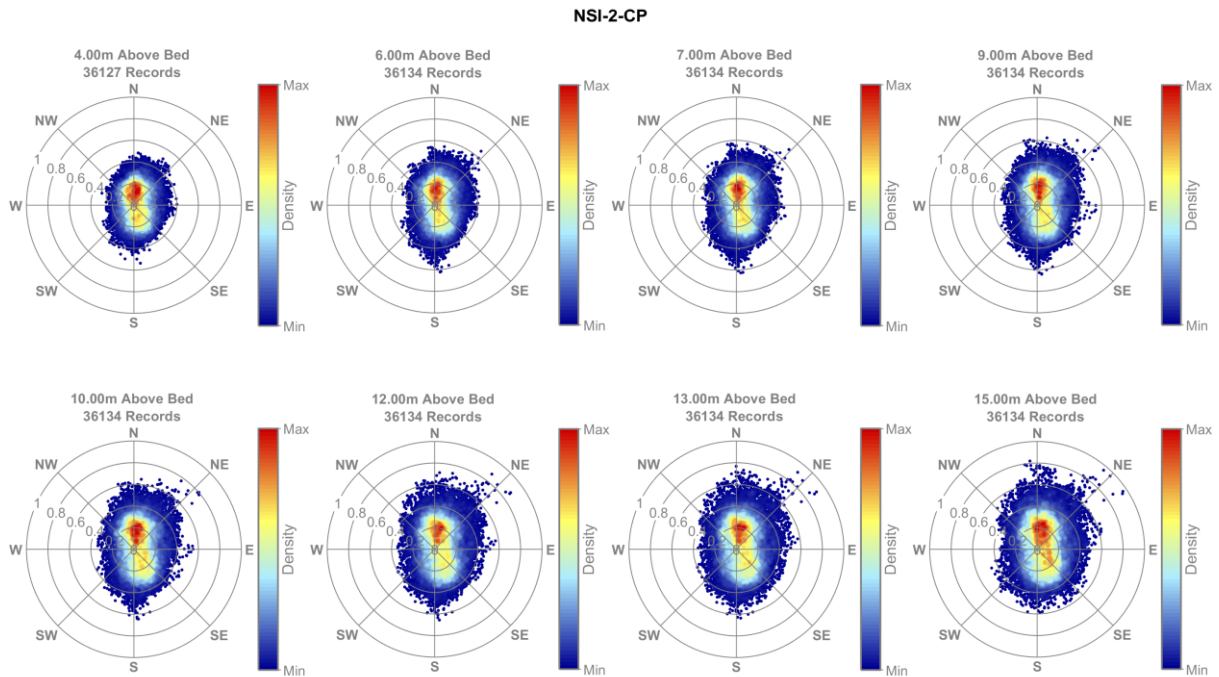


Figure D.4. Current speed and direction, NSI-2-CP.

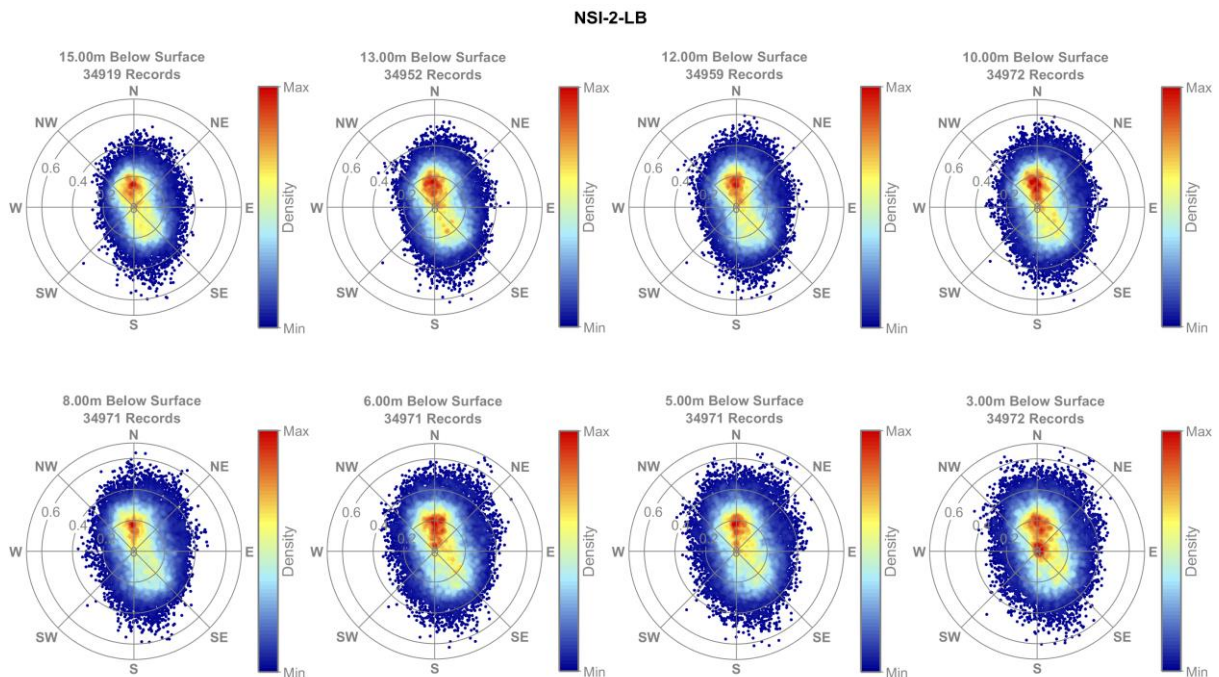


Figure D.5. Current speed and direction, NSI-2-LB.

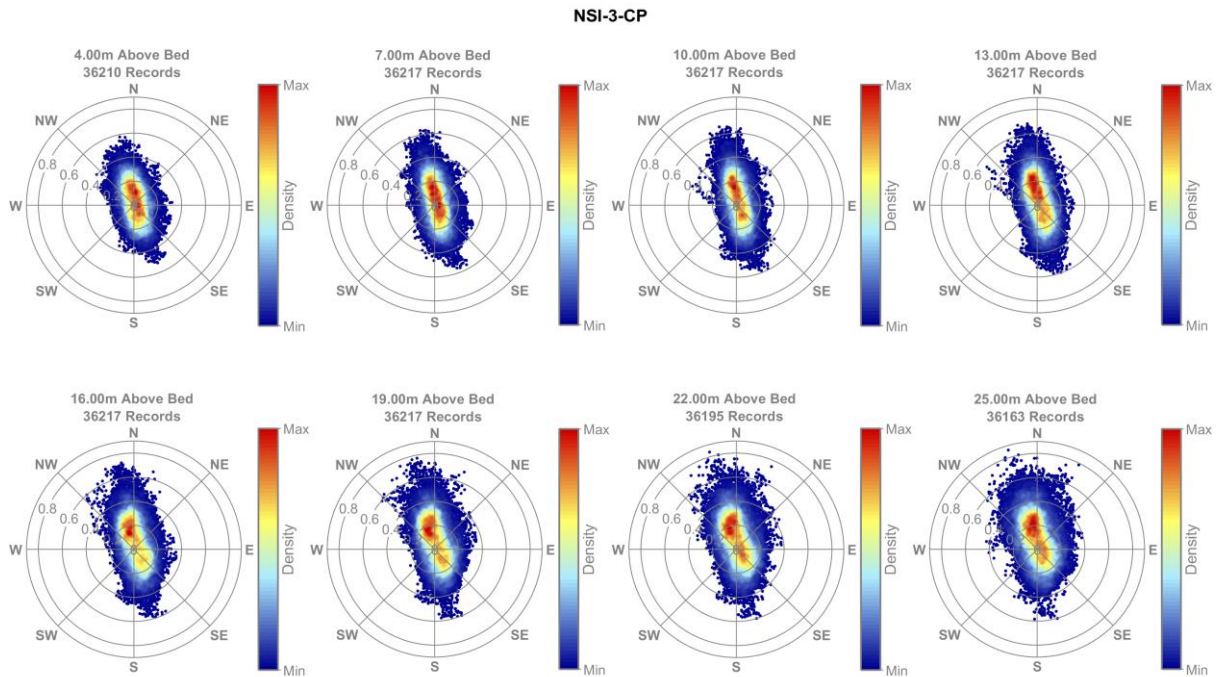


Figure D.6. Current speed and direction, NSI-3-CP.

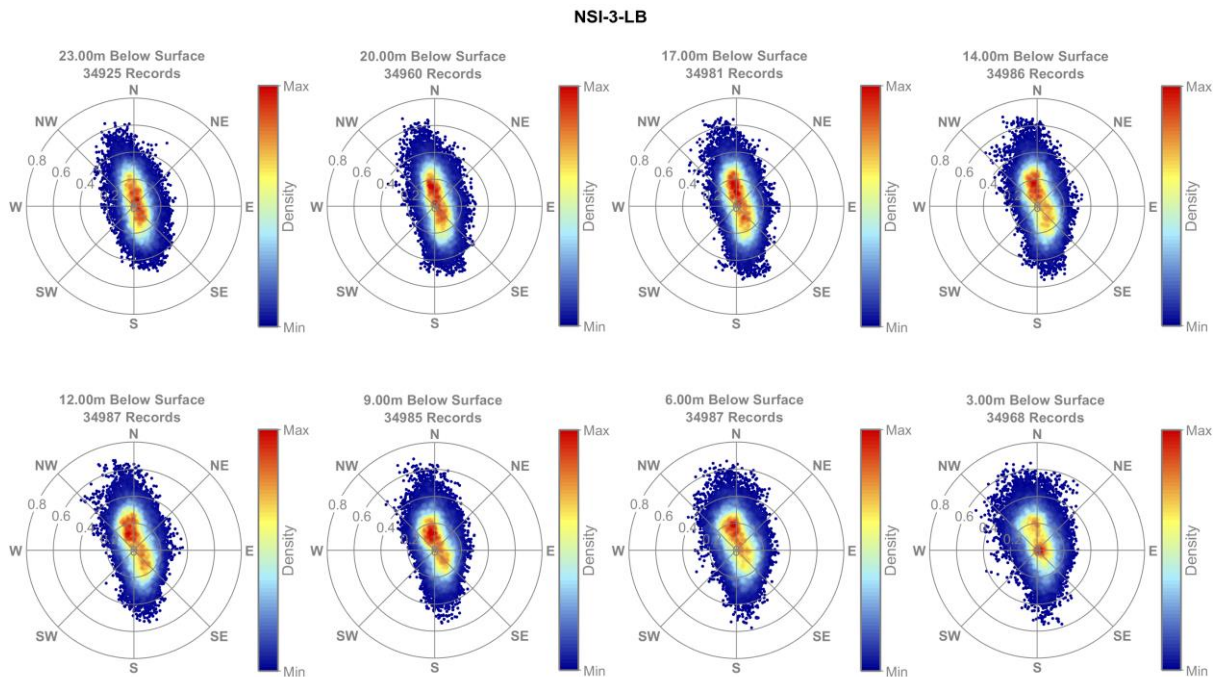


Figure D.7. Current speed and direction, NSI-3-LB.



D.4.2 Direction of Flow

Flow is generally tidally dominated and aligned along a north-south axis, as shown in Figure D.8 through Figure D.10. Directions between upward and downward looking instruments are closely matched, except at NSI-2 where an offset is apparent.

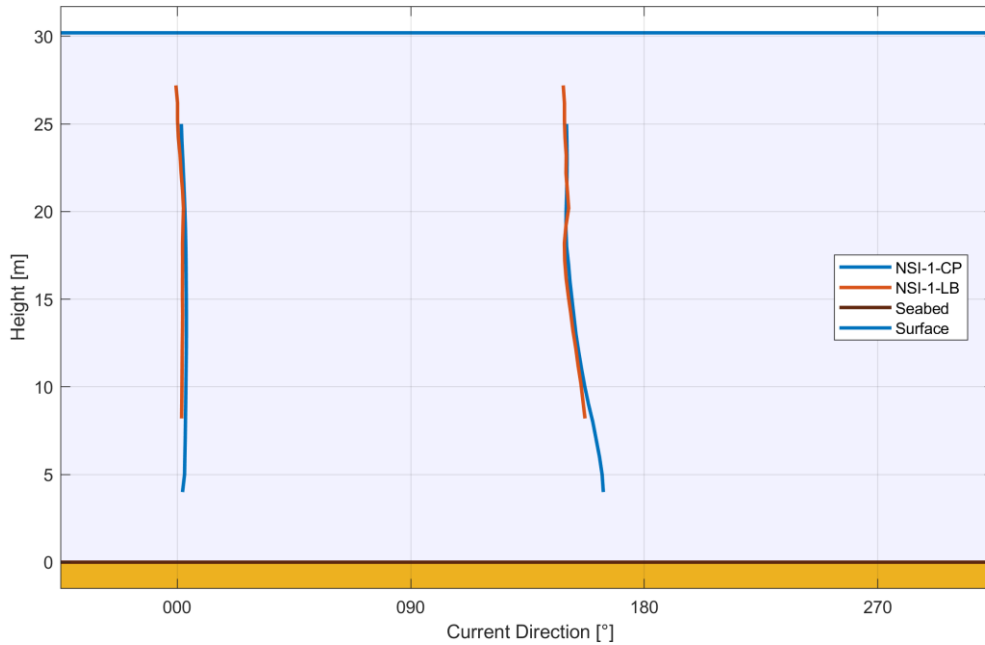


Figure D.8. Principal Flow Directions, NSI-1.

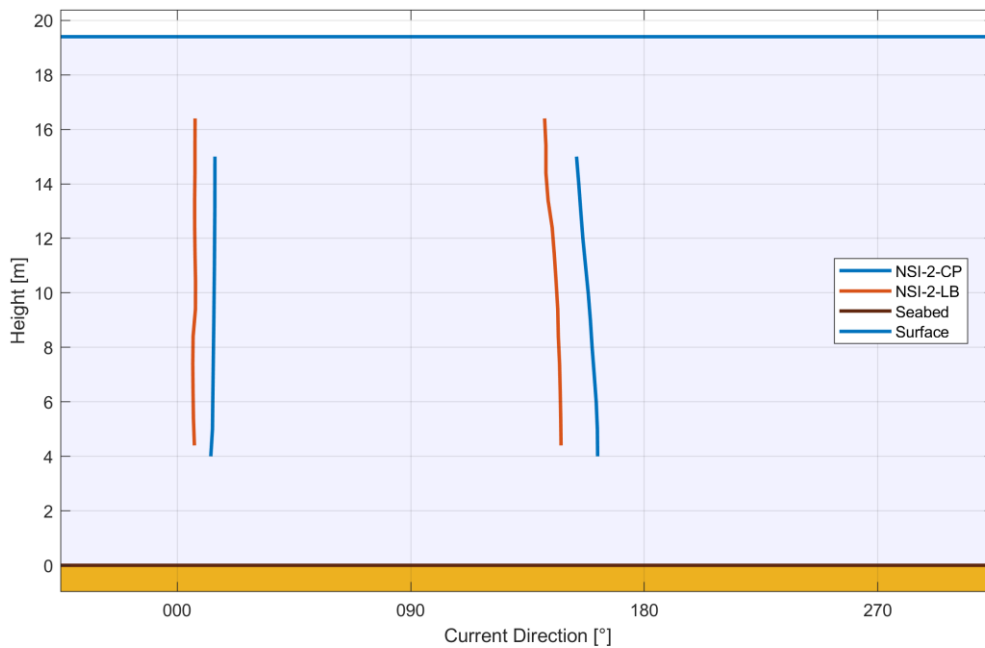


Figure D.9. Principal Flow Directions, NSI-2.

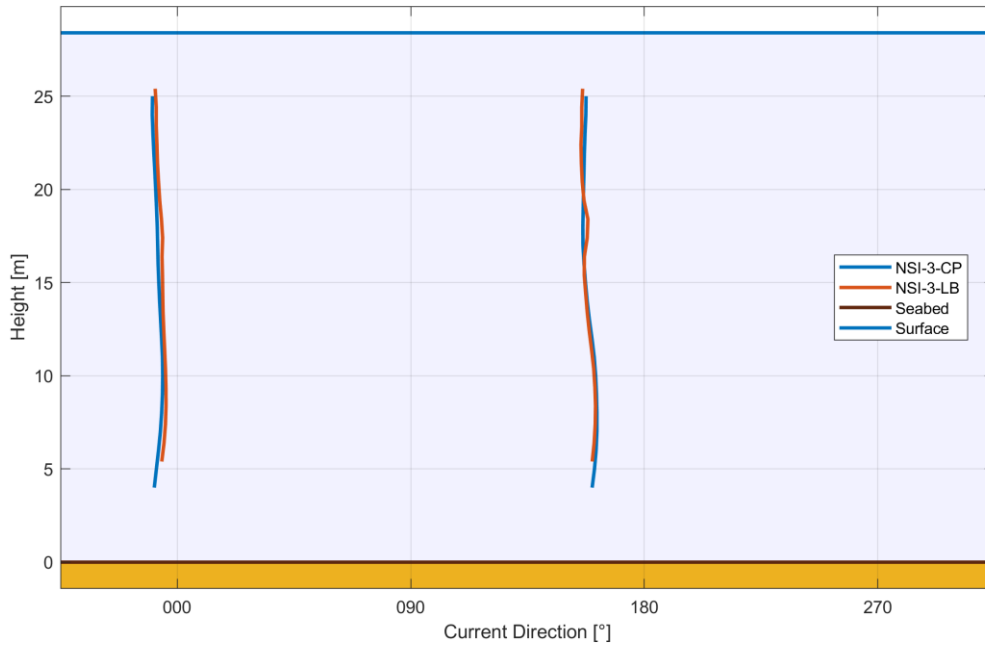


Figure D.10. Principal Flow Directions, NSI-3.



D.4.3 Current Speed Percentiles

Current speed percentiles are shown for the three locations in Figure D.11 through Figure D.13. In each case, current speeds are split along an axis midway between the two principal directions shown in the previous section. Northward flows are shown to the left, southward flows to the right. Two key behaviours are immediately apparent:

- Northward flows are stronger across all percentiles and across all locations.
- For northward flows, there are significant differences between the upward looking instruments (CP, shown with solid lines) and the downward looking instruments (LB, shown with dashed lines). Almost always, CP percentiles are higher, with perhaps the exception of maximum values at lower levels.

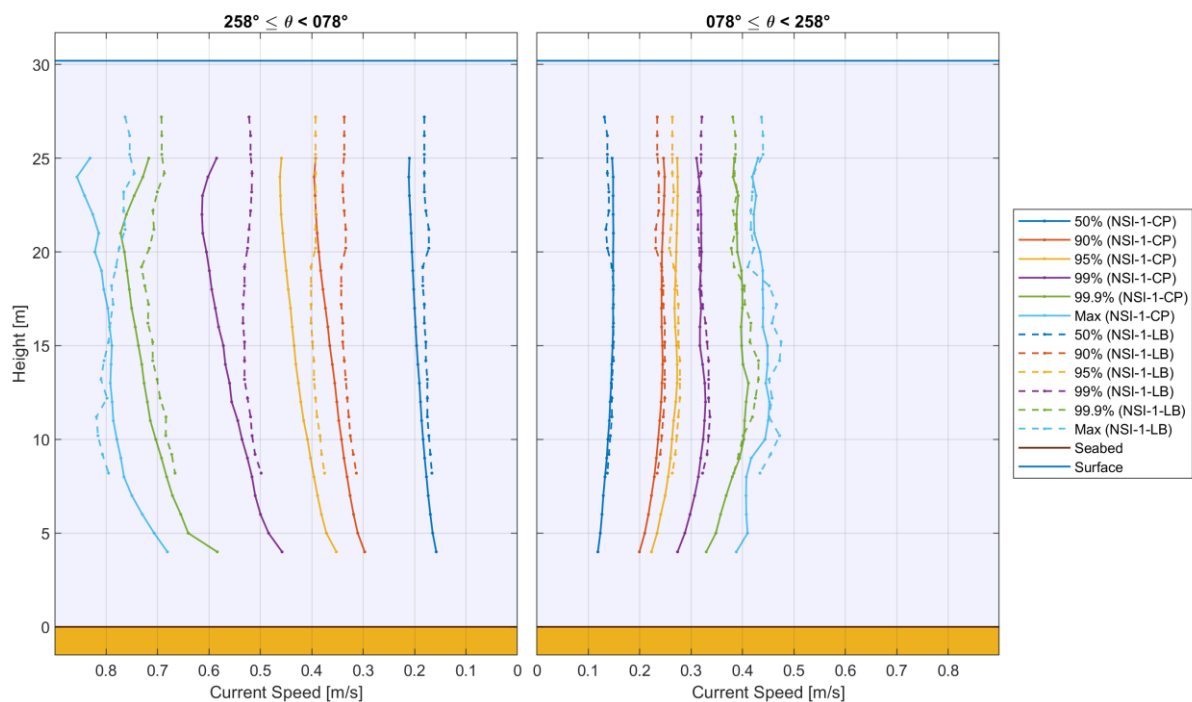


Figure D.11. Current Speed Percentiles, NSI-1.

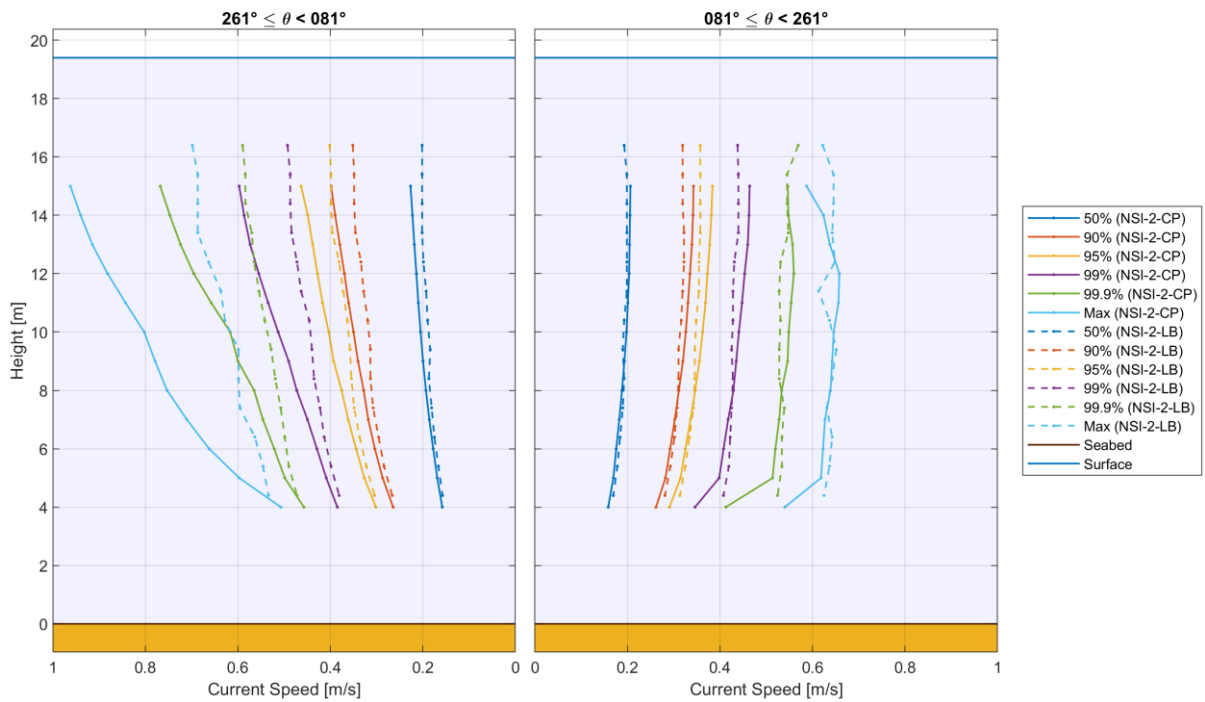


Figure D.12. Current Speed Percentiles, NSI-2.

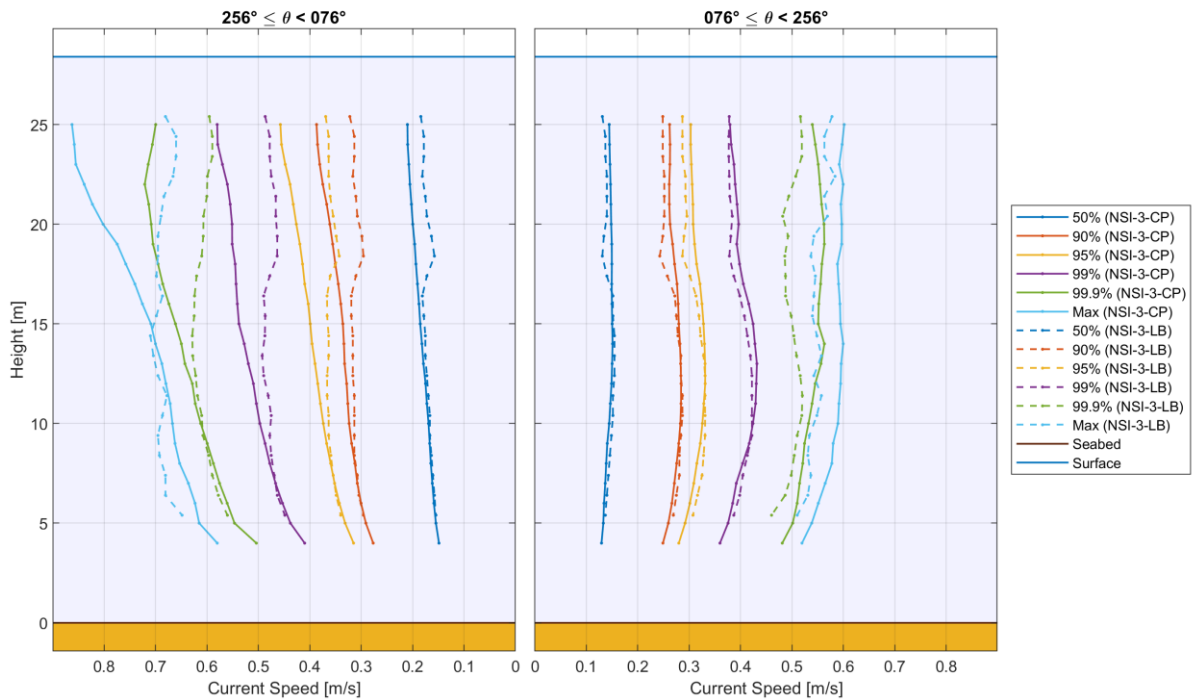


Figure D.13. Current Speed Percentiles, NSI-3.



D.4.4 Depth Averaged Current Speeds

The previous section showed significant discrepancies between current speed percentiles of the two instruments at each location. Given that one of the key model validation parameters is *depth averaged* current speed, it is worth also exploring such differences in this context. To this end, depth averages (see Section D.6 for calculation details) of NSI-1-CP are compared to those of NSI-1-LB in Figure D.14, followed by similar comparisons for NSI-2 (Figure D.15) and NSI-3 (Figure D.16). Throughout, current speeds from the near bed instrument are plotted along the x-axis and from the near surface instrument along the y-axis.

In all cases, depth average current speeds from the LiDAR buoy (LB) mounted profilers taken as a whole are significantly lower than from the corresponding near bed profiler, ranging from 5.5 % at NSI-2 to almost 10 % so at NSI-1. This is broadly in line with MetOceanWorks previous experience across such comparisons upwards looking near bed and downwards looking near surface measurements.

If water depths are split into, say, three equally sized sections – as shown in Figure D.17 through Figure D.19 – it is clear that these discrepancies exhibit large variations with depth. In the lower 1/3 of the water column (the lower plot of each figure), differences are much smaller and indeed for NSI-2 and NSI-3 data quantiles are within 1 %. As we move upwards, these differences increase and by the top 1/3 are over 14 % at both NSI-1 and NSI-3.

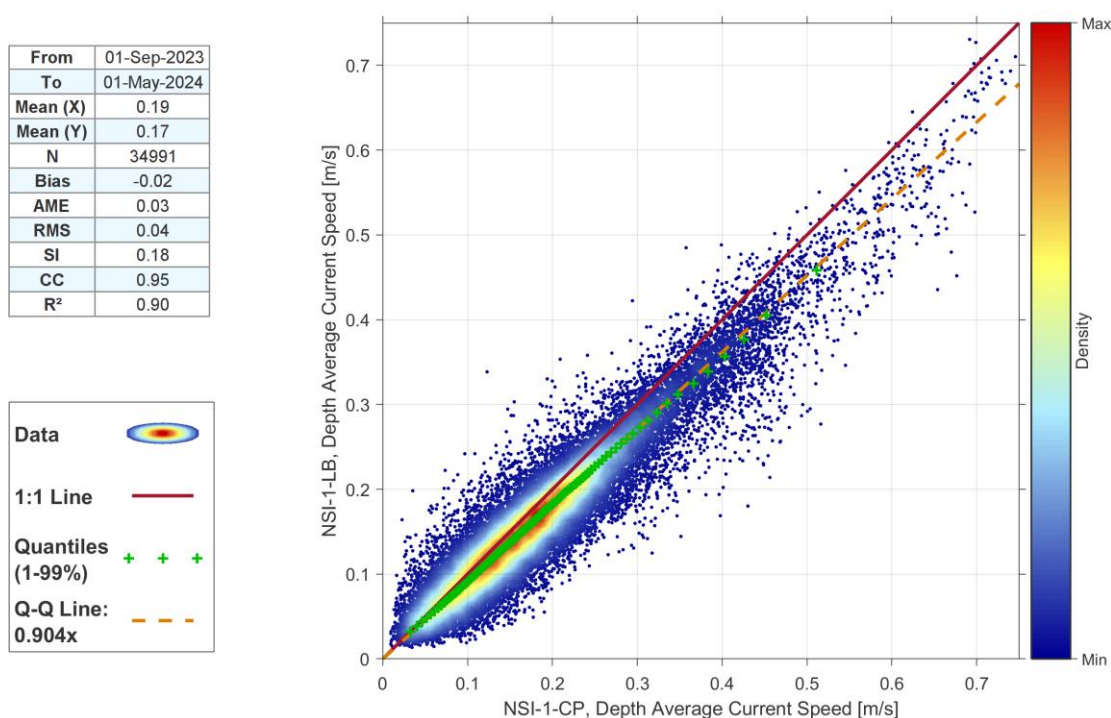
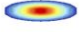




Figure D.14: Comparison of depth averaged currents, NSI-1 location.




From	01-Sep-2023
To	01-May-2024
Mean (X)	0.20
Mean (Y)	0.19
N	34992
Bias	-0.01
AME	0.03
RMS	0.04
SI	0.17
CC	0.93
R ²	0.86

Data 

1:1 Line 

Quantiles (1-99%) 

Q-Q Line: 0.945x 

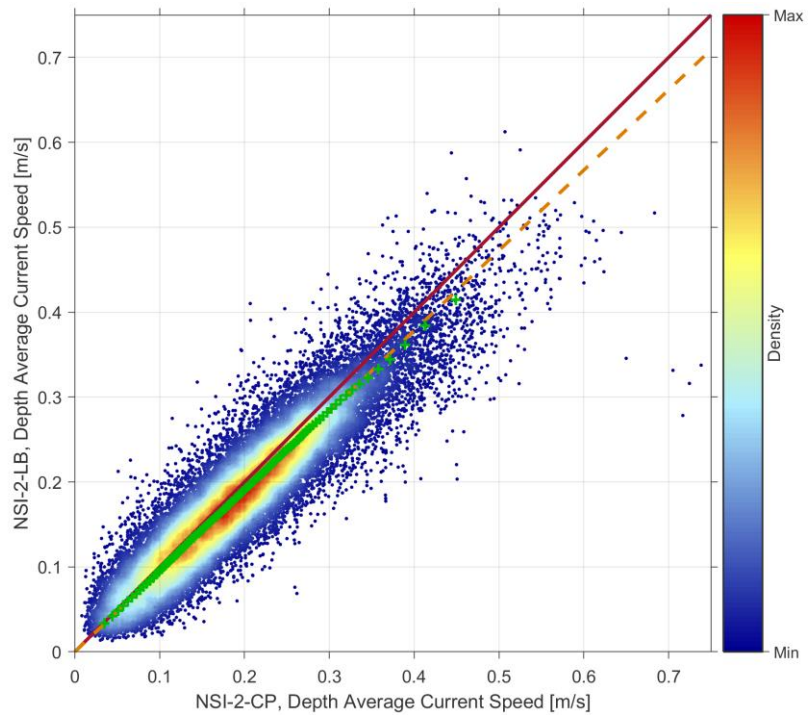
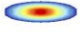





Figure D.15: Comparison of depth averaged currents, NSI-2 location.

From	01-Sep-2023
To	01-May-2024
Mean (X)	0.18
Mean (Y)	0.17
N	34992
Bias	-0.01
AME	0.02
RMS	0.03
SI	0.18
CC	0.93
R ²	0.87

Data 

1:1 Line 

Quantiles (1-99%) 

Q-Q Line: 0.929x 

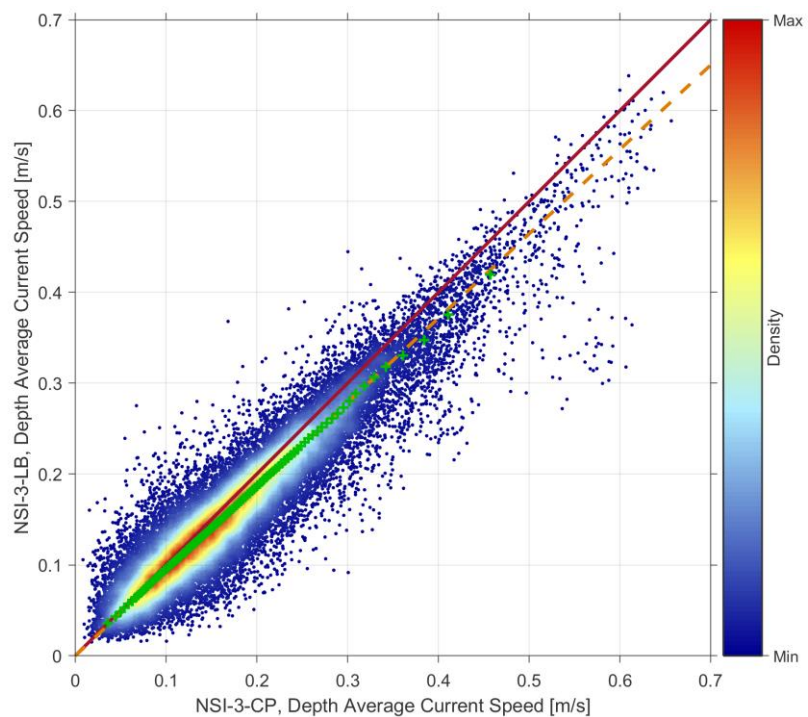
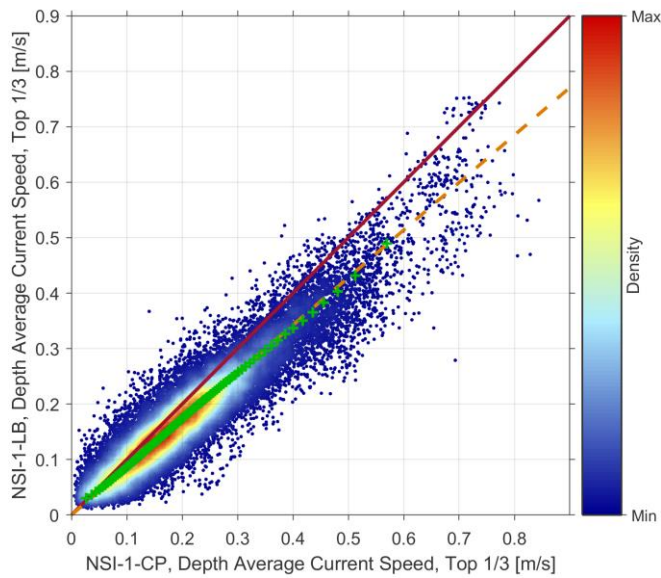


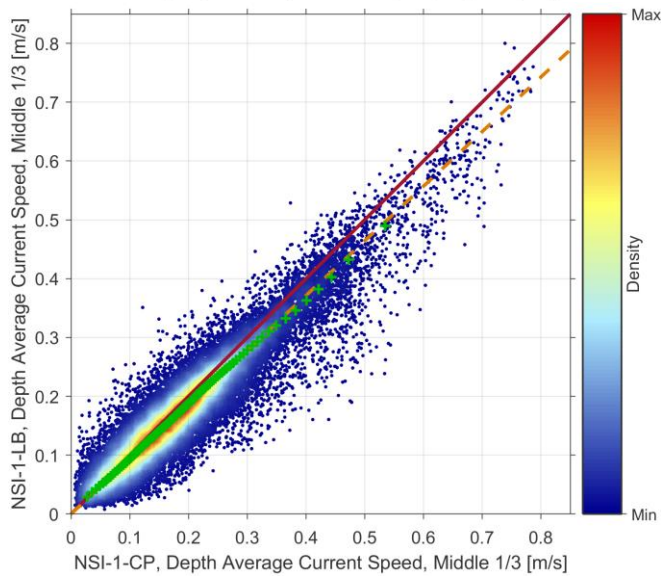
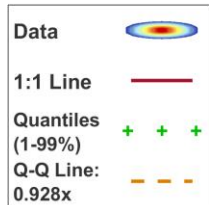
Figure D.16: Comparison of depth averaged currents, NSI-3 location.



From	01-Sep-2023
To	01-May-2024
Mean (X)	0.21
Mean (Y)	0.18
N	34991
Bias	-0.03
AME	0.04
RMS	0.05
SI	0.21
CC	0.93
R ²	0.87



From	01-Sep-2023
To	01-May-2024
Mean (X)	0.19
Mean (Y)	0.18
N	34991
Bias	-0.01
AME	0.03
RMS	0.04
SI	0.19
CC	0.94
R ²	0.88



From	01-Sep-2023
To	01-May-2024
Mean (X)	0.16
Mean (Y)	0.15
N	34981
Bias	-0.01
AME	0.02
RMS	0.03
SI	0.20
CC	0.93
R ²	0.87

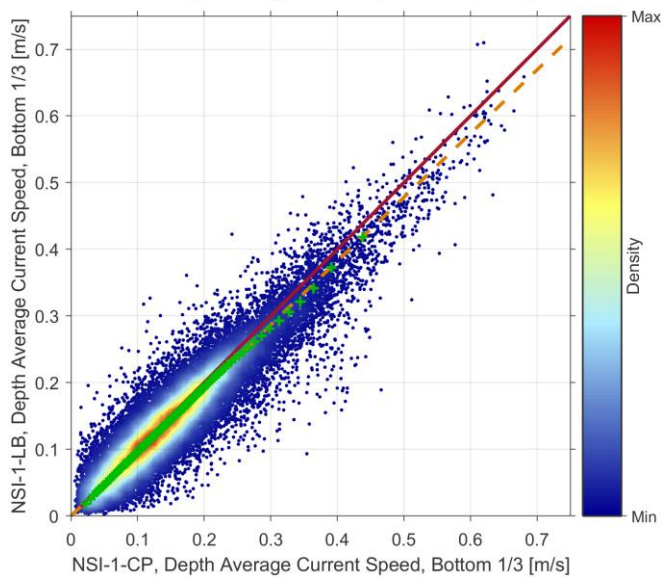
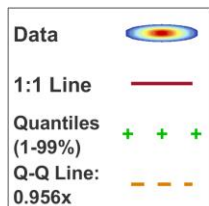
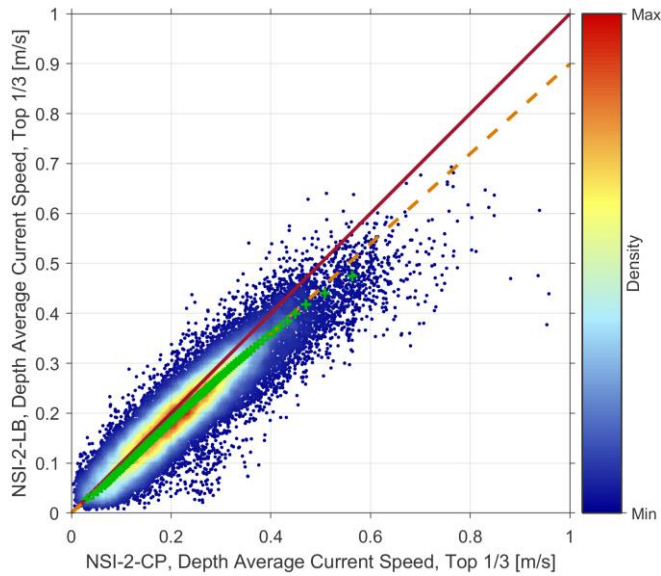
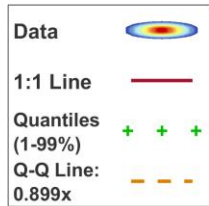


Figure D.17: Comparison of depth averaged currents split by water depth, NSI-1 location.

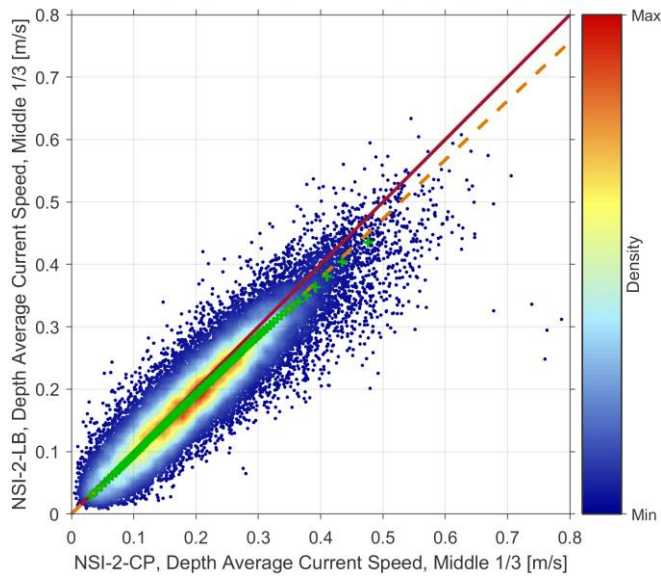
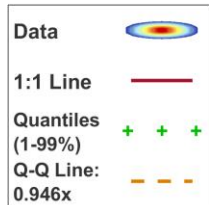


Metocean Data Overview – North Sea I Offshore Wind Farm

From	01-Sep-2023
To	01-May-2024
Mean (X)	0.23
Mean (Y)	0.21
N	34992
Bias	-0.02
AME	0.04
RMS	0.05
SI	0.19
CC	0.92
R ²	0.84



From	01-Sep-2023
To	01-May-2024
Mean (X)	0.21
Mean (Y)	0.20
N	34992
Bias	-0.01
AME	0.03
RMS	0.04
SI	0.19
CC	0.92
R ²	0.84



From	01-Sep-2023
To	01-May-2024
Mean (X)	0.16
Mean (Y)	0.16
N	34980
Bias	0.00
AME	0.03
RMS	0.04
SI	0.23
CC	0.89
R ²	0.79

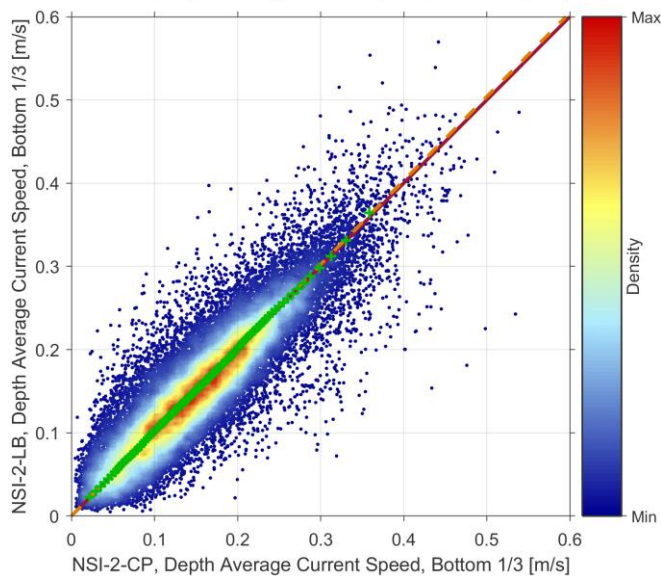
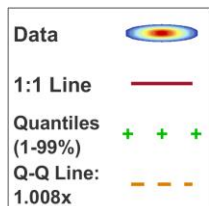
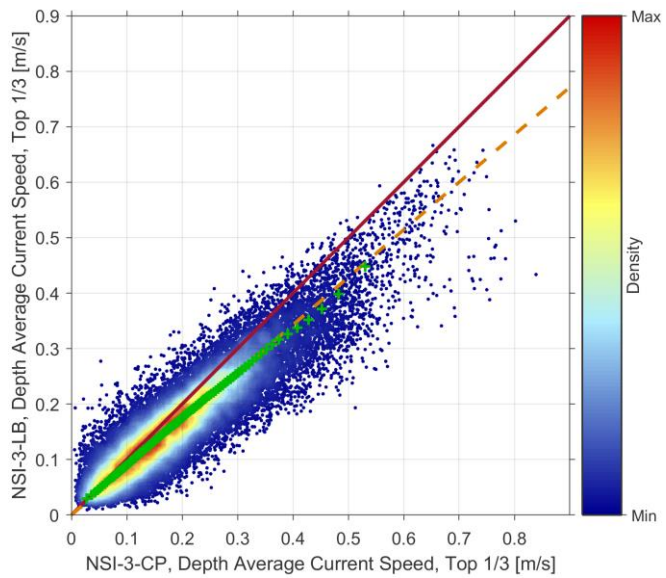


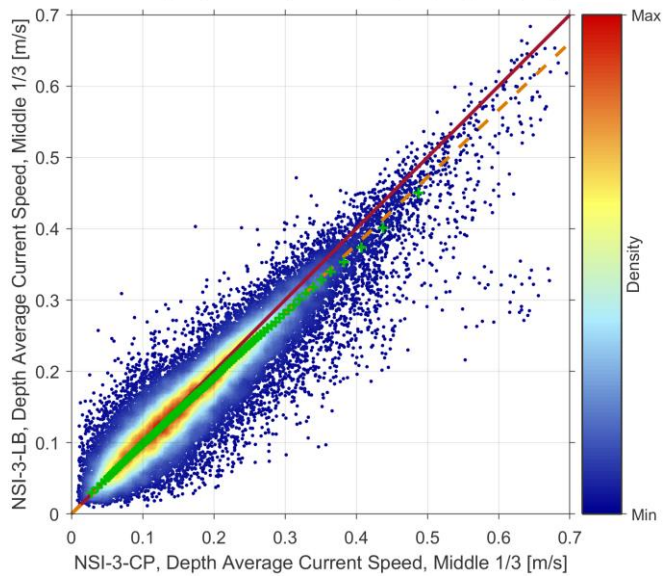
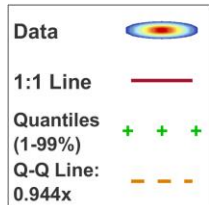
Figure D.18: Comparison of depth averaged currents split by water depth, NSI-2 location.



From	01-Sep-2023
To	01-May-2024
Mean (X)	0.20
Mean (Y)	0.17
N	34992
Bias	-0.03
AME	0.04
RMS	0.05
SI	0.24
CC	0.91
R ²	0.82



From	01-Sep-2023
To	01-May-2024
Mean (X)	0.18
Mean (Y)	0.17
N	34992
Bias	-0.01
AME	0.03
RMS	0.04
SI	0.21
CC	0.93
R ²	0.86



From	01-Sep-2023
To	01-May-2024
Mean (X)	0.15
Mean (Y)	0.15
N	34988
Bias	0.00
AME	0.02
RMS	0.03
SI	0.22
CC	0.92
R ²	0.85

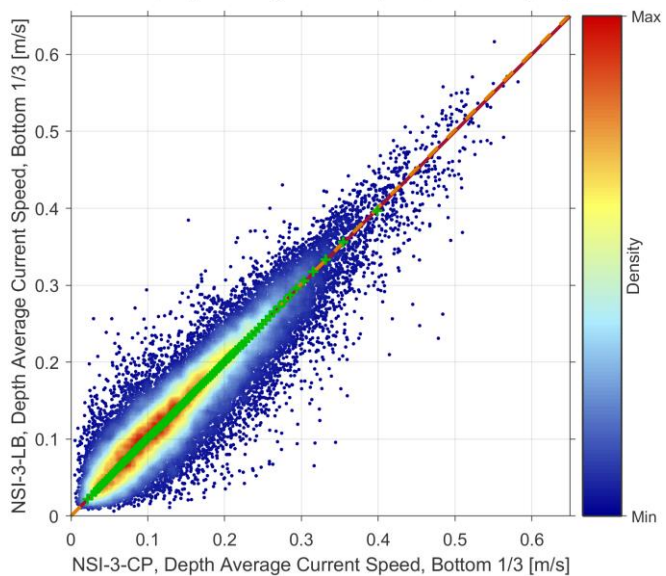
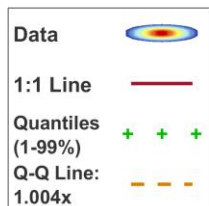


Figure D.19: Comparison of depth averaged currents split by water depth, NSI-3 location.



D.4.5 Summary

As seen through the previous sections, there are notable differences between measurements from the near bed (CP) and near surface (LB) instruments for all three NSI locations. Without further investigation, it is not immediately apparent which might be considered “best”. Instruments at the surface would likely be impacted more by winds and waves – and indeed stronger currents – though with compensation for such movements incorporated into their measurement processes. Perhaps the most unexpected feature in both NSI-1-LB and NSI-3-LB is a notable “kink” in current speeds approximately 10 metres below the surface. As seen, for example at lower percentiles in Figure D.13 (duplicated below as Figure D.20 for convenience), LB speeds decrease with depth until approximately 18 metres above bed, at which point they increase, or remain relatively constant until matching percentiles for the CP measurements at lower depths.

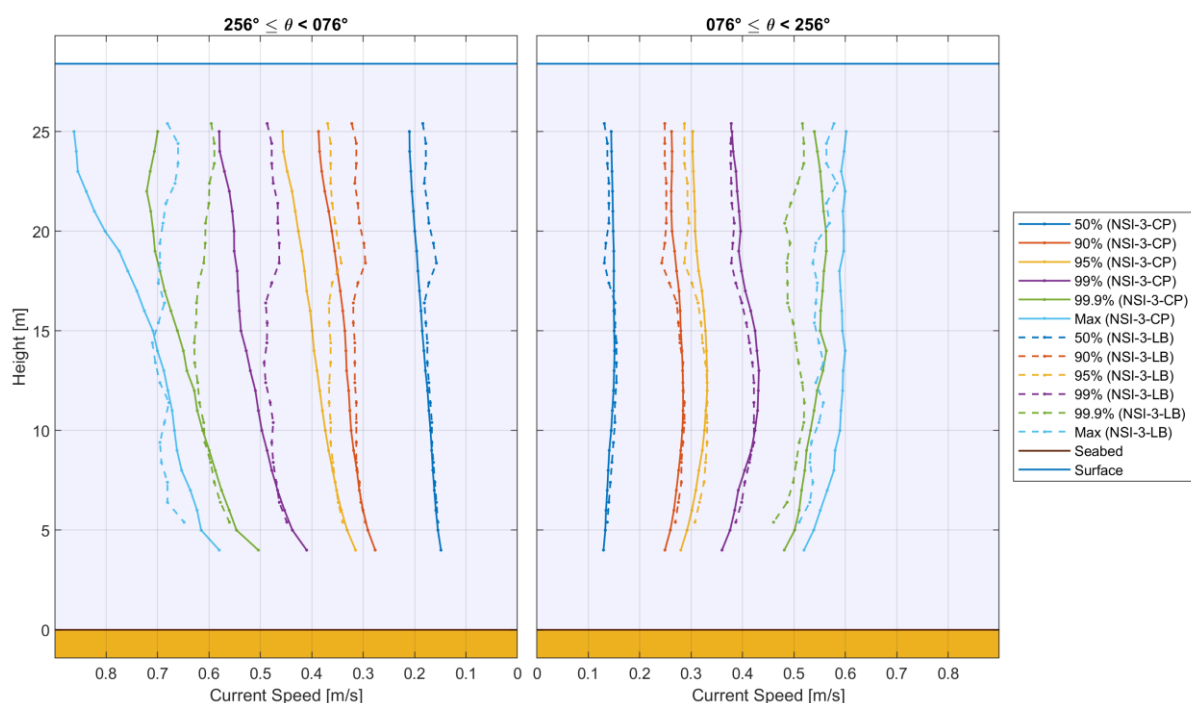


Figure D.20. Current Speed Percentiles, NSI-3.

Given the uncertainty such discrepancies create, and the impossibility of good model validations against two instruments in the *same* location which differ by almost 10% in some cases, for this work we have taken the more conservative approach of prioritising the near-bed upward looking (CP) measurements throughout.



D.5 Vertical Profile Shapes: Metocean Guidelines

As discussed in Section 5.7, *depth averaged* currents have been modelled for this project. To create a representation of currents across the full water column, these must be combined with a suitable description of variations in the vertical. In the sections which follow, two uses of the measurements are considered:

- Calculation of *measured* depth averages for model validation (see Section D.6).
- Vertical variations in the measurements are reviewed with a view to providing recommendations to describe such variations for both operational and extreme conditions (see Section D.7).

Throughout, based on the analyses of the previous section, only measurements from the upward looking near-bed instruments are used.

D.5.1 Power Law Profile

Before proceeding to analyse the measurements, it is first useful to summarize theoretical descriptions of vertical variations as given in pertinent metocean guidelines. ISO guidelines (ISO 19901-1, [19]) state that:

Typically, shallow water current profiles in which tides are dominant can often be characterized by simple power laws of velocity versus depth, whereas deep-water profiles are more complex and can even show reversals of the current direction with depth.

In this context, the sites of interest would generally be considered “shallow water” where “tides are dominant”. For such locations, the guidelines go on to specify that:

The power law current profile [as given below] can be used where appropriate (e.g. in areas dominated by tidal currents in relatively shallow water)

With an equation as follows:

$$v_c(z) = v_c(0) \left(\frac{d+z}{d} \right)^\alpha$$

Where:

z = the distance from still water level, positive *upwards*

$v_c(z)$ = the current speed at elevation z (hence $v_c(0)$ is the current speed at the surface)

d = the water depth to still water level (taken positive)

α = the exponent, which the ISO guidelines state is “typically 1/7”.



D.5.2 Wind Driven Currents

IEC guidelines (IEC 61400-3-1, [20]) and DNV guidelines (DNVGL-ST-0437, [22]) follow a similar format, though with two key differences:

- A value of 1/7 is specifically included in the equation in place of the exponent α .
- A second term is added to represent wind-generated currents.

If we denote this as, $v_{c,wind}$, then the general form is given by:

$$v_{c,wind}(z) = \begin{cases} kU \left(\frac{d_0 + z}{d_0} \right) & \text{for } -d_0 \leq z \leq 0 \\ 0 & \text{for } z < -d_0 \end{cases}$$

Where:

- d_0 is a reference depth at which the wind driven current becomes zero.
- U is the wind velocity at 10m (IEC 61400-3-1 specifically states that the wind-generated sea surface current velocity may be assumed to be aligned with the wind direction).
- k is an input parameter.

Despite the similarity between the guidelines, more precise definitions of the individual parameters show significant differences, as shown in Table D.2.

Table D.2: Wind driven current parameters.

Parameter	IEC 61400-3-1	DNVGL-ST-0437
d_0	20 m	50 m
U	1-hour mean value of wind speed at 10 m height above still water level	10-minute mean wind speed at 10 m height
k	0.01	0.016 to 0.033

These differences lead to a substantial range of possible wind-driven currents. For example, a 1-hour mean wind speed of 20 m/s at a height of 10 m would lead to a wind driven surface current speed of 0.2 m/s by the IEC guidelines. Alternatively, a 10-minute mean wind speed of 20 m/s at a height of 10 m would lead to a wind driven surface current between 0.32 m/s and 0.66 m/s according to the DNV guidelines. Further, the parameters from DNV-GL-0437 lead to non-zero wind driven current speeds much further down the water column: at 20 m depth, where IEC 61400-3-1 has zero wind driven current, DNV-GL-0437 still has 60 % of the surface value.



D.6 Depth Averages

Prior to investigating profile shapes themselves, it is first worth considering how *depth averages* are calculated from measurements. Various options might be considered, which we will describe using the somewhat arbitrarily selected set of measurements shown in Figure D.21.

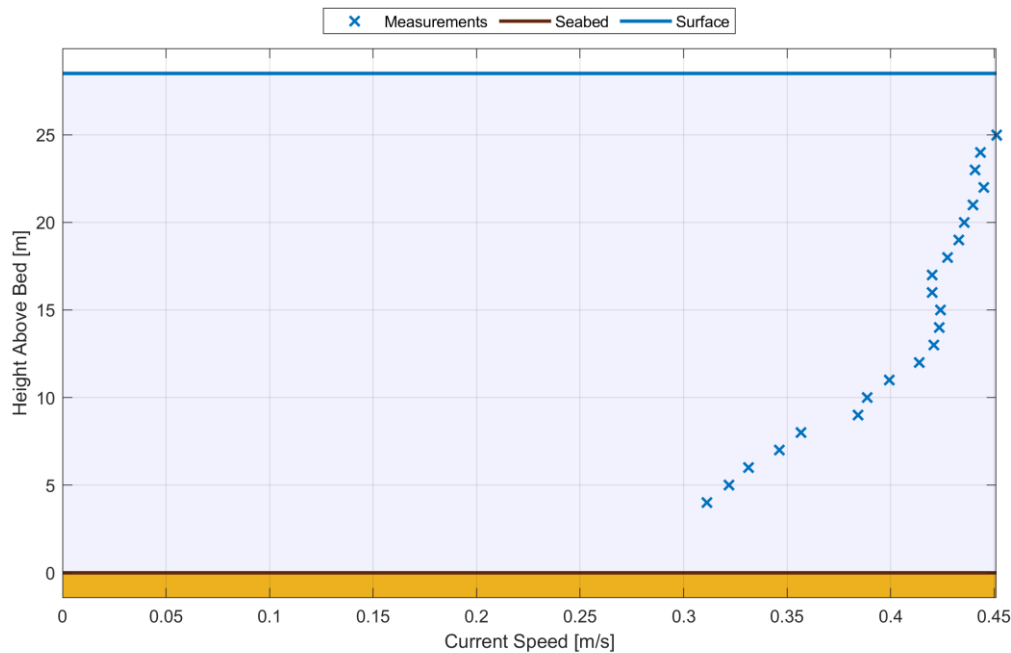


Figure D.21. Depth Averaging (1).

Perhaps the simplest option is to average the measurements themselves, in our case yielding a value of 40 cm/s. Though straightforward, such a calculation does not account for the absence of measurements very close to the sea bed, which would be expected to be lower, and those nearer the surface, would be expected to be higher.

An alternative option is to fit a theoretical profile to the data, such as a power law profile as outlined in Section D.5.1, then take the average from the *fitted profile*. Such fits are shown for our example in Figure D.22, with the profile for a fixed exponent of 1/7 shown in red, and for the best fit exponent of 1/5 shown in yellow. Indeed, use of such a theoretical shape is often simplified further to treat speeds at a height of 40 % of water depth as being representative of depth average, based on theoretical values for the power law profile.

Such options allow for behaviour above and below the measurements, but may not well-account for more complex features in the measurements themselves. To this end, for this project we take the following two stage approach with a view to finding a suitable balance between variations in the measurements and expected behaviour outside their range:

- The depth mean of the measurements is found by assigning the speed at each level to a full bin width and averaging (see left hand side of Figure D.23)
- For a theoretical 1/7 power law profile, the ratio between the mean of the full profile (red and green lines to the right of Figure D.23) and the mean across the measurement range (red line only) is determined, and the depth mean from a) scaled accordingly.

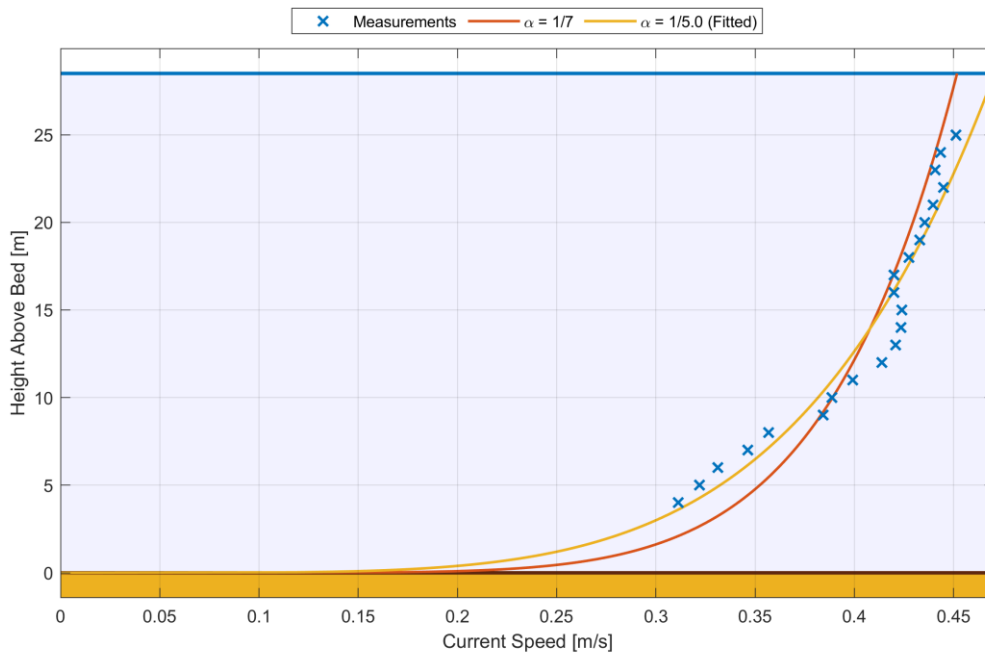


Figure D.22. Depth Averaging (2).

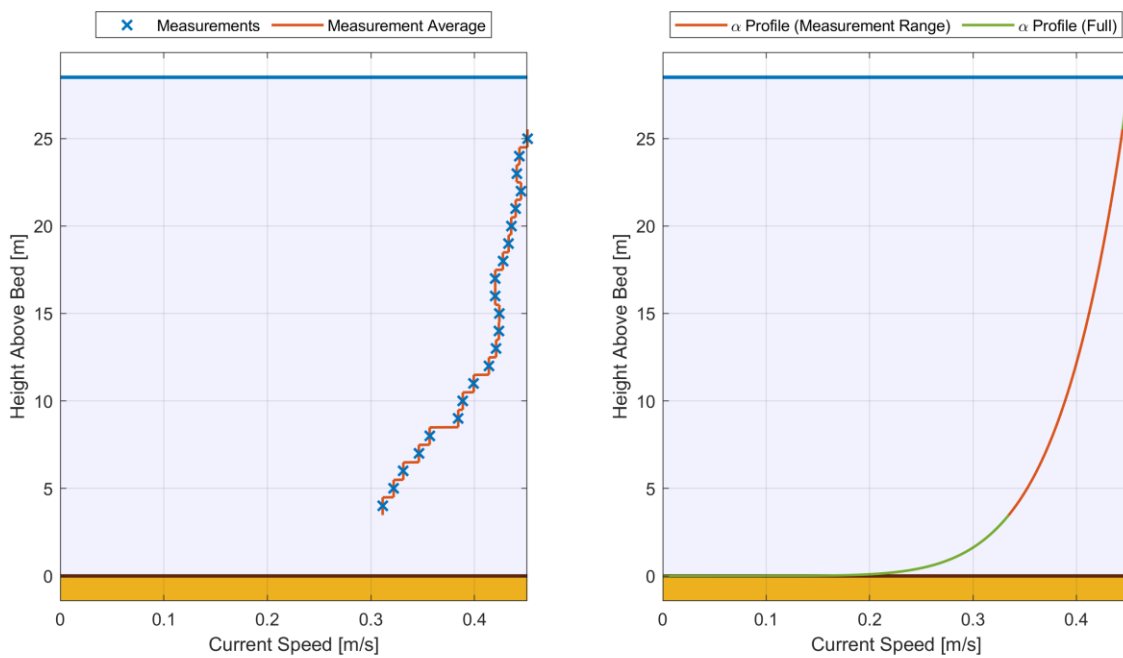


Figure D.23. Depth Averaging (3).



Metocean Data Overview – North Sea I Offshore Wind Farm

It is perhaps worth noting that for our example, the various methods make only approximately 2 % difference. Indeed, this would generally be expected to be the case for most of the data on this project, given that measurements span most of the water column, and on the whole are well represented by power law profiles. Indeed, by way of example, Figure D.24, shows a depth average from the ratio based method used in this project along the x-axis, and the best fitting power law profile for the full set of NSI-1-CP measurements. As a result, we would not expect the validation plots to be significantly impacted by the choice of depth averaging method.

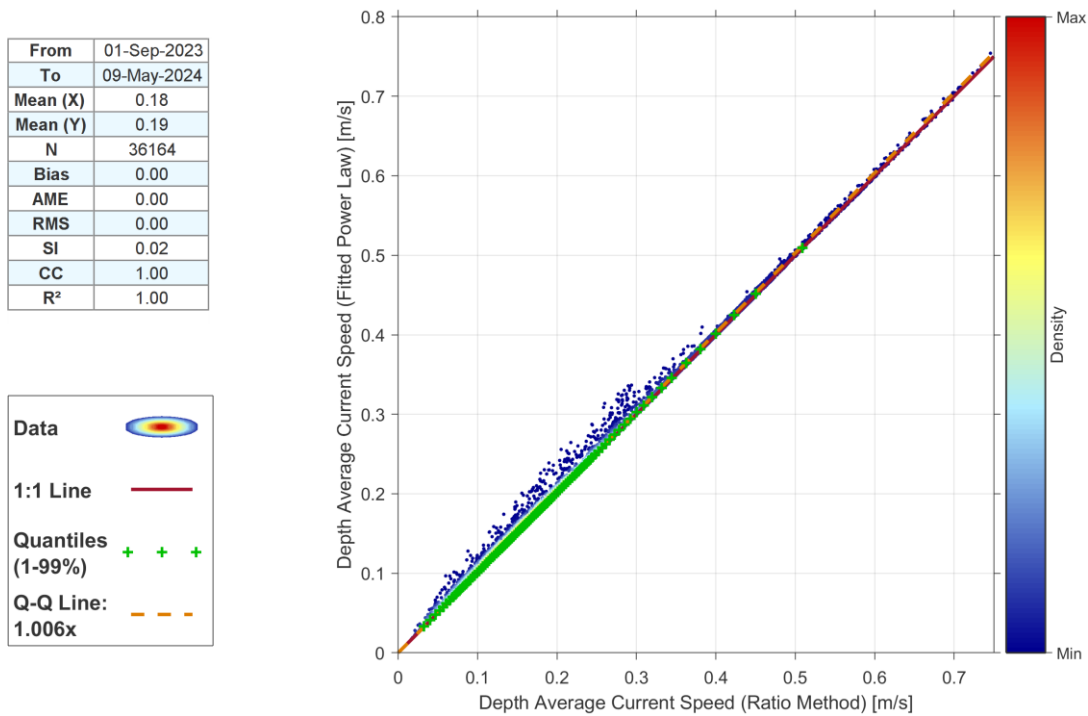


Figure D.24. Depth averaging using ratio method compared to best power law fit, NSI-1-CP.



D.7 Vertical Profile Shapes

D.7.1 Power Law Profile

We now turn our attention to the vertical shapes of profiles, initially considering only the power law profile as described in Section D.5.1. To this end, the power law exponent, α , fitted independently to each profile is plotted against depth averaged current speed for NSI-1-CP in Figure D.25. Overlaid are:

- Statistics (mean as well as 10th, 50th and 90th percentiles) calculated on moving depth average bins of 5 cm/s width.
- Commonly used α values as horizontal lines.

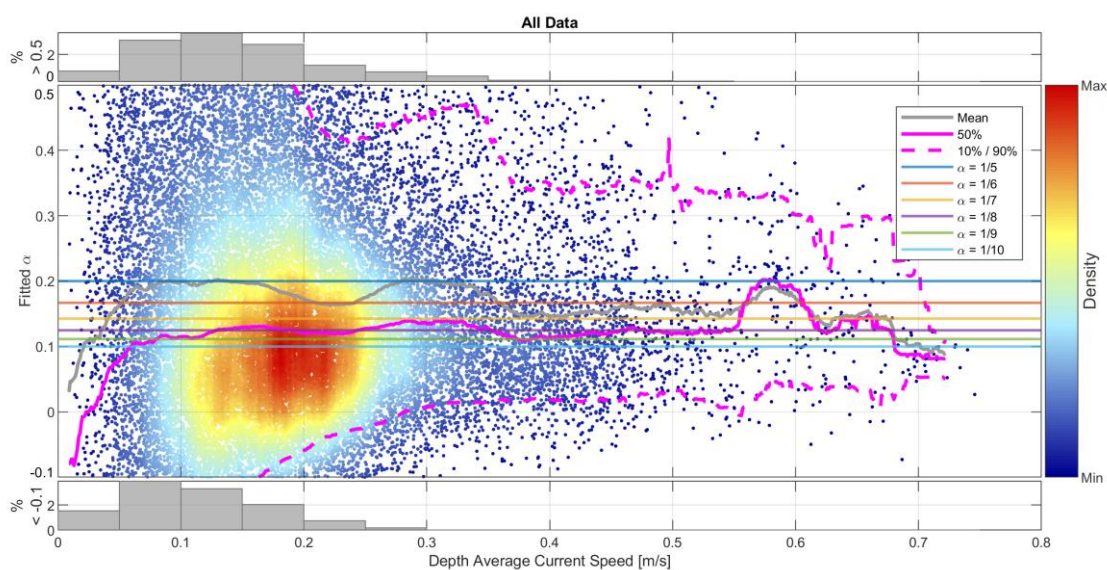


Figure D.25. Power law exponent versus depth averaged current speed, NSI-1-CP, all data.

At lower current speeds, a wide range of exponents are seen, including a significant number of *negative* α values, denoting that current speeds *increase* with depth. At higher speeds, the range of values narrows, with mean α generally between 1/6 and 1/7 and the 50 % close to 1/8 for much of the range, dropping further still at the very highest speeds.

To examine these higher current speeds further, Figure D.26 shows a histogram of all α values corresponding to depth averaged current speeds greater than the 99th percentile (0.51 m/s). Overlaid is a smoothed density estimate of the distribution, with its mode value of 1/9.35 highlighted as well as the commonly used exponent of 1/7.

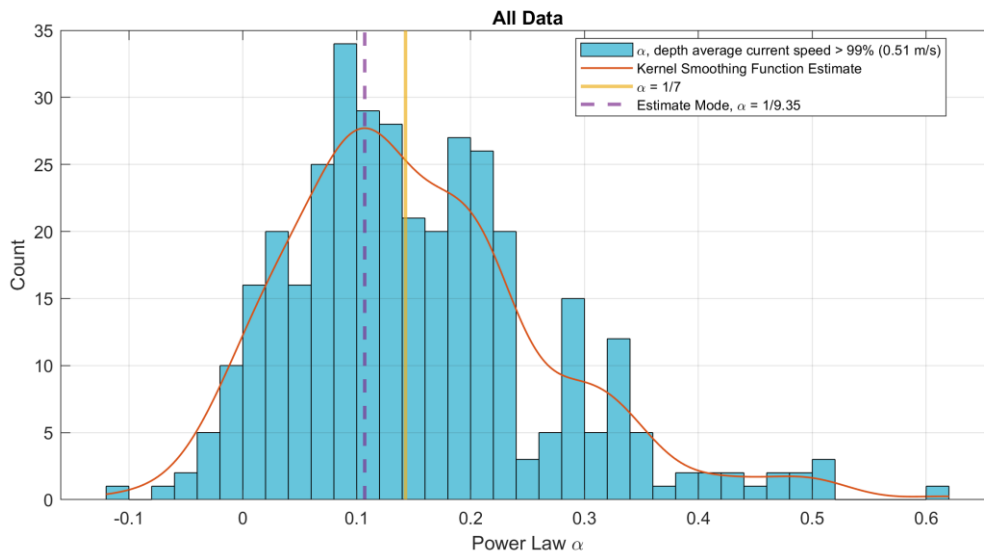


Figure D.26. Power law exponent, depth averaged current speeds > 99th percentile, NSI-1-CP, all data.

We saw previously that there are significant differences between northward and southward flows, and this is seen also when considering exponents. Figure D.27 shows flows for northward flows. For the sake of this project, this is taken to be those profiles where all elevations below 80 % of the water depth are from the 180° sector closest to the northernmost principal direction. Figure D.27 is not too dissimilar to the “All Data” case seen previously, though it is notable that central statistics are more stable through lower current speeds.

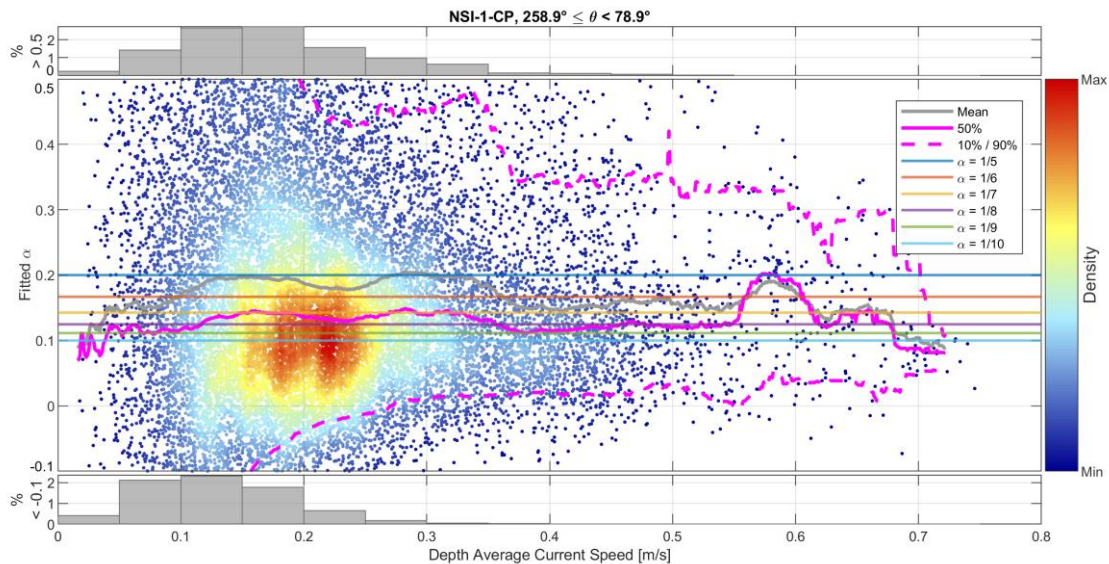


Figure D.27. Power law exponent versus depth averaged current speed, NSI-1-CP, northward flows.

Southward flows – with an analogous definition for this work – are shown in Figure D.28. Here, α values are consistently lower, representative of a more slab like profile with less variation in speed across the water column.

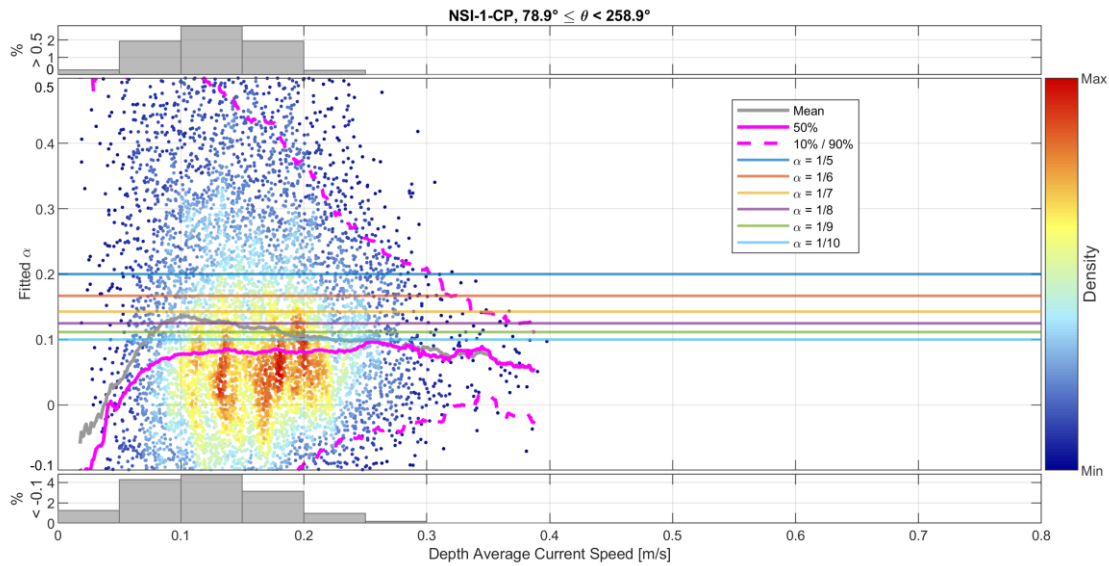


Figure D.28. Power law exponent versus depth averaged current speed, NSI-1-CP, southward flows.

The definitions used for “northward” and “southward” flows also require a third category, that of a “mixed” profile where currents at some levels travel northwards and some southwards. These generally correspond to small depth averaged current speeds and occur either when wind driven surface currents oppose smaller tidal flows, or due to relatively minor changes in tidal behaviour with depth (discussed further in Section D.7.3). Such mixed profiles are shown for the three NSI locations in Figure D.29. Given the relatively low current speeds seen, we do not focus further on these flows (with the exception of Section D.7.3) and instead concentrate only on the northward and southward categories.

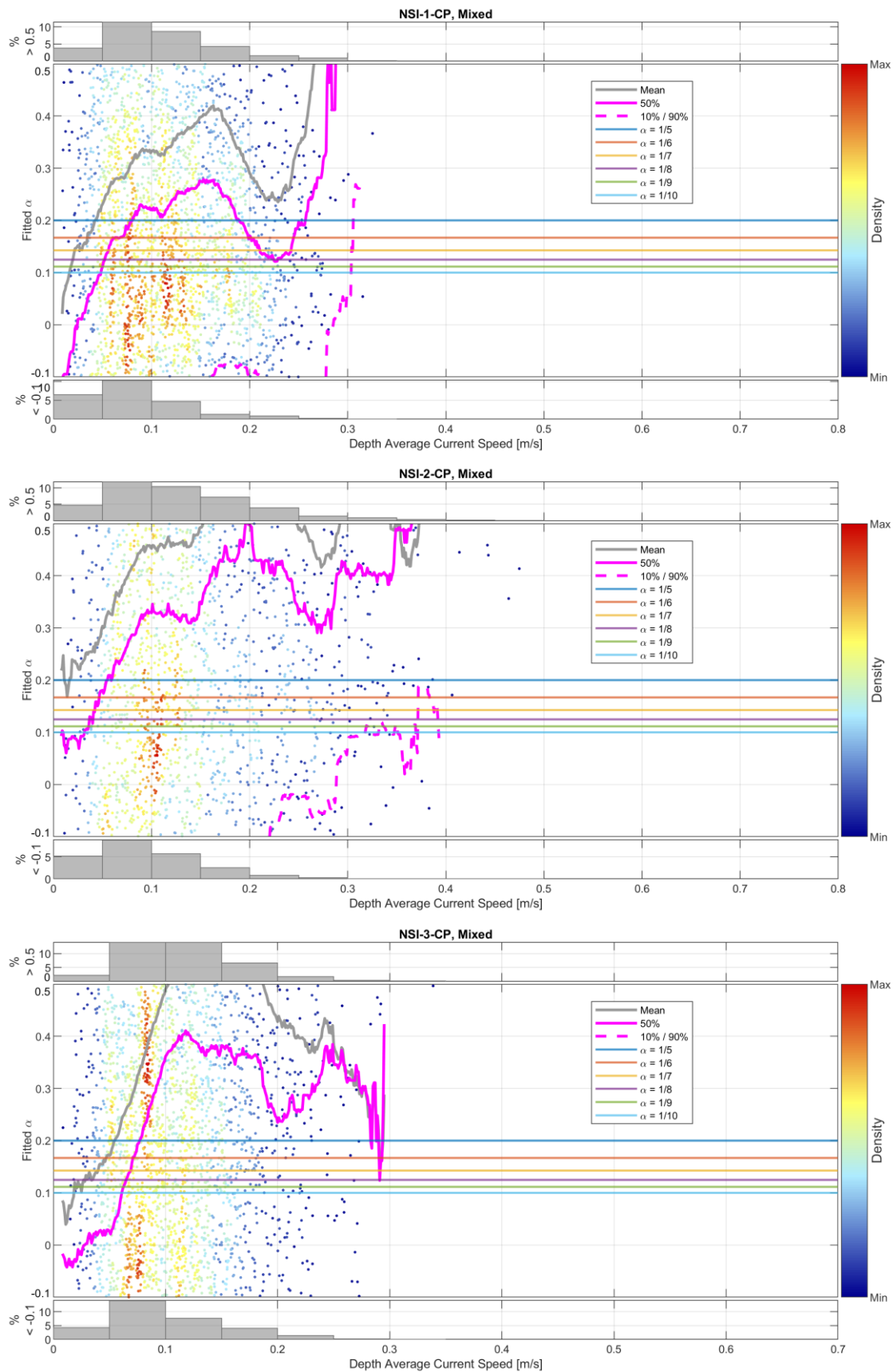


Figure D.29. Power law exponent versus depth averaged current speed, mixed flows.



In the pages which follow, a number of diagnostic plots are collated to help select appropriate power law profiles. Firstly, in Figure D.30 through Figure D.32, northward flows for NSI-1-CP, NSI-2-CP and NSI-3-CP are considered. These are then followed by southward flows for the three instruments in Figure D.33 through Figure D.35. In each case the following diagnostics are included:

- To the top left, percentiles are shown for each depth level, with fits overlaid.
- To the top right, a histogram of all α values above the 95th percentile is shown with an estimate of the most probable value overlaid alongside an α of 1/7.
- Beneath these plots, α values are plotted against depth average currents, with a number of commonly used profile shapes overlaid as horizontal lines.
- At the bottom, *normalized* current speeds are plotted against *normalized* heights for the full dataset. To obtain such “normalized” values:
 - Current speed is divided by depth average mean speed.
 - Measurement height is divided by water depth.

Such a normalization process allows a summary of profile *shape* only, which would not be possible without normalization given differences in scale of the profiles.

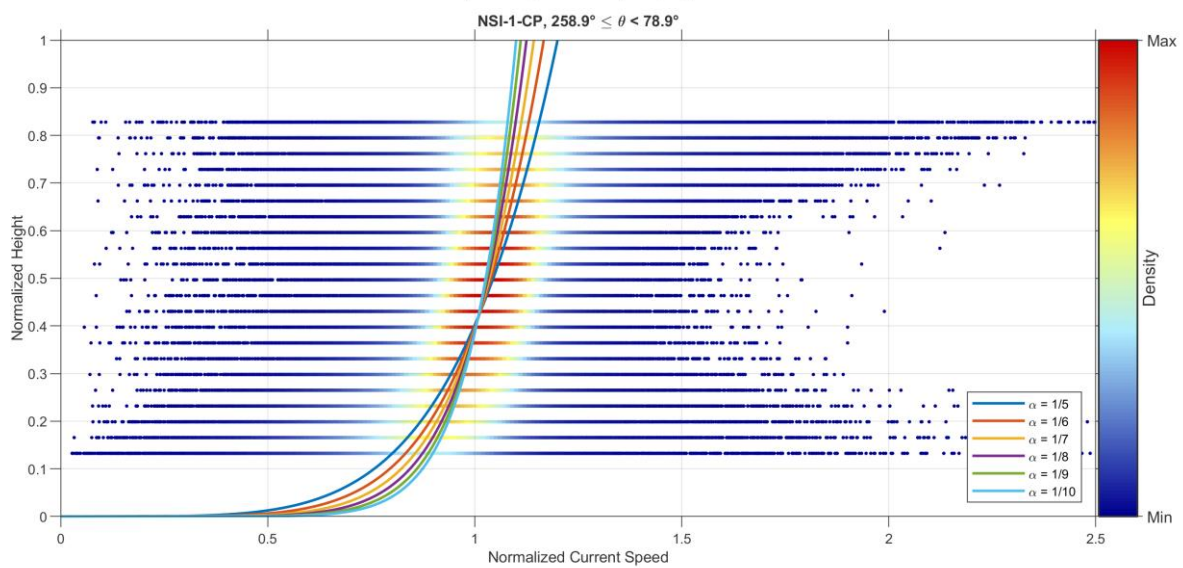
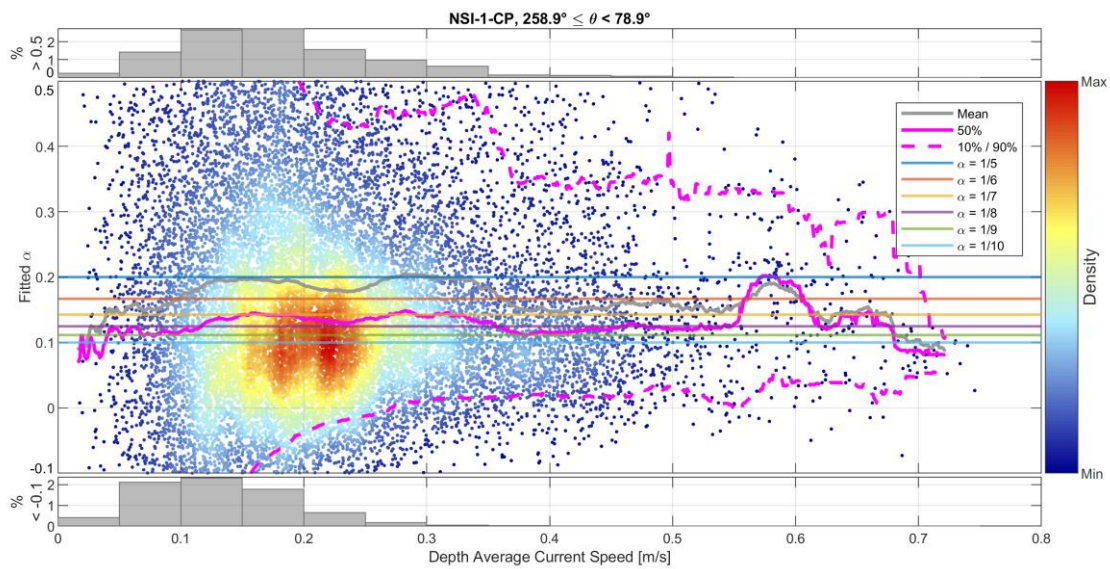
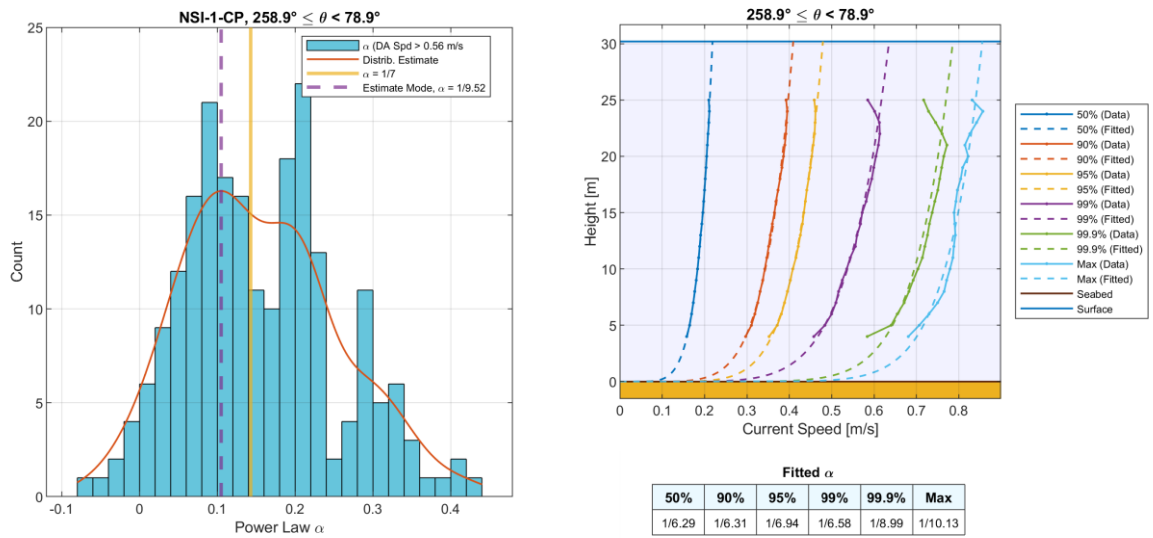


Figure D.30. Power law diagnostics, NSI-1-CP, northward flows.

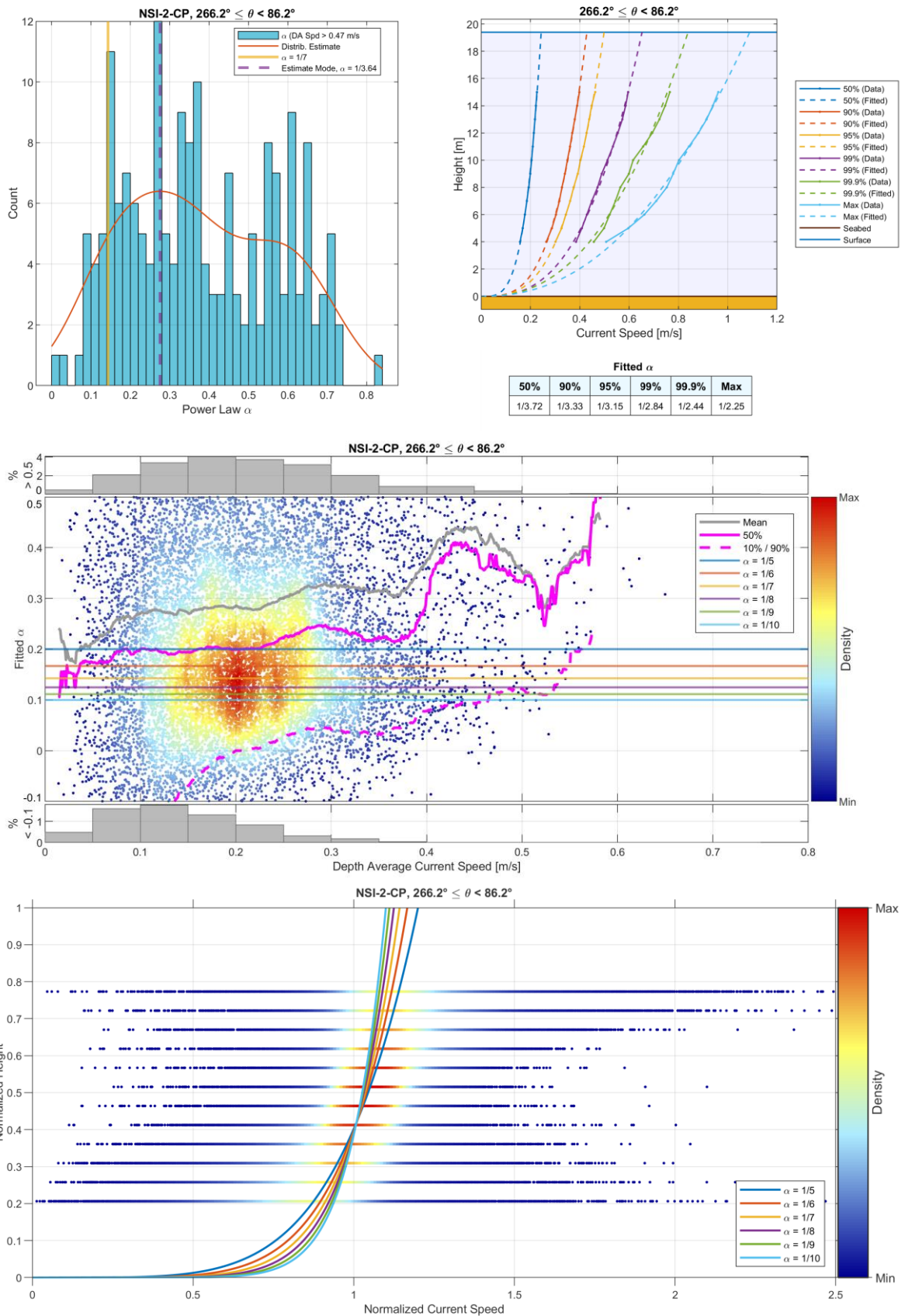


Figure D.31. Power law diagnostics, NSI-2-CP, northward flows.



Metocean Data Overview – North Sea I Offshore Wind Farm

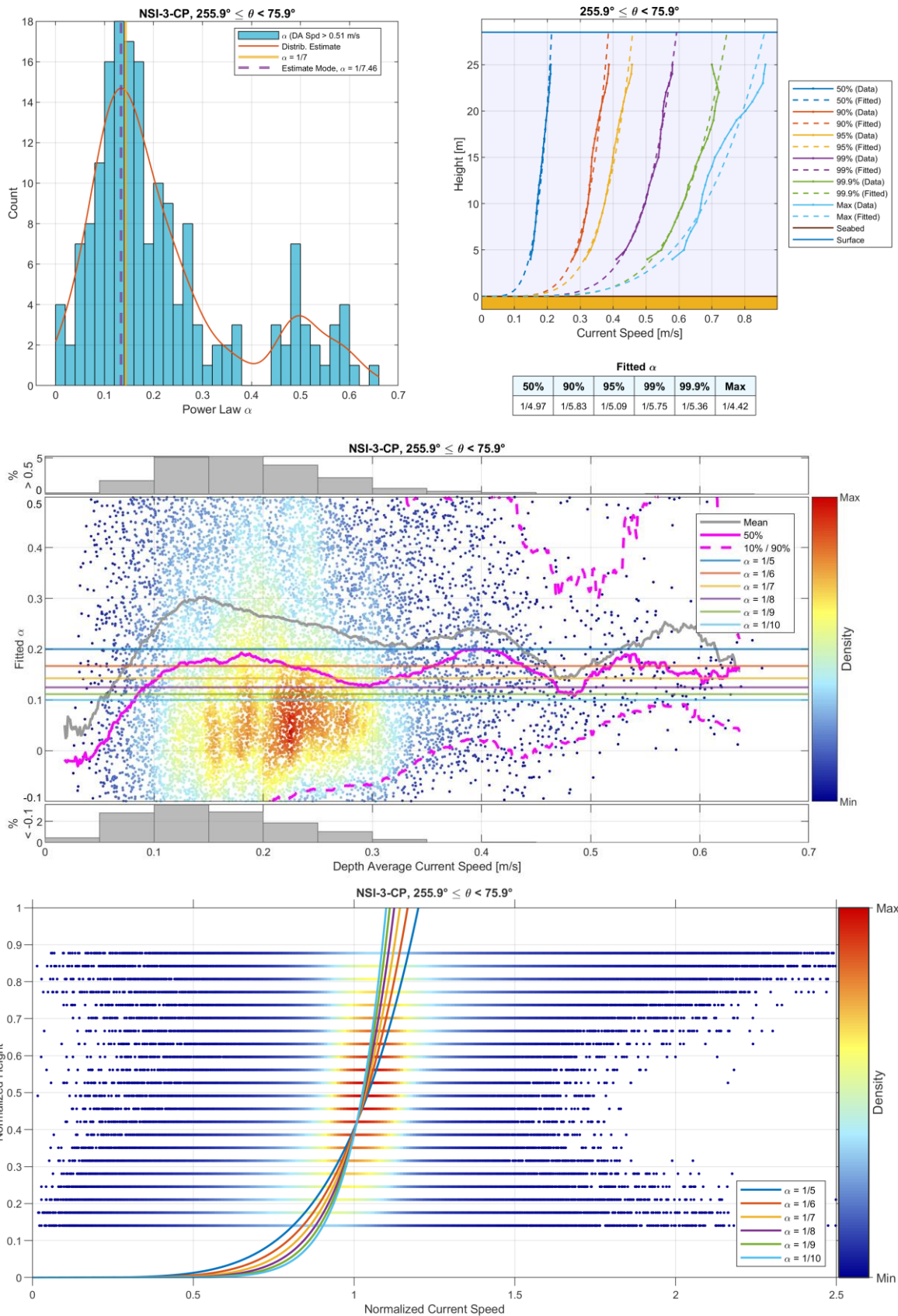


Figure D.32. Power law diagnostics, NSI-3-CP, northward flows.

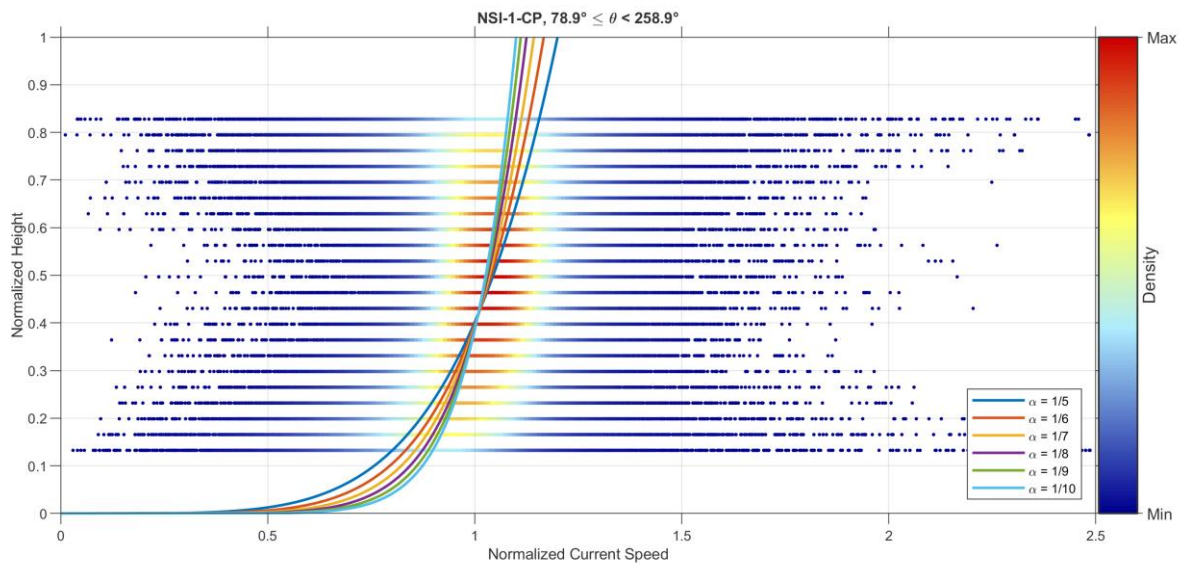
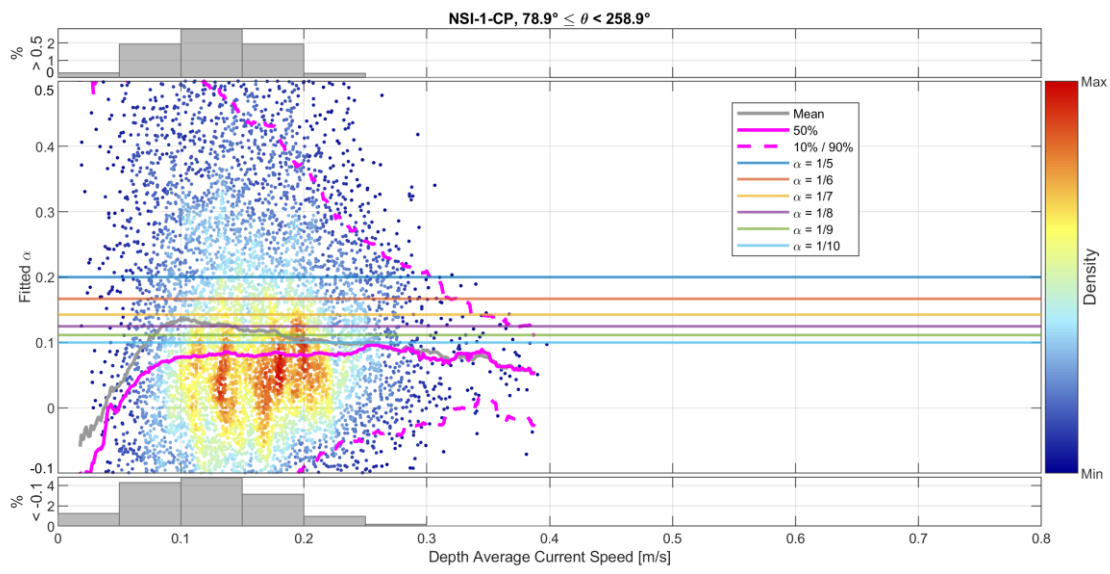
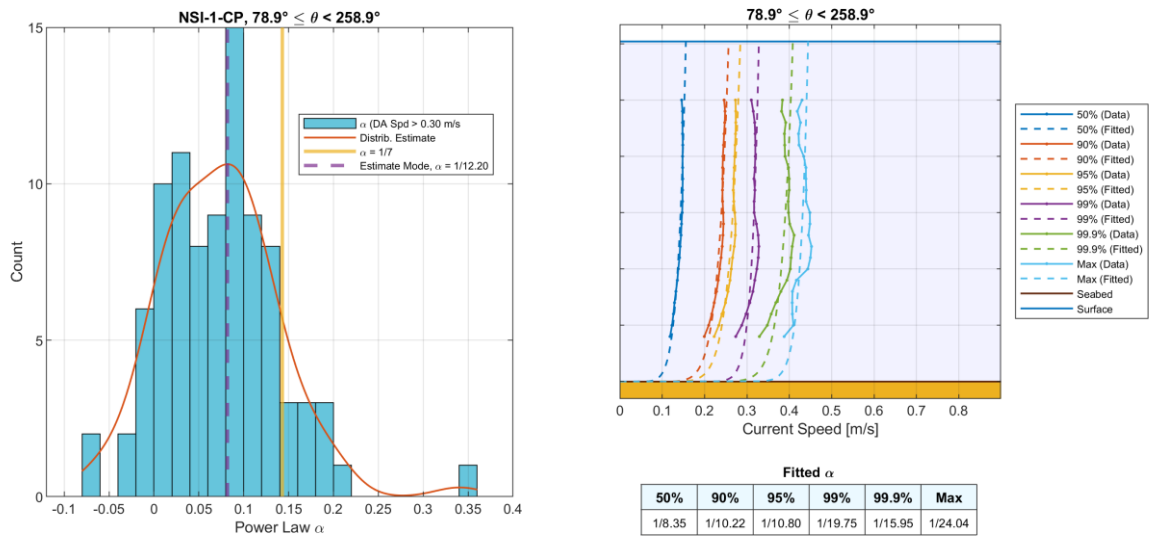


Figure D.33. Power law diagnostics, NSI-1-CP, southward flows.

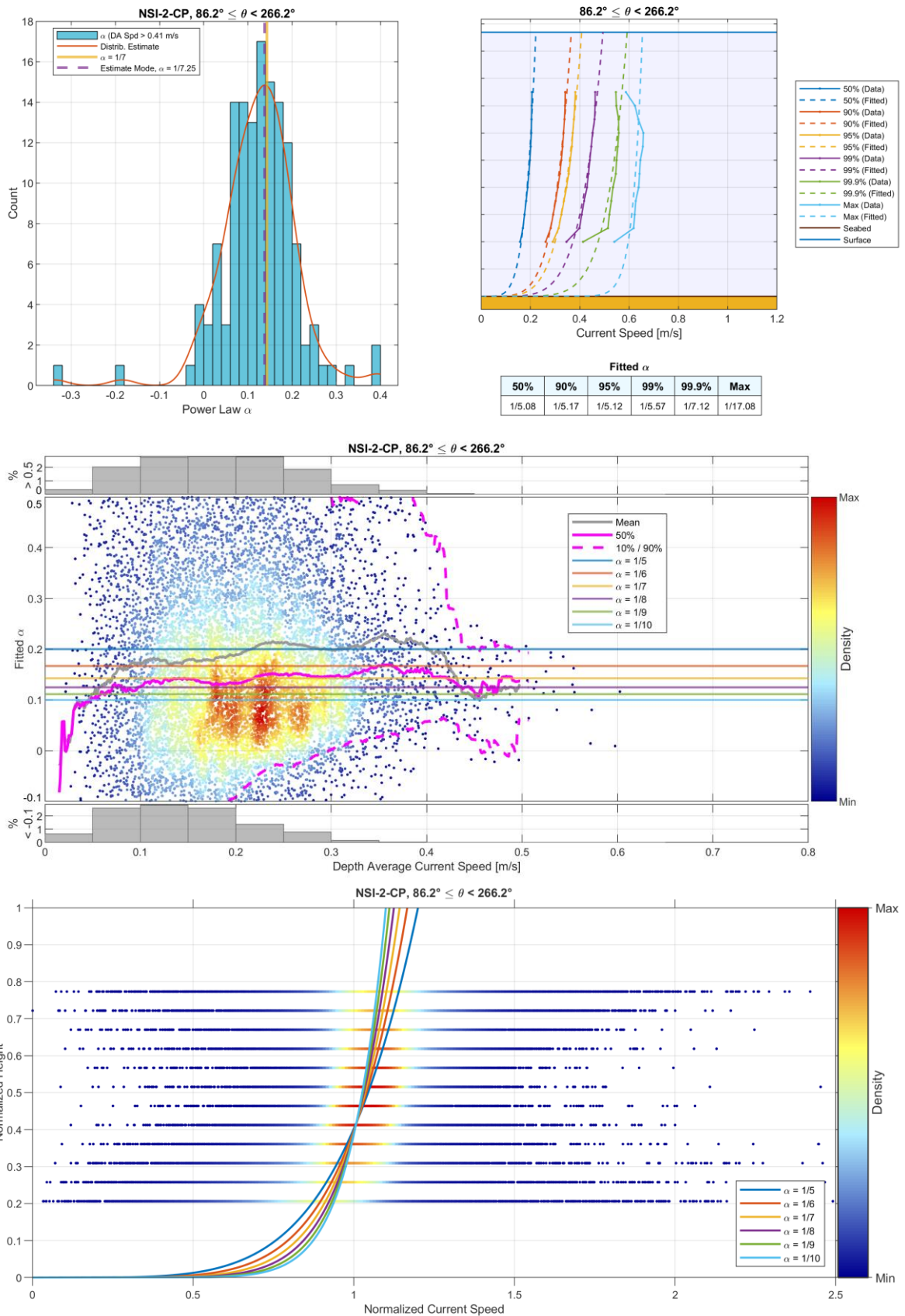


Figure D.34. Power law diagnostics, NSI-2-CP, southward flows.

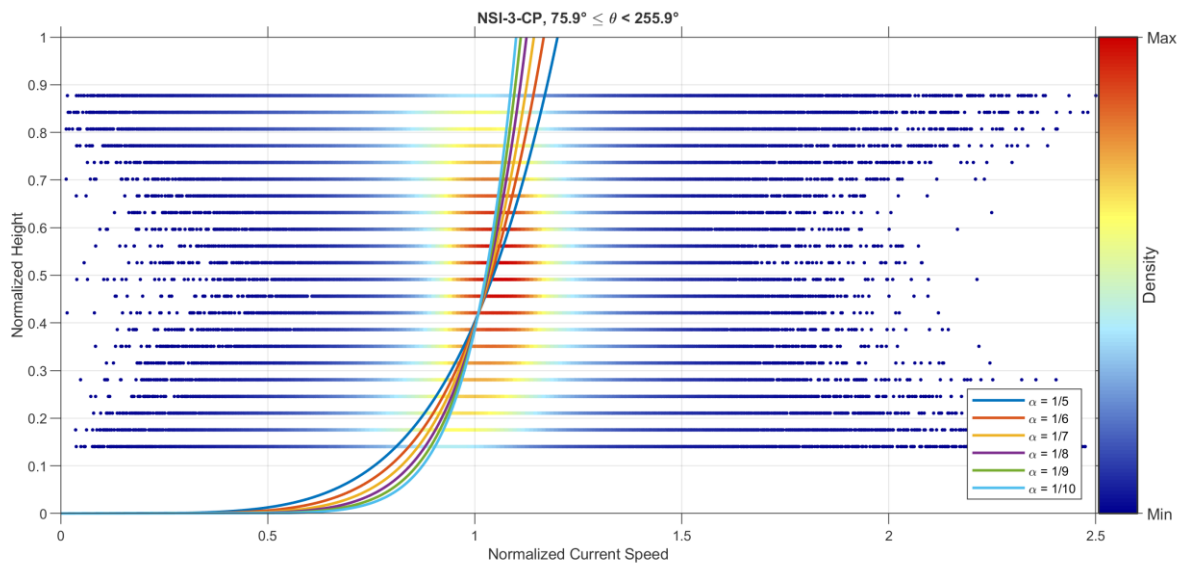
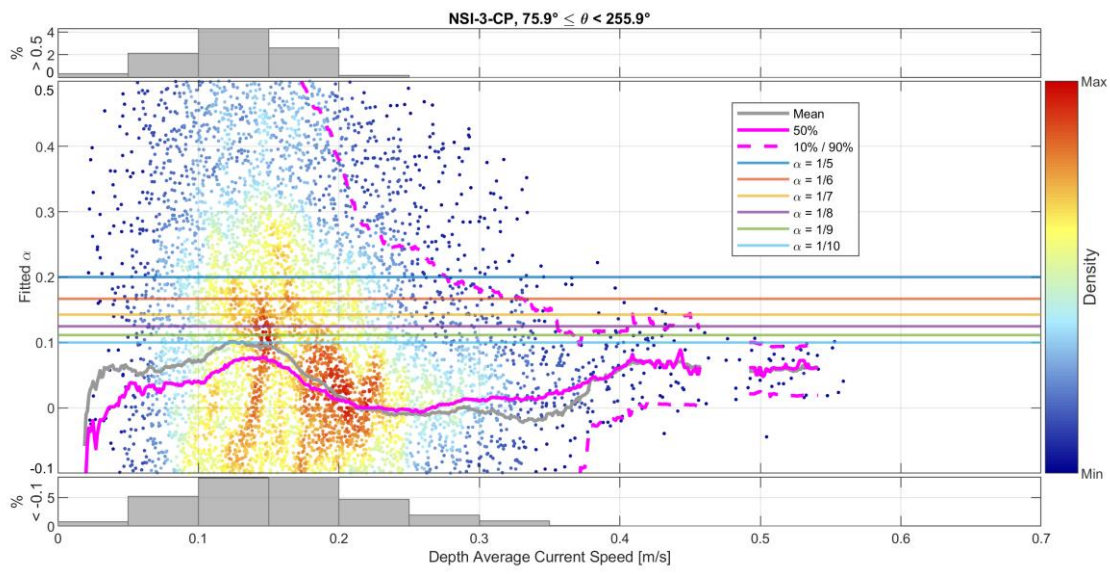
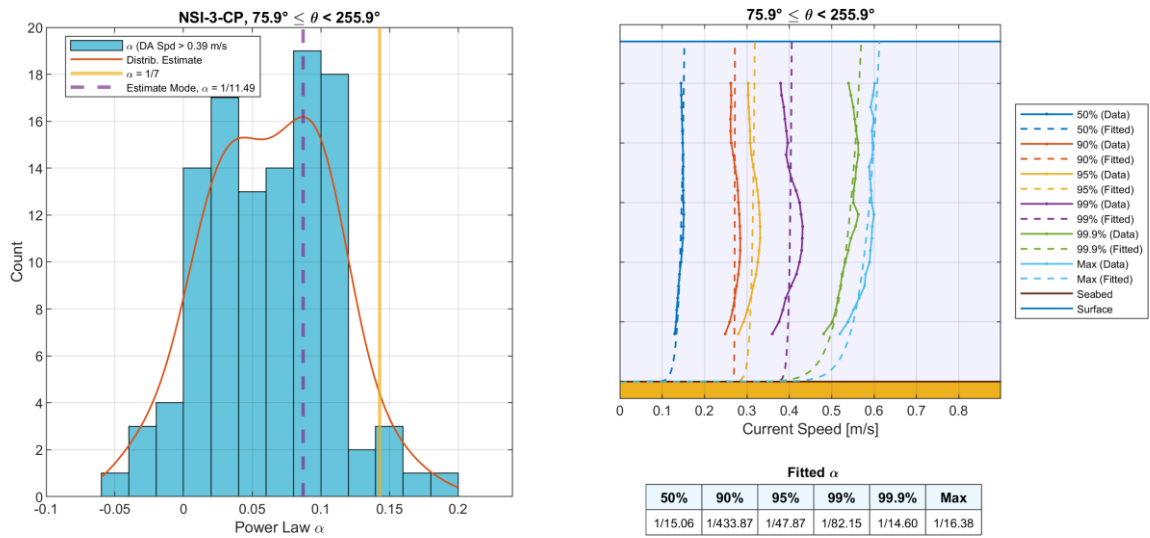


Figure D.35. Power law diagnostics, NSI-3-CP, southward flows.



D.7.2 Wind Driven Currents

To investigate the presence of wind driven currents, harmonic analysis was carried out independently on each level of the measured datasets using the UTide software [23]. Residual current speeds – i.e., those *not* attributed to astronomical forcings by the analysis – were then split into a component aligned with the prevailing wind direction, and a direction perpendicular to the wind direction. For the purposes of this analysis, wind speeds and directions are taken from calibrated ERA5 modelled data (See Section 4).

For the location NSI-1-CP, along-wind components of the residual current are shown in Figure D.36 and those perpendicular to it in Figure D.37. In both cases, there is considerable scatter but the component aligned with winds shows a clear increase with wind speed.

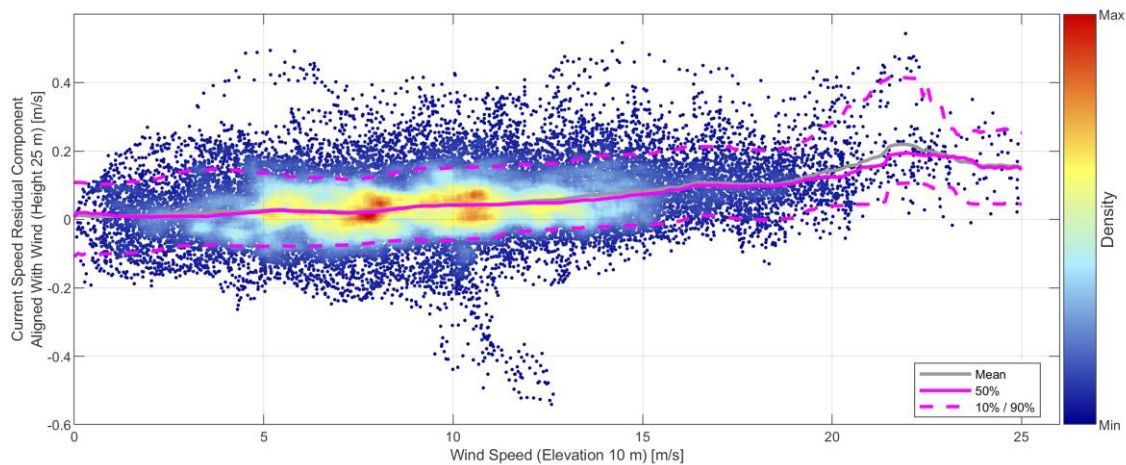


Figure D.36. Residual current speed aligned with wind, NSI-1-CP.

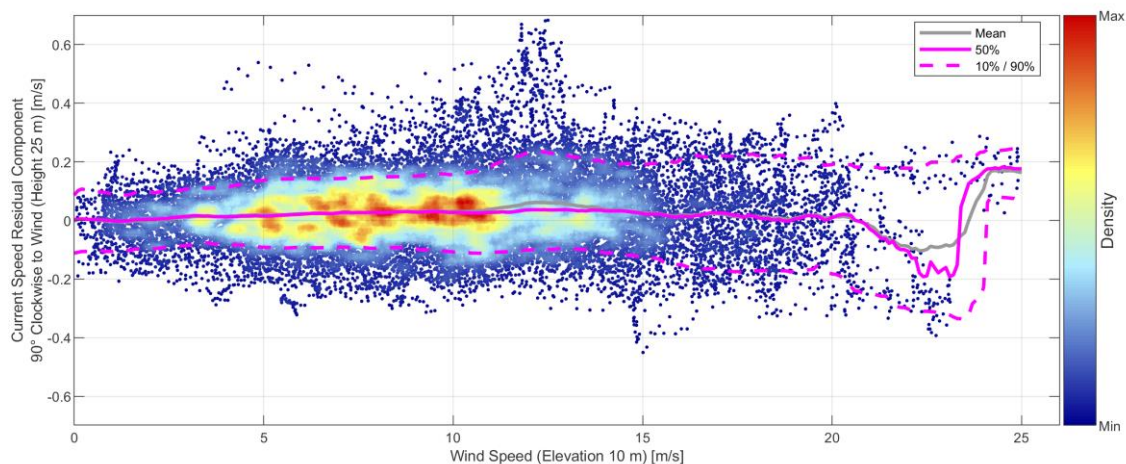


Figure D.37. Residual current speed perpendicular to wind, NSI-1-CP.



To investigate further the current speeds aligned with winds, a straight line passing through the origin was fitted to each level, as shown for near surface, mid-depth and near-bed levels at NSI-1-CP in Figure D.38. As might be expected from the theoretical equations of Section D.5.2, an increase is seen with wind speed at each level, though the gradient of this trend decreases with depth.

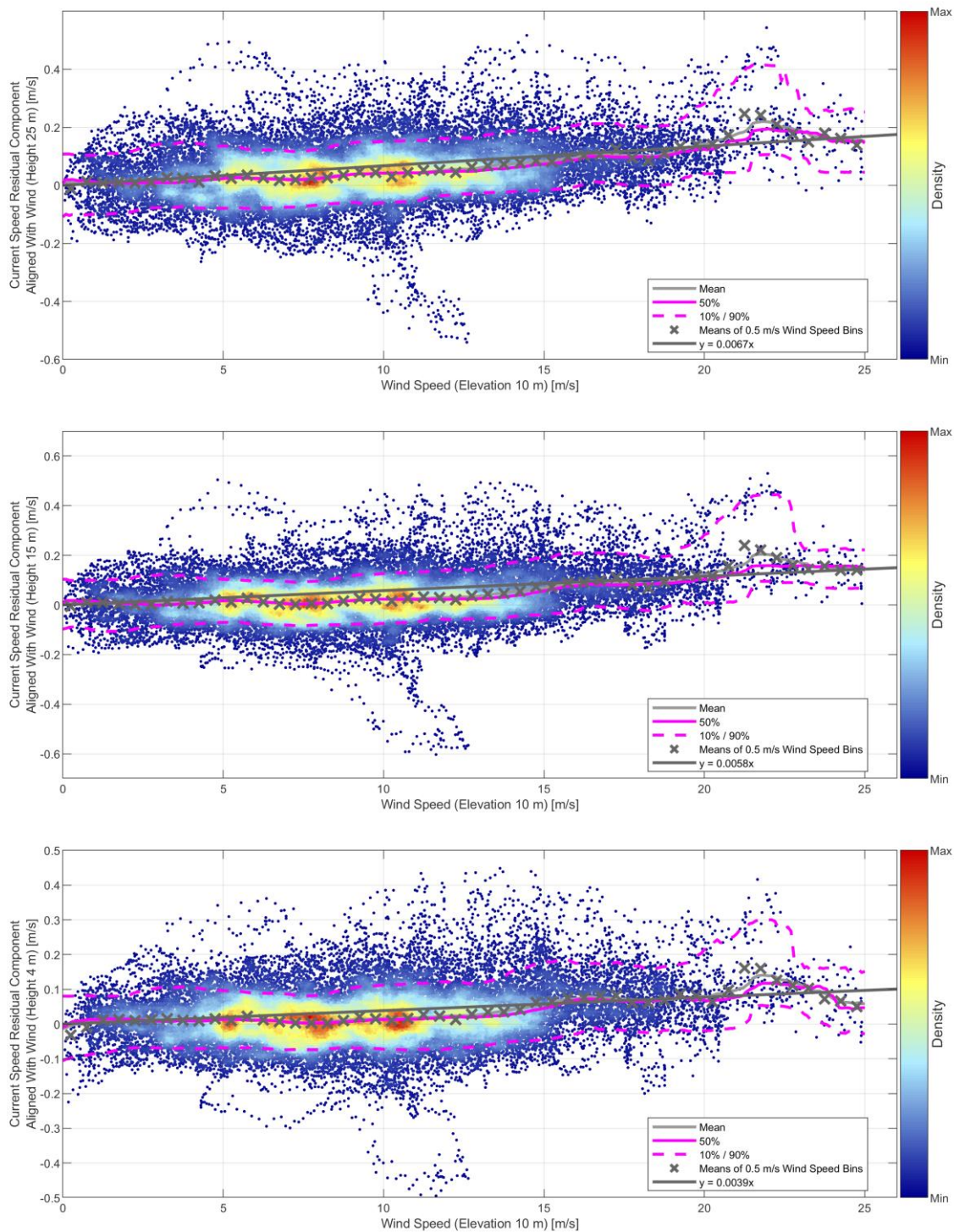


Figure D.38. Fitted multipliers for current speeds aligned with wind, selected levels, NSI-1-CP.



Collating multipliers at all levels leads to the line shown in blue in Figure D.39, to which the theoretical parameters d_0 and k described in Section D.5.2 can be fitted. In this case such a fit yields a d_0 of 61.8 metres and k of 0.0075, which can be compared to values given in metocean guidelines shown in Table D.3.

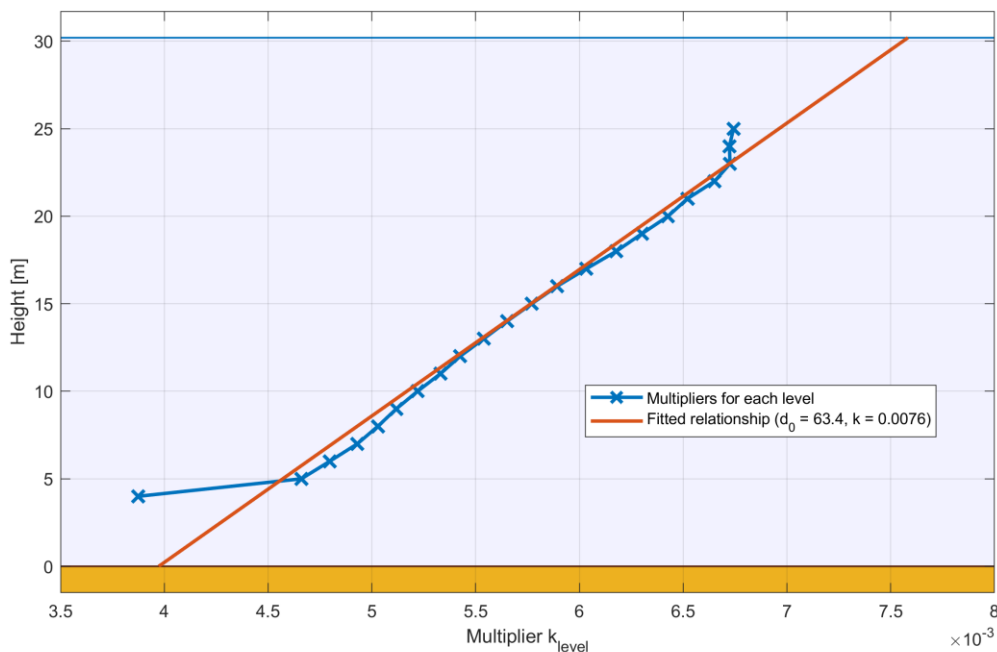


Figure D.39. Fitted multipliers at all levels, NSI-1-CP.

Table D.3: Wind driven current parameters from guidelines.

Parameter	IEC 61400-3-1	DNVGL-ST-0437
d_0	20 m	50 m
k	0.01	0.016 to 0.033

The results of analogous analyses for NSI-2-CP and NSI-3-CP are shown in Figure D.40 and Figure D.41 respectively. In both cases, a very clear trend is seen, though with notably different parameter values. If wind driven currents are included in design, given the variation seen, a slightly conservative option would be recommended of taking the largest d_0 and k seen across all sites.

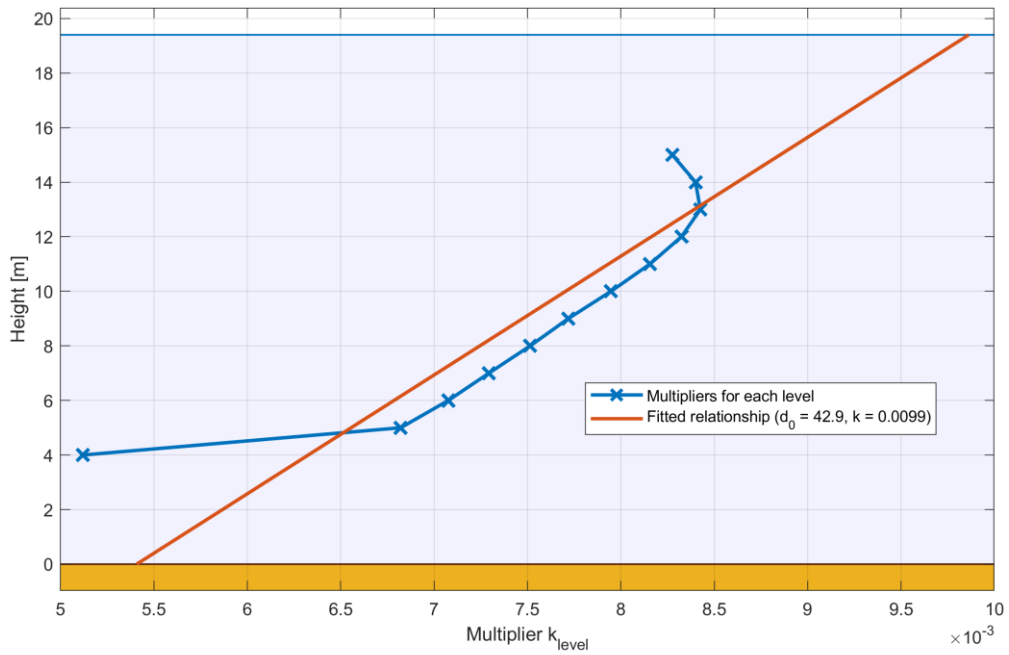


Figure D.40. Fitted multipliers at all levels, NSI-2-CP.

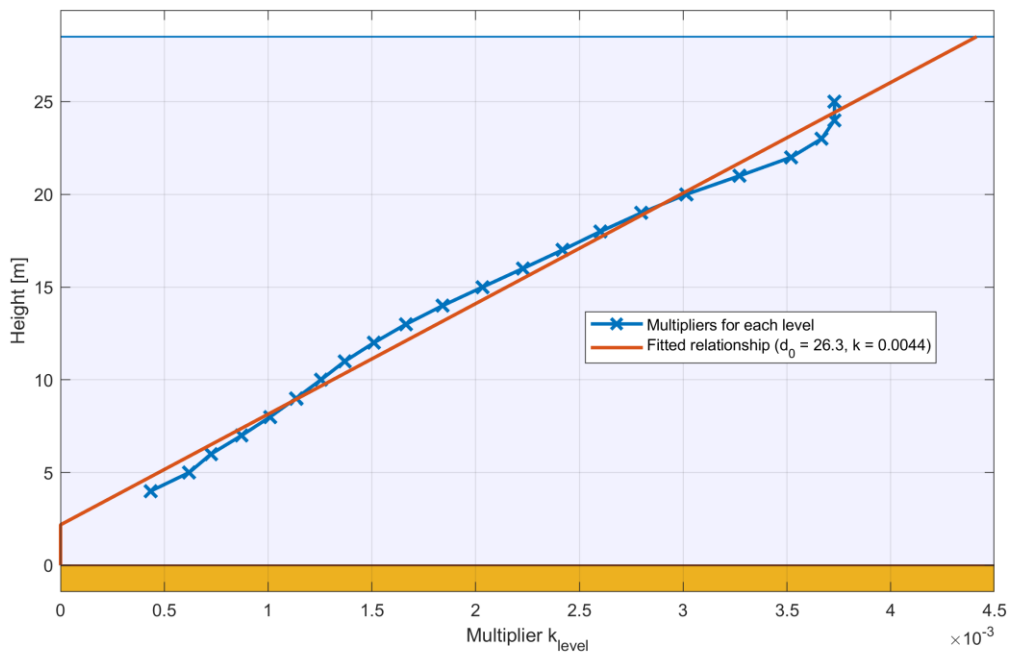


Figure D.41. Fitted multipliers at all levels, NSI-3-CP.



D.7.3 Additional Behaviours

Before concluding this review of measured currents, it is worth highlighting a couple of behaviours within the measurements. Firstly, mean current speeds and directions are shown by depth in Figure D.42 through Figure D.44. Throughout, a small flow towards the north is seen with relatively linear decrease in speed with depth. This was described in Section 2.4.4 and is caused by a gyre seaward of the site resulting from the confluence of southerly flowing Central North Sea water, and northward flowing South North Sea water.

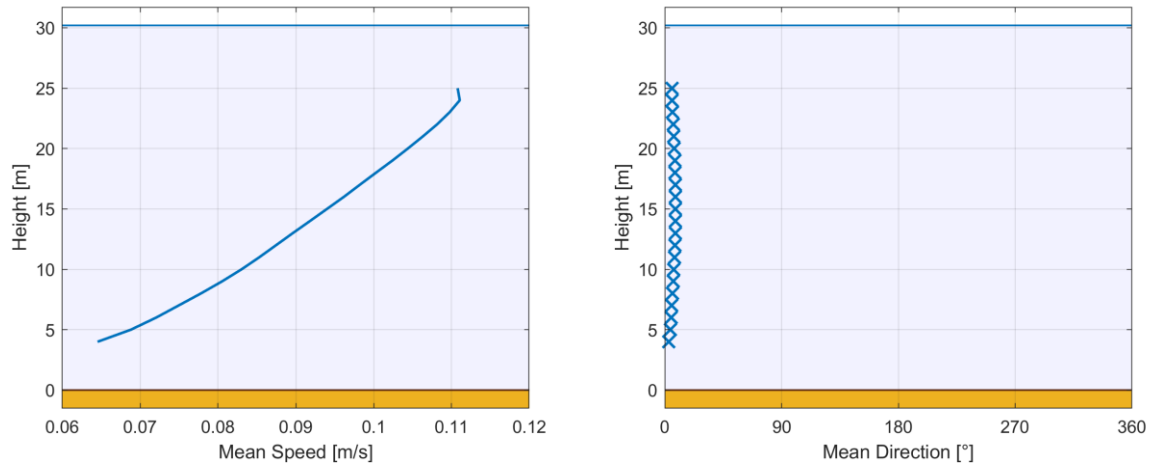


Figure D.42. Mean speed and direction, NSI-1-CP.

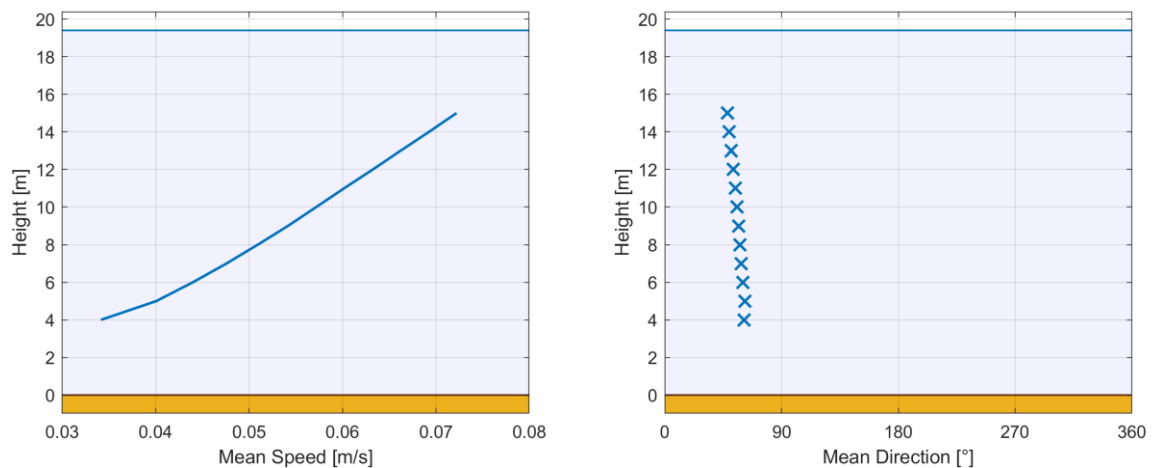


Figure D.43. Mean speed and direction, NSI-2-CP.

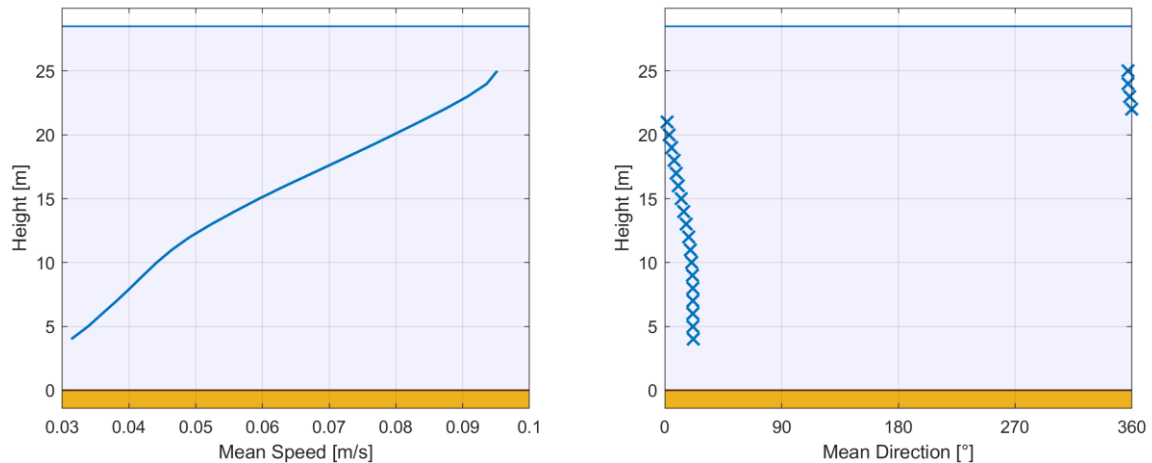


Figure D.44. Mean speed and direction, NSI-3-CP.

The second behaviour is more complex: the regular appearance of periods where near-bed currents are larger than those near the surface. Such a period is shown for NSI-3 in Figure D.45. Both the upward (CP) and downward (LB) looking instruments are included in this plot to highlight that this does not appear to be related to measurement error. For each level taken in isolation, speeds appear predominantly tidal. However, surface and near bed currents are almost entirely out of phase.

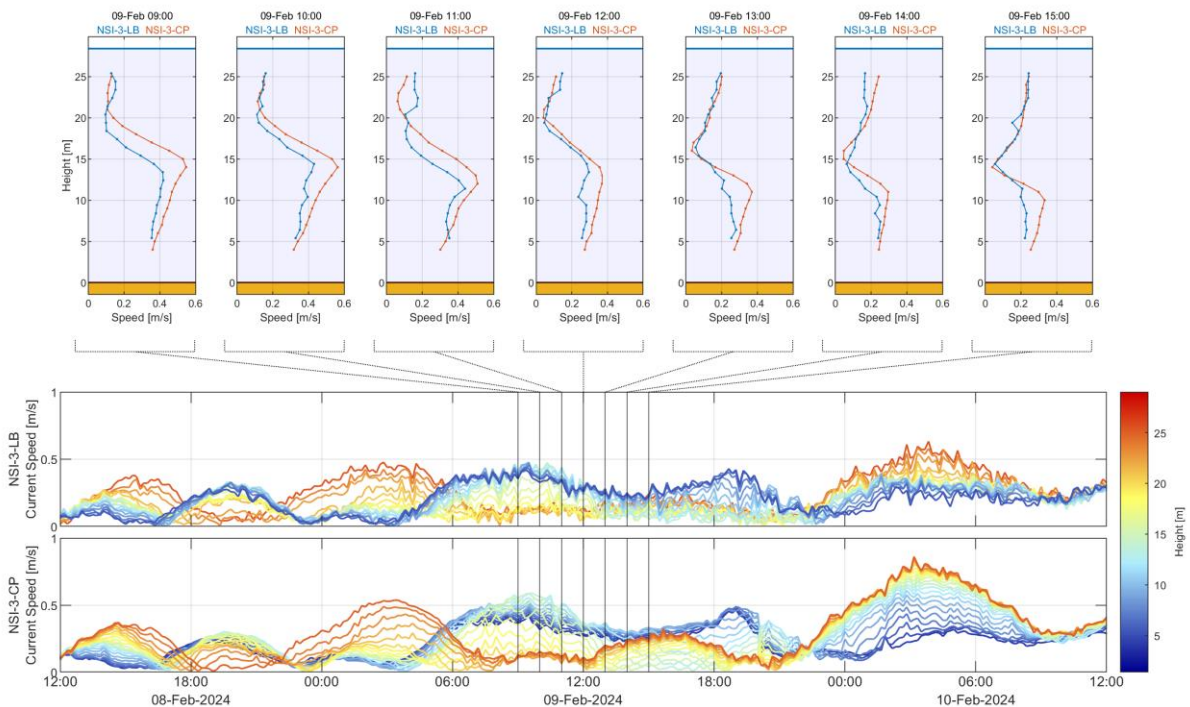


Figure D.45. Complex profiles, NSI-3.



The harmonic analysis used in Section D.7.2 offers some enlightenment here. The dominant constituent, with major axis amplitude at least 3.3 times that of the next strongest constituent across the 3 CP datasets, is the lunar semidiurnal constituent M2. A summary of the properties of this constituent, as fitted to data from NSI-1-CP is shown in Figure D.46. To the left, tidal ellipses are shown. These trace the tip of the current vector across one complete tidal cycle. Elevations coloured red rotate clockwise, those coloured blue counterclockwise. To the right, major and minor ellipse amplitudes are shown, alongside the orientation and the Greenwich phase lag of the constituent. Note that a positive minor axis amplitude denotes counterclockwise rotation, whilst a negative value denotes clockwise rotation.

Perhaps most notable are changes in eccentricity of the ellipses with depth, the change in rotational direction with depth, and the difference in phase of some 10 degrees. Analogous plots are shown for NSI-2-CP in Figure D.47 and for NSI-3-CP in Figure D.48.

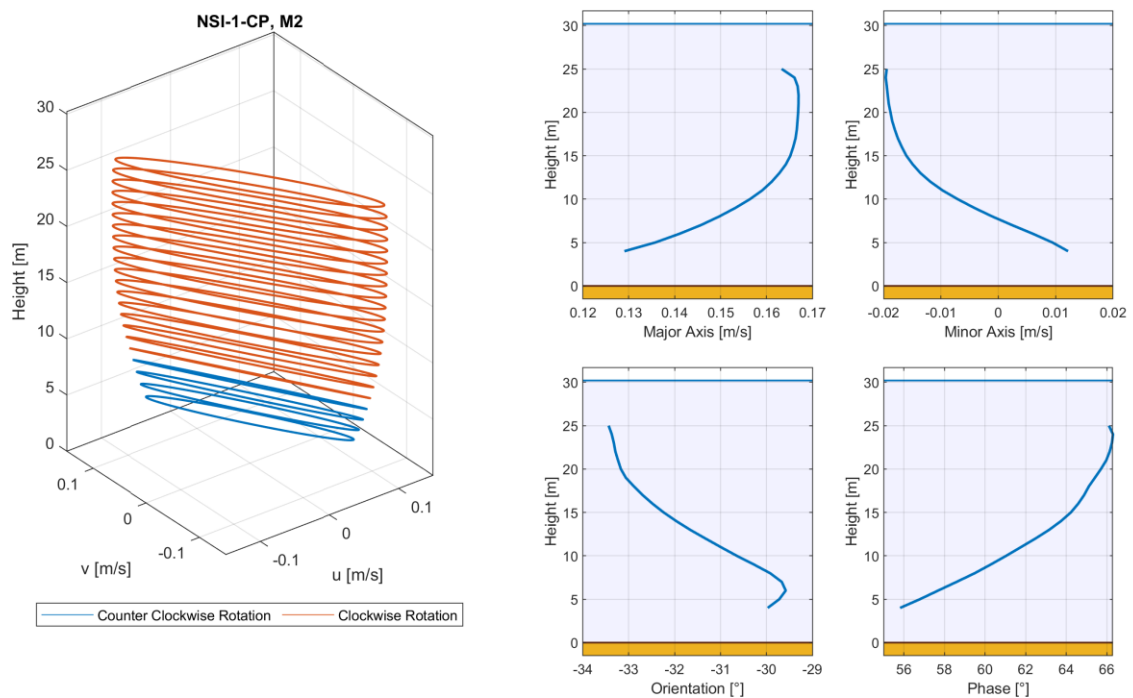


Figure D.46. M2 Constituent, NSI-1-CP.

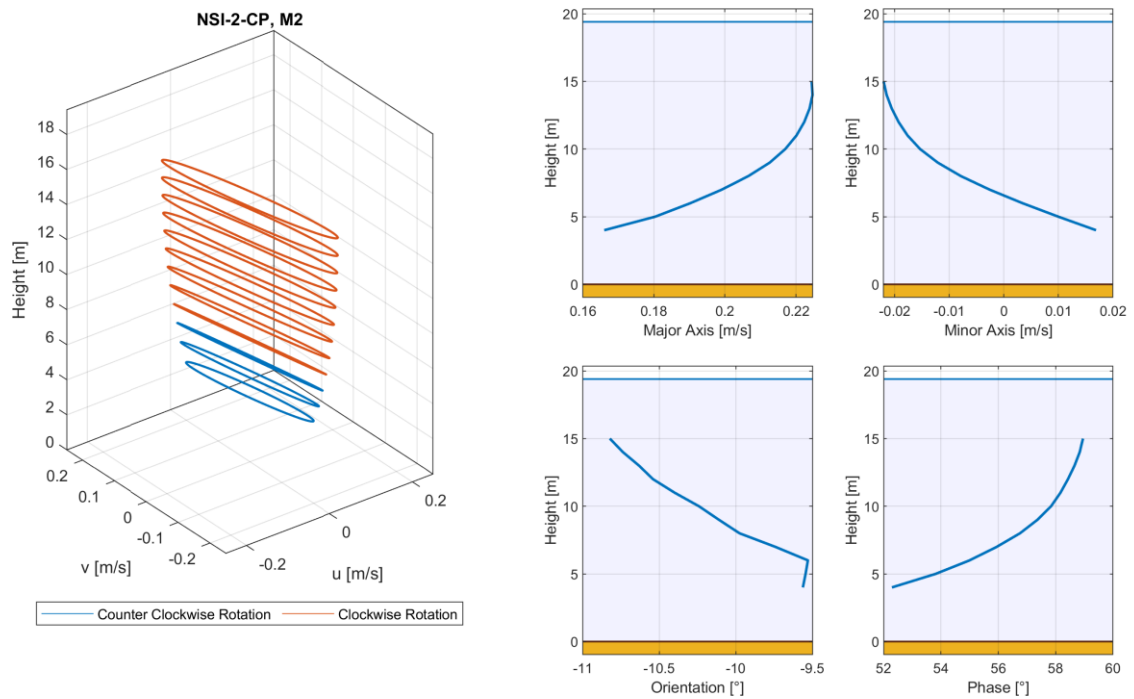


Figure D.47. M2 Constituent, NSI-2-CP.

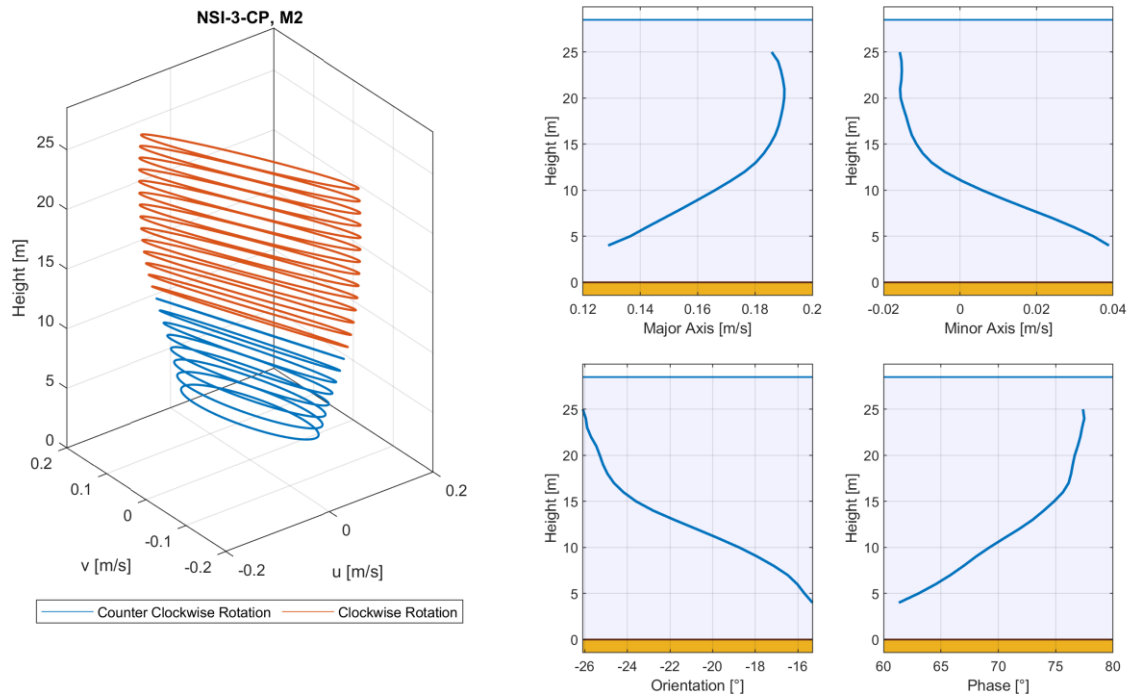


Figure D.48. M2 Constituent, NSI-3-CP.



D.7.4 Recommended Profile Shapes

Although the inclusion in any description of such features as those outlined in Sections D.7.2 and D.7.3 may lead to a more accurate representation of the measurements themselves, the benefits in any practical sense may be limited. Current speeds across the measurements are quite small in an absolute sense compared to those regularly encountered elsewhere regionally, and as such, a simpler power law representation would be expected to suffice. After review of the various diagnostics in Section D.7.1, we would recommend use of such a power law, with an exponent α of 1/8, for this location.



Appendix E. Zero-crossing Period Validation

E.1 Overview

Validation plots comparing mean zero-crossing wave period (T_{m02}) from modelled and measured data sources are included in Section 6.6. As briefly noted therein, the SWAN model and instrument measurements calculate this parameter in a slightly different way, and as such a little caution is needed in their comparison. This Appendix provides additional detail in this regard, highlighting the differences between the calculations, and the methods ultimately used for the validation of T_{m02} within this project.

At NSI-1 LiDAR Buoy (see Table 6-1 for details), values of T_{m02} as output *directly* from the SWAN model and the instrument are compared in Figure E.1.

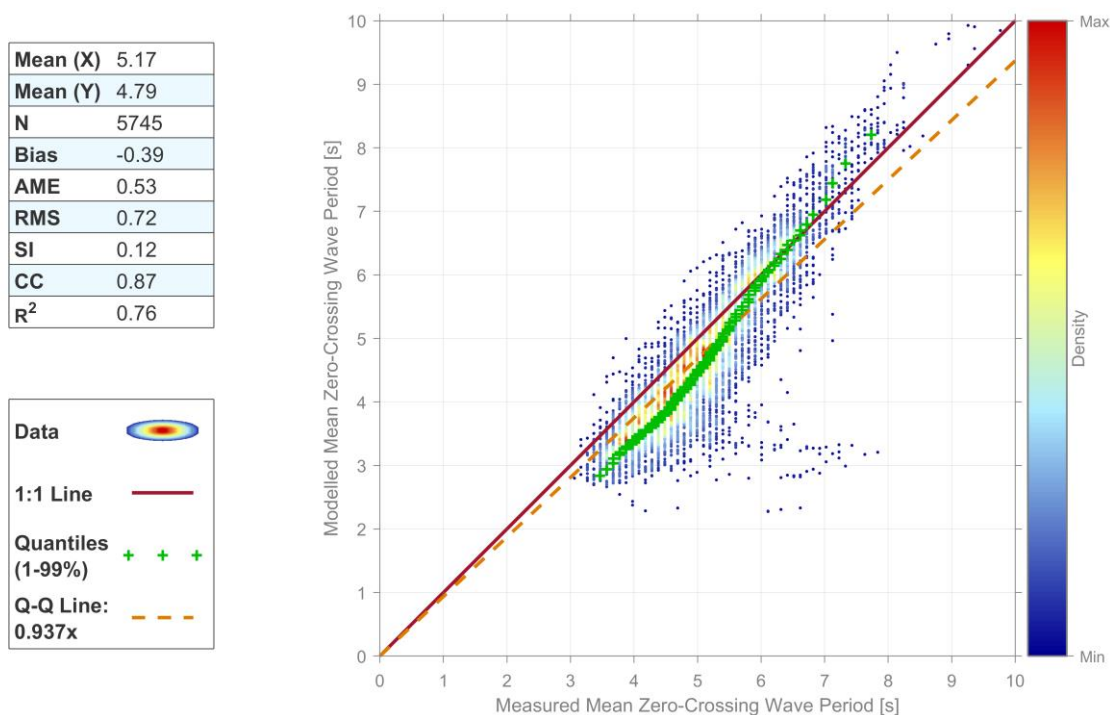


Figure E.1: SWAN parameter T_{m02} vs. NSI-1 LiDAR Buoy parameter T_{m02} .

It appears clear that the model is underpredicting T_{m02} at the lower end of the observed range. However, such behaviour is often symptomatic of comparing measurements which *only* consider data within a specific range of spectral frequencies against model parameters where a theoretical high frequency tail extrapolation has been included in the calculation (see [15] for details).

Whilst the difference sounds insignificant, and limited to a high frequency range where we might not expect a great deal of spectral energy, it is worth a more detailed investigation to see if this really is the case.



E.2 Example Spectrum

To consider the impact of the inclusion or exclusion of a high frequency tail, consider first the simple spectrum shown in Figure E.2 combined with a frequency cut-off of 0.5 Hz. This is in fact a JONSWAP spectrum with H_{m0} of 2.5 m, T_p of 7 s and γ of 1.5, though the same reasoning holds for any shape with high frequency content.

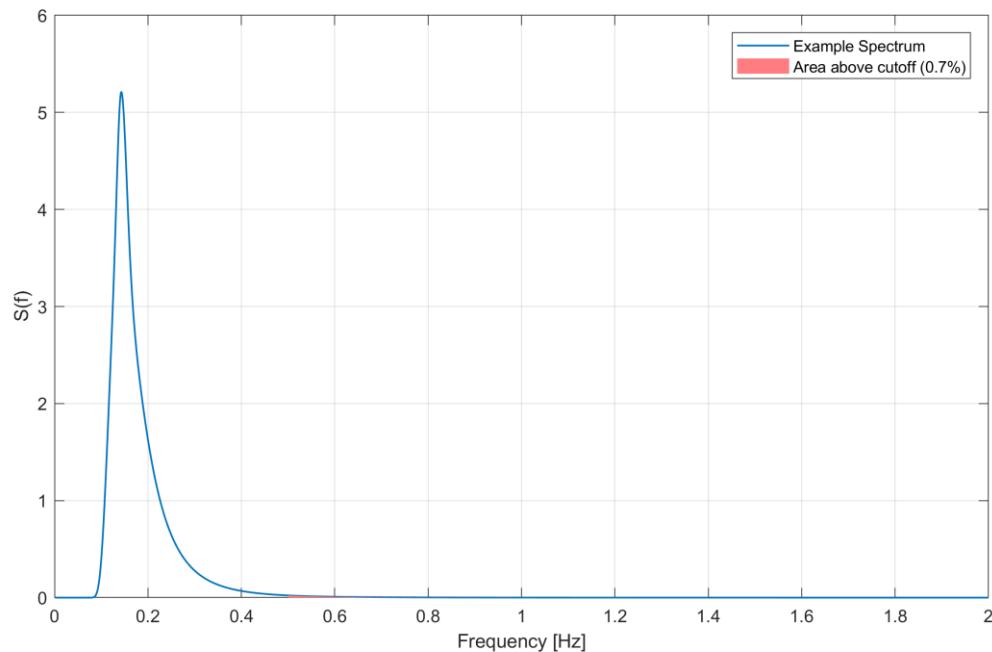


Figure E.2: Example wave spectrum.

The zeroth moment of the spectrum, m_0 , is given by:

$$m_0 = \int_0^{\infty} S(f) df$$

i.e., it is the area under the blue curve shown. Inclusion or exclusion of frequencies above a cut-off of, say, 0.5 Hz (shown in red here) has only a very small effect on the resulting m_0 . Since H_{m0} is given by four times the square root of m_0 , it is similarly barely affected by the inclusion or exclusion of this tail.

The first moment of the spectrum, m_1 , is given by:

$$m_1 = \int_0^{\infty} fS(f) df$$

i.e., the area under the blue curve in Figure E.3. For this parameter, the area above the cut-off is a slightly higher proportion, at 2.7 % of the total area. For parameters such as the mean wave period, T_{m01} , given by m_0 / m_1 , we begin to see differences dependent on whether this region is included or not.

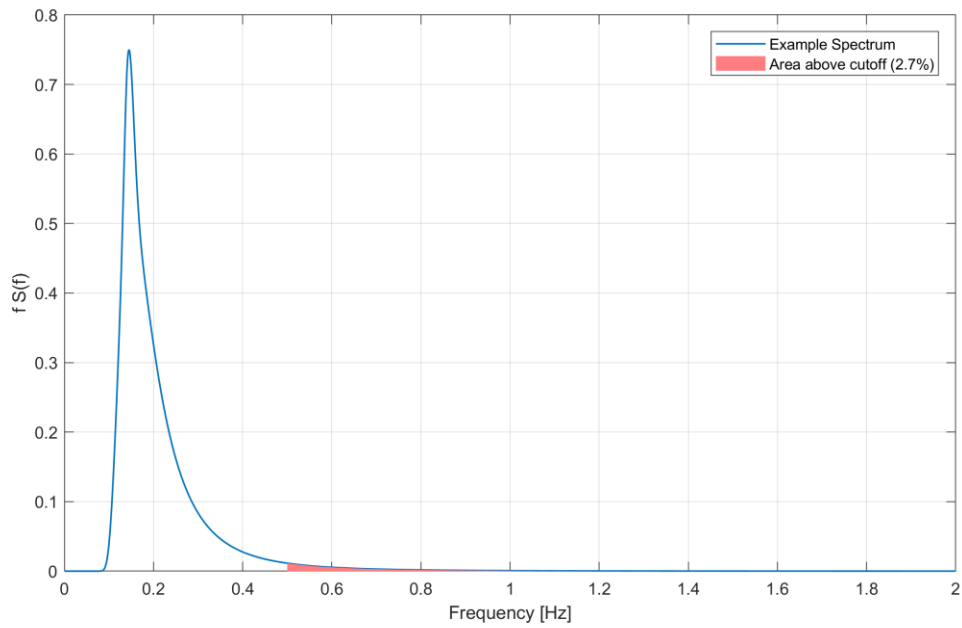


Figure E.3: Area for first moment.

By the time we reach the second moment, m_2 , given by:

$$m_2 = \int_0^{\infty} f^2 S(f) df$$

a more severe impact emerges, as shown in Figure E.4. Now the area above the cut-off is some 9.1 % of the total value of m_2 .

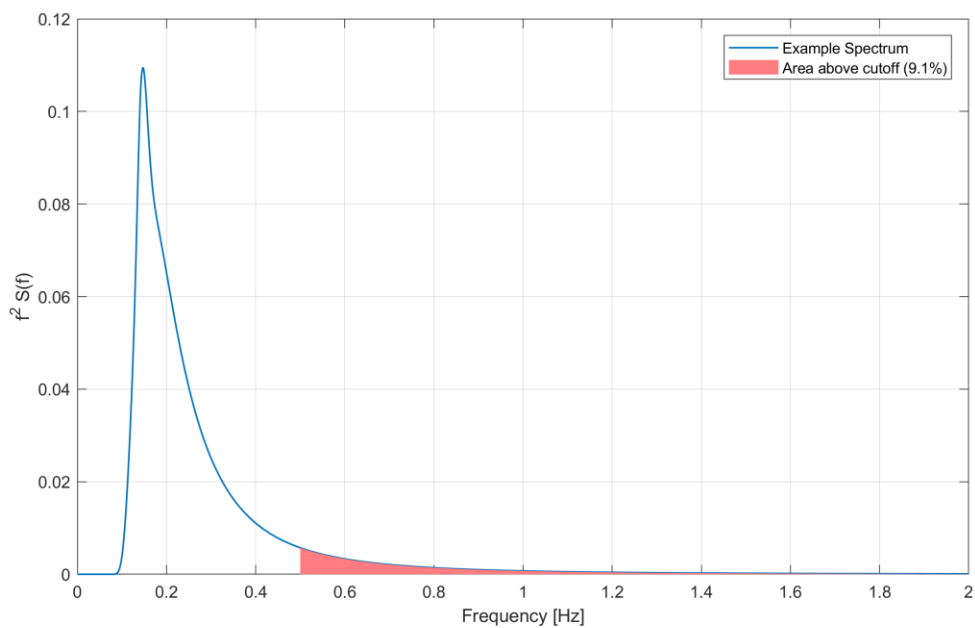


Figure E.4: Area for second moment.



In calculating the mean-zero crossing period, T_{m02} :

$$T_{m02} = \sqrt{m_0/m_2}$$

such a change starts to become noticeable. In this example, *without* the cut-off region, m_2 will be only 90.9 % of its value *with* the cut-off region included. We saw above though that m_0 remains relatively unchanged, *without* the cut-off being 99.3 % of the value with it being included.

In this case, we would end up with a T_{m02} of 5.1 seconds *with* the frequencies in the cut-off region, and 5.4 seconds *without* (m_2 is smaller, so T_{m02} larger).

E.3 Validation

Whilst the previous section only included a single, simplified spectrum, the same principle will apply to all modelled and measurement results if the calculation method is different. To consider the impact on the overall model validation, we look in more detail at the measurements taken at NSI-1 LiDAR Buoy. In Figure E.1, the difference between modelled T_{m02} (using a high frequency tail) and measured T_{m02} (with a fixed cut-off frequency of 0.6 Hz) were noticeable. However, since spectral data are available for the model, it is possible to recalculate T_{m02} from both in the same manner, with results shown in Figure E.5 for calculations carried out *without* a theoretical spectral tail for *both* datasets.

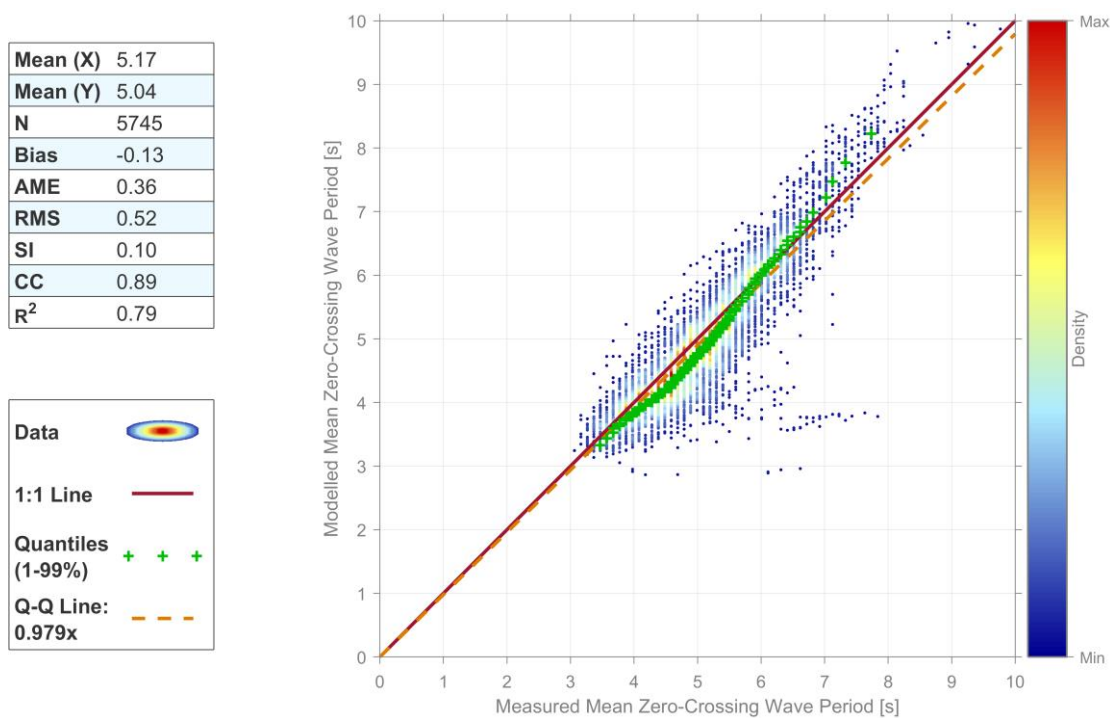


Figure E.5: Modelled T_{m02} vs. NSI-1 LiDAR Buoy Measured T_{m02} , both without theoretical tail.

Agreement now appears much closer overall, i.e., the model and measurements are well matched, and the discrepancies seen in Figure E.1 seem to be predominantly caused by the different methods used to calculate T_{m02} .



E.4 Summary

When comparing SWAN modelled and instrument measured Tm02 parameters directly, differences are apparent. However, the main source of such discrepancies appears to be a subtle difference between how spectral moments are calculated. Within the model, a theoretical high frequency tail is included, however measurements often use a fixed cut-off. In the main body of this document, comparisons are included for Tm02 calculated with the same method (no high frequency tail, and the same high frequency cut-off) in both modelled and measured cases.



Appendix F. Spectral Wave Validation

F.1 Introduction

In this Appendix, comparisons of measured and modelled spectra are provided. Given the need in the project deliverables for JONSWAP spectral characterisation for total-sea state, wind-sea, and swell components, we consider not just the modelled spectral directly output from the wave model, but instead *three* different versions as follows:

1. **Raw modelled spectra:** Wave spectra directly output by the wave model with no treatment applied. For conciseness, these are labelled **Modelled** in the Figures which follow.
2. **2 peak spectra:** For each output time step, the raw modelled spectrum is partitioned into one swell and one wind-sea component. To each partition, a JONSWAP spectrum is fitted, resulting in five parameters per partition: significant wave height, peak wave period, peak enhancement factor, mean wave direction and a directional spreading parameter. A second version of the modelled spectra, labelled **2 JONSWAP** in the Figures which follow, reconstructed from only these ten parameters (five for swell, five for wind-sea) is subsequently used throughout the validation.
3. **1 peak spectra:** For each output time step, a JONSWAP spectrum is fitted to the full raw spectrum, resulting in five parameters for the entire spectrum: significant wave height, peak wave period, peak enhancement factor, mean wave direction and a directional spreading parameter. A third version of the modelled spectra, labelled **1 JONSWAP** in the Figures which follow, reconstructed from only these five parameters, is subsequently used throughout the validation.

More details on the construction of the 1 and 2 JONSWAP spectra can be found in Appendix G.

F.2 Measured Spectra

Measured directional spectra were provided by Energinet for the locations NSI-1-LB and NSI-2-LB. Accompanying documentation [21] states that:

Raw and smoothed directional spectra are calculated from the distribution of wave elevation as a function of both wave frequency and wave direction using the Burg Maximum Entropy Method. Fourier coefficients are determined from cross and quad spectra and directional wave parameters are calculated.

The wave parameters are based on a time series of 2048 2 Hz values, i.e. 17 minutes (1024 s \approx 17 min). When the acquisition is complete, the analysis phase starts using FFT (Fast Fourier Transform) algorithms. Wave bursts overlap by 424 s, i.e. data is collected for 1024 s, but data is analyzed and written to file every 600 s. Approximately 25 minutes in total are needed for a full measurement cycle, including "heat-up", 17 min sampling and time to run FFT analysis. The measurements are taken continuously and the processing windows overlap.

Given that the modelled spectra are considered representative of a 3-hour sea-state (see Section 6), throughout these comparisons, spectra have been similarly averaged across a 3-hour window centred on each hour.



F.3 Mean Spectra

We begin with comparisons of means of modelled and measured spectra. In Section F.3.1, the dataset NSI-1-LB is reviewed as follows:

- Section F.3.1.1 considers the omni-directional case.
 - Figure F.1 shows the mean of modelled spectra (red line) and measured spectra (blue line) across *all* time-steps for which both datasets are available. Overlaid are also means of the 2 JONSWAP spectra (green) and 1 JONSWAP (dashed purple). In the top right corner, the number of modelled spectra which have been averaged are shown (red text) along with the number of measured spectra averaged (blue text).
 - Thereafter, in Figure F.2, spectra are grouped by measured Hm0 and Tp, and a single comparison of mean spectra for each grouping is included.
- Section F.3.1.2 groups data by direction.
 - In Figure F.3, spectra are split into the 45° directional sectors and mean spectra compared for each sector are compared. This splitting is based on *measured* mean wave directions: measured spectra are assigned to a bin directly, along with modelled spectra that are closest temporally, i.e. *model* wave direction is not used.
 - In Figure F.4 through Figure F.11, for each sector in turn, spectra are again grouped by Hm0 and Tp, and a single comparison of mean spectra for each grouping in that directional sector is included.

Thereafter, analogous figures are included for the dataset NSI-2-LB in Section F.3.2.



F.3.1 NSI-1-LB

F.3.1.1 Omni-Directional

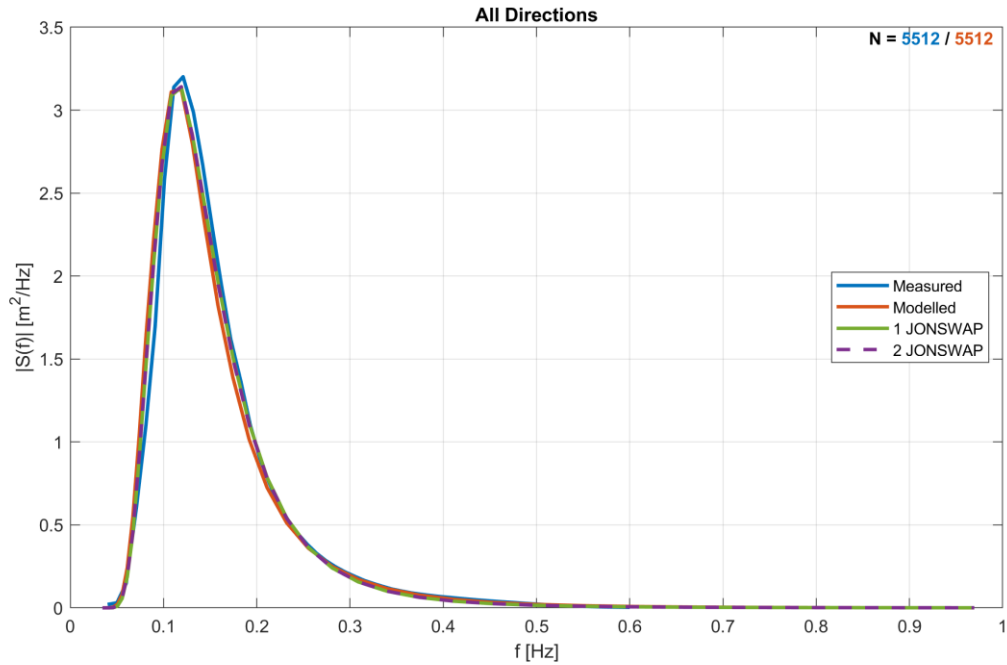


Figure F.1. NSI-1-LB, omni-directional spectral validation, all data.

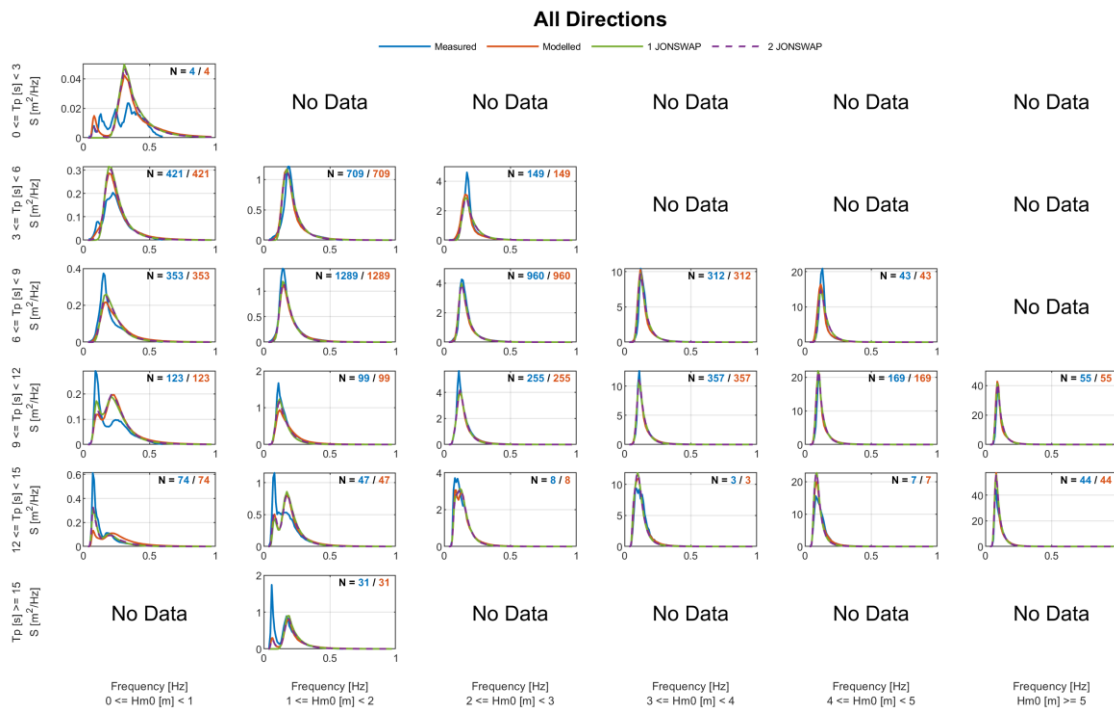


Figure F.2. NSI-1-LB, omni-directional spectral validation, by Hm0 and Tp, all directions.



F.3.1.2 45° Sectors

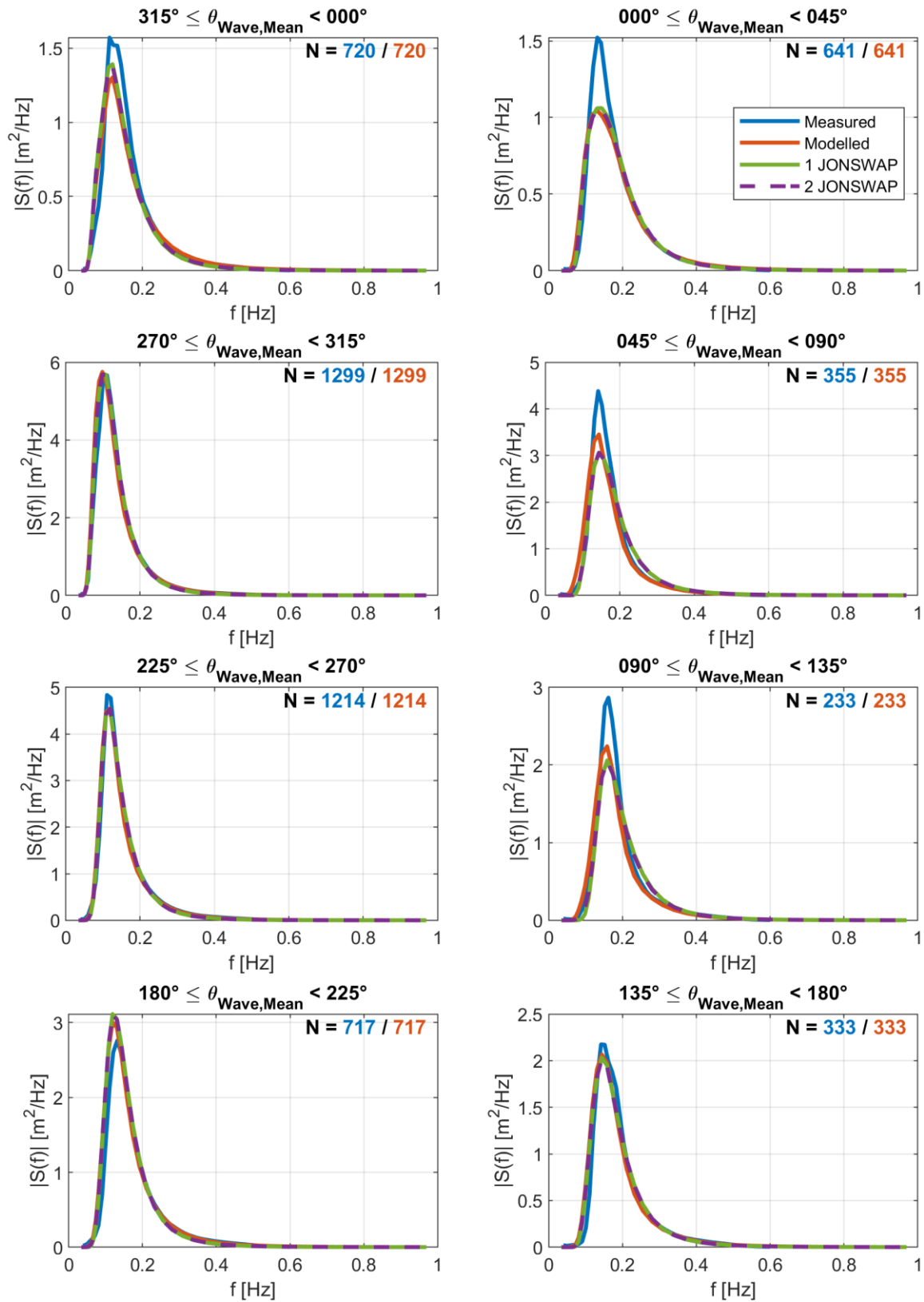


Figure F.3. NSI-1-LB, spectral validation, 45° sectors.

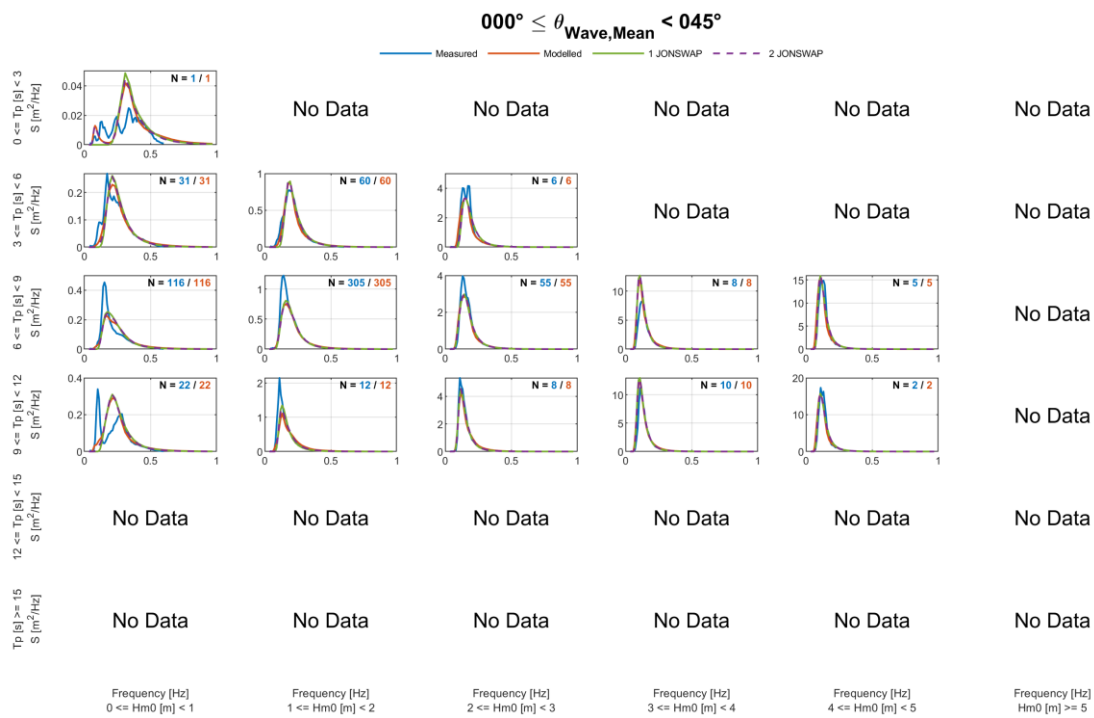


Figure F.4. NSI-1-LB, spectral validation, by Hm0 and Tp, 0-45° sector.

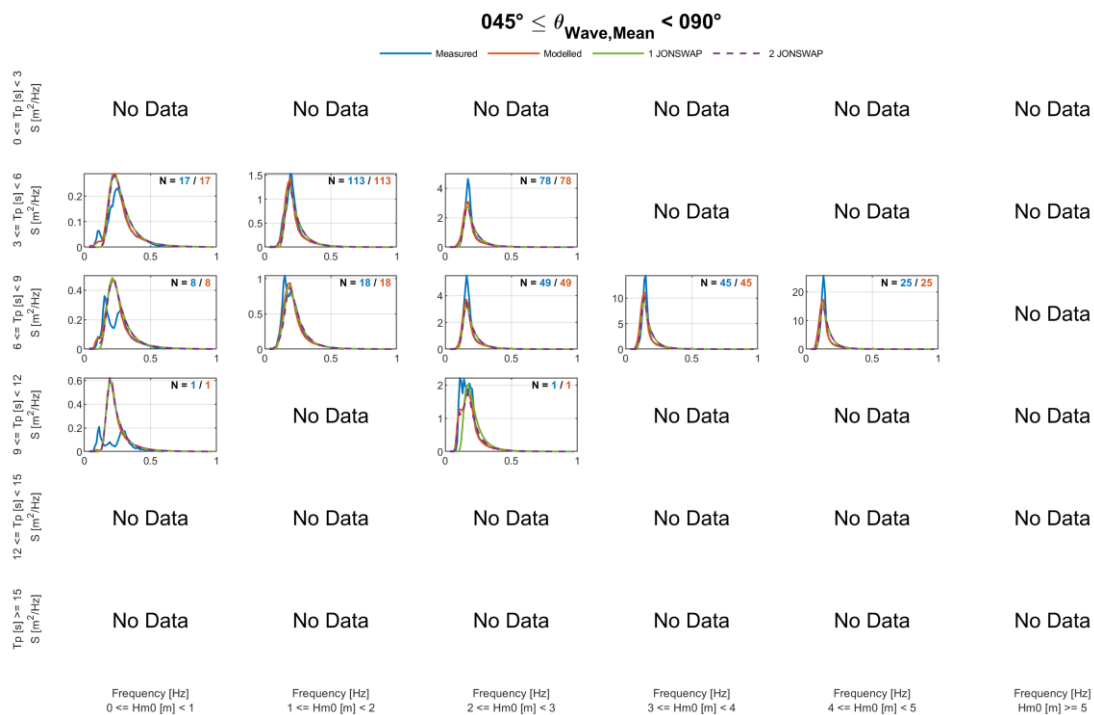


Figure F.5. NSI-1-LB, spectral validation, by Hm0 and Tp, 45-90° sector.

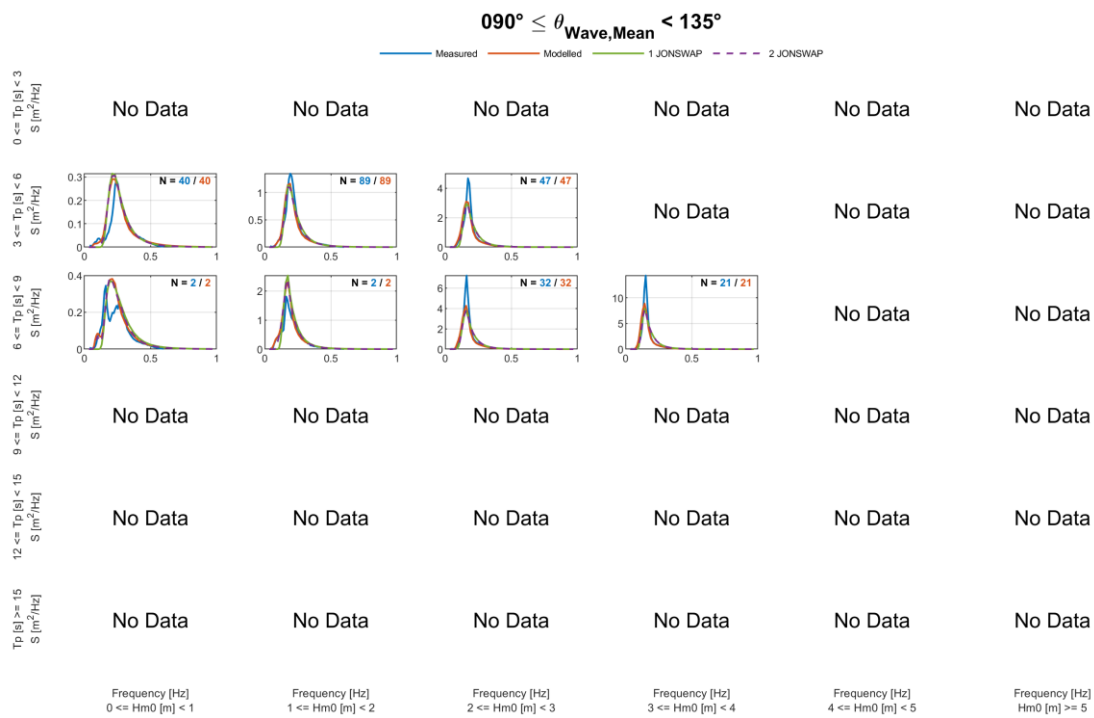


Figure F.6. NSI-1-LB, spectral validation, by Hm0 and Tp, 90-135° sector.

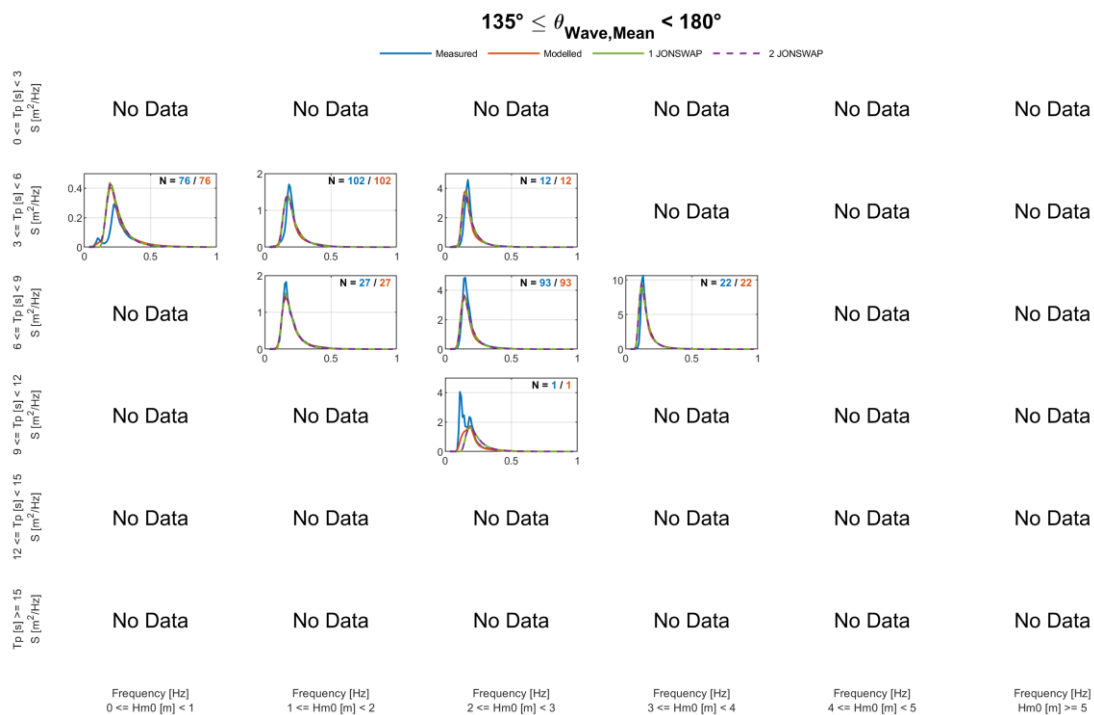
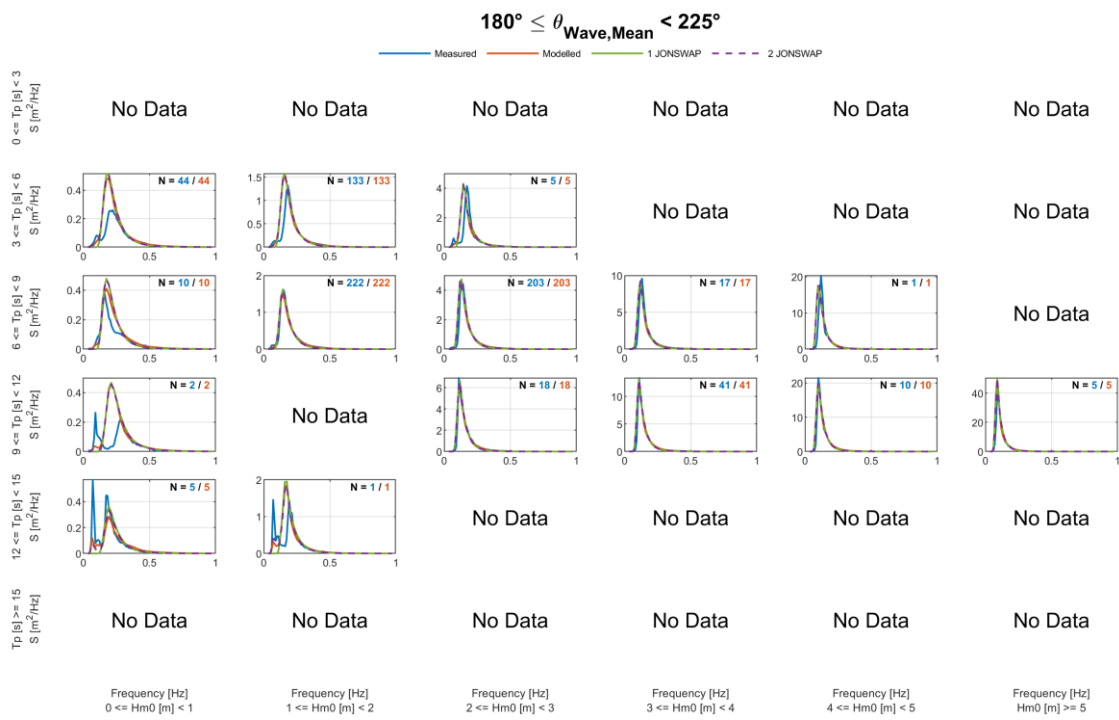


Figure F.7. NSI-1-LB, spectral validation, by Hm0 and Tp, 135-180° sector.



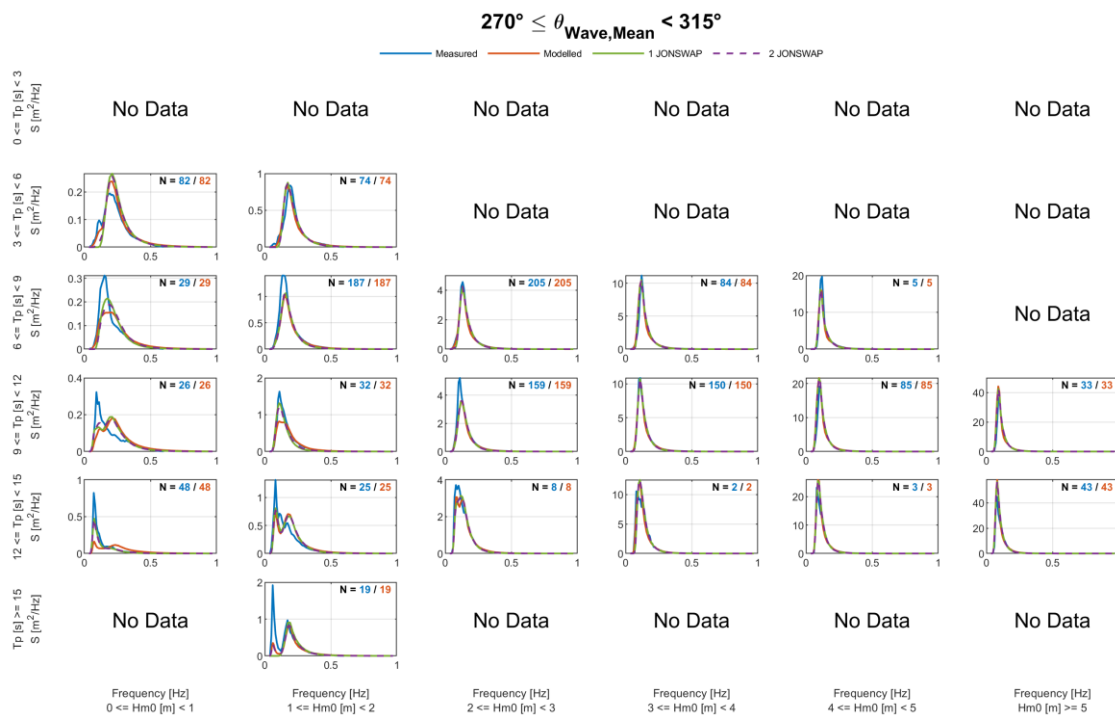


Figure F.10. NSI-1-LB, spectral validation, by Hm0 and Tp, 270-315° sector.

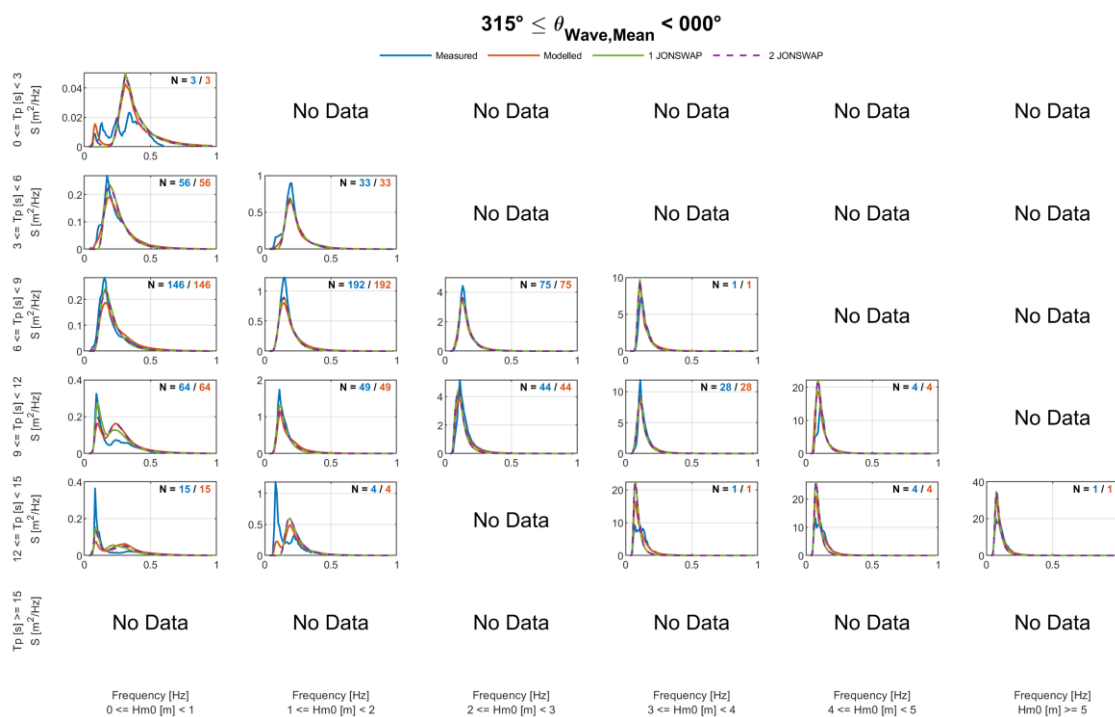


Figure F.11. NSI-1-LB, spectral validation, by Hm0 and Tp, 315-0° sector.



F.3.2 NSI-2-LB

F.3.2.1 Omni-Directional

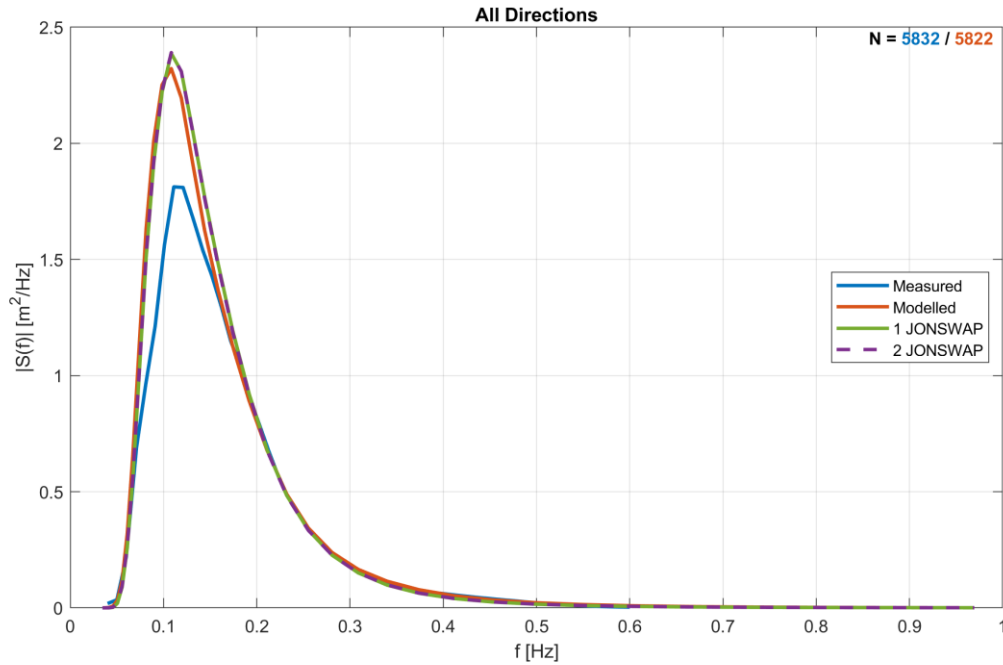


Figure F.12. NSI-2-LB, omni-directional spectral validation, all data.

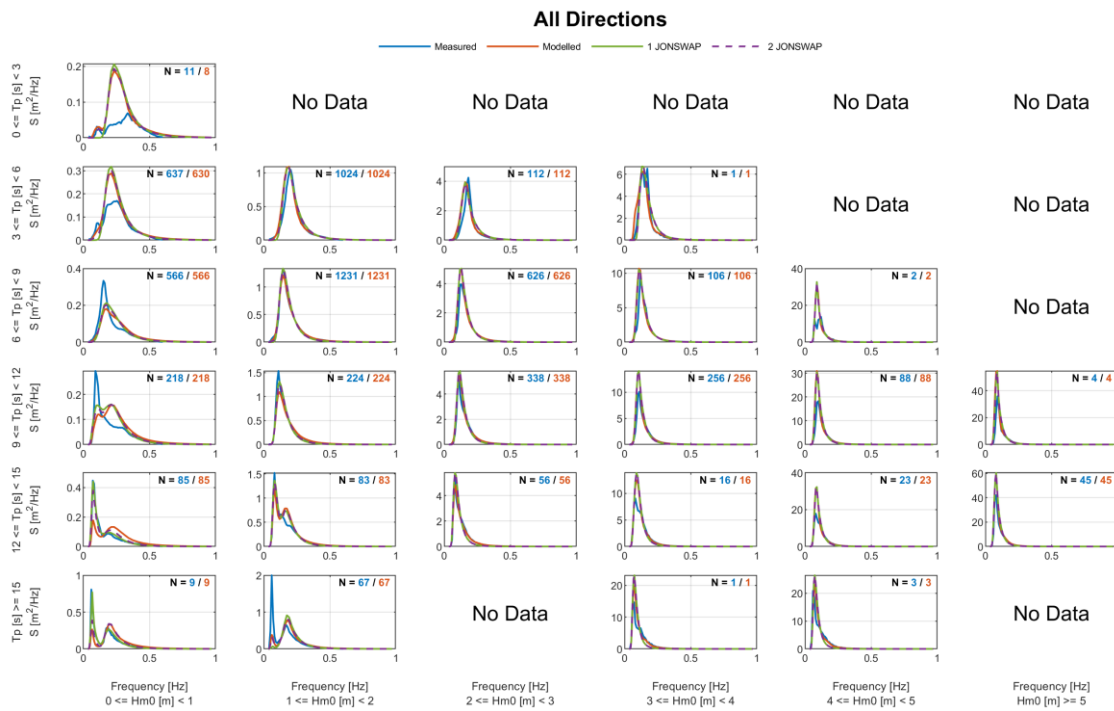


Figure F.13. NSI-2-LB, spectral validation, by Hm0 and Tp, all directions.



F.3.2.2 45° Sectors

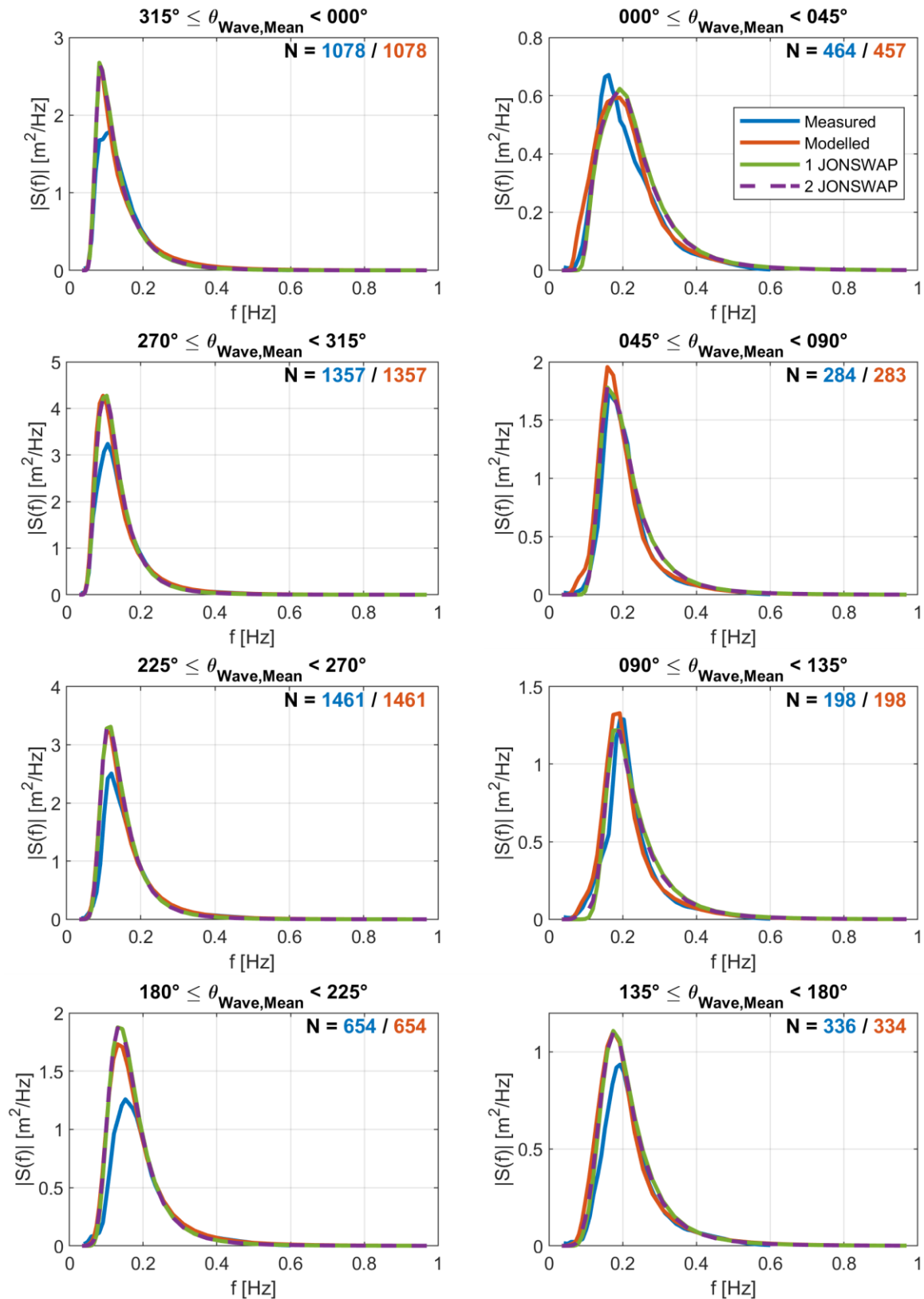


Figure F.14. NSI-2-LB, spectral validation, 45° sectors.

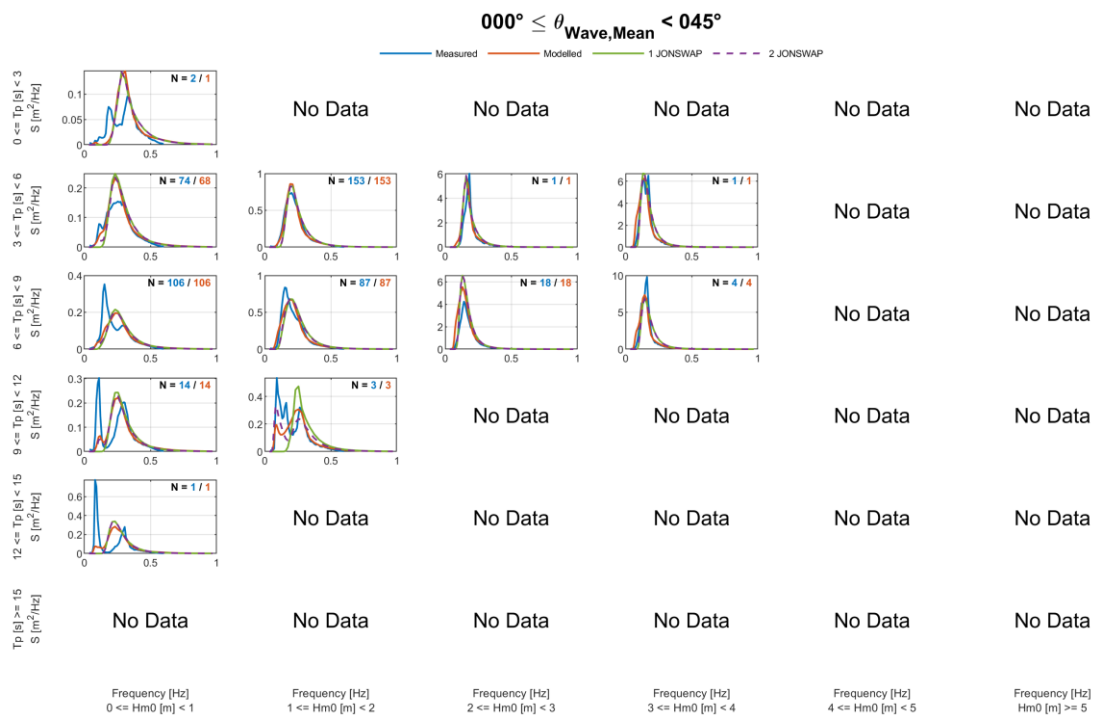


Figure F.15. NSI-2-LB, spectral validation, by Hm0 and Tp, 0-45° sector.

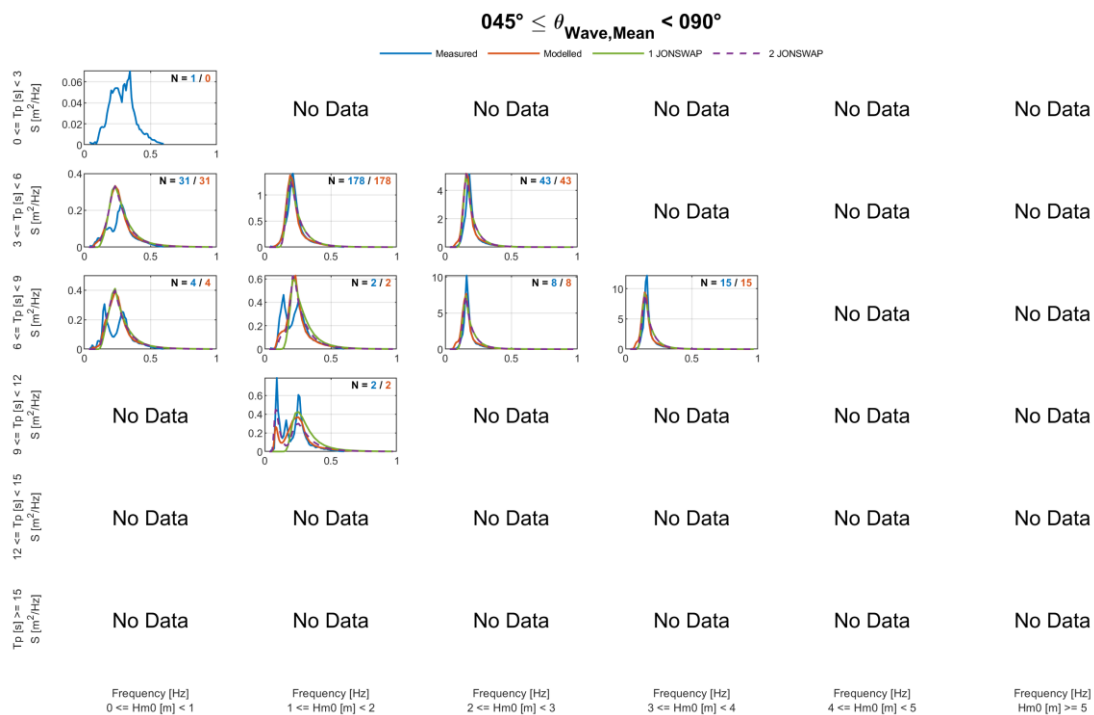


Figure F.16. NSI-2-LB, spectral validation, by Hm0 and Tp, 45-90° sector.

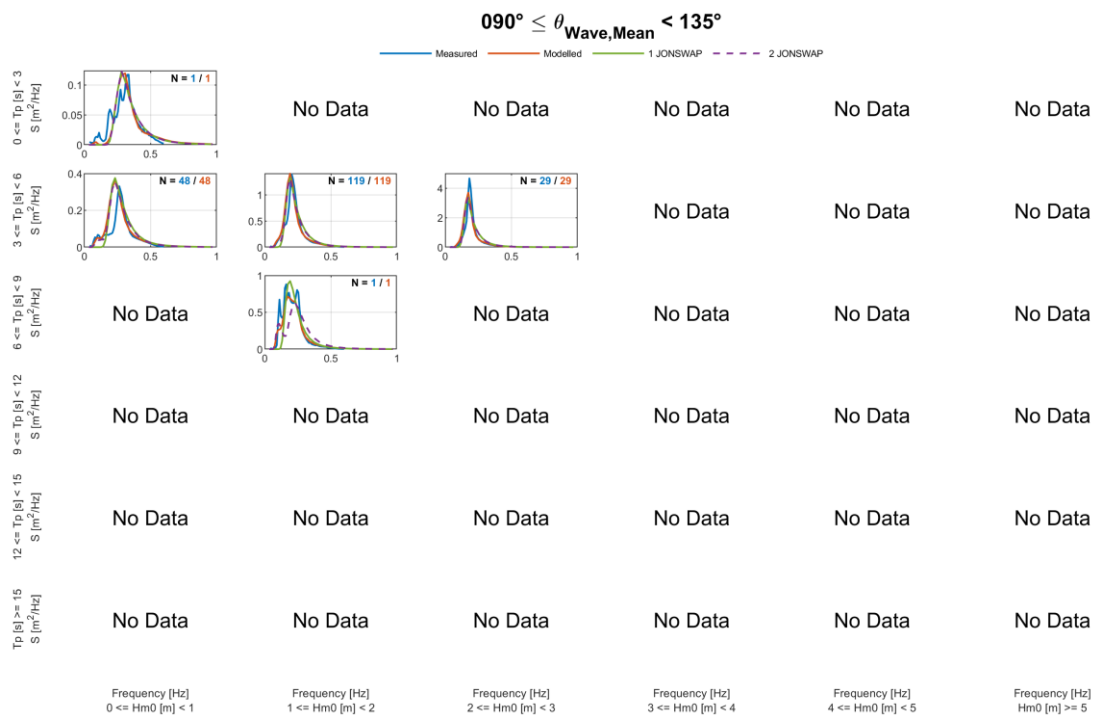


Figure F.17. NSI-2-LB, spectral validation, by Hm0 and Tp, 90-135° sector.

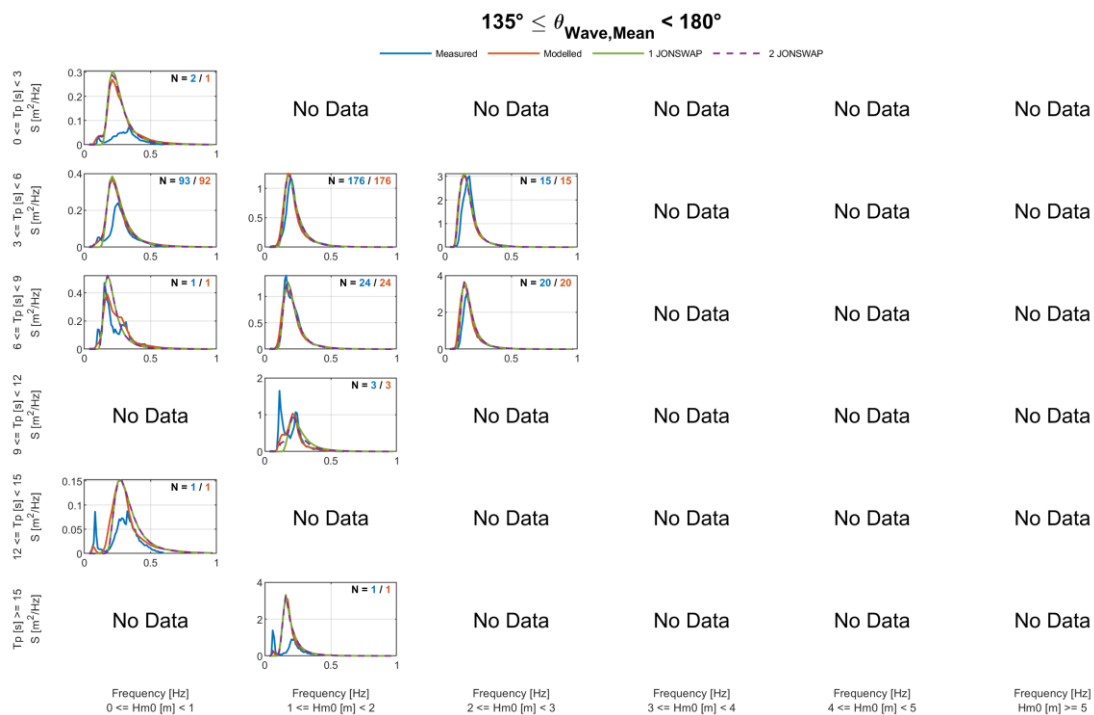


Figure F.18. NSI-2-LB, spectral validation, by Hm0 and Tp, 135-180° sector.

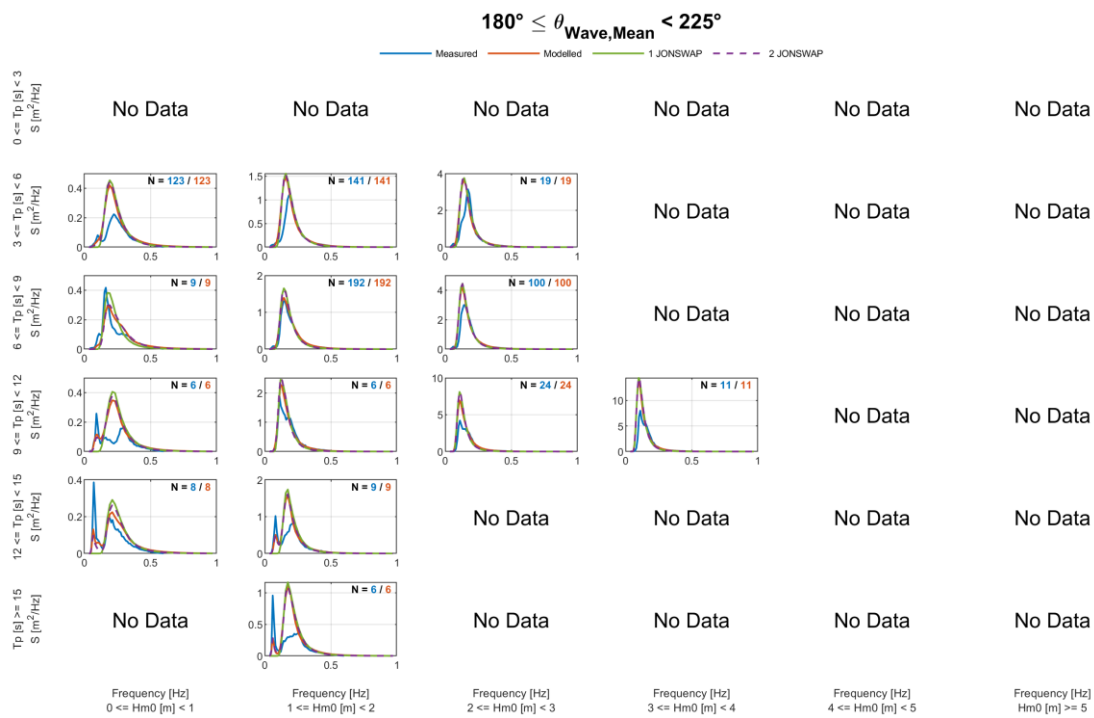


Figure F.19. NSI-2-LB, spectral validation, by Hm0 and Tp, 180-225° sector.

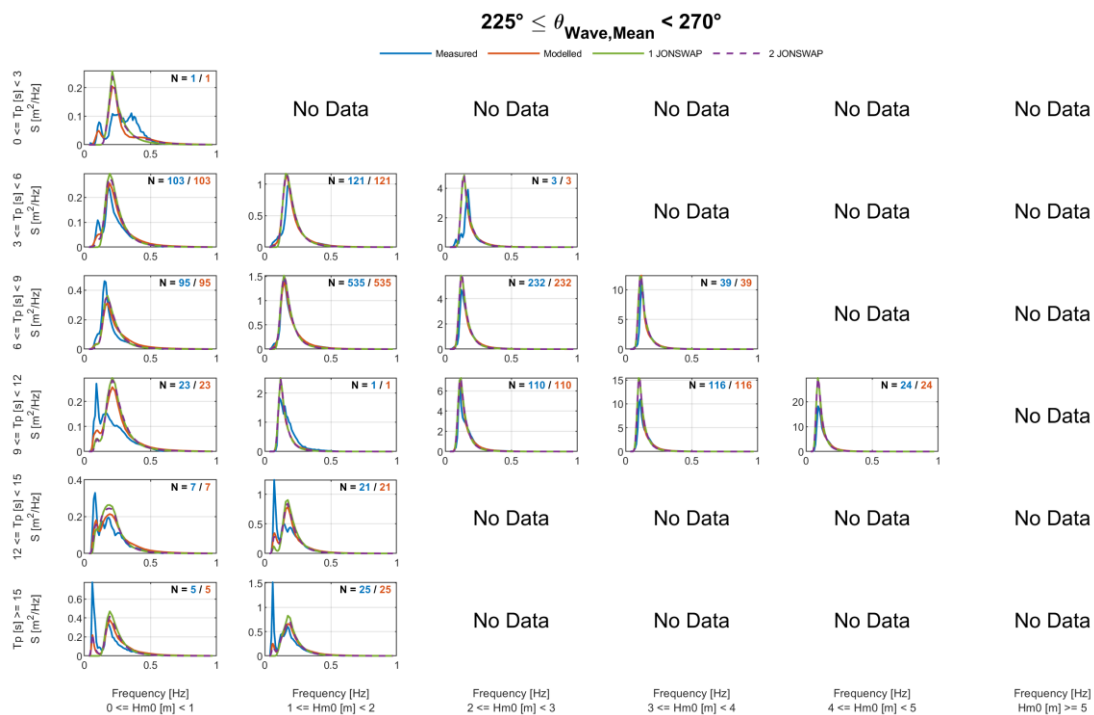


Figure F.20. NSI-2-LB, spectral validation, by Hm0 and Tp, 225-270° sector.

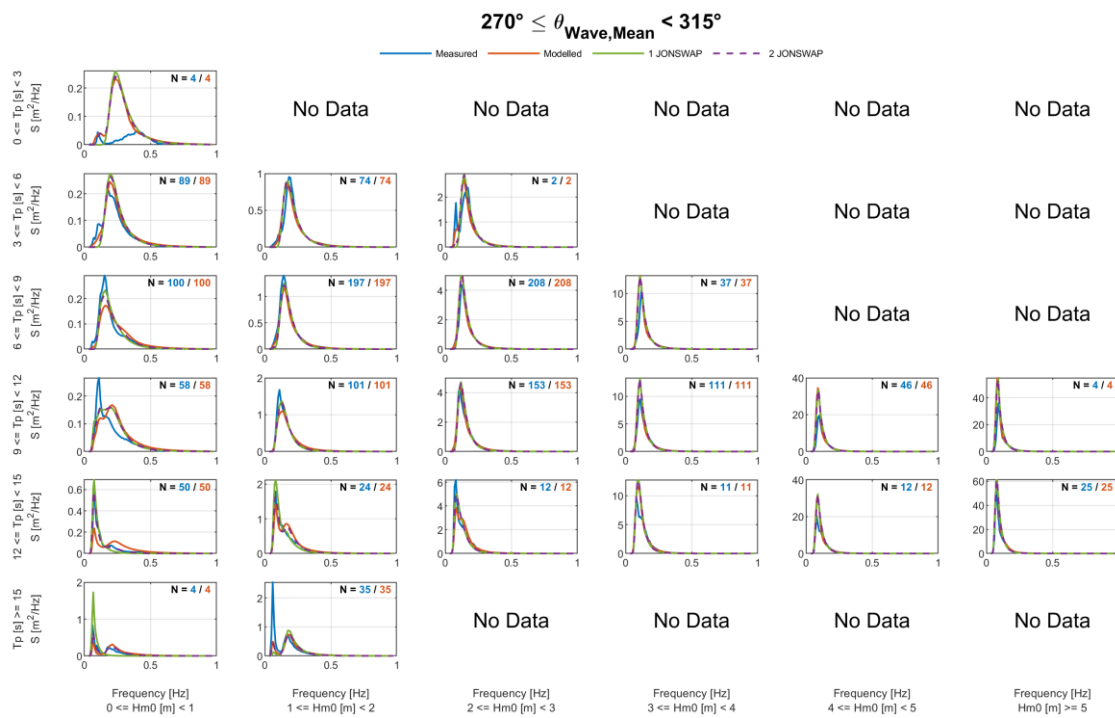


Figure F.21. NSI-2-LB, spectral validation, by Hm0 and Tp, 270-315° sector.

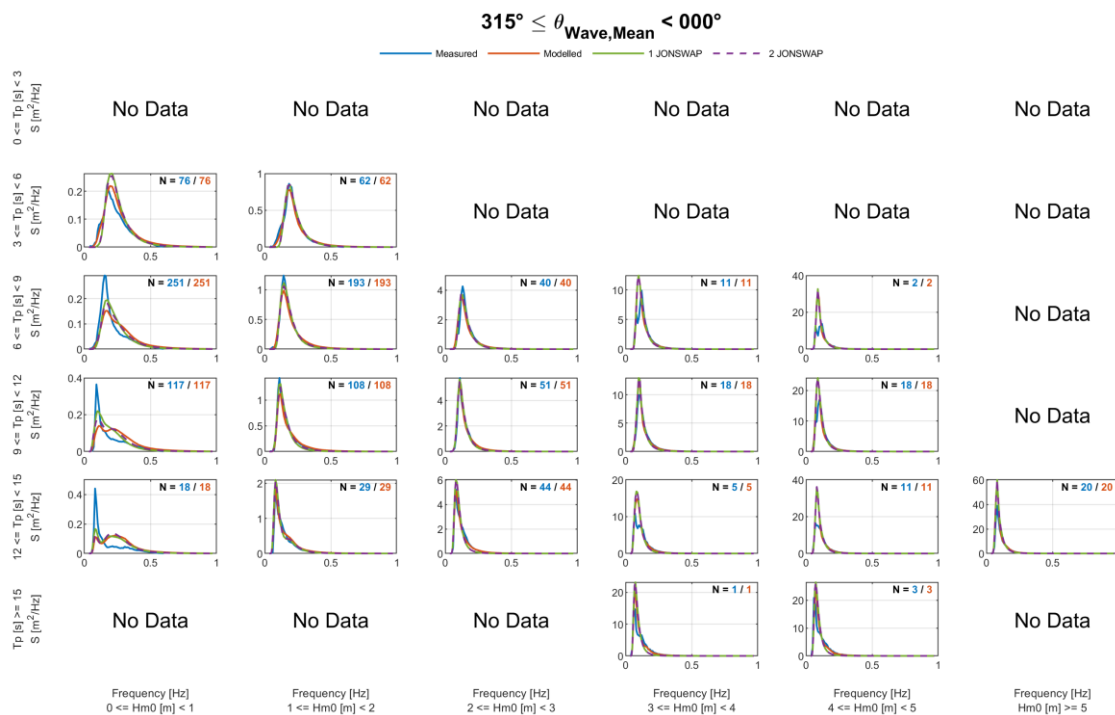


Figure F.22. NSI-2-LB, spectral validation, by Hm0 and Tp, 315-0° sector.



F.4 Selected Events

In this Section, plots are included to explore the temporal evolution of modelled and measured parameters and spectra around:

- Time stamps corresponding to the highest measured values of Hm0.
- Time stamps corresponding to the largest wind speeds from the north, south, east and west quadrants.

For NSI-1-LB, such plots are included in Section F.4.1, with those NSI-2-LB in Section F.4.2. In each case, the five events with the highest Hm0 are shown, and one event for each of the four wind direction quadrants. Each figure contains the following:

- Time-series of significant wave height (Hm0, second row), peak wave period (Tp, third row) and mean wave direction (Mdir, fourth row). Throughout, these have been rederived from 3-hour averaged spectra; measurements are shown in blue, model data in red.
- Time-series of wind speed and wind direction (fifth and sixth rows respectively). Again, measurements are shown in blue, model data in red. Please note that measurements are taken from the lowest level of the LiDAR whilst model data comes from ERA5 modelled data at 10 mAMSL for the LiDAR location. Since the wind speeds are provided for indicative purposes only in reviewing the wave model, no adjustments have been made to account for the differences in elevations.
- Omni-directional spectra at three-hour intervals from nine hours before the peak Hm0 to three hours after the peak Hm0 (top row). Note that if data are not available exactly at the required time, the closest spectrum is plotted. For clarity, the timestamp of each spectrum is shown in the top right of each omni-directional spectrum plot. Again, measurements are shown in blue, model data in red. 1 JONSWAP and 2 JONSWAP representations of the model data are overlaid in dashed purple and green respectively.
- Directional spectra at three-hour intervals from nine hours before the peak Hm0 to three hours after the peak Hm0 (row five: measured data; row six: modelled data; row seven: 2 JONSWAP representation; row eight: 1 JONSWAP representation). As with omni-directional spectra, if data is not available exactly at the required time, the closest spectrum is shown. For clarity, the timestamp of each spectrum is shown directly above where it is drawn.
- Time-series of omnidirectional spectra (bottom two rows).

When comparing *directional* spectra, it should be noted that some features of the measured spectra, such as the level of blurring/sharpness of energy peaks, is dependent on the method used for their estimation (see Section F.2). As a result, such comparisons should be used for guidance only.



F.4.1 NSI-1-LB



Metocean Data Overview – North Sea I Offshore Wind Farm

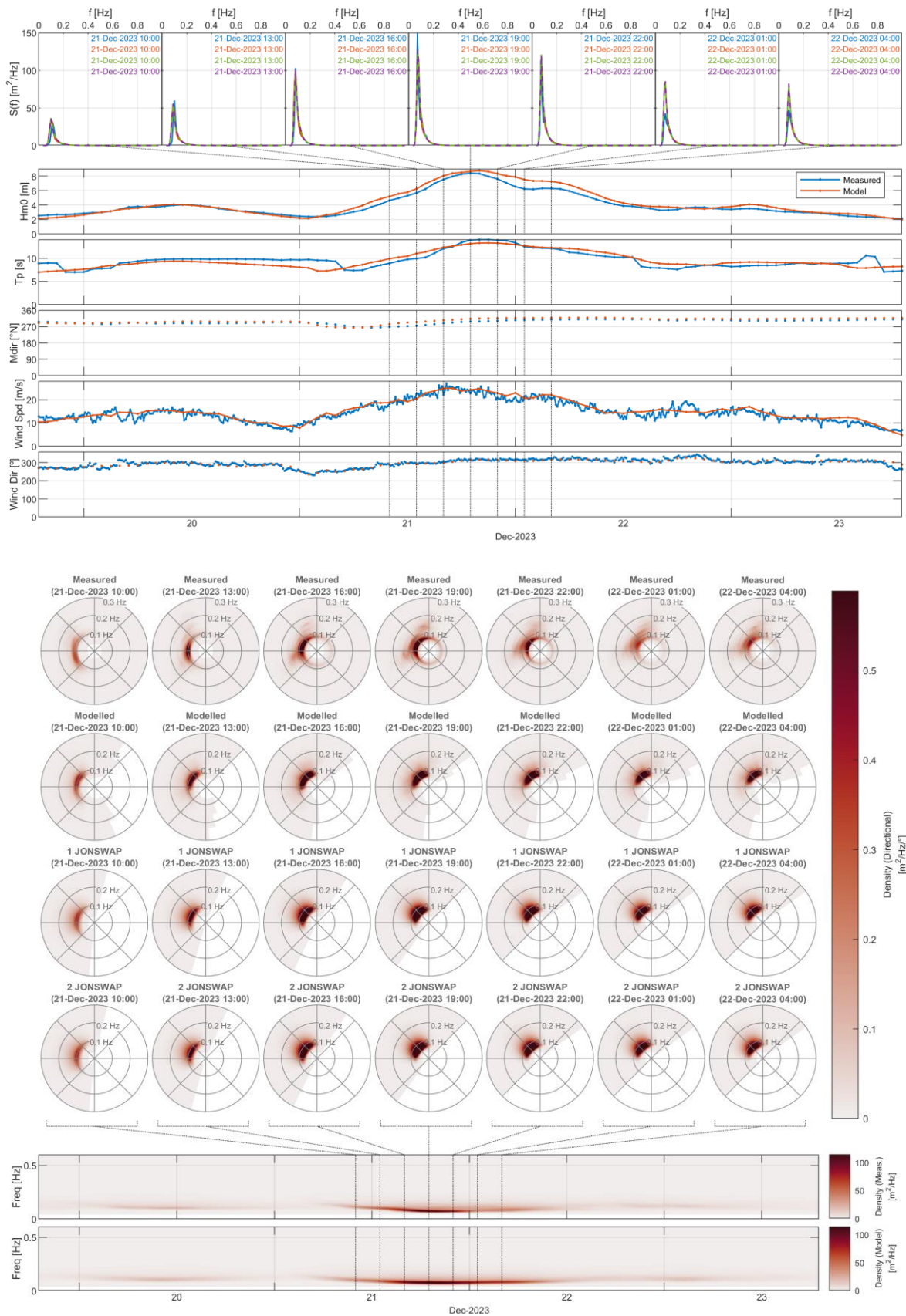


Figure F.23. NSI-1-LB, largest Hm0 peak.



Metocean Data Overview – North Sea I Offshore Wind Farm

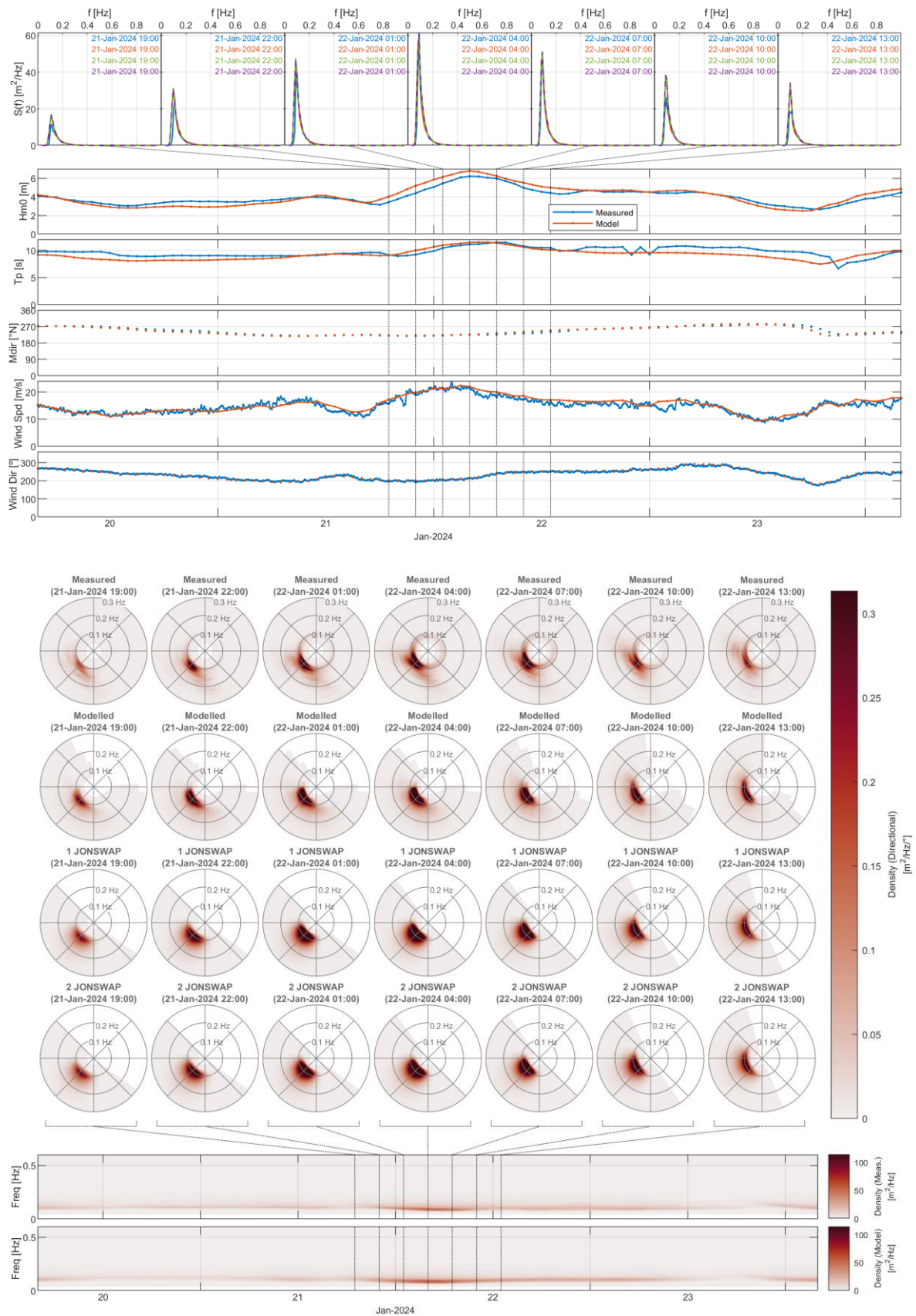


Figure F.24. NSI-1-LB, second largest Hm0 peak.



Metocean Data Overview – North Sea I Offshore Wind Farm

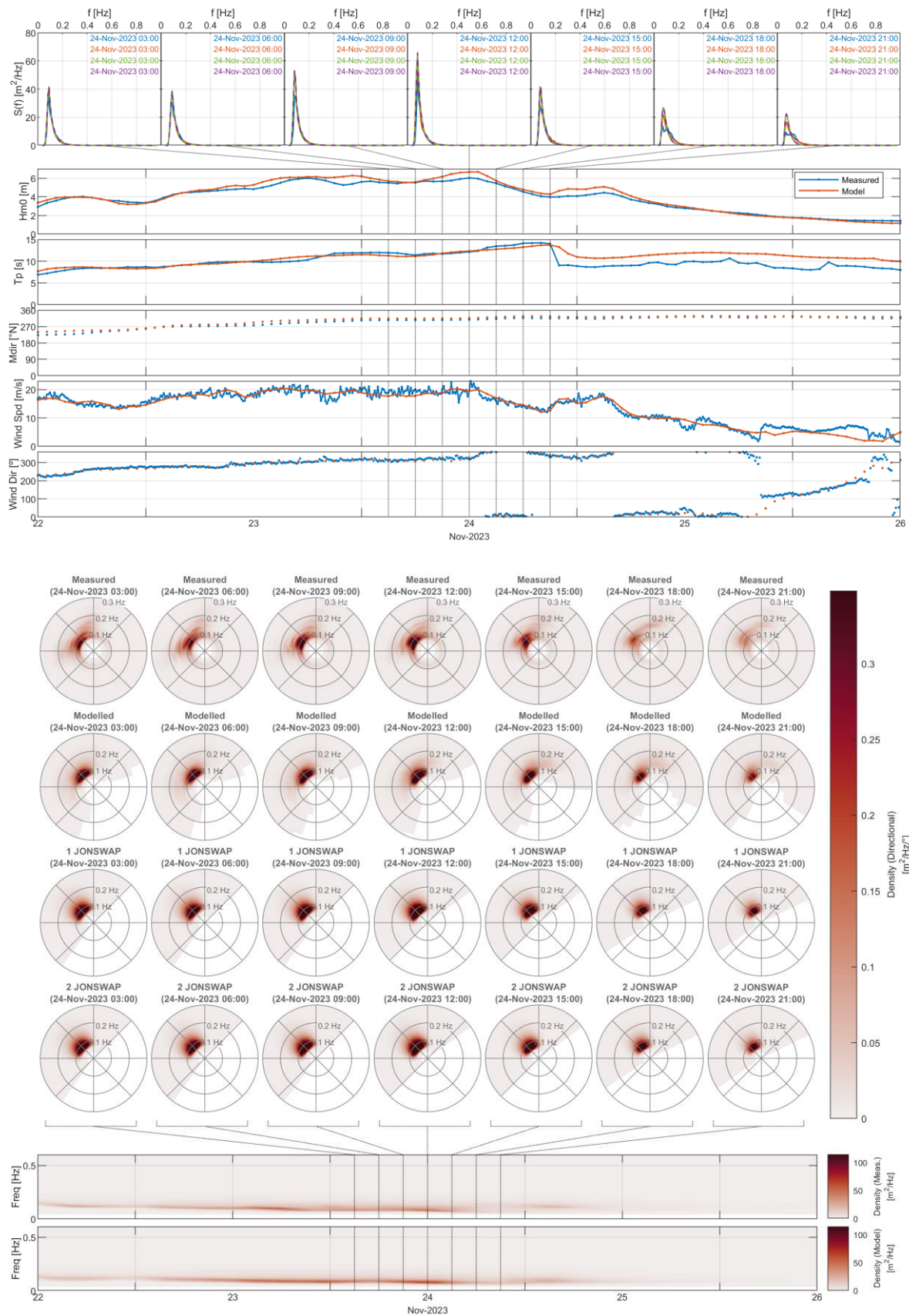


Figure F.25. NSI-1-LB, third largest Hm0 peak.



Metocean Data Overview – North Sea I Offshore Wind Farm

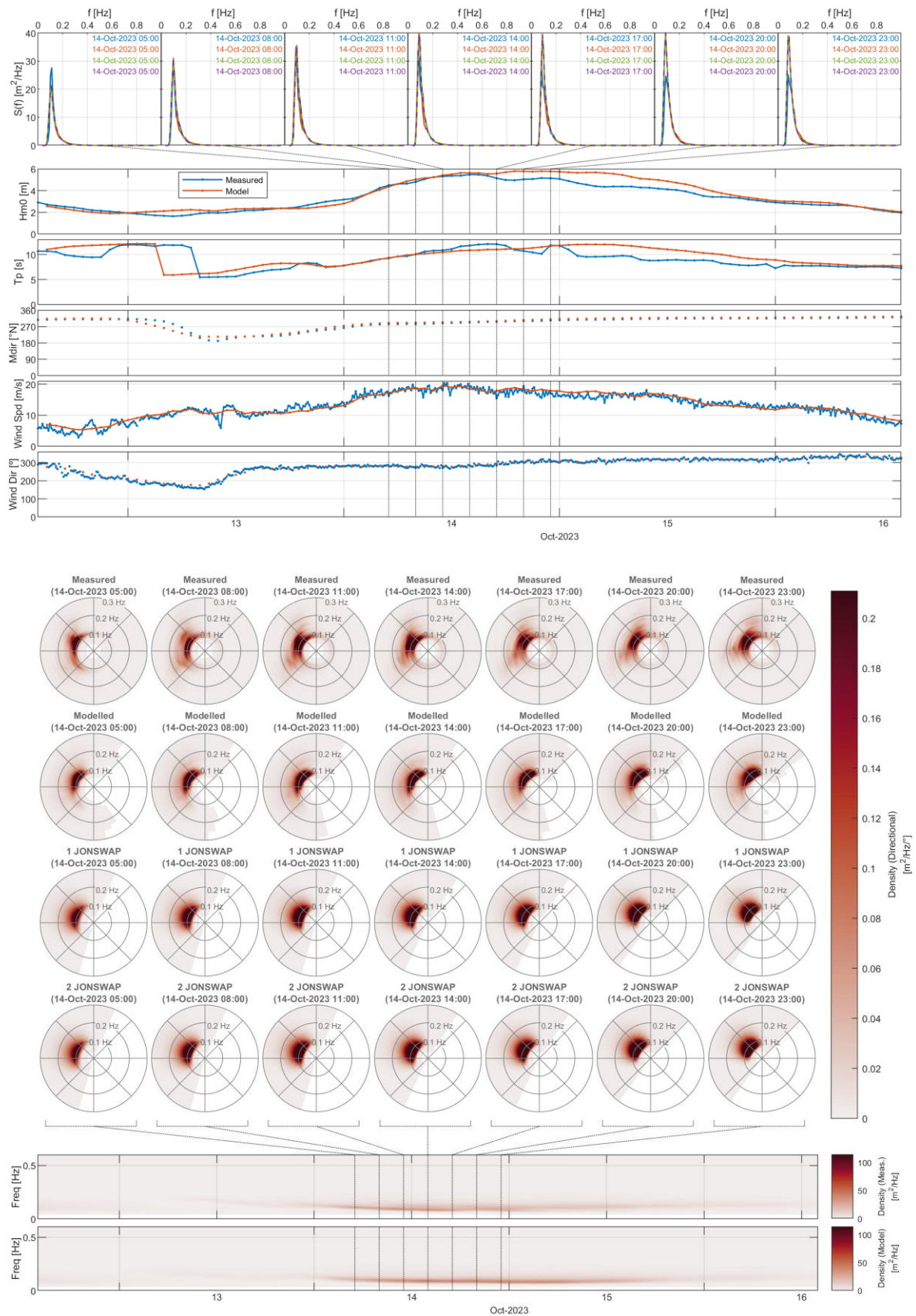


Figure F.26. NSI-1-LB, fourth largest H_{m0} peak.



Metocean Data Overview – North Sea I Offshore Wind Farm

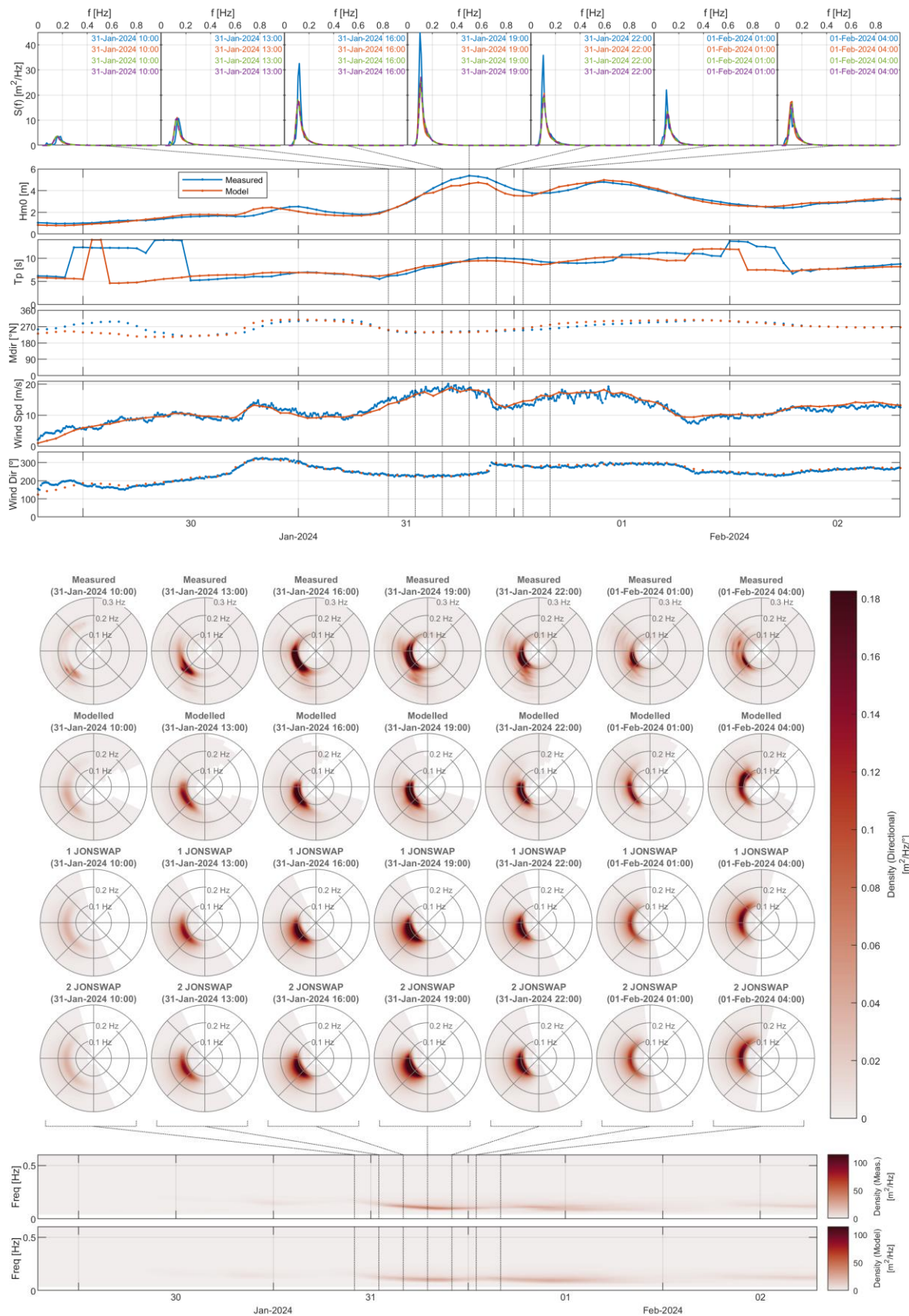


Figure F.27. NSI-1-LB, fifth largest H_{m0} peak.



Metocean Data Overview – North Sea I Offshore Wind Farm

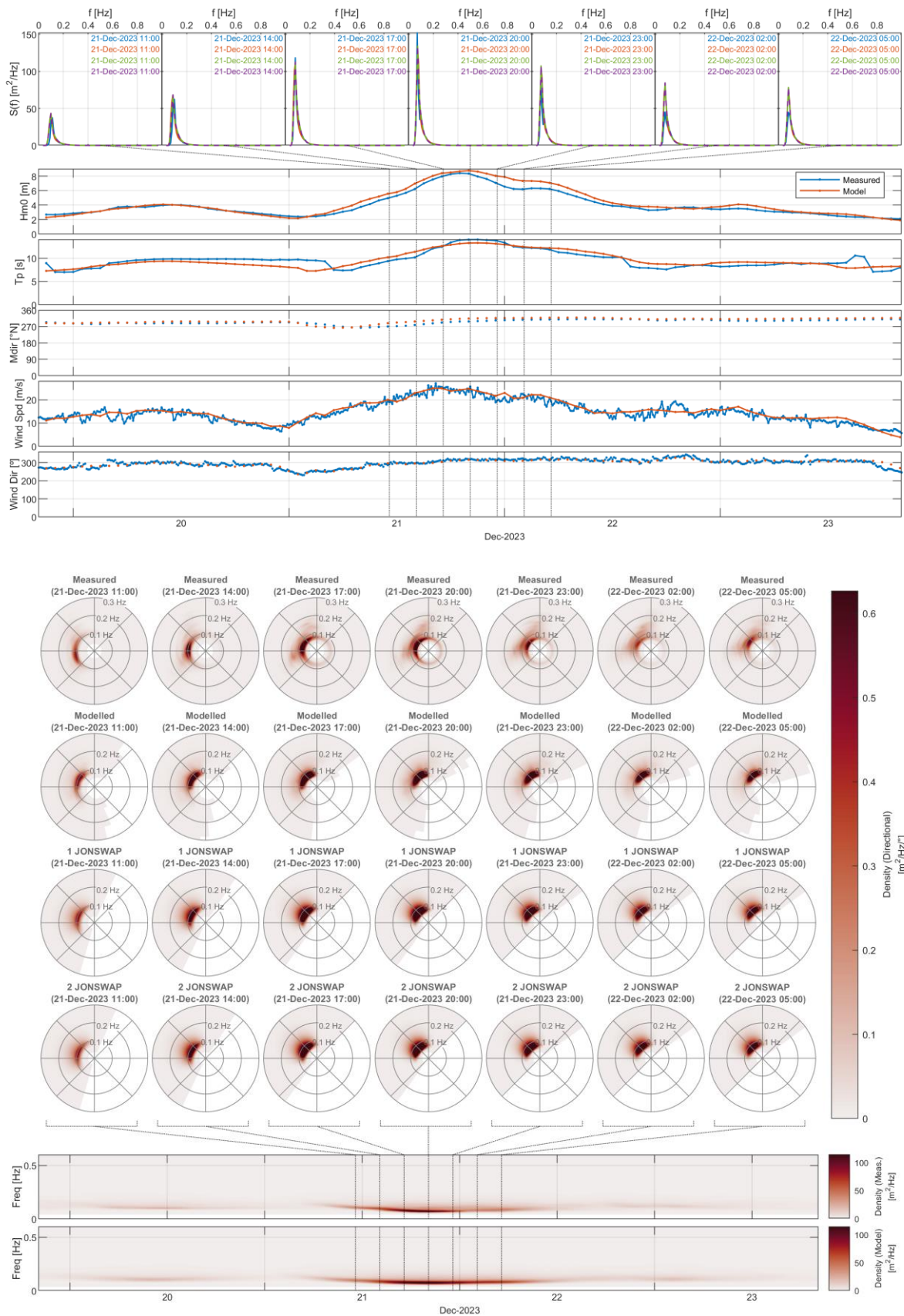


Figure F.28. NSI-1-LB, largest measured wind speed from the north.



Metocean Data Overview – North Sea I Offshore Wind Farm

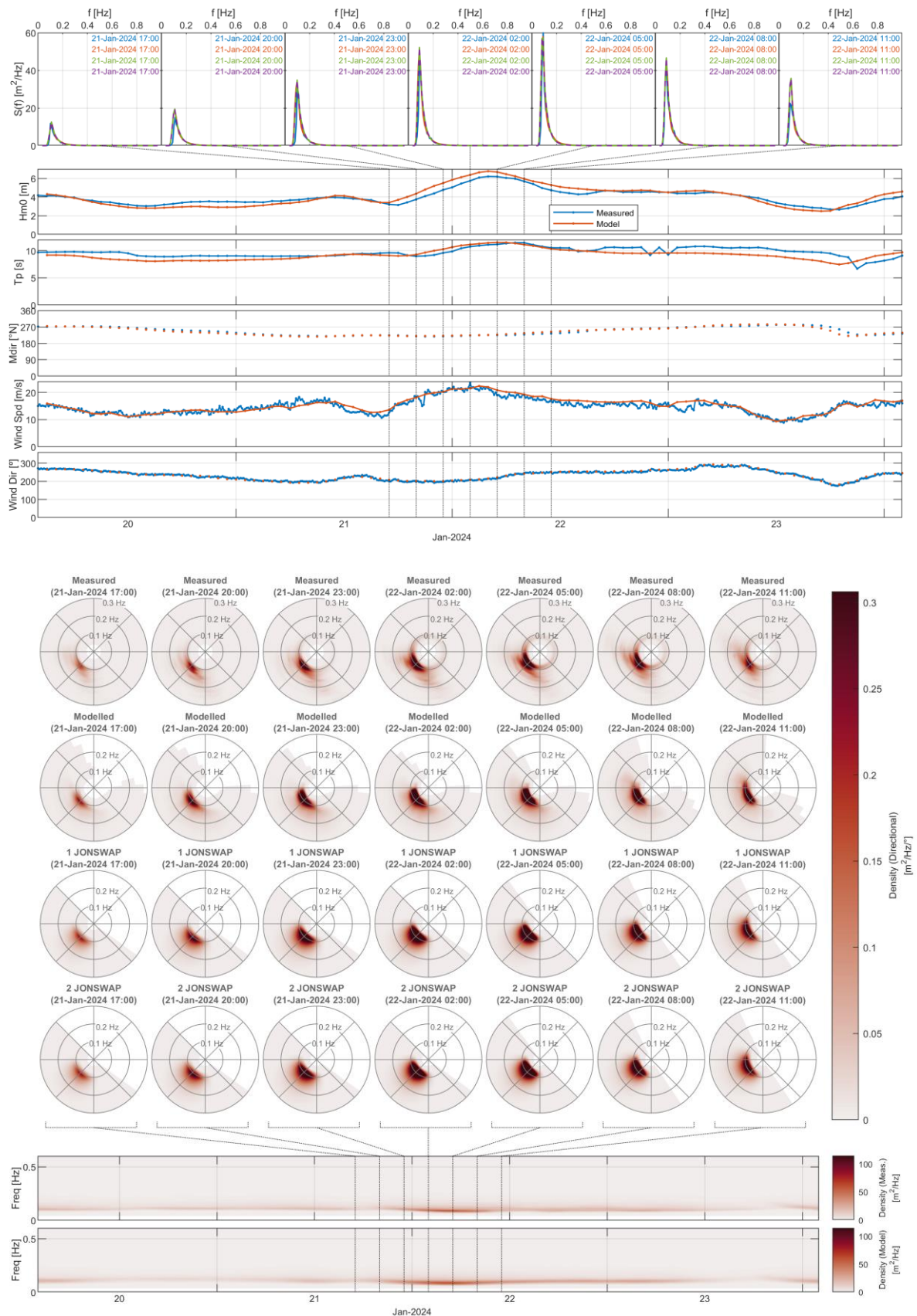


Figure F.29. NSI-1-LB, largest measured wind speed from the south.



Metocean Data Overview – North Sea I Offshore Wind Farm

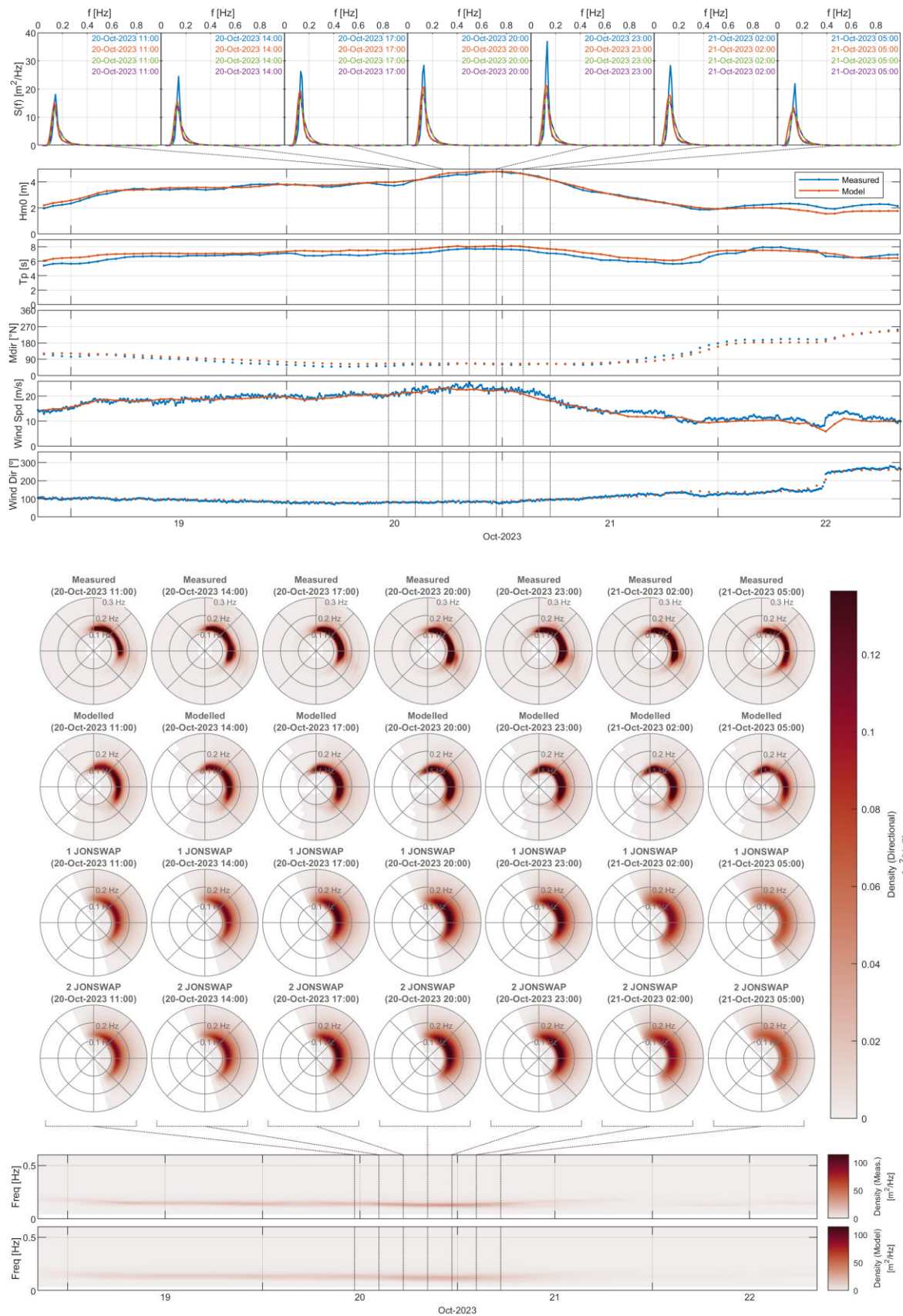


Figure F.30. NSI-1-LB, largest measured wind speed from the east.



Metocean Data Overview – North Sea I Offshore Wind Farm

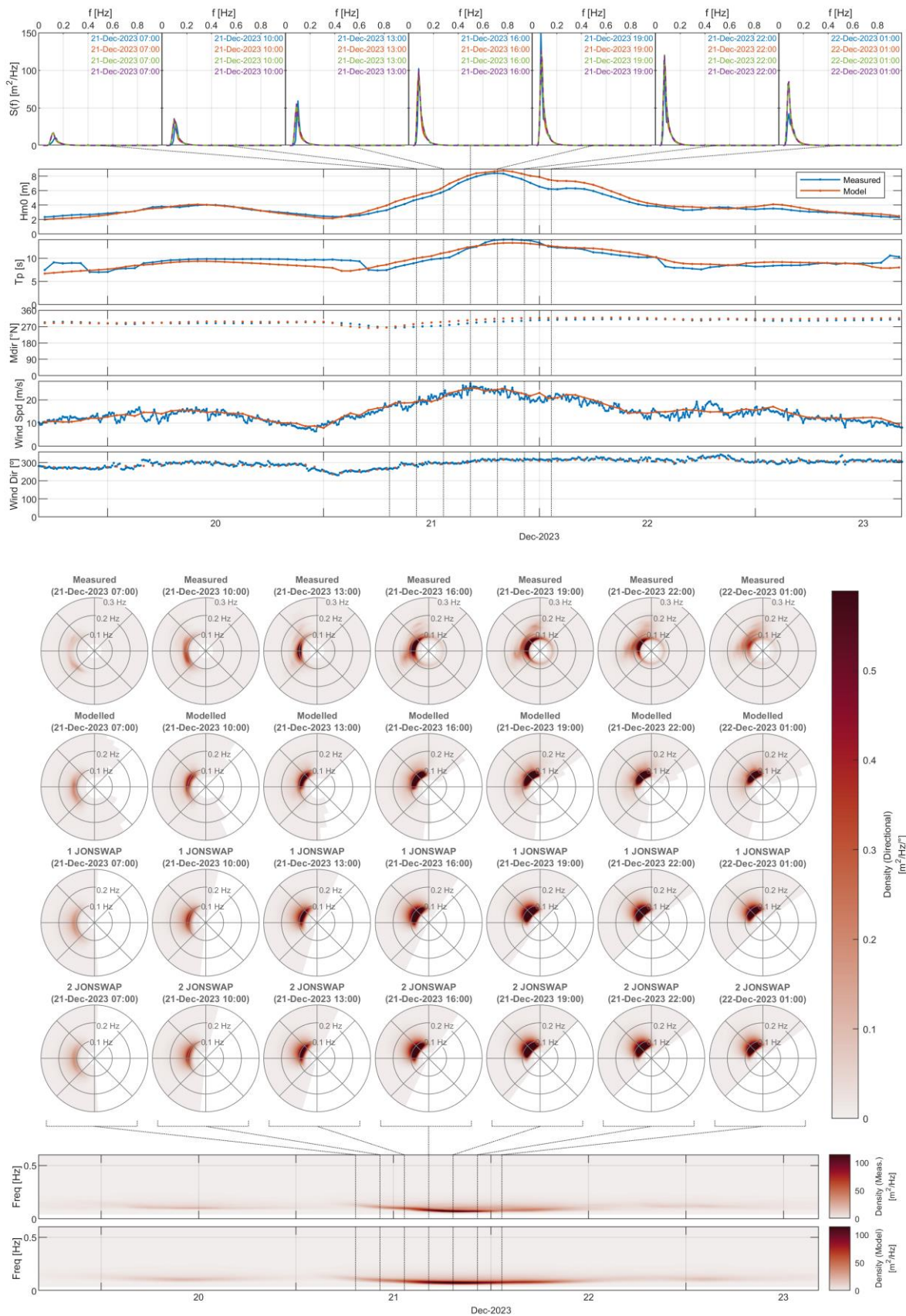


Figure F.31. NSI-1-LB, largest measured wind speed from the west.



F.4.2 NSI-2-LB



Metocean Data Overview – North Sea I Offshore Wind Farm

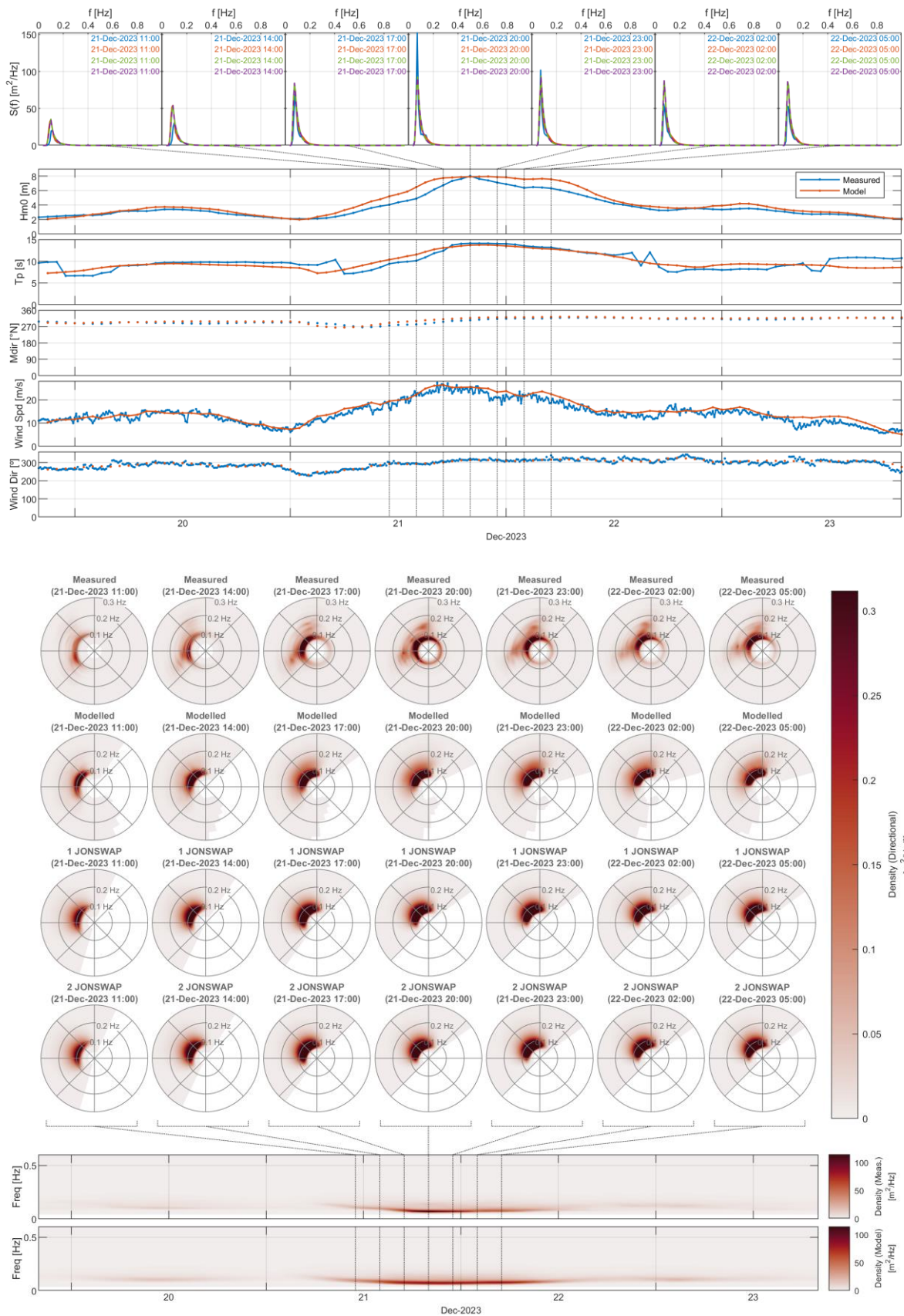


Figure F.32. NSI-2-LB, largest Hm0 peak.



Metocean Data Overview – North Sea I Offshore Wind Farm

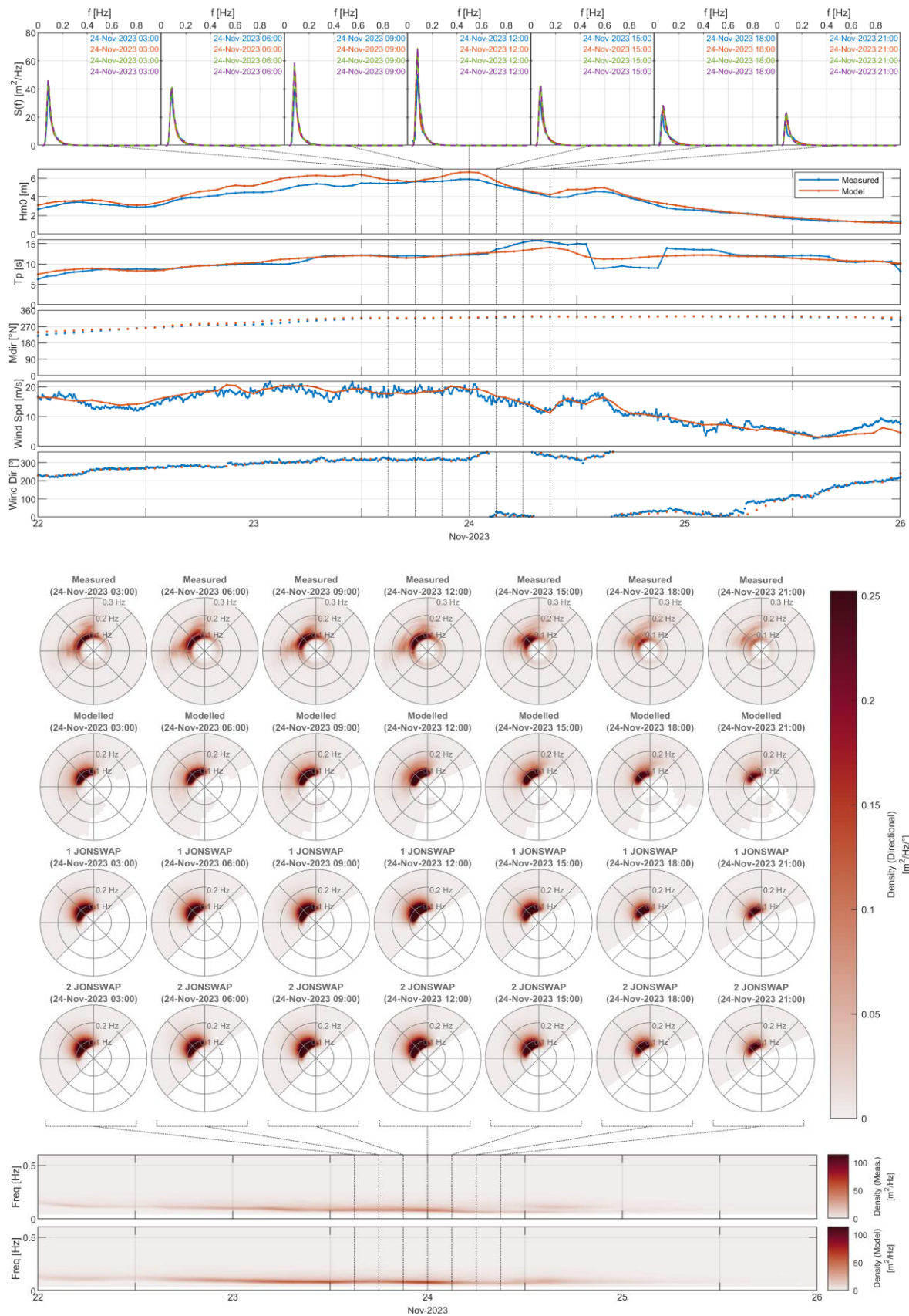


Figure F.33. NSI-2-LB, second largest Hm0 peak.



Metocean Data Overview – North Sea I Offshore Wind Farm

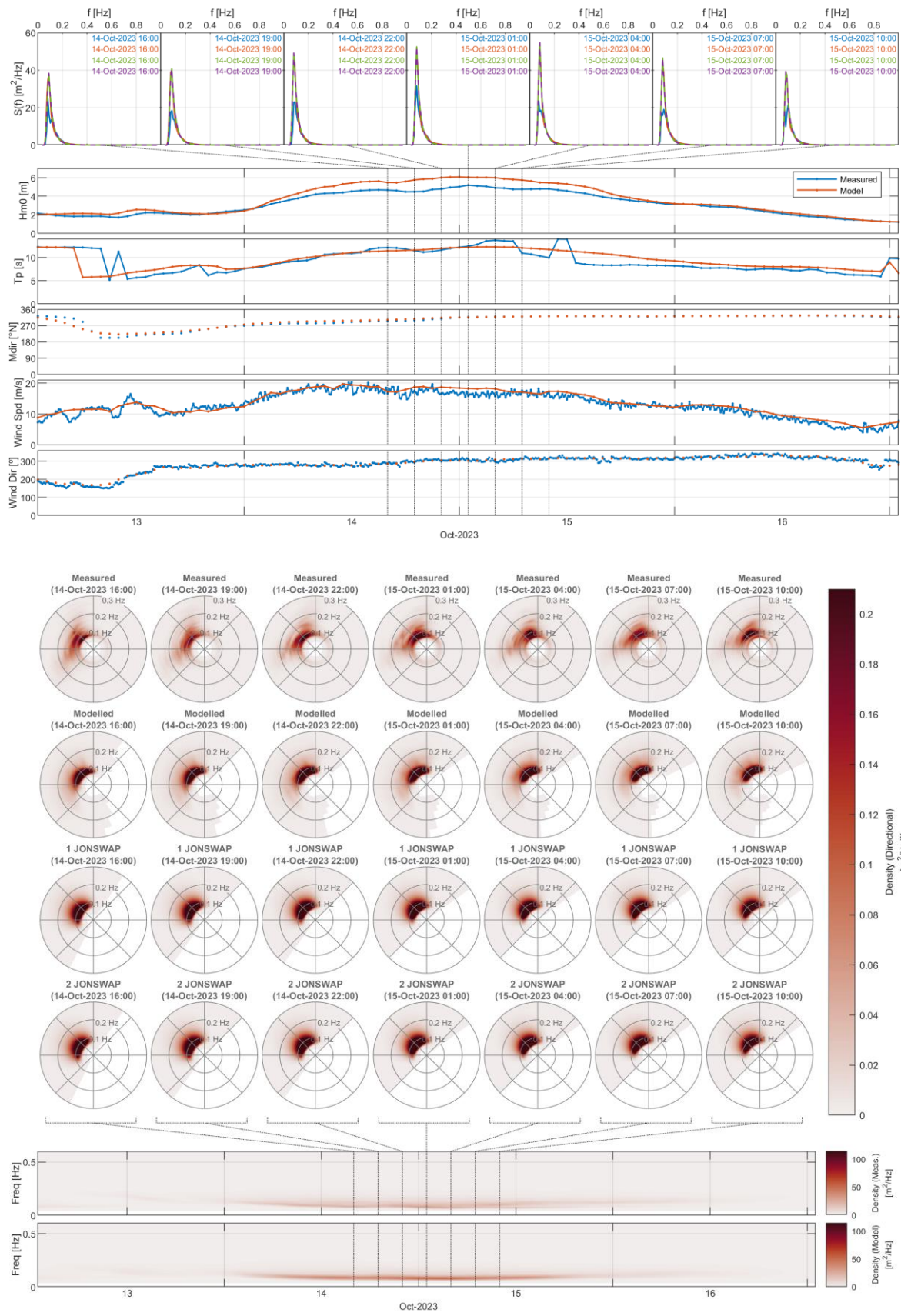


Figure F.34. NSI-2-LB, third largest Hm0 peak.



Metocean Data Overview – North Sea I Offshore Wind Farm

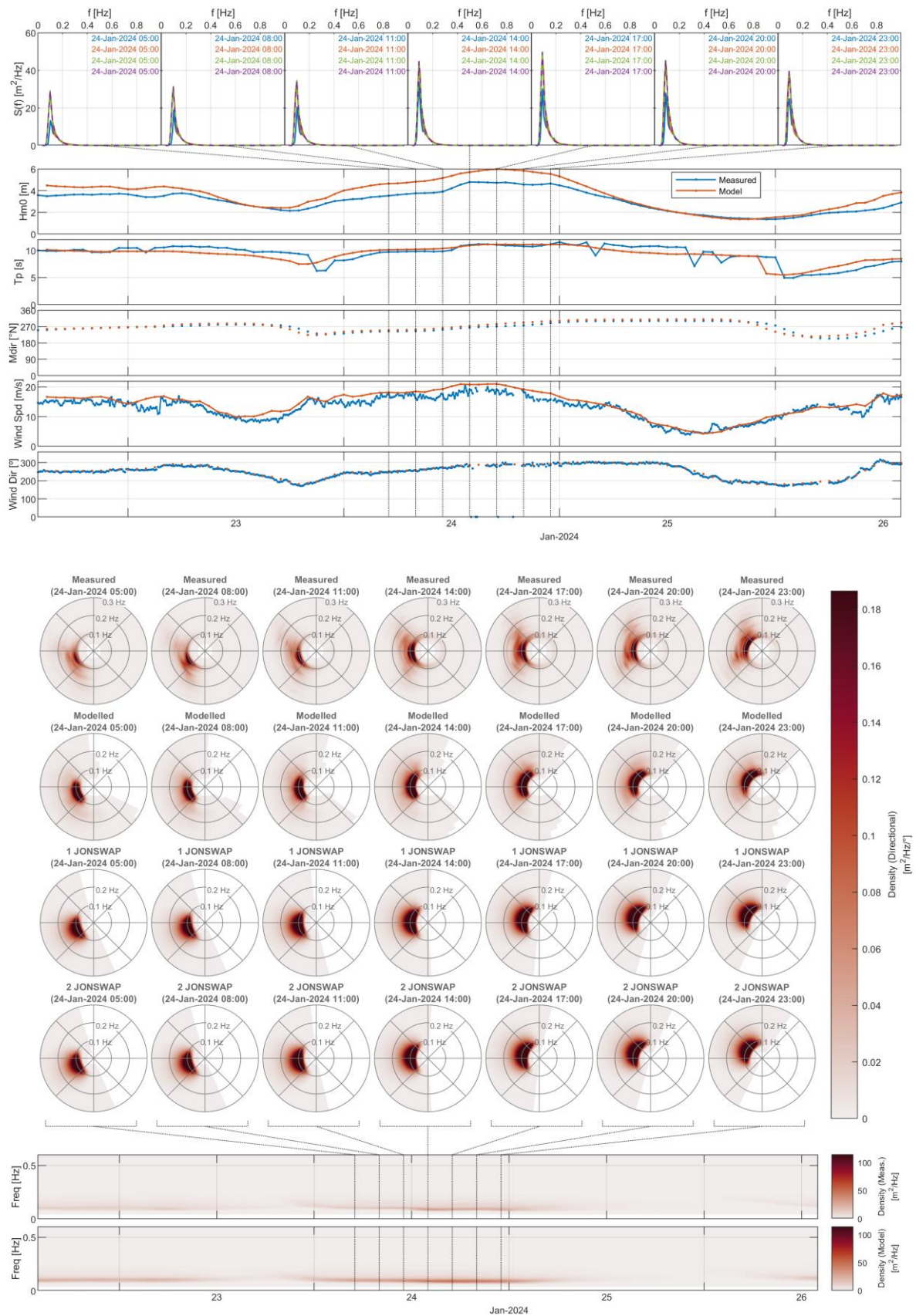


Figure F.35. NSI-2-LB, fourth largest H_{m0} peak.



Metocean Data Overview – North Sea I Offshore Wind Farm

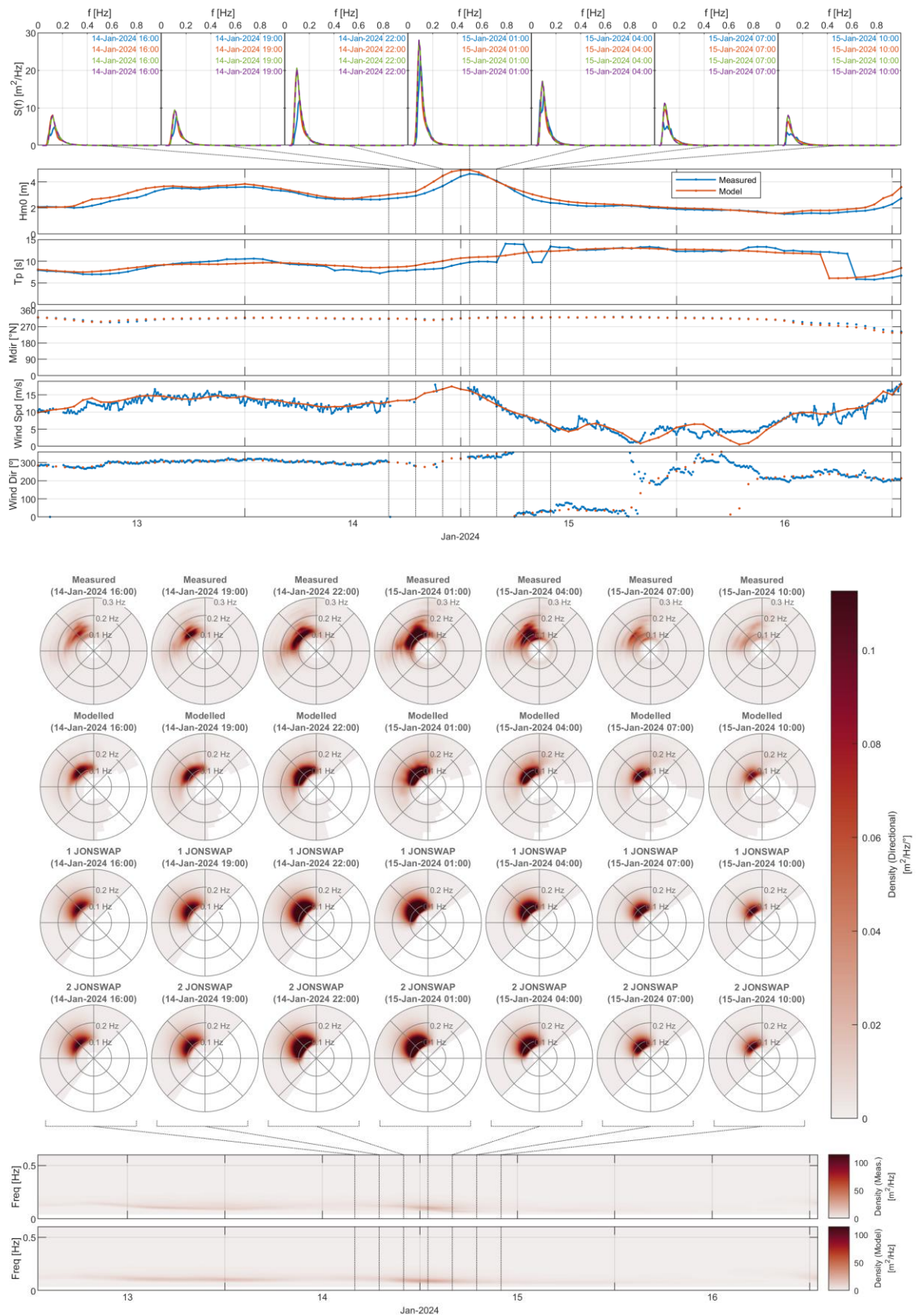


Figure F.36. NSI-2-LB, fifth largest Hm0 peak.



Metocean Data Overview – North Sea I Offshore Wind Farm

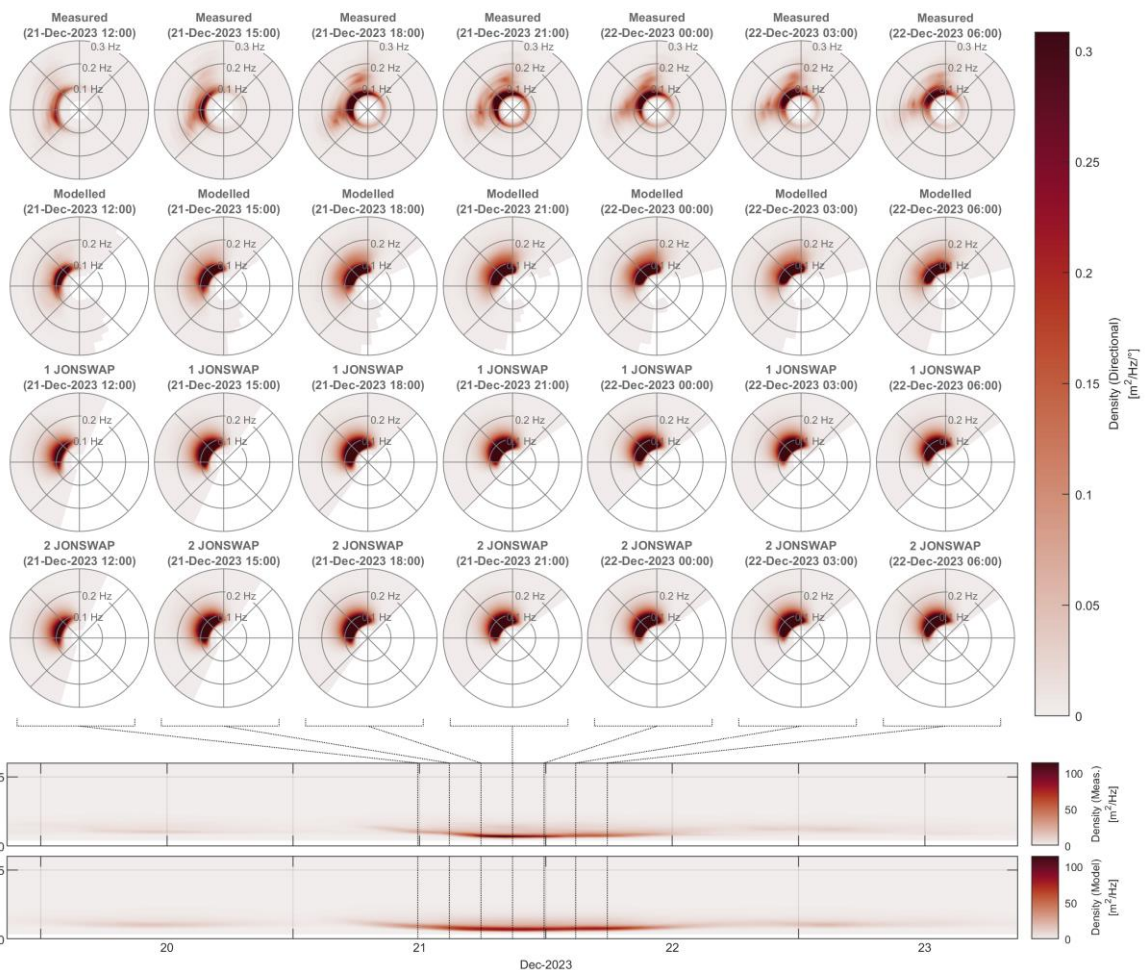
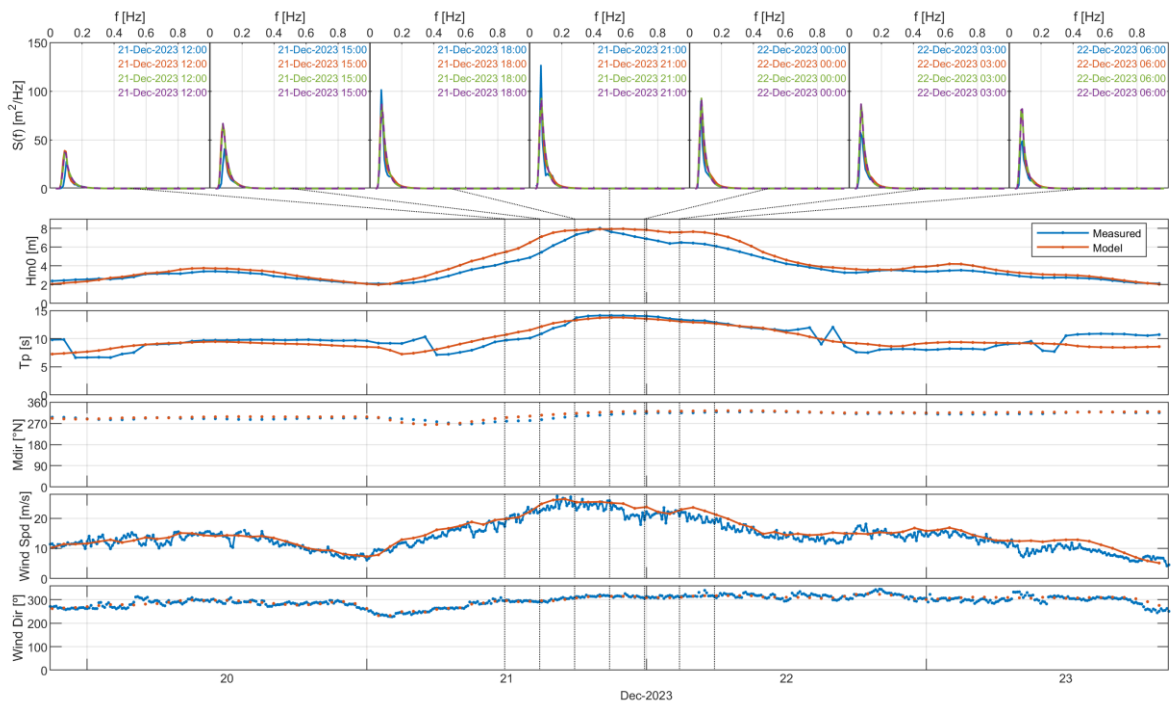


Figure F.37. NSI-2-LB, largest measured wind speed from the north.



Metocean Data Overview – North Sea I Offshore Wind Farm

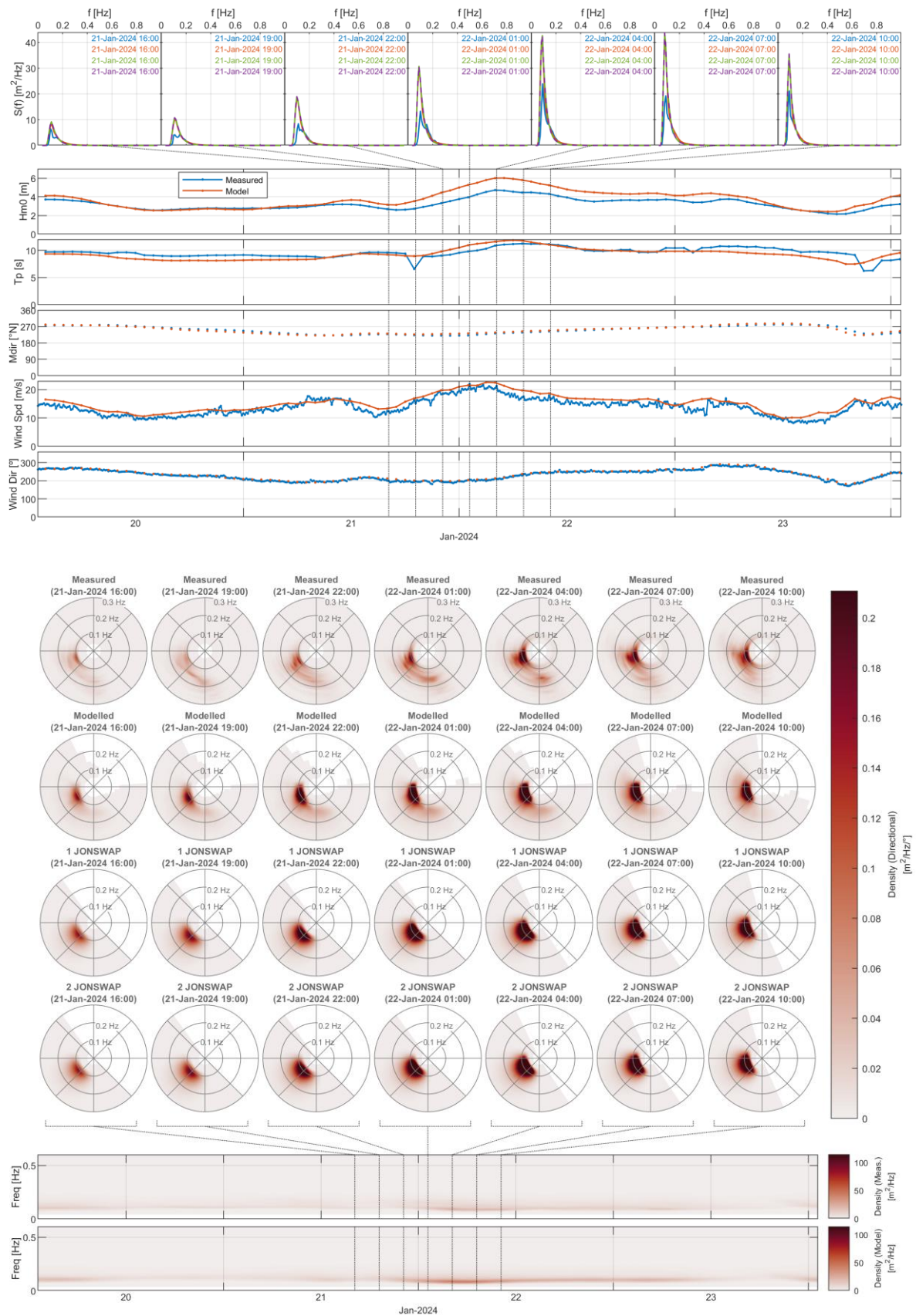


Figure F.38. NSI-2-LB, largest measured wind speed from the south.



Metocean Data Overview – North Sea I Offshore Wind Farm

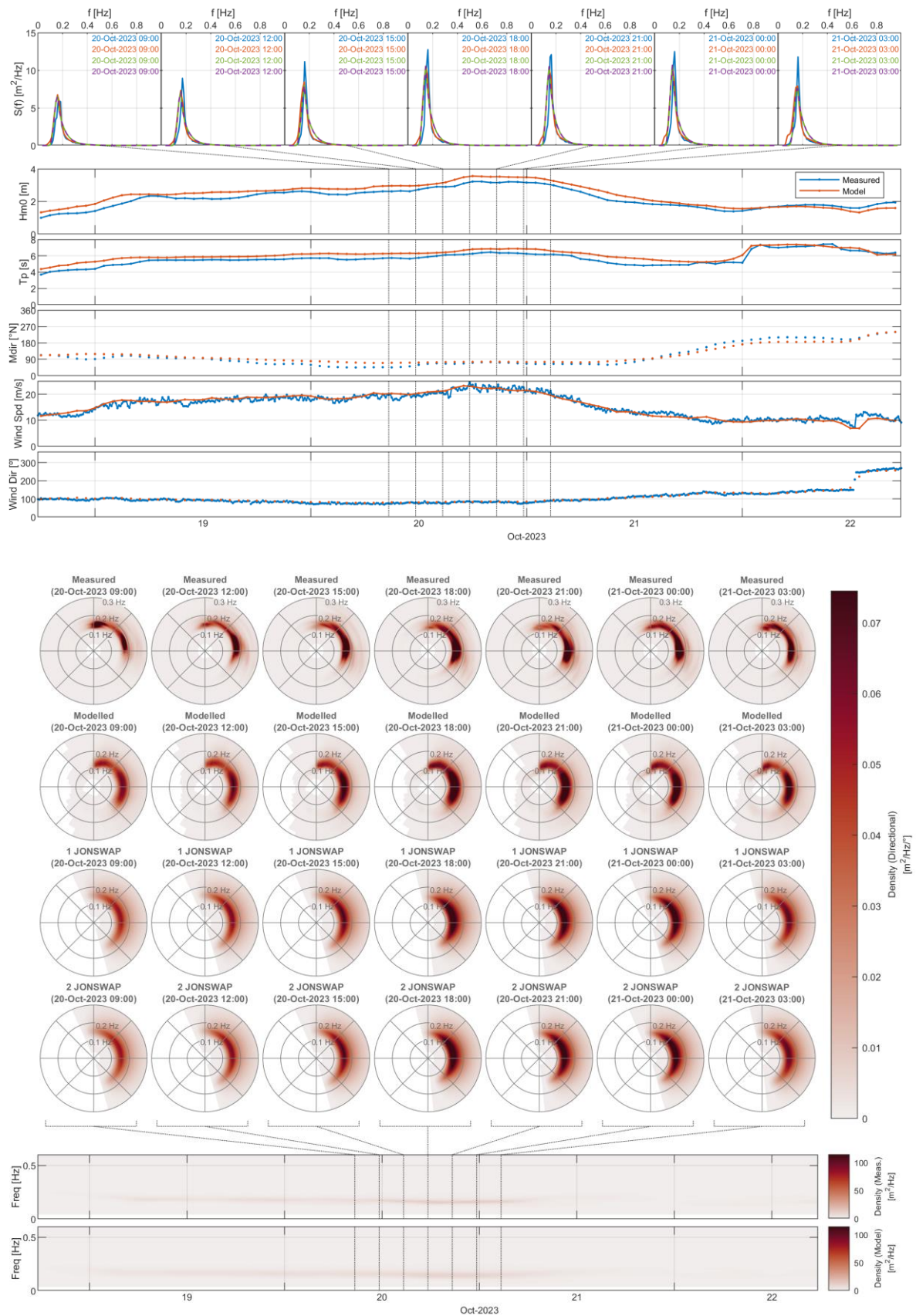


Figure F.39. NSI-2-LB, largest measured wind speed from the east.



Metocean Data Overview – North Sea I Offshore Wind Farm

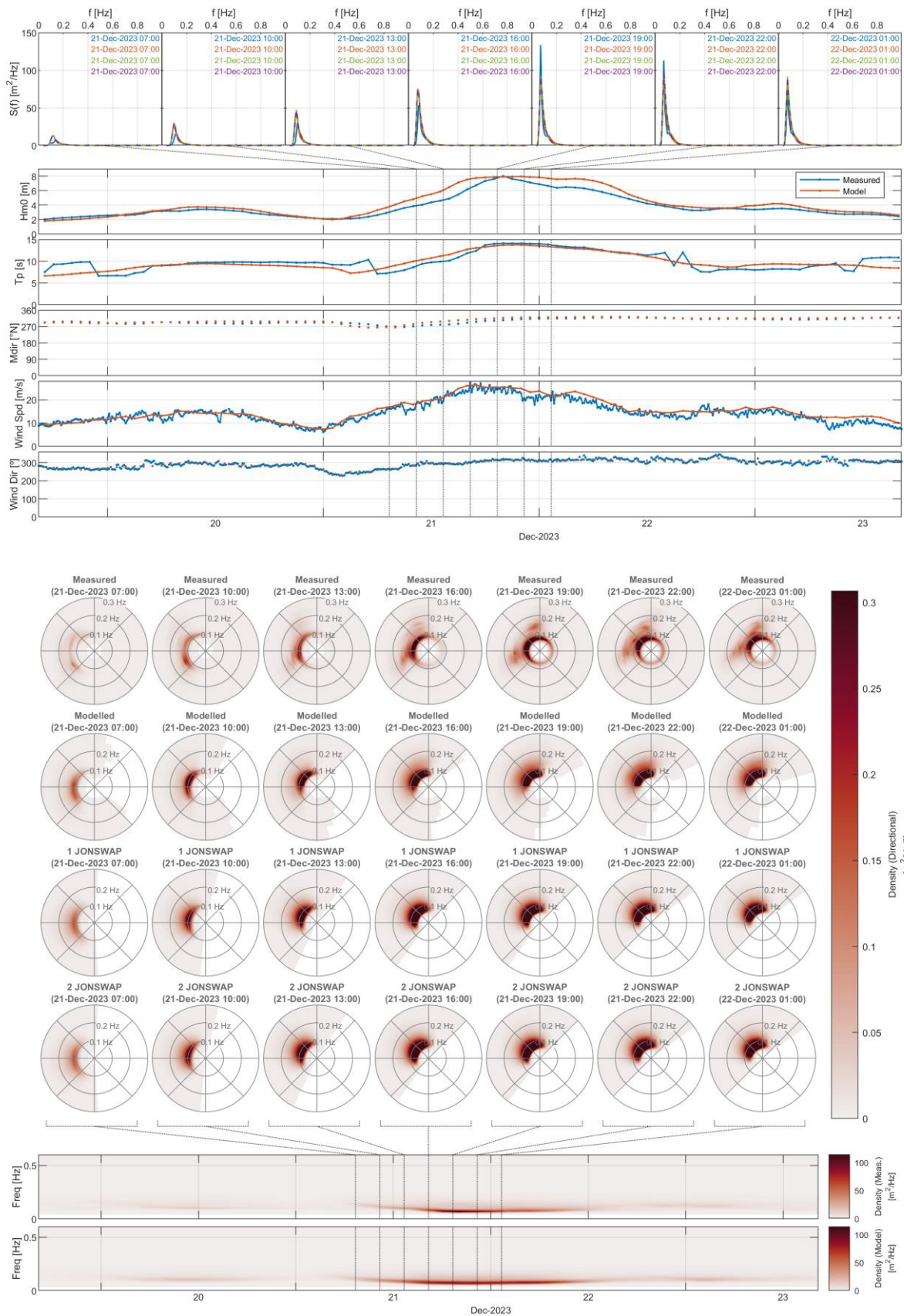


Figure F.40. NSI-2-LB, largest measured wind speed from the west.



Appendix G. JONSWAP Fitting

G.1 Introduction

In Appendix F measured wave spectra were compared to not only modelled spectra, but also spectral representations given by 1 and 2 JONSWAP spectra. In general terms, these representations are constructed as follows:

2 JONSWAP

- a) Separate each modelled spectrum into at most one wind-sea and one swell component.
- b) For each component, fit a JONSWAP spectral shape to the omni-directional spectrum, and use a \cos^2n directional distribution to represent the directional behaviour.

1 JONSWAP

- a) Fit a JONSWAP spectral shape to the omni-directional spectrum as a whole, and use a \cos^2n directional distribution.

This Appendix provides more details on these steps, with the method used to partition spectra described in Section G.2, and the fitting of spectral shapes described in Section G.3.

G.2 Partitioning

In order to determine the 2 JONSWAP representation, modelled spectra were first separated into wind-sea and swell partitions, before fitting a JONSWAP spectral shape

For separating wind-sea and swell components, a multi-stage approach has been used as follows:

1. Partition the spectrum into separate systems using a watershed method.
2. Determine which systems are considered wind-sea and which swell.
3. Merge systems as appropriate, e.g. if peaks are close, or we seek a final description with a limited number of systems, e.g. a single wind-sea and a single swell.

This is carried out using XWaves, a third-party ocean surface wave field analysis toolbox for MATLAB. Please see <https://www.waveforcetechnologies.com/xwaves> for more details.

By way of example of the process, we will consider the spectrum shown⁶ in Figure G.1. Overlaid (green line) is the wind direction. Here we can see what appears to be wind-sea from an easterly direction, with a more concentrated swell from the north, and perhaps a second swell from NNW.

⁶ Please note that this is just a useful spectrum to describe the methodology, taken from a location in the southern North Sea, rather than being specific to this project.

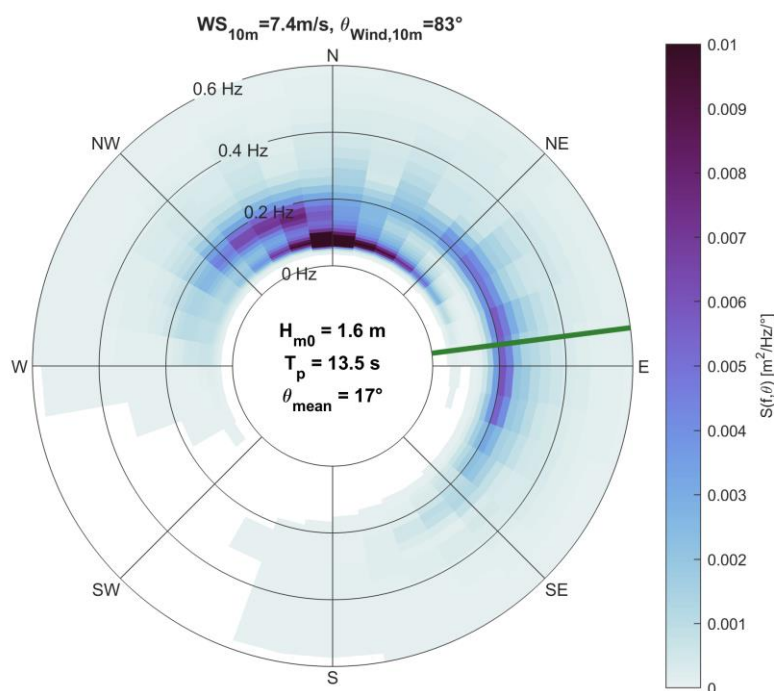


Figure G.1. Example directional spectrum for watershed method.

G.2.1 Wave System Identification

As noted above, the first stage in the partitioning algorithm is to split the spectrum into different systems. For performance reasons, this calculation is carried out using watershed algorithms commonly used in image processing applications. These are certainly beyond the scope of this document, however to conceptually understand the process, we consider a slightly simpler approach (as described in Hansen & Phillips, 2001 [24]).

Firstly, we take the spectrum as a three-dimensional surface, whose elevation corresponds to spectral energy. For our example spectrum, this is shown in Figure G.2.

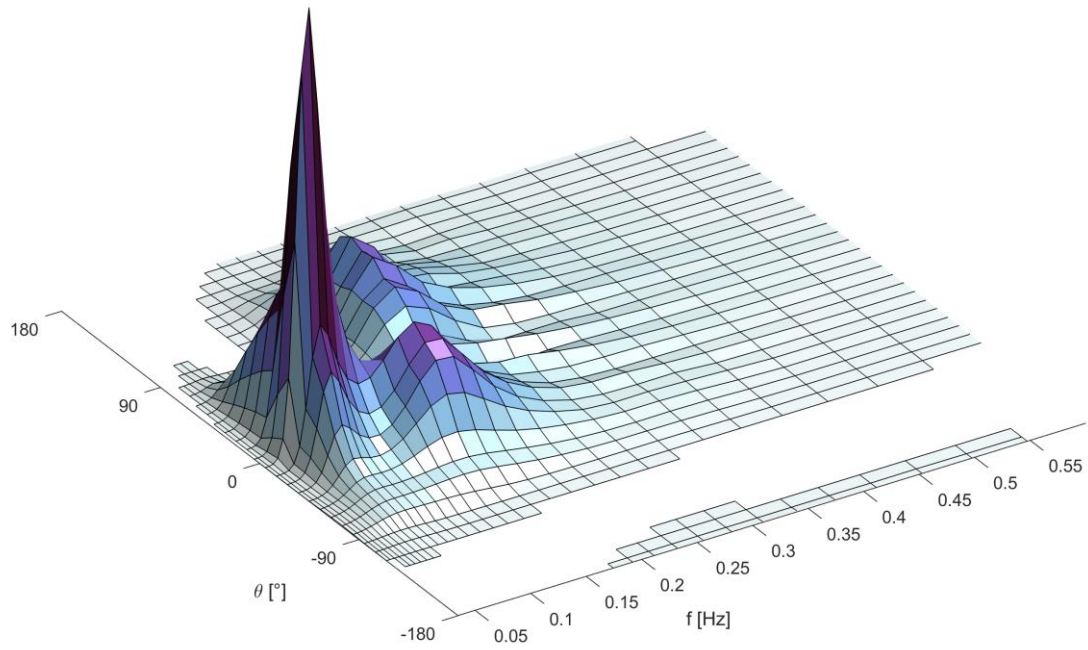


Figure G.2. Directional spectrum, with $S(f, \theta)$ used to give elevations.

Then we *invert* elevations, as shown in Figure G.3.

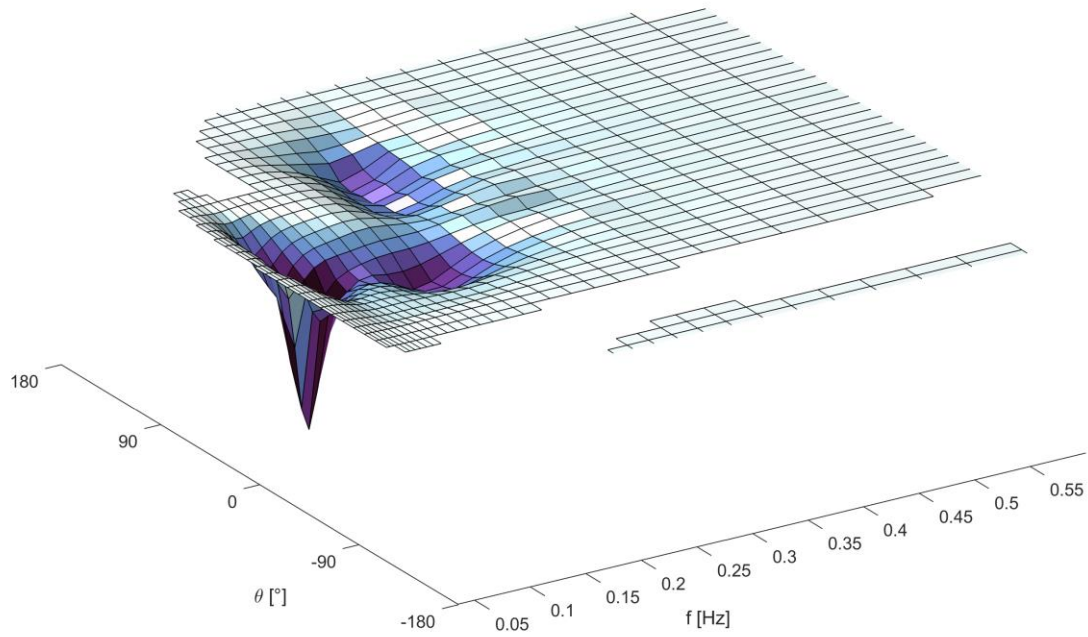


Figure G.3. Directional spectrum, with minus $S(f, \theta)$ used to give elevations.



Now imagine a drop of water falling on this surface. Under the assumption that the drop flows downhill in the direction of the steepest slope, if the drop falls at, say $f = 0.35$ Hz, $\theta = 95^\circ$ (green dot in Figure G.4) it will follow such a downhill path (magenta line in Figure G.4) until it reaches the bottom of a trough (red dot in Figure G.4).

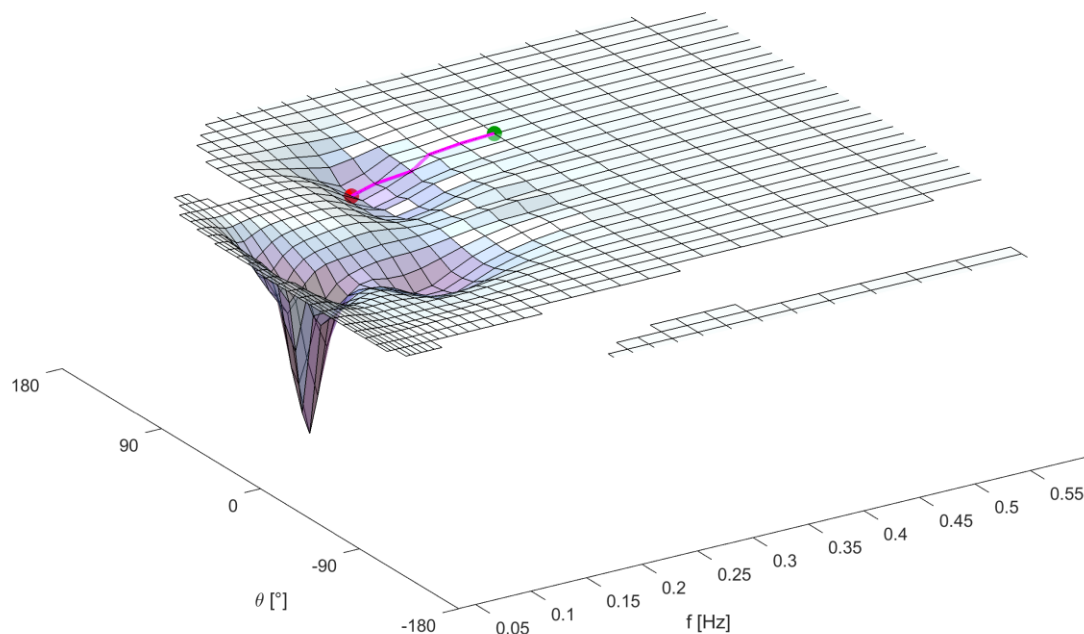


Figure G.4. Downward path for example frequency/direction bin.

If we repeat this for all frequency and direction bins with non-zero values of $S(f, \theta)$, there will be some collection of start points for which the rain drop ends up in the deepest minimum. Let us term this collection of points “Partition 1”. Similarly, there will be another collection for which it ends up at a second minimum, say, “Partition 2”, etc. If some additional caution is taken with regard to flat sections, or indeed local minima which are little different to their surroundings, ultimately all values with non-zero energy will be assigned to a relatively small number of discrete sets of partitions.

Whilst the actual steps used differ – more analogous with flooding the surface with a rising water level from below, and assigning boundaries when two basins join – the resultant partitions are very similar. In our example, such a method leads to the boundaries shown in Figure G.5, and ultimately three partitions.

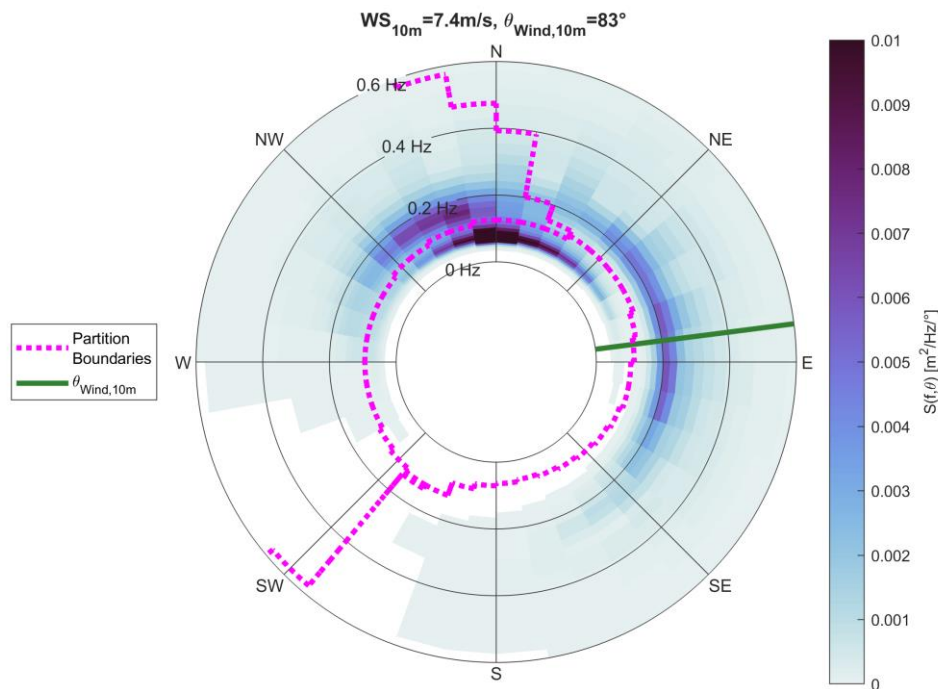


Figure G.5. Example directional spectrum, with watershed boundaries.

G.2.2 Wave System Classification

After splitting the spectrum into various partitions, they are subsequently categorised as wind-sea or swell based on a variant of the wave-age criterion. This is carried out for each identified partition independently as follows:

STEP 1: Split into wind-sea and swell

Each spectral bin of the partition is classified as swell if the following condition is met:

$$\frac{WS_{10m}}{c} \cdot \cos\left(\frac{\theta_{Wave} - \theta_{Wind,10m}}{2}\right) < WA_{SL}$$

Where:

- WS_{10m} is the wind speed at 10 m.
- $\theta_{Wind,10m}$ is the wind direction at 10 m.
- θ_{Wave} is the direction of the spectral bin.
- c is the wave phase velocity of the spectral bin.
- WA_{SL} is a user defined wave-age swell limit.

If the condition is not met, the spectral bin is considered wind-sea.

It is worth noting that this step is very similar to the standard wave-age criterion, which may be used to partition waves by simply assigning each spectral bin to wind-sea or swell directly using a condition of the form:

$$\frac{WS_{10m}}{c} \cdot \cos(\theta_{Wave} - \theta_{Wind,10m}) < WA_{SL}$$



One key difference here is the halving of the angle between wind and wave directions, which ultimately means a widening of the directions which are considered wind-sea. This can significantly improve performance with turning winds, or where coastal effects play a significant role. A second key difference is that here the criterion only forms *part* of the overall process. In particular, misclassification of an individual frequency bin at this stage will not necessarily mean that it is misclassified in the final results, as would be the case if the wave-age criterion alone is used.

STEP 2: Classify partition based on fraction of energy that is wind-sea

An entire partition is considered wind-sea if:

$$F_{wind-sea} = \frac{E_{wind-sea}}{E_{total}} \geq WF$$

For some “wind-force limit”, WF , where $E_{wind-sea}$ is the sum of the partition spectral energy considered wind-sea, and E_{total} the total partition energy.

The results of applying this method to our example spectrum are shown in Figure G.6. Here, each of the three partitions identified by the watershed method are shown. Overlaid are the wind direction (green line) and the boundary determined by STEP 1 of this process with a typical WA_{SL} value of 0.59 (brown dashed line).

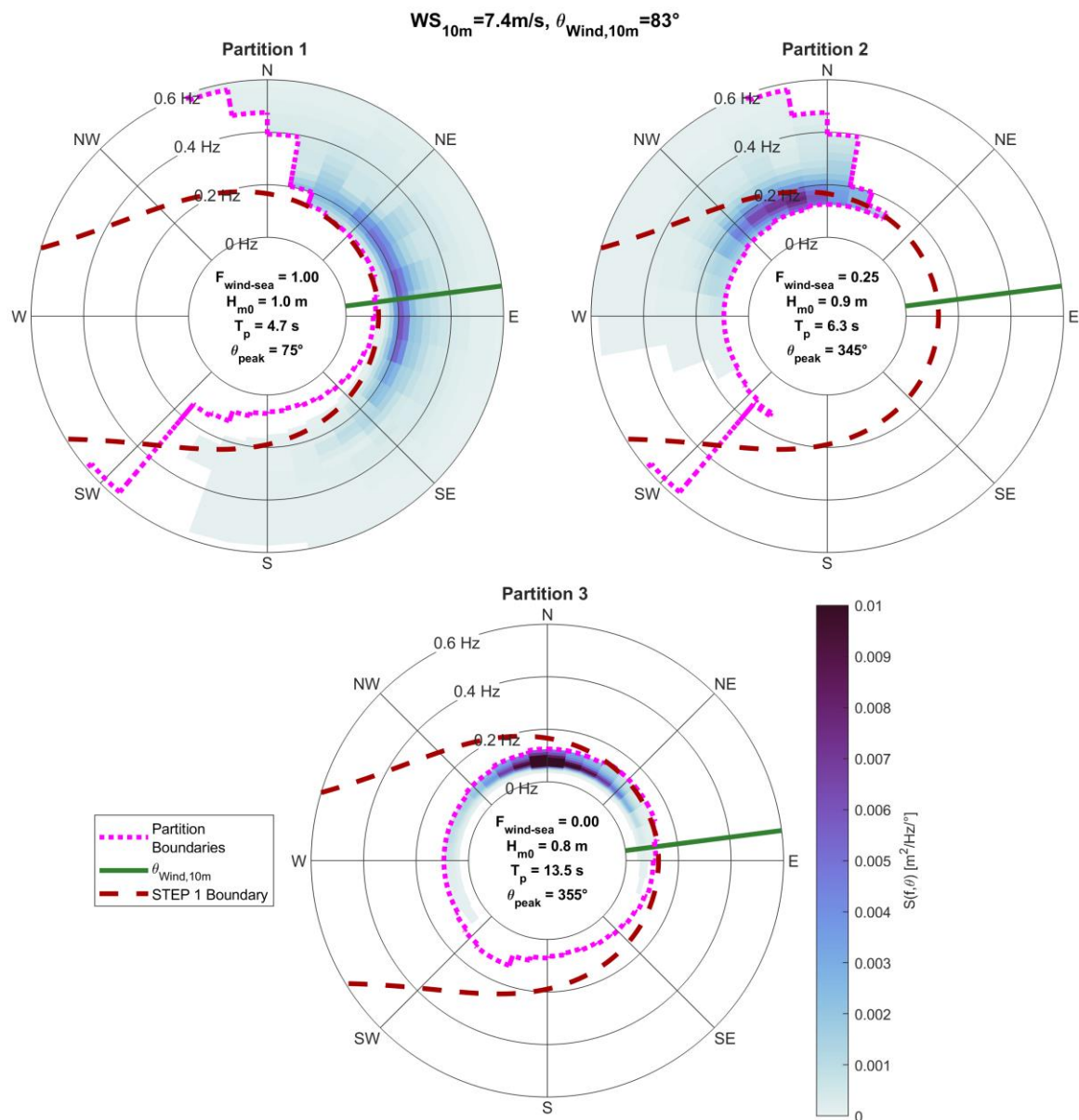


Figure G.6. Example directional spectrum, system classification.

Here we see that for the partition denoted “Partition 1”, almost all of the energy is to the right of this boundary, i.e. on the same side of the boundary as the wind. Indeed, the fraction of the partition energy that is determined to be wind-sea by STEP 1 (denoted $F_{wind-sea}$) is 1.00. Thus, for any reasonable choice of wind-force-limit, this entire partition would be considered wind-sea. Similarly, Partition 3, with $F_{wind-sea} = 0.00$, would be considered swell. Classification of Partition 2, $F_{wind-sea} = 0.25$, is certainly more dependent on the threshold, WF . In most cases a value of 0.5 is reasonable – if more than half the energy is wind-sea then the partition itself is deemed to be wind-sea, otherwise it is swell – and in such a case, Partition 2 would also be classified as swell.



G.2.3 Combining Systems

It is certainly possible that the previous steps can lead to more partitions than are ultimately required. The first case to consider is that where the watershed algorithm splits the data into too many partitions. For example, local minima caused by noisiness in measured data may lead to such over-partitioning. This can be addressed through a variety of steps, including:

- Combining systems deemed to be wind-sea such that there is only one such partition.
- Combining swells whose peaks are close to each other in direction and/or frequency when compared to the spreads of each system.
- Combining swells where the lowest value between them is close in value to the smaller peak.

The second case to consider is that where the required description includes less partitions than are actually present in the spectrum. For example, we may wish to describe all spectra using *one* swell partition and *one* wind-sea partition, but the spectrum we are using as an example consists of three systems. The simplest approach is perhaps to simply combine all components considered swell. However, if our ultimate aim is an accurate representation of the spectrum through two systems described by a small number of parameters (for example, two JONSWAP spectra) this may not be optimal. So instead, the partitions are sorted in order of energy, and those swells whose ranking is below the number of systems required are merged with their nearest neighbours in frequency-direction space. Whilst this may ultimately lead to systems which were previously considered swell being merged with those considered wind-sea, as a whole it leads to less merging of dissimilar systems.

In our example, the partition with least energy, that labelled Partition 3, is merged with its nearest neighbour (Partition 2) yielding a final split as shown in Figure G.7.

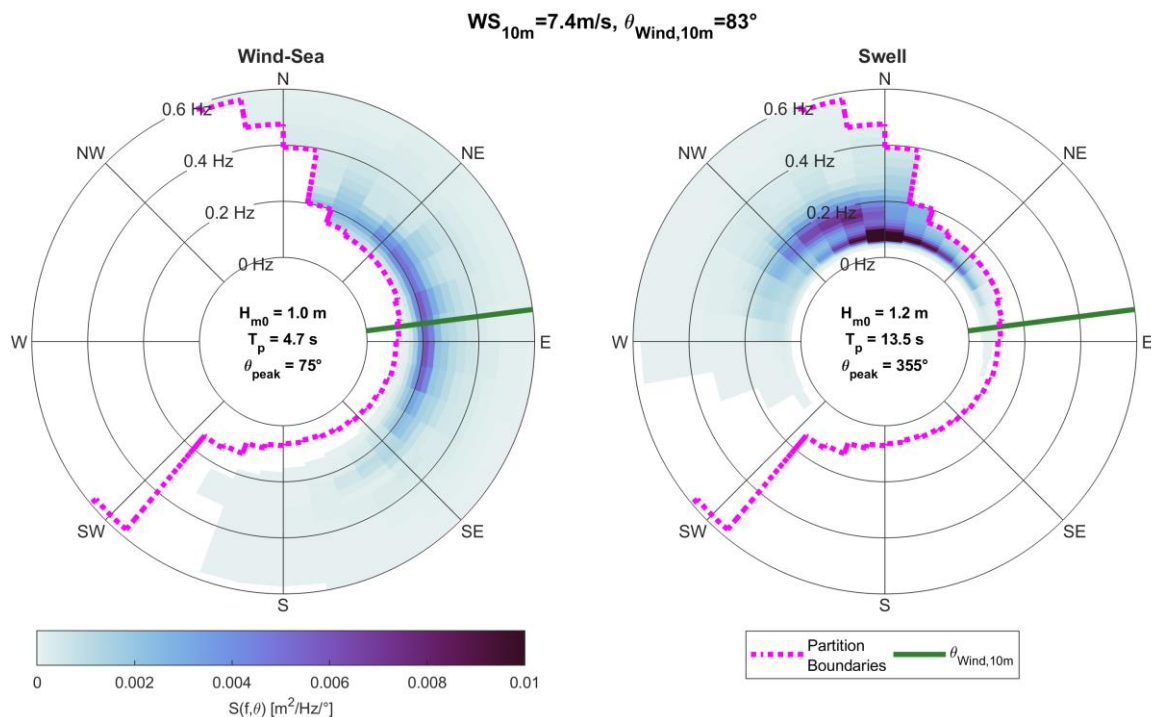


Figure G.7. Example directional spectrum, final partitions.



G.2.4 Additional Considerations

When compared to the wave-age criterion method alone, the watershed method does have advantages, most notably:

- a) In using spectral energy, in addition to wind speed and direction, it is able to ensure that systems as a whole are kept together, rather than regularly split in two.
- b) It is not limited to a single swell partition, and as such can be used to give a much more detailed view of wave systems at a particular location, even if merging is ultimately required to give a more concise final description.

However, it is also important to remember that it is by no means a “perfect” solution. Often systems will merge, leaving no dip in energy at which to divide them. This may be particularly problematic when both wind-sea and swell come from exactly the same direction. Similarly, small dips in noisy spectra may lead to over-partitioning, although this can be to some extent addressed with a variety of smoothing algorithms. Finally, it is worth noting that the line between what should be considered “wind-sea” and “swell” can be somewhat subjective – a problem for any partitioning method.

G.3 Fitting of Spectral Shapes

We now move our attention to the fitting of parametric spectral shapes to the directional spectra. For each timestamp independently:

- For the **1 JONSWAP** dataset, a single parametric spectrum is fitted to the directional spectrum in its entirety.
- For the **2 JONSWAP** dataset, a parametric spectrum is fitted to any wind-sea and swell partitions identified. These are then added together to form the full spectrum.

Each parametric spectrum consists of two parts:

- a) A JONSWAP spectral shape to represent the omni-directional spectrum.
- b) A cos²ⁿ directional distribution, specified through a single central direction and directional spread value for each spectrum.

All fitting is carried out in the XWaves software mentioned in Section G.2. For reference, more details on the spectral shapes used are included in the sections below.

G.3.1 JONSWAP Spectral Shape

The JONSWAP spectrum (see for example Annex B of IEC 61400-3 [25]) specifies that the omni-directional spectral density, S_{JS} , of the surface elevation is given, for frequency f in Hertz, by:

$$S_{JS}(f) = C(\gamma) \cdot S_{PM}(f) \cdot \gamma^\alpha$$

Where:

- $S_{PM}(f)$ is the Pierson-Moskowitz spectrum, which for significant wave height, H_{m0} , and peak frequency, $f_p = 1/T_p$, is defined as:

$$S_{PM}(f) = 0.3125 \cdot H_{m0}^2 \cdot f_p^4 \cdot f^{-5} \cdot \exp\left(-1.25 \left(\frac{f_p}{f}\right)^4\right)$$



- The exponent, α , is given by:

$$\alpha = \exp\left(-\frac{(f - f_p)^2}{2\sigma^2 f_p^2}\right)$$

With $\sigma = 0.07$ for $f \leq f_p$ and $\sigma = 0.09$ for $f > f_p$

- $C(\gamma)$ is a normalizing factor, with various empirical forms included in the guidelines. For example, IEC 61400-3 states:

$$C(\gamma) = 1 - 0.287 \cdot \ln(\gamma)$$

whilst DNVGL-RP-C205 [12] gives:

$$C(\gamma) = \frac{0.2}{0.065\gamma^{0.803} + 0.135}$$

and ISO 19901-1 [19] gives:

$$C(\gamma) = \frac{0.0624}{0.3125 \cdot (0.230 + 0.0336\gamma - 0.185 \cdot (1.9 + \gamma)^{-1})}$$

Note that in practise, there is little difference between these three forms for $1 \leq \gamma < 5.5$, nor between the DNV and ISO options for at least $1 \leq \gamma < 10$. For this work, we have used the DNV equation, largely because its inclusion in an earlier (2005) issue of ISO 19901-1 for $1 \leq \gamma < 10$ gives at least some corroboration between guidelines.

G.3.2 Cos2n Directional Distribution

After the JONSWAP parameters have been determined for the *omni*-directional spectrum, a central wave direction, θ_c , and directional spreading parameter, n , are determined through a least-squares fit, such that the full parametric directional spectrum, $S_p(f, \theta)$, is represented by:

$$S_p(f, \theta) = S_{JS}(f)D(\theta)$$

With:

$$D(\theta) = \begin{cases} D_{2n} \cos^{2n}(\theta - \theta_c) & \text{if } |\theta - \theta_c| \leq 90^\circ \\ 0 & \text{otherwise} \end{cases}$$

And D_{2n} is a normalization function given by:

$$D_{2n} = \frac{\sqrt{\pi} \Gamma(n + 1)}{180 \Gamma(n + 1/2)}$$

Where Γ is the Gamma function.

Though not of concern in the current work, a little caution is generally necessary in interpreting the spread parameter n here, since some sources (e.g. XWaves and thus this report) describe the distribution through an equation of the form \cos^{2n} whilst others (e.g. DNVGL-RP-C205 [12]) use an equation of the form \cos^n . Whilst these are just two ways to describe the same distribution, the value of the parameter n is not directly interchangeable between the two without being doubled/halved as necessary.